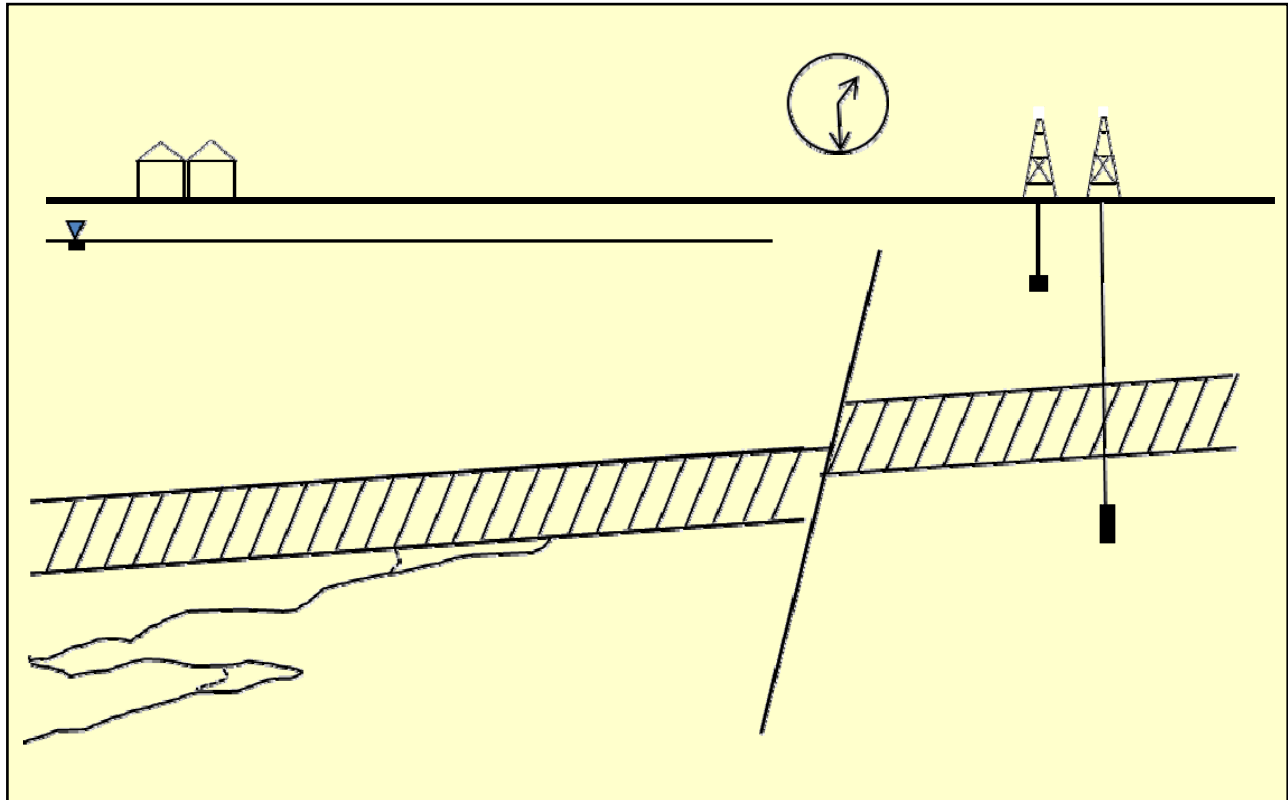


April 2012

Impact of CO₂ Impurities on Storage Performance and Assurance



**Report on Tasks 1 and 2 Prepared for:
CO₂ Capture Project (Phase III)
Revision 1**

by

Jean-Philippe Nicot and Silvia V. Solano

with collaboration of

R. T. Johns^{*,#}, A. Venktraman^{*}, H. Ramachandran^{*}, and G. A. Pope^{*}

^{*}: Department of Petroleum and Geosystems Engineering, The University of Texas at Austin

[#]: now at Department of Energy and Mineral Engineering, The Pennsylvania State University

Bureau of Economic Geology

John A. and Katherine G. Jackson School of Geosciences

The University of Texas at Austin

Austin, Texas 78713-8924

Impact of CO₂ Impurities on Storage Performance and Assurance

Revision 1

**Jean-Philippe Nicot and Silvia V. Solano
with collaboration of**

R. T. Johns^{*,#}, A. Venktraman^{*}, H. Ramachandran^{*}, and G. A. Pope^{*}

^{*}: Department of Petroleum and Geosystems Engineering, The University of Texas at Austin

[#]: now at Department of Energy and Mineral Engineering, The Pennsylvania State University

Bureau of Economic Geology

John A. and Katherine G. Jackson School of Geosciences
The University of Texas at Austin
Austin, Texas 78713-8924

Executive Summary

The goal of this study was to understand the impact of impurities (mostly N₂, O₂, and Ar, to which might be added CH₄, commonly present to saturation levels in the subsurface) on CO₂ plume dynamics, injectivity, and capacity. The study considered up to 15% volume for N₂, 5% volume for O₂, and 5% volume for Ar. Other gases such as CO, H₂, and SO_x, which could have non-negligible mole fractions, are not considered in the study. The problem is approached through an extended desktop study using the numerical modeling tool (multiphase flow code CMG-GEM). In order to work with accurate PVT data (Peng-Robinson EOS), laboratory experiments were performed early in the study to access viscosity and density of the mixtures. CMG-GEM relies on many empirical mixing rules for density and viscosity calculations that need to be calibrated and tuned. In parallel, a comprehensive literature survey was undertaken to collect information on solubility of those various mixture components into the aqueous phase under various subsurface pressure, temperature, and salinity conditions. The differential partitioning of gas components in the aqueous phase impacts the gas phase composition. The work presented in this document is part of a larger study that includes geochemical impact of impurities (reactivity of gas components with other components and with minerals), an aspect not treated here. Overall, geochemical processes could affect near-field properties such as injectivity and well integrity whereas larger-scale regional impacts can be studied through an understanding of plume dynamics. An important observation controlling all the results of the study is that viscosity and density of mixtures are lower than that of neat CO₂ at identical temperature and pressure. Equally important to note, viscosity and density contrast between mixtures and neat CO₂ decreases with depth.

The numerical models used grow in complexity from simple box-like generic models, to which heterogeneity is added in a second step, to more realistic models constructed from two actual U.S. Gulf Coast Region locations (clastic sediments) and from a Canadian (Alberta) carbonate formation but representative of many sites around the world. The objective was to reproduce end-members of aquifer architecture such as (1) clean homogeneous, medium permeability sand; (2) homogeneous sand/clay, and (3) heterogeneous sand with discontinuous shale partings and continuous baffles. Progressively more complex systems, binary, ternary, and beyond, were investigated. The results are normalized with respect to corresponding neat CO₂ case and draw on two key metrics, time to hit the top and maximum extent, are contrasted for 2 depths “shallow” (~5,000 ft, ~60°C, 2500 psi, 100,000 mg/L) and “deep” (~10,000 ft, 125°C, 4500 psi, 180,000 mg/L). Because O₂, N₂, and Ar have similar properties and behavior, they impact the CO₂-dominated mixtures in a similar way, particularly at the concentration level of a couple percent molar and they can be merged in one unique component with properties of N₂. However, the approximation deviates from the “true case” beyond a few percents.

Impurities impact density and viscosity of the CO₂-rich mixture. A lower density impacts CO₂ capacity not only because of the smaller fraction injected and space needed for storing impurities but also because of the generally lower density of the impurities at the same conditions. An approximate proxy for capacity change owing to impurities is given by the density ratio. The loss in capacity can be as high as >50% at very shallow depths (~3000 ft, CO₂ and 15% molar N₂) but the difference quickly decreases with depth. Similarly, mass injectivity, that can be represented by the proxy metric of density over viscosity ratio, also shows a decreased value at very shallow depths that quickly recovers with increasing depth.

In terms of plume shape and extent, the impact of impurities is again more marked at shallow depth where the contrast in density and viscosity with neat CO₂ is the largest. It decreases with depth. For example, about 4% mole fraction in a binary system suffices to increase plume length in “shallow” low-dip sloping layers by 25% whereas 9 to 15%, depending on the component, are needed in a “deep” system. In all cases, plume extent is greater with impurities however residual trapping occurs faster. This relationship mostly holds for all systems whatever the level of heterogeneity and complexity. The contrast is most extreme in very simple systems and heterogeneity assuming adequate operational choices seems to dampen impacts of impurities. This presumably occurs because heterogeneity creates multiple tongues blunting the impact of impurities.

It also suggests a trade-off between plume extent (area of review with risk of CO₂ leakage) and decreased risk owing to faster trapping. A larger plume translates into a larger area to inspect for leakage pathways such as faults and abandoned wells but a faster trapping translates into a shorter period of time to monitor the site.

Table of Contents

Executive Summary	i
Table of Contents	iii
List of Tables	ix
Acknowledgments	xi
Acronyms	xi
I. Introduction	1
II. Approach	3
II-1. Impurity Data Collection and Characterization	3
II-1-1 Literature Search on Stream Composition	5
II-1-2 Associated Issues	7
II-2. Metrics	8
II-3. Reservoir Models	13
II-3-1 Description of Generic Models	13
II-3-2 Description of the Shallow Model (Texas Gulf Coast)	16
II-3-3 Description of the Deep Model (Mississippi Gulf Coast)	18
II-3-4 Description of the Carbonate Model (Alberta)	19
II-4. Reservoir Properties	20
II-4-1 Generic and Gulf Coast Models	20
II-4-2 Canadian Carbonate Model	21
II-5. Previous Results	26
III. Results	29
III-1. Impact on Capacity and Injectivity	29
III-2. Generic Model Results	33
III-2-1 Parametric Study of Stream Composition	33
III-3. Tentative Specifications for Mixed CO ₂ Stream	60
III-4. Impact of Heterogeneity	62
III-5. Results from Actual Field Cases	66
III-5-1 Gulf Coast Cases	66
III-5-2 Carbonate Aquifer Case	73
III-6. Associated Issues	76
IV. Conclusions	77
V. References	79
VI. Appendix A: Phase Behavior Modeling of Gas Mixtures	83
VI-1. Flow Properties of the Gas Mixtures	83
VI-1-1 Summary	83
VI-1-2 Literature review and available experimental data	83
VI-1-3 New experimental data	89
VI-2. Synthetic Gas Mix Density and Viscosity Test Report (Schlumberger)	97
VI-3. Peng-Robinson EOS model for the estimation of the solubility of flue gas components in brine under a range of P, T, S conditions	101
VII. Appendix B: Properties of Pure Components and Gas Mixtures	123
VII-1. Pure Component Properties	123
VII-2. Mixture Properties	126

VIII. Appendix C: GEM Input Files.....	139
IX. Appendix D: Generic and Other Cases.....	148

List of Figures

Figure 1. Impact of dissolution at gas composition at plume front	8
Figure 2. Illustration of how maximum extent and time to reach the top are extracted from run results.	11
Figure 3. Contrast in phase fraction for the two definitions of mobile gas	12
Figure 4. Cross section and map view of the generic model (a, b) with baffles (c, d).	15
Figure 5. Cross-section of the generic model with an heterogeneous permeability field (Realization 1).....	16
Figure 6. 3D view of the shallow Gulf Coast model showing cell depth and wells on the boundary	17
Figure 7. 3D view of the Mississippi Gulf Coast model showing cell depth	18
Figure 8. 3D view of the carbonate reservoir model showing cell depth	20
Figure 9. Permeability and rock type distributions for carbonate aquifer model	20
Figure 10. Relative permeability curves used in generic and Gulf Coast models.	21
Figure 11. Normalized porosity vs. Reservoir Quality Index	22
Figure 12. Permeability histogram from downloaded Petrel model for carbonate aquifer	22
Figure 13. Example of relative permeability curves for different carbonate formations: (a)-(b) water wet rocks and (c)-(d) oil wet rocks	24
Figure 14. Liquid-gas relative permeability curves for the six rock types used in the carbonate reservoir model	25
Figure 15. Mixture density relative to neat CO ₂ (a and c) and mixture density (b and d) as a function of depth. Pressure gradient is 0.465 psi/ft (all) and geothermal gradient is 18°F/1000ft (a and b) or 10°F/1000ft (c and d).....	30
Figure 16. Inverse of mixture viscosity relative to that of neat CO ₂ (a and c) and inverse of mixture density (b and d) as a function of depth. Pressure gradient is 0.465 psi/ft (all) and geothermal gradient is 18°F/1000ft (a and b) or 10°F/1000ft (c and d).....	31
Figure 17. Mixture density-viscosity ratio relative to that of neat CO ₂ (a and c) and density-viscosity ratio (b and d) as a function of depth. Pressure gradient is 0.465 psi/ft (all) and geothermal gradient is 18°F/1000ft (a and b) or 10°F/1000ft (c and d).....	32
Figure 18. Time (years) to reach the top of various ternary mixtures at shallow Gulf Coast conditions: CO ₂ -N ₂ -Ar (a), CO ₂ -N ₂ -O ₂ (b), CO ₂ -N ₂ -CH ₄ (c). (injection period is 30 years).....	36
Figure 19. Time (years) to reach the top of various ternary mixtures at deep Gulf Coast conditions: CO ₂ -N ₂ -Ar (a), CO ₂ -N ₂ -O ₂ (b), CO ₂ -N ₂ -CH ₄ (c). (injection period is 30 years).....	37
Figure 20. Plume extent (ft) of various ternary mixtures at shallow Gulf Coast conditions: CO ₂ -N ₂ -Ar (a), CO ₂ -N ₂ -O ₂ (b), CO ₂ -N ₂ -CH ₄ (c). (injection period is 30 years)	38
Figure 21. Plume extent (ft) of various ternary mixtures at deep Gulf Coast conditions: CO ₂ -N ₂ -Ar (a), CO ₂ -N ₂ -O ₂ (b), CO ₂ -N ₂ -CH ₄ (c). (injection period is 30years).....	39
Figure 22. Plume extent for the 4-component Composition A system, GC shallow and deep cases (with dissolution, at 100 years)	40
Figure 23. Plume extent for the 4-component Composition C system, GC shallow and deep cases (with dissolution, at 100 years)	41
Figure 24. Impact of dissolution on results for GC shallow (a) and deep (b) cases.	42

Figure 25. Plume extent in feet at 100 years with dissolution for GC Shallow and GC deep cases	43
Figure 26. Composition A, dissolution, GC shallow – relative plume extent (a), time to hit the top (b), and mobile fraction at 100 years (c).....	45
Figure 27. Composition A, dissolution, GC deep – relative plume extent at 100 years (a), time to hit the top (b), and mobile fraction at 100 years (c)	46
Figure 28. Composition C, dissolution, GC shallow – relative plume extent (a), time to hit the top (b), and mobile fraction at 100 years (c).....	48
Figure 29. Composition C, dissolution, GC deep – relative plume extent (a), time to hit the top (b), and mobile fraction at 100 years (c).....	49
Figure 30. Gas density (a and b) and compressibility (c and d) for variations in injection stream, GC shallow (a and c) and deep (b and d) reservoirs.	50
Figure 31. Neat CO ₂ phase distribution through time: shallow Gulf Coast (a) and deep Gulf Coast (b) cases	52
Figure 32. Phase distribution of components of Injection Stream A through time: shallow GC (a) and deep GC (b) cases	53
Figure 33. Phase distribution of components of Injection Stream C through time: shallow GC (a) and deep GC (b) cases	55
Figure 34. Mobile fraction as a function of time (a) 0-1000 years; (b) 0-50 years; (c) 0-100 years; and (d) 100-1000 years.....	57
Figure 35. Mobile fraction as a function of time (a) 0-1000 years; (b) 0-50 years; (c) 0-100 years; and (d) 100-1000 years for the shallow (1) and deep (2) Gulf Coast case.....	58
Figure 36. Relative increase in plume extent relative to neat CO ₂ for various binary systems for GC shallow (a, squares) and GC deep (b, diamonds) sites	61
Figure 37. Simple homogeneous case with baffles displaying vertical cross sections along main axis of model for various binary mixtures	63
Figure 38. Comparison of plume extent of homogeneous permeability cases with homogeneous with baffles (“heterogeneous”).....	64
Figure 39. Comparison of plume extent (deep GC case) for 2 realizations.....	64
Figure 40. Permeability field (cross-section) and simulation results (plume extent after 100 years) from Realization #7 (a), #8 (b), and #13 (c) assuming injection stream of neat CO ₂ , Stream A, and Stream C. LHS plots compared plume extent for homogeneous and heterogeneous fields.....	65
Figure 41. Shallow Gulf Coast case, injector well location (a) Case 1: Injector located in lower part of the reservoir (b) Case 2: Injector well located in the upper part of the reservoir (well location of original model)	67
Figure 42. Results (time to reach the top) for injector well located downdip	68
Figure 43. Results comparison for different well locations (Case 1: Injector down dip, Case 2: Injector up dip).....	68
Figure 44. 3D view of shallow Gulf Coast case (injection period 5 years, injection rate 4.73×10^6 scf/day, gas saturation and global mole for: 100% CO ₂ (a); Stream A (b); Stream C (c).	69
Figure 45. Gas Saturation cross-sectional view GC Deep -Stream composition 100% CO ₂ (Realization # 2) after 1000 years.....	70

Figure 46. Plume extent for 2 realizations of the deep Gulf Coast case for 3 injection streams: neat CO ₂ , Stream A, and Stream B after 100 years of injection, open downdip boundary.	70
Figure 47. Plume extent for 2 realizations of the deep Gulf Coast case for 3 injection streams: neat CO ₂ , Stream A, and Stream B after 1000 years of injection, open downdip boundary.	71
Figure 48. Gas Saturation after 1000 years (closed boundaries – GC deep)	71
Figure 49. Plume extent for 2 realizations of the deep Gulf Coast case for 3 injection streams: neat CO ₂ , Stream A, and Stream B after 100 years of injection, closed boundaries ...	72
Figure 50. Plume extent for 2 realizations of the deep Gulf Coast case for 3 injection streams: neat CO ₂ , Stream A, and Stream B after 1000 years of injection, closed boundaries .	72
Figure 51. Gas saturation cross-section for: (a) neat CO ₂ ; (b) stream composition A; and (c) stream composition C.	73
Figure 52. Impact on injection stream composition on parametric study for Nisku aquifer: (a) plume extent at 100 yr; (b) plume extent at 1000 yr; and (c) time to hit the top	74
Figure 53. Impact on injection stream composition (95% CO ₂) on parametric study for Carbonate Aquifer: (a) plume extent at 100 yr; (b) plume extent at 1000 yr; and (c) time to hit the top	74
Figure 54. Impact on injection stream composition (85% CO ₂) on parametric study for Carbonate Aquifer: (a) plume extent at 100 yr; (b) plume extent at 1000 yr; and (c) time to hit the top	75
Figure 55. Impact on injection stream composition (75% CO ₂) on parametric study for Carbonate Aquifer: (a) plume extent at 100 yr; (b) plume extent at 1000 yr; and (c) time to hit the top	75
Figure 56. Densities for pure nitrogen at 80°F measured in the lab and from the NIST data base	95
Figure 57. Comparison of NIST viscosities and densities to measured experimental data for pure CO ₂ at 175°F.	95
Figure 58. Change in density and viscosity with composition at 175oF and 4000 psia	96
Figure 59. Match between experimental and calculated data a T = 194°F and S = 34750 ppm .	102
Figure 60. Variation of BICs for H ₂ O-CO ₂ pair with salinity	102
Figure 61. Variation of CO ₂ solubility with temperature for different pressures for pure water	103
Figure 62. Match between experimental and calculated data a T = 194°F and S = 34,750 ppm	104
Figure 63. Variation of BICs for H ₂ O-N ₂ pair with salinity	104
Figure 64. Variation of N ₂ solubility with temperature for different pressures for pure water ...	105
Figure 65. Match between experimental and calculated O ₂ solubility data a T = 194°F and S = 67,216 ppm	106
Figure 66. Variation H ₂ O-O ₂ BICs with salinity	107
Figure 67. Match between experimental and calculated Ar solubility data a T = 32.36°F and S = 34,750 ppm	108
Figure 68. Variation of BICs for H ₂ O-Ar pair with salinity	109
Figure 69. Solubility of gas mixtures in water.....	111
Figure 70. Solubility of gas mixtures in water (blow up of Figure 58)	111
Figure 71. Solubility of gas mixture in 100,000 ppm brine.....	112
Figure 72. Blow up of Figure 60.....	113
Figure 73. Solubility of gas mixture in 200,000 ppm brine.....	114

Figure 74. Blowup of Figure 62.....	114
Figure 75. Solubility of gas mixture in pure water	115
Figure 76. Blowup of Figure 64.....	116
Figure 77. Solubility of gas mixture in 100,000 ppm brine.....	117
Figure 78. Blowup of Figure 66.....	117
Figure 79. Solubility of gas mixture in 200,000 ppm brine.....	118
Figure 80. Blowup of Figure 68.....	119
Figure 81. Density vs. depth for pure components (0.43 psi/ft and 12°F/1000 ft).....	123
Figure 82. Viscosity vs. depth for pure components (0.43 psi/ft and 12°F/1000 ft)	124
Figure 83. Comparison of CO ₂ density with depth for two different temperature gradients.....	124
Figure 84. Solubility of CO ₂ , N ₂ , O ₂ , and Ar for a TDS of 50,000 (a), 100,000 (b), and 200,000 ppm (c) as a function of depth; solubility of CO ₂ for various TDS as a function of depth(d).....	125
Figure 85. Compressibility vs. depth of pure components	126
Figure 86. Density (kg/L) of various ternary mixtures at shallow Gulf Coast conditions: CO ₂ - N ₂ -Ar (a), CO ₂ -N ₂ -O ₂ (b), CO ₂ -N ₂ -CH ₄ (c).....	128
Figure 87. Density (kg/L) of various ternary mixtures at deep Gulf Coast conditions: CO ₂ -N ₂ - Ar (a), CO ₂ -N ₂ -O ₂ (b), CO ₂ -N ₂ -CH ₄ (c).....	129
Figure 88. Viscosity (cp) of various ternary mixtures at shallow Gulf Coast conditions: CO ₂ - N ₂ -Ar (a), CO ₂ -N ₂ -O ₂ (b), CO ₂ -N ₂ -CH ₄ (c).....	130
Figure 89. Viscosity (cp) of various ternary mixtures at deep Gulf Coast conditions: CO ₂ -N ₂ - Ar (a), CO ₂ -N ₂ -O ₂ (b), CO ₂ -N ₂ -CH ₄ (c).....	131
Figure 90. Density/Viscosity ratio of various ternary mixtures at shallow Gulf Coast conditions: CO ₂ -N ₂ -Ar (a), CO ₂ -N ₂ -O ₂ (b), CO ₂ -N ₂ -CH ₄ (c).....	132
Figure 91. Density/Viscosity ratio of various ternary mixtures at deep Gulf Coast conditions: CO ₂ -N ₂ -Ar (a), CO ₂ -N ₂ -O ₂ (b), CO ₂ -N ₂ -CH ₄ (c).....	133
Figure 92. Buoyant driving force of various ternary mixtures at shallow Gulf Coast conditions: CO ₂ -N ₂ -Ar (a), CO ₂ -N ₂ -O ₂ (b), CO ₂ -N ₂ -CH ₄ (c).....	134
Figure 93. Buoyant driving force of various ternary mixtures at deep Gulf Coast conditions: CO ₂ -N ₂ -Ar (a), CO ₂ -N ₂ -O ₂ (b), CO ₂ -N ₂ -CH ₄ (c).....	135
Figure 94. Aqueous phase density (kg/L) of brine at equilibrium with various ternary mixtures at shallow Gulf Coast conditions: CO ₂ -N ₂ -Ar (a), CO ₂ -N ₂ -O ₂ (b), CO ₂ -N ₂ -CH ₄ (c).....	136
Figure 95. Aqueous phase density (kg/L) of brine at equilibrium with various ternary mixtures at deep Gulf Coast conditions: CO ₂ -N ₂ -Ar (a), CO ₂ -N ₂ -O ₂ (b), CO ₂ -N ₂ -CH ₄ (c).....	137

List of Tables

Table 1. Gas component density close to standard conditions	4
Table 2. Critical properties of common mixture components	4
Table 3. Compilation of stream compositions from oxy-fuel combustion (molar compositions).....	6
Table 4. Maximum, minimum, average and median compositions (molar compositions).....	6
Table 5. Typical stream compositions from oxy-firing a steam generator	6
Table 6. Molar composition of base cases	6
Table 7. Base-case characteristics of the generic model.....	14
Table 8. Base-case characteristics of the shallow Gulf Coast model (from Table 1 in Ghomian et al. (2008)).	17
Table 9. Base-case characteristics of the deep Gulf Coast model.	18
Table 10. Base-case characteristics of the Canadian Carbonate model.....	19
Table 11. Summary of rock properties for different carbonate formations	23
Table 12. Mobile gas fraction (mass fraction) through time for neat CO ₂ , Stream A, and Stream C injection streams	51
Table 13. Binary system impurity level at which the plume extend is increases by some amount.....	60
Table 14. Comparison of Stream A, stream C, and neat CO ₂ (base case) plume extent in various conditions of heterogeneity (GC shallow case)	63
Table 15. Comparison of Stream A, stream C, and neat CO ₂ (base case) plume extent in various conditions of heterogeneity (GC shallow and deep case).....	67
Table 16. Impact of methane-saturated brine of plume metrics	76
Table 17. Experimental data for various mixtures of CO ₂ in the literature	84
Table 18. Available density data for various mixtures of CO ₂ in the literature.....	85
Table 19. Available viscosity data for various mixtures of CO ₂ in the literature.....	87
Table 20. Available viscosity and density data for various mixtures of CO ₂ in the literature.....	88
Table 21. Pressure and temperatures for new experimental data.....	93
Table 22. Gas compositions for new experimental data.....	93
Table 23. CO ₂ viscosity measurements (check of viscometer calibration)	93
Table 24. CO ₂ viscosity measurements at various temperatures and pressures requested	93
Table 25. Experimental data for pure CO ₂	93
Table 26. Experimental data for synthetic gas 1 (mole fract.: 85% CO ₂ , 5% N ₂ , 5% O ₂ , 5% Ar).....	93
Table 27. Experimental data for Synthetic Gas 2 (mole fractions: 70% CO ₂ , 10% N ₂ , 10% O ₂ , 10% Ar).....	94
Table 28. Initial input parameters for PREOS for all components.....	94
Table 29. Final input parameters for PREOS for all components that are to be used in GEM	94
Table 30. Coefficient values for the JST viscosity model	94
Table 31. Assumed flue gas composition	101
Table 32. BICs for other CO ₂ related mixtures from literature	110
Table 33. Gas mixture used for testing.....	110

Table 34. Binary interaction coefficients used for the above mixture at 140°F	110
Table 35. Binary interaction coefficients used for the gas mixture at 140°F	112
Table 36. Binary interaction coefficients used for the gas mixture at 140°F	113
Table 37. Binary interaction coefficients used for the gas mixture at 210°F	115
Table 38. Binary interaction coefficients used for the gas mixture at 210°F	116
Table 39. Binary interaction coefficients used for the gas mixture at 210°F	118
Table 40. Single-component viscosity, density, and compressibility of injection stream components as a function of depth.....	127
Table 41. List of generic cases.....	148

Acknowledgments

The authors would like to thank the CO₂ Capture Project for funding this project and, in particular, the project manager, Scott Imbus. We are also grateful to the Computer Modeling Group (CMG), Calgary, Canada, for giving us ~free access to their GEM software. Discussions with several individuals at the BEG were also instrumental in the development of this report, in particular Seyyed Hosseini and Jong-Wong Choi. We are grateful to several individuals who helped us gain access to the WASP model database including William Sawchuk (ARC Resources) and Jerry Jensen (University of Calgary). We also would like to acknowledge the project manager, Scott Imbus, for constant support and original input. The report also benefited from a thorough editing by Lana Dieterich.

Acronyms

BEG	Bureau of Economic Geology
BIC	Binary interaction coefficient
CCP3	CO ₂ Capture Project Phase III
CMG-GEM	Name of the computer code used in the study
EOS	Equation of state
GC	Gulf Coast
IFT	Interfacial tension
MMSCFD	Millions of standard cubic feet per day
Mt	Megatons (10 ⁶ metric tons)
PR-EOS	Peng-Robinson equation of state
SCFD	Standard cubic feet per day

I. Introduction

This work is funded by Phase III of the CO₂ Capture Project (<http://www.co2captureproject.org/>) (CCP3). CCP3 is a partnership of seven major energy companies interested in advancing the technologies that will support the deployment of industrial-scale CO₂ capture and storage. CCP3 requested a proposal from the Bureau of Economic Geology at the University of Texas at Austin (BEG) to address some of the issues related to non-pure CO₂ stream. Geologic sequestration of carbon dioxide (CO₂) is poised to become an important technology for addressing high CO₂ atmospheric concentrations and global warming. The impurities of interest consist of N₂, O₂, H₂, CO, Ar, SO_x to which CH₄, often present in the subsurface, can be added. However, little work has been done to explain the impact of impurities on subsurface behavior of the CO₂-dominated injection stream. In particular, this report investigates the impact of impurities on two of the trapping mechanisms generally put forward: (1) dissolution of CO₂ into formation brine and (2) immobile residual saturation. Concerns about capture economics provided the incentive to investigate those issues. In general, the purer the CO₂ stream, the more expensive the capture process. Leaving some of the impurities in the injection stream could save both capital and operational costs possibly without consequences to the storage part of the project. For example, pipelines and compressors could be re-engineered to handle impurities. In this context, the work attempts to understand the impact of impurities on the behavior of the system. It does not address legal and regulatory issues such as the permissible level of impurities before which an injection scheme would become a waste disposal operation rather than a CO₂ injection operation. The submitted proposal intended to evaluate and understand the impact of CO₂ capture stream impurities on plume dynamics and trapping and fluid-rock interactions. The contract between CCP3 and BEG was executed in December 2009 with an end date of March 31, 2011. It was subsequently extended to September 30, 2012 with additional tasks, in particular related to the Alberta CO₂ Purity Project (ACPP). The technical tasks consisted of:

1. Accessing the PVT data through literature search and experimental work
2. Conducting a parametric study on impact of impurities on plume dynamics and rate and extent of trapping mechanisms in saline aquifers. This task is mostly a desktop numerical study performed with synthetic simplified cases and on actual field models.
3. Conducting rock-fluid interaction studies. This task has a large laboratory component
4. Conducting reactive transport numerical modeling
5. Integrating the results to qualitatively assess the impact of gas impurities on (1) plume shape and evolution, (2) CO₂ permanence, (3) CO₂ storage capacity, (4) well injectivity, (5) storage reservoir integrity, and (6) trace elements released/absorbed during dissolution / precipitation caused by addition of impurities.

This report document full results of Tasks 1 and 2. An earlier version of this report was submitted to stakeholders in November 2011. Changes to this Revision 1 consists mainly in adding results of numerical simulations of a Canadian carbonate aquifer to complement earlier results focused on clastic aquifers. Results for Tasks 3 to 5 will be reported elsewhere. Summary of an earlier preliminary study (Nicot et al., 2008) investigating Task 2 but limited to injection of CO₂, CH₄, and N₂ into a saline aquifer is provided in Section II-5.

Overall, the objectives of the project are (1) to understand plume dynamics as it impacts Area of Review and permanence / containment / leakage (including impacts on trapping mechanisms); (2) to assess impact on capacity; and (3) to assess impact on injectivity. Simulations of CO₂

injection floods with selected impurities levels are conducted on generic models broadly representative of major onshore / near-shore clastic systems in North America and Europe (low to moderate permeability). This document neglects potential geochemical impacts of the injection stream on porosity and permeability, including the dry-out effects next to the wellbore.

The general approach followed in this interim report consists of a parametric study and sensitivity analyses of a generic case and of two previously studied sites in the Gulf Coast but modified slightly to meet our objectives. The following sections contain a description of the models used, the software, and a summary of results. In addition, Appendix A contains information on development of the user-supplied EOS. Appendix B discusses and illustrates properties of pure components and gas mixtures of interest in the study. Appendix C provides sample GEM input files. Appendix D displays a table summarizing all cases run.

II. Approach

This section describes the methodology and the models used. Runs were performed with the *Computer Modeling Group* (CMG) software packages GEM and WINPROP. GEM is a compositional multi-phase flow code that can accommodate multiple gas components and their interaction with a liquid phase (water in this document). WINPROP is an allied module useful to determine and to tune equations of state. To take advantage of these compositional features, we defined the aqueous phase as water-rich “oil,” and “water” is not modeled. Internally, the “oil” phase in GEM is used to model the aqueous phase so that Peng-Robinson Equation of State (PR-EOS) formalism can be used for flash calculations. Note that if water had been treated as an individual phase and not a component, thermo-physical interactions between other components present in the model and water as a phase would have been impossible. The biggest CMG-GEM drawback when dealing with models spanning hundreds to thousands of feet of vertical range, as in this work, is the assumption of an isothermal system. Although GEM can handle temperature variations in a simple way, it does not allow for coupling and flow and heat transport. Because our CMG model is isothermal and H₂O is modeled as a component, temperature and salinity dependence of the flow parameters do not appear explicitly. This dependence is included implicitly by making the binary coefficient (BIC) between the components a function of temperature and brine salinity (see Appendix A).

In consultation with CCP3 technical experts, we set generic models covering at least 3 end-members relative to aquifer architecture and run them with GEM. The focus is on clastic formations due to their abundant distribution relative to carbonate formations.

- Clean homogeneous, medium permeability sand,
- Homogeneous sand / clay, and
- Heterogeneous sand with discontinuous shale partings and continuous baffles.
- Alberta carbonate reservoir

In this section, we detail the approach, including (1) determination of the injection stream composition; (2) description of the metrics used; and (3) description of the generic and actual site models.

II-1. Impurity Data Collection and Characterization

This section reports on CO₂-rich gas stream composition originating from various technologies and collected from the literature. The purpose of the search was to put the maximum concentration of the gas stream components in context. The contract lists the following maximum concentrations (volume fraction): N₂ = 15%; O₂ = 5%; H₂ = 4%; CO = 2%; Ar = 5%, and SO_x = 0.15%. Note that the high H₂ concentration as stated in the contract is a typo and a more reasonable value is 400ppm. This typo has no impact on the results of the tasks presented in this document. The volume fraction gas input needs to be translated into mole fraction, which is independent of pressure and temperature and required by the software. For a given mole fraction distribution, the volume fraction will change as a function of the density of the gas component. Assuming ~standard conditions for which ideal gas law is appropriate, molar fractions can be expressed as a function of the gas density (Table 1) and volume fraction:

$$z_i = \frac{V_i \rho_i}{\sum_i V_i \rho_i}$$

where z_i is mole fraction, V_i is volume fraction, and ρ_i is gas density. For example, a 15% N₂ – 85% CO₂ mixture has a ~10% N₂ mole fraction. A 15% N₂, 5% O₂, and 80% CO₂ has a slightly larger N₂ mole fraction at ~10.2%. The more alike the individual component densities, the closer the numerical values of molar and volume fractions.

Table 1. Gas component density close to standard conditions

Component	Density at 1 atm - 21°C (kg/m³)
CO ₂	1.834
N ₂	1.161
O ₂	1.327
H ₂	0.0835
CO	1.162
Ar	1.654
CH ₄	0.666
SO ₂	2.681
H ₂ S	1.424
H ₂ O	0.759

Gases are often placed in categories such as condensable / non-condensable or reactive / non-reactive. Those definitions primarily apply to pipeline and other engineered systems. Such qualifiers are also attached to those same gases when they are injected into the subsurface even if pressure increase rather than temperature decrease would generate a liquid phase. Reactivity relative to metals, alloys, or plastics might also be different from reactivity with respects to minerals such as feldspars, carbonates, and clays. CO₂, N₂, O₂, H₂, CO, and Ar are generally considered as non condensable. Only trace elements such as hydrocarbons, glycol, and other residues of surface treatment and processes could be placed in that category. CO₂, O₂, H₂, CO, and SO_x are generally considered as reactive; however they are not assumed so in these tasks dedicated to plume dynamics, object of the present interim report. An additional description, more useful to understand the subsurface behavior, consists in quantifying the gas component compressibility. CO₂ is compressible whereas the other significant gases are essentially non-compressible or at least less compressible (as illustrated in Appendix B).

An additional look at the critical properties of the different components (Table 2) suggests that the 4 gases arranged in the following 2 subgroups, N₂ and CO, and, O₂ and Ar, behave similarly.

Table 2. Critical properties of common mixture components

Component	Pc (atm)	Tc (K)	Component	Pc (atm)	Tc (K)
CO₂	72.8	304.2	CO	34.532	132.9
N₂	33.5	126.2	SO₂	77.809	430.8
O₂	49.8	154.6	CH₄	45.4	190.6
Ar	48.1	150.8	H₂O	217.6	647.3
H₂	12.958	33.19			

Capacity Study.xlsx

II-1-1 Literature Search on Stream Composition

There are several sources for CO₂-rich gas mixtures amenable to geological storage:

- capture from conventional power plants
- oxy-fuel flue gas stream (power plants)
- IGCC flue gas stream) power plants)
- Ethanol plants and other chemical facilities

For the first three categories, flue gas composition depends not only on the process but also on the fuel (natural gas or various coals). For example, oxyfiring of natural gas (oxy-gas) can generate a methane content in the flue gas as high as 500 ppv (written com., Clifford Lowe, 2009). Coal introduces sulfur in the system and its combustion in reducing conditions (IGCC) could lead to formation of H₂S and COS, as well as HCN and NH₃ (Birkholzer et al., 2008).

The CCP3 capture team made clear that the focus was on oxy-gas and provided us with impurities maximum volume fractions. However, it was less clear what a typical gas stream composition might be. Other relevant questions include: what is a normal range? How are concentrations correlated? The oxy-gas technology is still developing and unknown details of the process will have an impact on nature and amount of impurities. A literature search was performed in order to gather common oxy-fuel compositions (combustion of the flue gas takes place in presence of pure or high purity oxygen to optimize the amount of CO₂ existing in the final gas stream). Table 3 summarizes the compositions reported in each study for the ultimate injection stream. Table 4 contains maximum, minimum, average and median composition for each component from Table 3. Values reported in Table 4 together with those in Table 5 and the impurities upper ranges established by the CCP3 Capture Team (N₂:15%, O₂: 5%, Ar: 5%) were used to define the injection stream composition and to set simulation base cases and their corresponding variations. Eventually, in the context of this study we defined 3 base cases: neat CO₂ (100% CO₂), composition Stream A, and composition Stream C (Table 6). More complicated streams can also be envisioned because of possible mixing in a trunk pipeline but were not considered in this study.

Table 3. Compilation of stream compositions from oxy-fuel combustion (molar compositions).

	Wet Recycle ⁽¹⁾ (pure O ₂)	Dry Recycle ⁽¹⁾ (pure O ₂)	95% Oxygen purity ⁽²⁾	98% Oxygen purity ⁽²⁾	99.5% Oxygen purity ⁽²⁾	Wilkinson, 2003 ⁽³⁾	Wilkinson, 2001 ⁽⁴⁾
Ar	-	-	5.761	3.570	0.950	1.1	1.35
CO	-	-	0.030	0.030	0.030	-	-
CO ₂	92.745	93.278	86.469	91.879	94.679	96.2	95.67
H ₂	-	-	-	-	-	-	-
H ₂ S	-	-	-	-	-	-	-
N ₂	4.488	4.508	3.580	0.500	0.330	1.9	1.65
NO	-	-	0.160	0.020	0.010	-	-
O ₂	2.767	2.194	4.000	4.000	4.000	0.7	0.57
SO ₂	-	-	-	-	-	0.1	0.76
N ₂ +Ar	-	-	-	-	-	-	-
Total	100.0	100.0	100.0	100.0	100.0	100.0	100.0

(1) Zanganeh et al. (2004); (2) Aimard et al. (2008); (3) Wilkinson et al. (2003); (4) Wilkinson et al. (2001)

Table 4. Maximum, minimum, average and median compositions (molar compositions)

	Maximum Composition (%)	Minimum Composition (%)	Average composition (%)	Median composition (%)
Ar	5.761	0.950	2.546	1.350
CO	0.030	0.030	0.030	0.030
CO ₂	96.200	86.469	92.989	93.278
H ₂	-	-	-	-
H ₂ S	-	-	-	-
N ₂	4.508	0.330	2.422	1.900
NO	0.160	0.010	0.063	0.020
O ₂	4.000	0.570	2.605	2.767
SO ₂	0.760	0.100	0.430	0.430
N ₂ +Ar	-	-	-	-

Table 5. Typical stream compositions from oxy-firing a steam generator

	Stream A: 97% Oxygen purity (no air in leakage)	Stream B: 97% Oxygen purity (3% of air in leakage)	Stream C: 99.5% Oxygen purity (no air in leakage)
CO ₂ (mole %)	96	96	92
N ₂ (mole %)	0.2	2	1
O ₂ (mole %)	2.1	1.1	6.5
Ar (mole %)	1.7	0.9	0.5

Note: from Jadhav, R. (Chevron), email communication, October 18, 2010

Table 6. Molar composition of base cases

Component (mol %)	Neat CO ₂	Composition Stream A	Composition Stream C
CO ₂	100	96	92
N ₂	—	0.2	1
O ₂	—	2.1	6.5
Ar	—	1.7	0.5

II-1-2 Associated Issues

In the study we also considered the following issues:

Methane, hydrocarbons, and water

Methane may have to be considered in an analysis of impact of impurities even if not included in the injection stream. Many hydrocarbon provinces contain methane-saturated (or close to saturation) brines. When a CO₂-rich gas phase is introduced, CH₄ tends to exsolve/outgas from the brine into the gas phase whereas some of the CO₂ will partition into the brine (as it has been observed in a site monitored by BEG scientists, Cranfield, MS – several papers to be published in the peer-reviewed literature). This process might be particularly important at the front and on the edges of the plume. A selected few runs tested the import of such a process on plume dynamics. The same process is also likely true for C₂+ hydrocarbons. In addition, because the injected gas stream is obviously in contact with the omnipresent subsurface water, H₂O component will also partition into the gas phase.

Other trace gases

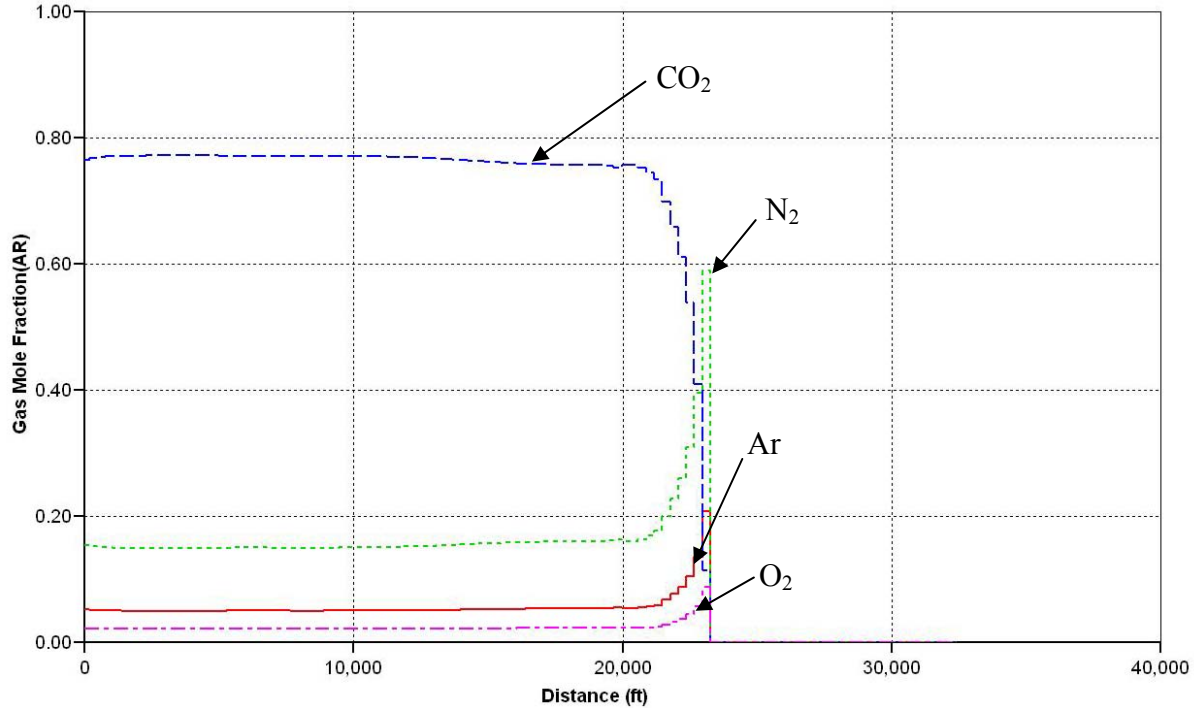
Additional gas components are also frequently mentioned in the context of CO₂ sequestration, particularly as they impact pipeline operations. H₂S is a reactive gas which is commonly co-injected with CO₂ in Canada and some parts of the US. In some basins, H₂S can also exsolve in a process similar to that described for methane above. Above some threshold concentration, presence of H₂S will modify the status of the gas stream from greenhouse gas to waste, which operates under a different set of rules. Other additional reactive gases include NO_x, HCl, and HCN; a quick high-level analysis will be provided in a stand-alone report.

Combining gases

To limit modeler's and computing efforts, it may be advantageous to combine gases together, for example non-condensable N₂ and Ar, to which CO can be added. Results presented later show that it is an appropriate action if their concentrations stay reasonably low.

Solubility

As a general rule, gas solubility increases with increasing pressure, and decreases with increasing temperature and increasing salinity. Mole fraction solubility for selected gases is provided in Appendix B. As an example, 2% molar CO₂ in 1 kg of water (55.6 moles) is approximately 1 mole CO₂, that is, ~44 g/L (that is, approximately an additional 50,000ppm; which can be compared to brine salinities that generally range from 50,000ppm to >200,000 ppm). We ran cases with and without solubility. The assumption of thermodynamic equilibrium and that the brine always dissolves as much CO₂ as allowed is not very realistic as dissolution rate must be included. Dissolution occurs at the interface between the brine and CO₂-rich phase but the interfacial area may be small. Runs suggest that dissolution occurs at the edges of the plume and, in particular at the front (Figure 1).



Note: 100 years after start of injection; ~78% CO₂, 15% N₂, 5% Ar, and 2% O₂ mole fraction; profile along the main axis of the plume.

Figure 1. Impact of dissolution at gas composition at plume front

II-2. Metrics

There are several ways to measure impact of impurities on CCS. Potential geochemical impact on injection formation and seal materials might be the most recognizable but is not treated in this document. Impurities induce non-linear changes in physical properties, particularly density and viscosity, and they impact the usually accepted trapping mechanisms. Structural trapping, for example, assuming that transient emplacement with and without impurities is identical, will exhibit a decrease in CO₂ storage capacity due to both slight decrease in CO₂ volume injected and, more importantly, to a sharp decrease in the gas mixture density. We measure *impact on capacity* by assessing the change in density from neat CO₂ to CO₂ mixtures.

Injectivity J is usually defined as the ratio of flow rate over pressure drop at the wellbore

$$J = \frac{q}{p_{wf} - p_a}$$

Where q is injection rate and p_{wf} and p_a are bottom hole flowing pressure and reservoir-averaged pressure. As a proxy for injectivity, we calculated ratio of inverse of viscosity values. We assume that there is no WAG and that a continuous gas stream is injected, limiting the relative permeability effects. We also neglect any impact on interfacial tension and any subsequent change on pressure. IEAGHG (2011) cites references suggesting that IFT of a mixture with N₂ or O₂ is higher than that of neat CO₂, likely increasing the maximum residual saturation and maybe balancing the decrease in density and mole fraction. The injection rate q_v is expressed by the commonly-used extension of Darcy's law to multiphase flow which combined with the conservation of mass equation yields:

$$q_v = \frac{4\pi kb\Delta P}{\mu} \left[\ln \left(\frac{2.25kt}{\phi c \mu r^2} \right) \right]^{-1}$$

where c is the compressibility of the fluid. Note that c intervenes within a log term mitigating any impacts of its variations on injectivity compared to viscosity. Appendix B details compressibility value variations and reveals that they stay within a factor of 2 or 3 for the various mixtures numerically tested. An approximate metric of injectivity change is then the ratio of the inverse of the viscosities. An alternate definition of injectivity is defined not in terms of volume flux q_v , but in terms of mass flux q_m , $q_m = \rho q_v$. In this case, an approximate metric of injectivity change is the ratio of the density-viscosity ratios. Impact on capacity and injectivity are briefly discusses in Section III-1.

This report focuses on the residual saturation trapping mechanism when applied to a site consisting of a dipping aquifer with no structural traps. Such a geometry is of interest to this work because (1) it may represent actual large-scale field operations in which several structural traps may or may not be present and subsequently filled and (2) it is richer in non-necessarily intuitive results. Metrics for the residual trapping mechanism are illustrated on Figure 2 and include:

- Maximum lateral distance traveled from the injector (that is, until plume stops migrating)
- Total mobile gas mixture in the aquifer at a given time and time at which all gas mixture had just been trapped.
- Time the plume takes to reach the top seal

The maximum lateral distance is equivalent to capacity and capacity variations under different gas mixture composition is a function of mostly density contrast. Because all the supercritical fluid is at residual saturation at that time it is a function of the maximum residual saturation, which is a likely function of gas composition through its effect on interfacial tension, and of hysteresis. Both are assumed constant for all gas composition in this work. The other parameter controlling this metric is density.

As described in Nicot et al. (2008) total mobile CO₂ (Figure 3) can be understood as either (1) the amount of CO₂ that is not trapped as residual gas or is not dissolved; or (2) the amount of gas that is still mobile, that is, amount from definition (1) minus the amount of CO₂ that will be trapped once the mobile plume has moved away and that the water has imbibed the cell.

Definition (1) has been retained in this document. Factors controlling time, that is, fluxes, are the ratio of density to mixture viscosity and of mixture-brine density difference to mixture viscosity.

The results are to be understood relative to each other, in particular relative to the base cases, because of numerical and gridding issues. For example, in homogeneous models, plume extent is a function of cell size but mostly of cell height (for example, Yamamoto and Doughty, 2011). Scaling the plume extent from various runs to a base line minimizes this effect. We present results as % variation from one of the base cases. Heterogeneity can also have a large impact on plume extent. However, the purpose of this document is not to investigate impact of heterogeneity but rather to understand impact of impurities on plume dynamics. So, again, results from runs with impurities are comparison with a base case showing the same heterogeneities.

In order to inform results from Section III-3 on ACPP work, we develop an additional derived metric for binary, ternary, and higher-order systems by comparing their plume extent to a neat

CO₂ system. The latter system always shows a shorter plume. The metric is the component mole fraction at which the extent of the plume is **15%** or **25%** longer than the base case.

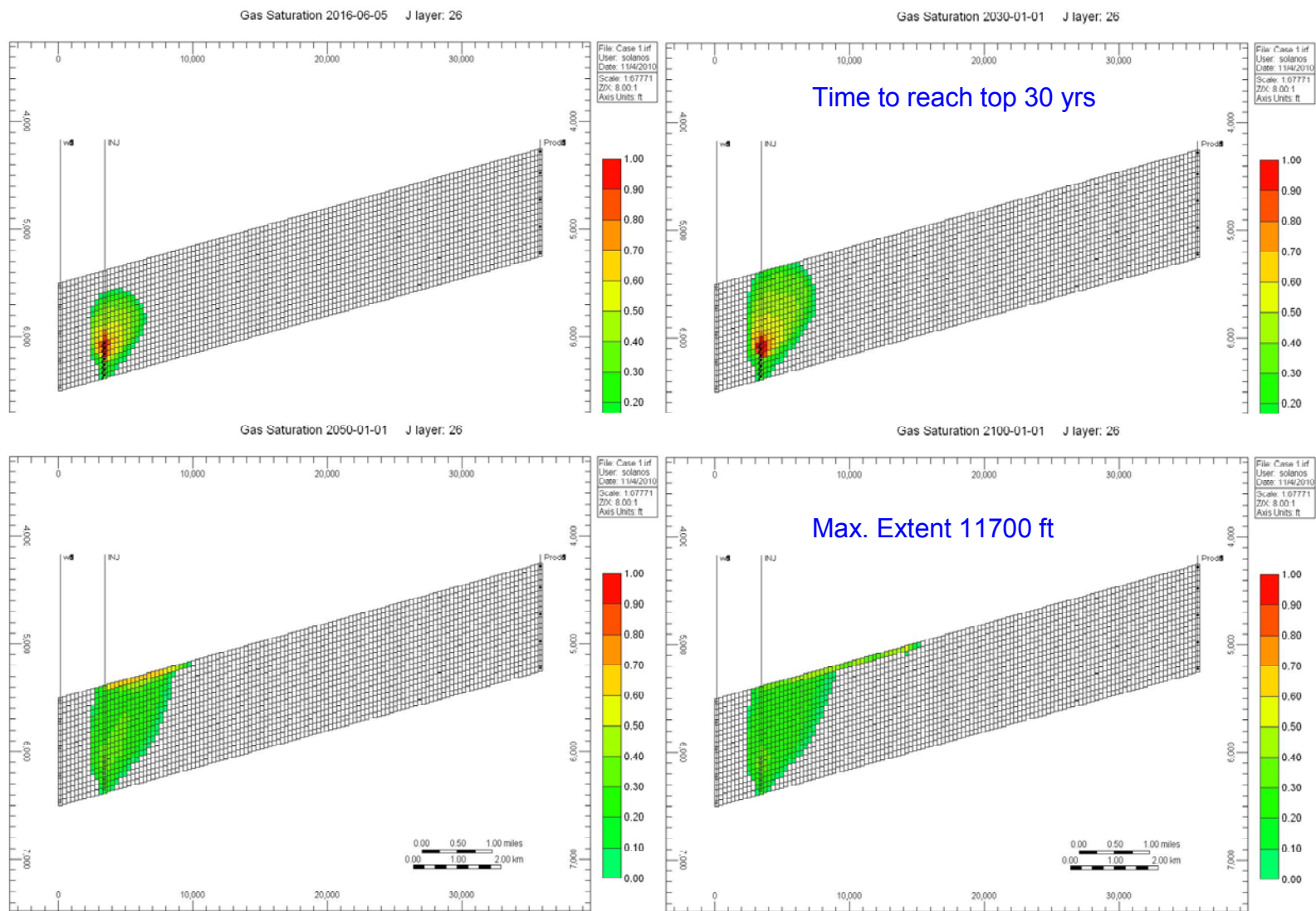
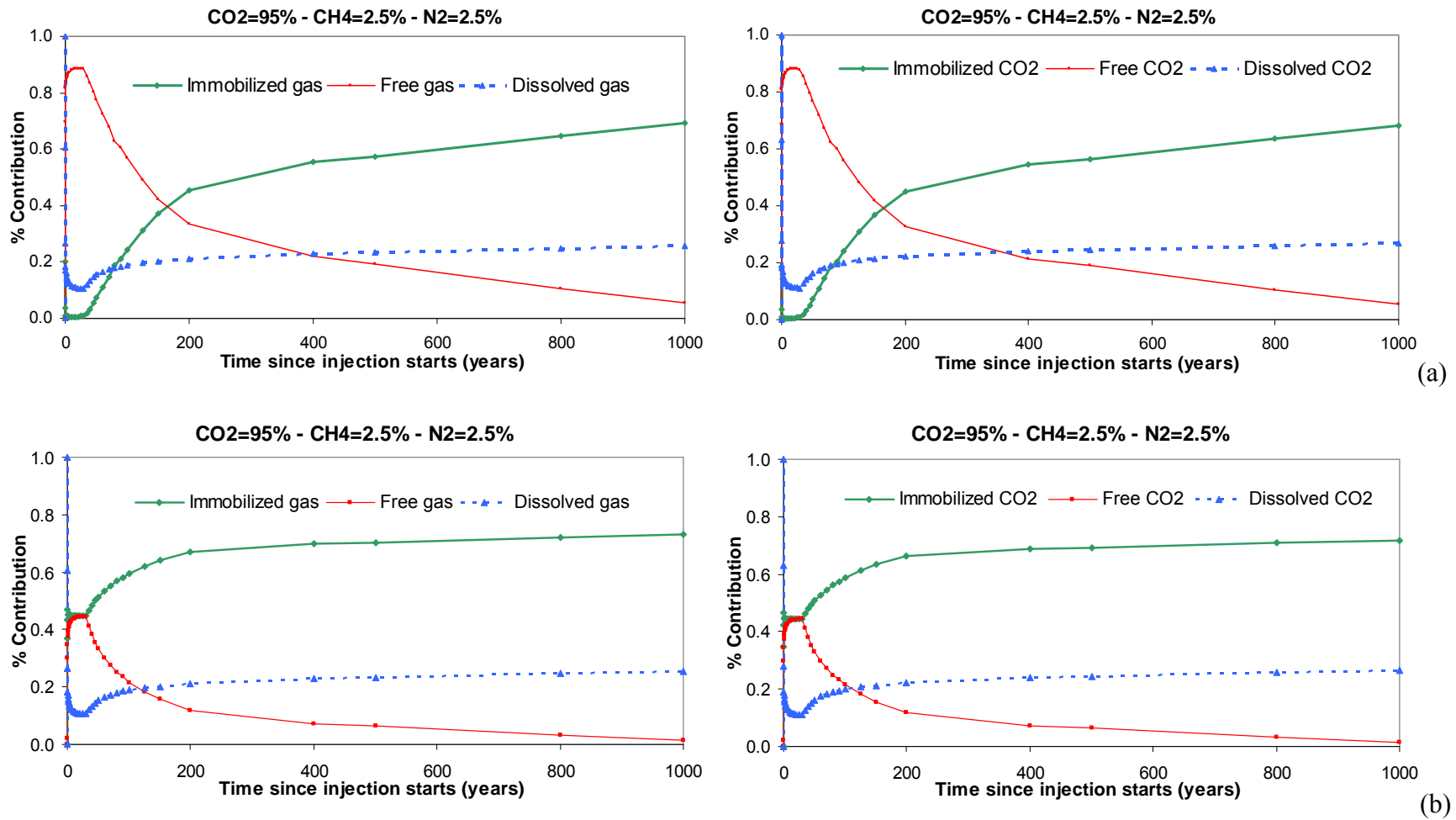


Figure 2. Illustration of how maximum extent and time to reach the top are extracted from run results.



Note: (a) assumes that all gas is mobile, including gas that will become trapped later; (b) assumes that some of the mobile gas will never move out of the cell and will be trapped later as residual gas and consequently does not tally it as mobile (from Nicot et al., 2008)

Figure 3. Contrast in phase fraction for the two definitions of mobile gas

II-3. Reservoir Models

Our general approach consisted of varying the injection-stream composition and flow parameters and in monitoring selected output properties as described in the previous section. We performed sensitivity analyses on the relative importance of gas-stream composition. We applied the CMG-GEM model to simple generic cases and to three more realistic sites (1) a clastic aquifer in the Texas Gulf Coast (Ghomian et al., 2008) (~60°C, 2500 psi, 100,000 mg/L), (2) another deeper clastic site of the Northern Gulf Coast in Mississippi (125°C, 4500 psi, 170,000 mg/L), and a carbonate aquifer in Alberta. All run results are collected in Appendix D, but a limited number of variables selected as representative of a run (e.g., Kumar, 2008) are discussed in the Results Section.

Typical reservoir depth ranges for 3,000 to 10,000+ ft, which translates into typical pressures of 1,500 psi to 4,500 psi assuming an average hydrostatic pressure gradient of ~0.45 psi/ft. Note that pressure can be much lower than hydrostatic in depleted or close to depleted fields. Formations can also be overpressured, at pressures much higher than hydrostatic, but they are not considered good targets for injection. In the subsurface, pressure is correlated with temperature. Both typically increase more or less linearly. The temperature gradient, also called the geothermal gradient, varies around 1.5 °F/100 ft (25-30 °C/km), higher in some areas such as the Gulf Coast, lower in others such as the Permian Basin. Combined the average surface temperature, knowledge of the geothermal gradient can yield the approximate temperature at any depth. For example, assuming a surface temperature of 60°F and a gradient of ~2 °F/100 ft would yield a temperature of ~260°F at a depth of ~10,000 ft.

II-3-1 Description of Generic Models

In the spirit of previous similar work (e.g., Kumar, 2004; Ozah, 2005; Kumar, 2008), we used a simple generic model whose geometric characteristics are described in Table 7. Model outputs are monitored for 100 yr after start of injection, and the gas stream is injected at a volumetric flow rate of 26×10^6 SCFD for 30 yr, translating into a yearly mass rate of 0.5 Mt/yr of pure CO₂. The formation modeled consists of a 1,000-ft-thick reservoir consistent, for example, with the Utsira Formation thickness at Sleipner, where 1 Mt/yr is injected and located at an average depth of approximately 6,000 ft. The model box is 2.9×6.8 mi ($36,000 \times 15,300$ ft), and the formation is assumed to have a constant dip of 2°. The grid is coarse, with uniform dimensions of $300 \times 300 \times 50$ ft. The sole injection well is located far downdip, next to the downdip boundary (Figure 4). Injection is limited to the lower-third interval. Porosity and permeability are constant at 0.25 and 300 md, respectively. Heterogeneity is handled in a simplistic way by adding four baffles with null porosity parallel to the formation top and bottom just upstream of the injection well and short of a few cells, all the way up to the updip boundary and across the whole width of the model (Figure 4).

Boundaries are closed on five sides of the model grid: top and bottom boundaries are assumed to be bounded by impermeable layers; side boundaries are assumed no-flow, mimicking the possibility of having multiple injection wells in a line source; and the downdip boundary is assumed to be close because, for example, a geopressured zone and sharp decrease in permeability limit water fluxes. The updip boundary is open to flow and is set as a constant pressure boundary by setting five horizontal wells along the y-axis (Figure 4). The updip boundary is located far enough away not to impact multiphase-flow processes following CO₂

injection in most cases. Pore space is initially fully saturated with component “water.” Initial pressure is hydrostatic and computed by the model assuming a typical hydrostatic gradient of 0.465 psi/ft. PVT properties are user specified (Appendix A) and set for the model salinity (100,000 mg/L or 170,000 mg/L).

Two generic models are used: a shallow model reproducing conditions present at the Frio site (Ghomian et al., 2008; Hovorka et al., 2006; Doughty, 2007) and a deep model reproducing conditions present at Cranfield (Choi et al., 2011; Nicot et al., 2009). Both actual sites are on the Gulf Coast but were stripped from any specific retaining mostly environmental conditions: pressure, temperature, and salinity.

The only trapping mechanisms available in the model are dissolution and residual-phase mechanisms. Mineral-phase trapping is not generally understood as occurring in a meaningful way before hundreds or thousands of years. Structural trapping—that is, CO₂ trapped in the manner of oil and gas accumulations—is not included in the design of the generic model. It helps little in explaining the interplay of all processes and is very site specific.

The runs have limitations, such as the assumption of no change in residual saturation as the interfacial tension (IFT) changes with mixture composition. IEAGHG (2011, p.22) mentions that IFT of the gas mixture increases with fraction of N₂ or CH₄ suggesting higher residual saturation at the end of the imbibition process. It is unclear how much this change in IFT would offset the decrease in density in terms of capacity. Typical run times on a Dell Optiplex 745 (with a 2.4GHz CPU and 4.0 GB of RAM) were 1.5 h for the generic model, 2 h and 4 h for the shallow and deep Gulf Coast models, respectively (both at 100 yr). The base-case CMG-GEM input file is listed in Appendix C.

Table 7. Base-case characteristics of the generic model.

Reservoir Property	Shallow Reservoir Case	Deep Reservoir Case
Model length	36,000 ft	36,000 ft
Model width	15,300 ft	15,300 ft
Model thickness	1,000 ft	1,000 ft
Number of cells x × y × z	120 × 51 × 20	120 × 51 × 20
Cell dimensions	300 × 300 × 50 ft	300 × 300 × 50 ft
Dip in x direction	2°	2°
Permeability	300 md	300 md
Porosity	0.25	0.25
Rock compressibility	$5 \times 10^{-6} \text{ psi}^{-1}$	$5 \times 10^{-6} \text{ psi}^{-1}$
Vertical perm. anis. (kv/kh)	0.01	0.01
Origin (cell 1,1,1)	Top downdip	Top downdip
Depth at origin center cell	5,500 ft	9,976 ft
Hydrostatic pres. gradient	0.465 psi/ft	0.465 psi/ft
Initial pressure	V.E. ~2,550 psi at origin	V.E. ~4701 psi at origin
Geothermal gradient	15°F/1,000 ft	18°F/1,000 ft
Temperature	135°F	257°F
Injection rate	26 MMSCFD	26 MMSCFD
Hysteresis	on	on
Maximum res. saturation	0.30	0.30
Formation water TDS	~100,000 mg/L	~170,000 mg/L
Injection period	30 yr	30 yr
Simulation period	100 yr	100 yr

Note: V.E. = vertical equilibrium

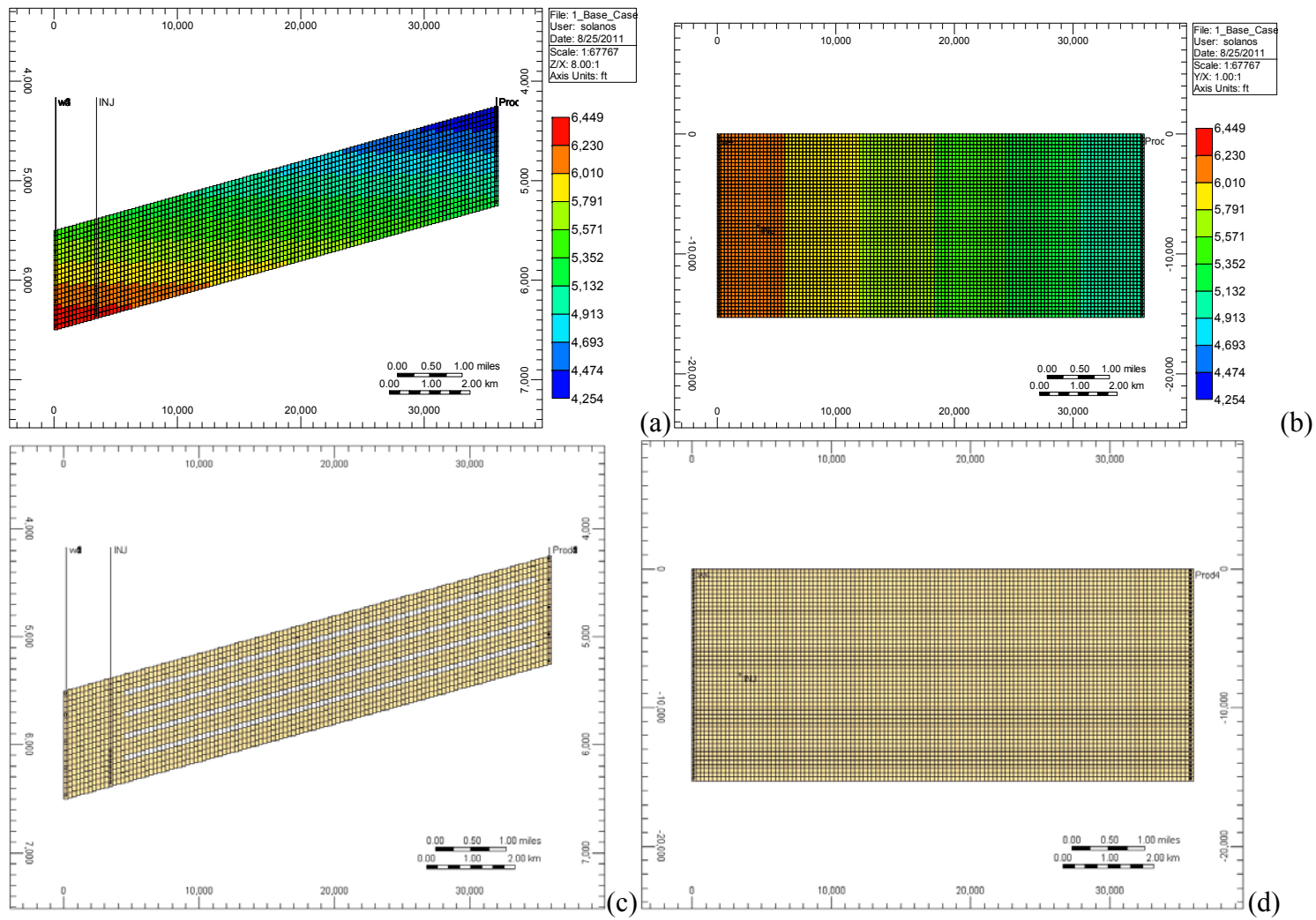


Figure 4. Cross section and map view of the generic model (a, b) with baffles (c, d).

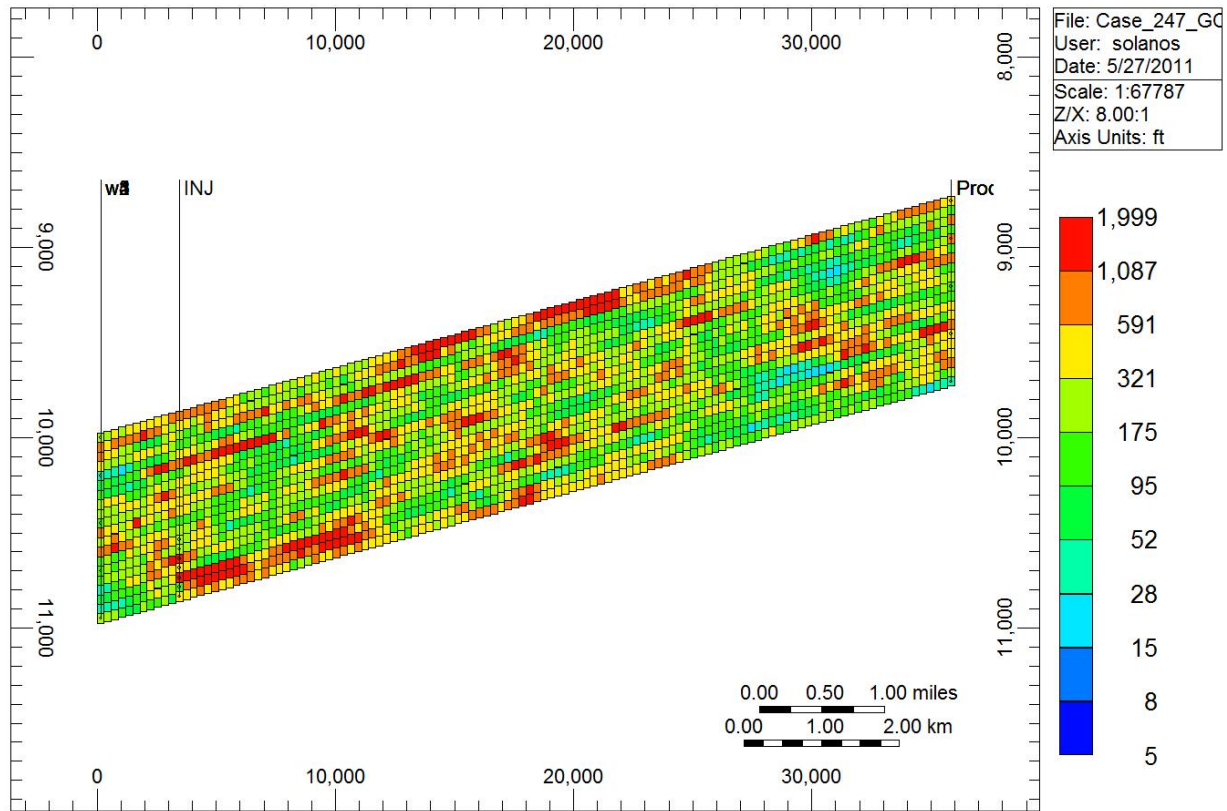


Figure 5. Cross-section of the generic model with an heterogeneous permeability field (Realization 1)

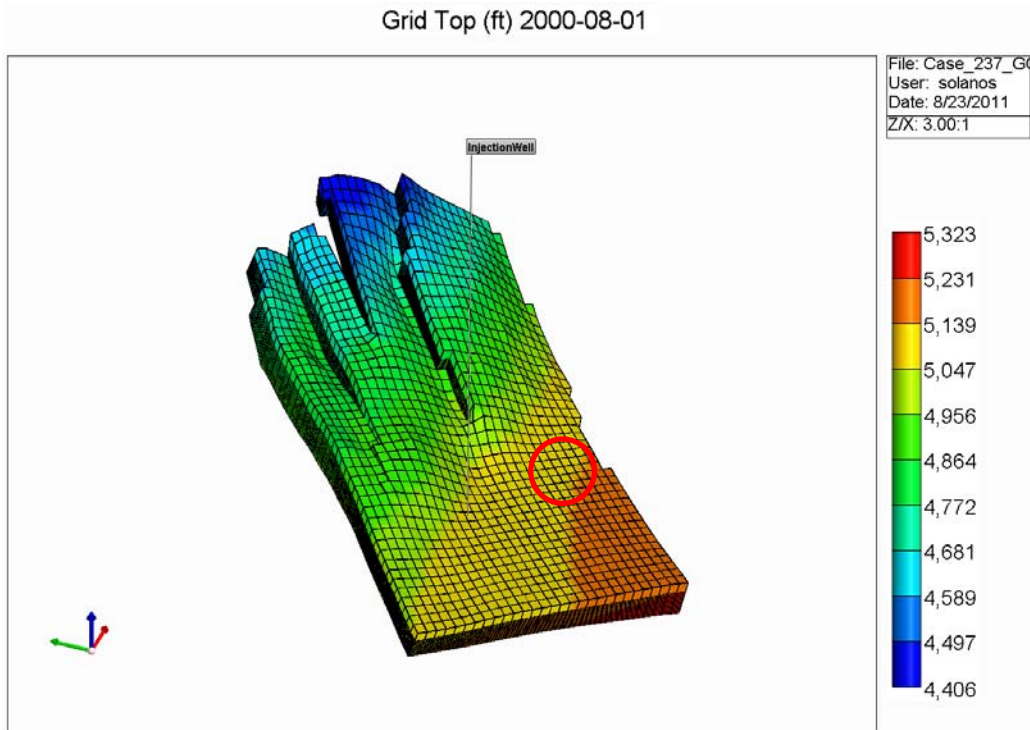
II-3-2 Description of the Shallow Model (Texas Gulf Coast)

The Texas Gulf Coast model (Table 8, Figure 6) is taken as described in Ghomian et al. (2008), with the following changes: (1) longer injection and monitoring periods from 12.5 d to 5 yr and from 8+ yr (3,000 d) to 100 yr, respectively; (2) decreased injection rate from 4.73 to 3 MMSCFD; and (3) injection-well location changed to a more downdip location. Please refer to Ghomian et al. (2008) for additional information of this Gulf Coast model. Note that an actual brine experiment (Hovorka et al., 2004, 2006) took place in a similar environment but impacted only a limited area of the domain modeled in this study. Stratigraphy and other properties used in the Ghomian et al. (2008) work and this work were worked out for a much larger domain than that of the brine experiment.

A quick computation shows that, relative to the generic model, the Gulf Coast model total volume is approximately 500 times smaller. To ensure minimal structural trapping at saturation higher than residual, injection rate was decreased from 2.6×10^7 SCFD (generic case) to 3×10^6 SCFD, whereas the injection period was reduced from 30 (generic case) to 5 yr.

Table 8. Base-case characteristics of the shallow Gulf Coast model (from Table 1 in Ghomian et al. (2008).

Property	Value
Model length	3,517 ft
Model width	2,296 ft
Model thickness	100 to 200 ft
Number of cells x × y × z	43 × 28 × 26
Dip	5° - 35°
Average permeability	374 md
Average porosity	0.214
Rock compressibility	$5 \times 10^{-6} \text{ psi}^{-1}$
Vertical permeability anisotropy (kv/kh)	0.1
Origin (cell 1,1,1)	Top southernmost cell
Max and min depth	5,323 and 4,406 ft
Hydrostatic pressure gradient	0.465 psi/ft
Initial pressure	2,000 psi
Temperature	135°F
Injection rate	3 MMSCFD
Hysteresis	on
Formation water TDS	~100,000 mg/L
Injection period	5 yr
Simulation period	100 yr



Note: Red circle shows approximate location of injection well

Figure 6. 3D view of the shallow Gulf Coast model showing cell depth and wells on the boundary

II-3-3 Description of the Deep Model (Mississippi Gulf Coast)

The Mississippi Gulf Coast model (Table 9, Figure 7) is taken from a model summarized in Nicot et al. (2009) and Choi et al. (2011), with the following changes: (1) longer injection and monitoring periods from < 2 yr to 30 yr and from 1+ yr (365 d) to 1000 yr, respectively; (2) decreased injection yearly mass rate from 1 Mt/yr to 0.5 Mt/yr; and (3) number of injection wells reduced to one-downdip injector well. A quick computation shows that, relative to the generic model, the Gulf Coast model total volume is approximately 30 times smaller.

Table 9. Base-case characteristics of the deep Gulf Coast model.

Property	Value
Model length	20,000 ft
Model width	14,000 ft
Model thickness	300 ft
Number of cells x × y × z	100x100x10
Average dip	2°
Average permeability	280 md
Average porosity	0.255
Rock compressibility	$5 \times 10^{-6} \text{ psi}^{-1}$
Vertical permeability anisotropy (kv/kh)	0.01
Origin (cell 1,1,1)	Top cell
Max and min depth	10,207 and 9741 ft
Hydrostatic pressure gradient	0.465 psi/ft
Initial pressure	4,701 psi
Temperature	257°F
Injection rate	4.73 MMSCFD
Hysteresis	on
Formation water TDS	~170,000 mg/L
Injection period	30 yr
Simulation period	100 yr

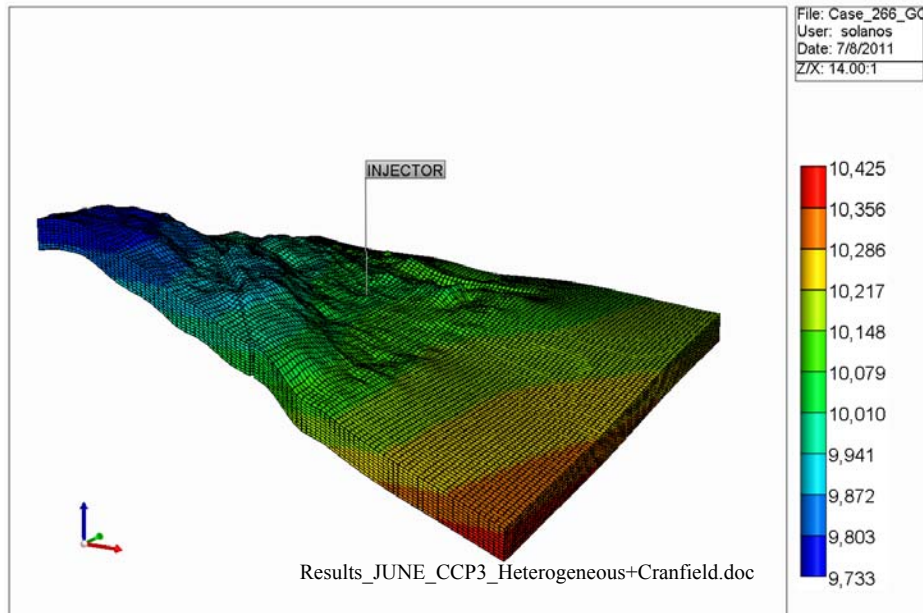


Figure 7. 3D view of the Mississippi Gulf Coast model showing cell depth

II-3-4 Description of the Carbonate Model (Alberta)

The model used in the simulations was developed by others within the framework of the Wabamun Area Sequestration Project (WASP) program (<http://www.ucalgary.ca/wasp/>). All information about the site was downloaded from a data repository located at the University of Calgary, Alberta, Canada. The focus is on the saline aquifer of the Nisku formation of Devonian age. The Nisku aquifer is located in the Wabamun Lake Area, part of the Western Canada Sedimentary Basin. The formation is a gently dipping carbonate ramp belonging to the Devonian Winterburn Group. The succession consists of mainly carbonate and evaporitic strata with few intervening shales (Bennion and Bachu, 2005). Grid distribution was exported from Petrel as well as three permeability and porosity realizations. Additional reservoir and fluid properties were taken from the initial Eclipse 100 files with corresponding modifications to convert the Eclipse black oil model into a GEM compositional model. Table 10 contains a description of the current Nisku aquifer reservoir model. Figure 9 shows a 3D view of reservoir depth while Figure 8 shows cross-sections of permeability and rock types. The number of injector wells in the modified Nisku/carbonate compositional model has been reduced to one downdip injector with an injection rate equivalent to 1 Mton/yr of CO₂. Boundary conditions are no-flow in all directions. The total injection time is 30 years and monitoring takes place for 1000 years. Typical run time on a Dell Optiplex 745 (with a 2.4GHz CPU and 4.0 GB of RAM) was approximately 48 hours (for 1000 yr). A quick computation shows that, relative to the generic model, the Nisku aquifer model total volume is approximately 13 times bigger. A major difference compared to the clastic models is the use of multiple rock types.

Table 10. Base-case characteristics of the Canadian Carbonate model

Property	Value
Model length	96,000 m (315,000 ft)
Model width	60,500 m (198,500 ft)
Model thickness	variable
Number of cells x × y × z	122x193x30
Average dip	0.6°
Average permeability	28 mD
Average porosity	5 %
Rock compressibility	$6.9 \times 10^{-7} \text{ kPa}^{-1}$ ($2.1 \times 10^{-5} \text{ psi}^{-1}$)
Vertical permeability anisotropy (kv/kh)	0.1
Origin (cell 1,1,1)	Top southernmost cell
Max and min depth	1,884 and 823 m (6181 and 2700 ft)
Fracture pressure	40,000 kPa (5800 psi)
Initial pressure	10,000 kPa (1450 psi)
Temperature	60 °C (140°F)
Injection rate	1.5 MMSCMD
Hysteresis	on
Formation water TDS	~190,000 mg/L
Maximum res. saturation	$0.2 < S_{grmax} < 0.35$
Injection period	30 yr
Simulation period	1000 yr

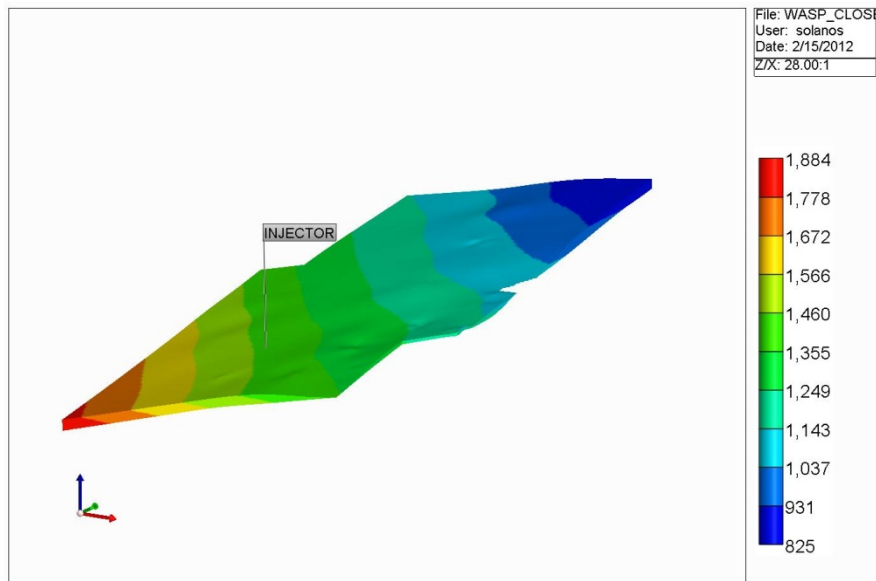


Figure 8. 3D view of the carbonate reservoir model showing cell depth

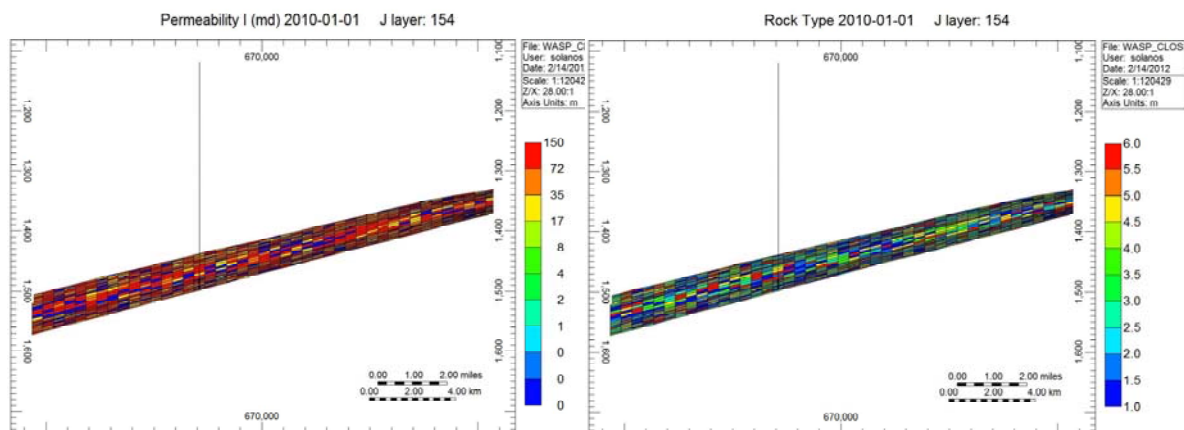


Figure 9. Permeability and rock type distributions for carbonate aquifer model

II-4. Reservoir Properties

II-4-1 Generic and Gulf Coast Models

Relative permeability data used in this study are identical to the set described in Ghomian et al. (2008) and are used in both generic and Gulf Coast models. Relative permeability end points follow relationships established by Holtz (2002) on the Gulf Coast Frio sandstone, and intermediate values follow a Corey model (Figure 10). Holtz (2002), who used published data, suggested that maximum gas residual saturation S_{gr} be a sole function of the porosity ϕ : $S_{gr} = 0.5473 - 0.9696\phi$. It is important to include hysteretic behavior in order to model gas residual saturations accurately. Not including hysteresis will underestimate the amount of gas phase trapped (e.g., Doughty, 2007). Other examples of relative permeability curves are in the public domain (e.g., Bennion and Bachu, 2005) but were not used in this study. In addition, Burton (2008), Kumar (2008), and others showed that it is important to extend relative

permeability curves to a gas saturation of 1 (Figure 10) to account for drying effects (residual water partitioning into the gas phase) and subsequent enhanced residual-phase trapping.

We already know that impurities impact IFP and capillary pressure, and therefore relative permeability. Due to a lack of data, such influence was not included in the modeling.

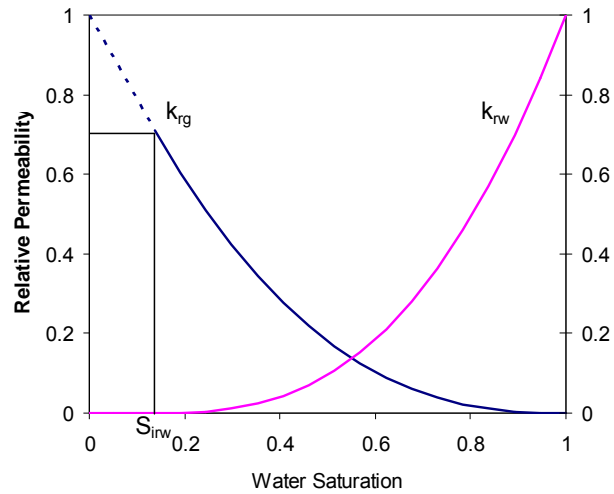


Figure 10. Relative permeability curves used in generic and Gulf Coast models.

II-4-2 Canadian Carbonate Model

A major interest to this study was to investigate the impact of heterogeneity on behavior of plume of impure CO₂. Heterogeneity is also investigated in the generic model section. In this model we add an additional level of complexity by considering multiple rock types, each with their own relative permeability characteristics. Applying the methodology used by Hosseini et al. (2011) to the core data available for the Nisku aquifer, at least 12 rock types can be identified from the normalized porosity (ϕ_z) vs. reservoir quality index (RQI) plot (Figure 11). This methodology establishes that the equation below yields a straight line on a log-log plot of RQI vs. ϕ_z with a unit slope. Samples with different flow zone indicator (FZI) values lie on other parallel lines while samples lying on the same straight line have similar pore throat characteristics and, therefore, represent a flow unit (Tiab and Donaldson, 2004) or areas with similar flow properties.

$$\log RQI = \log \phi_z + \log FZI$$

According to Tiab and Donaldson (2004) straight lines with slopes equal to unity are to be expected primarily in clean sandstones. Because of the similarity in distribution and movement of fluids within clastic and carbonate rock having intercrystalline-intergranular porosity, this zoning process can be directly applied to these reservoir systems. This process is, however, not applicable to carbonate reservoirs with vugular solution channels and/or fractures. Choice of the number of rock types to be used in the model is guided by (1) the flow unit analysis, and (2) permeability and porosity distributions from the initial Petrel model. Based on the permeability frequency distribution observed in realization #1 (Figure 12), a total of six rock types were identified within the following permeability ranges: <20 mD, 20-60 mD, 60-70 mD, 70-90 mD, 90-100 mD and > 100 mD.

Because of the importance of accurate relative permeability curves to precisely model the process of CO₂ residual trapping, a literature review on carbonate rocks saturation functions and rock properties was conducted and summarized in Table 11 for different carbonate formations. Figure 13 displays selected oil-water relative permeability curves characteristic of carbonate rocks found in the literature.

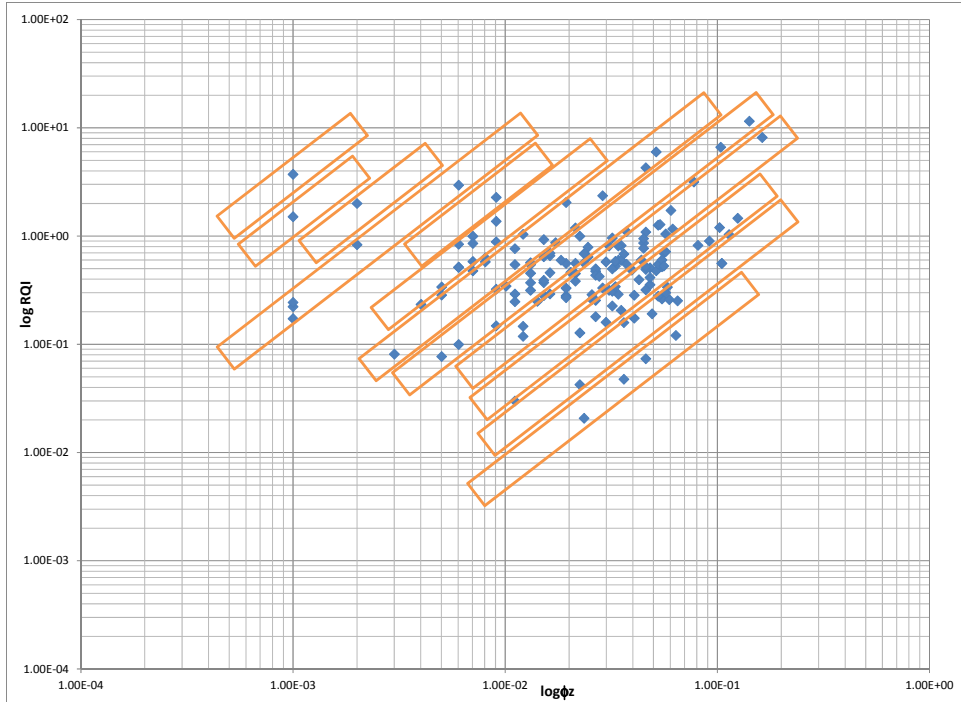
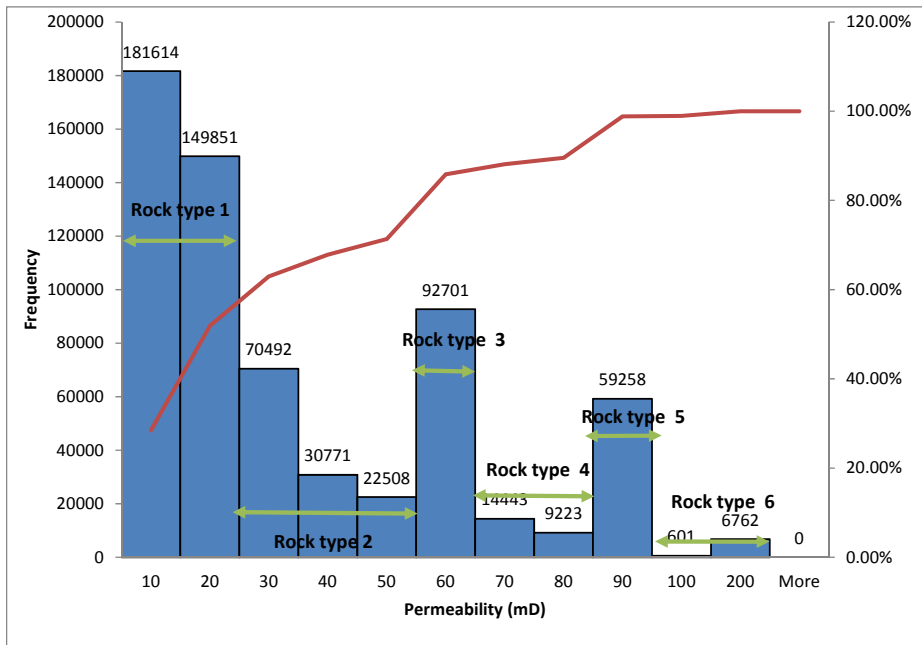


Figure 11. Normalized porosity vs. Reservoir Quality Index



Note: Realization #1 from the WASP dataset, 706,380 gridblocks

Figure 12. Permeability histogram from downloaded Petrel model for carbonate aquifer

Table 11. Summary of rock properties for different carbonate formations

Source	Formation	Location	Sample Name/ Charact.	Wettability	Swirr	k (mD)	ϕ (%)
Okasha et al, 2007	Arab-D	Ghawar Field-Saudi Arabia	HWYH	oil wet	0.431		
Okasha et al, 2007	Arab-D	Ghawar Field-Saudi Arabia	HRDH	mixed wet	0.0677		
Okasha et al, 2007	Arab-D	Ghawar Field-Saudi Arabia	UTMN	mixed wet	0.161		
Wang et al, 1998	San Andres Unit	Permian Basin	3WC/126/8.5	oil wet	0.18		
Wang et al, 1998	San Andres Unit	Permian Basin	4WC/0.15/32	mixed wet	0.18		
Wang et al, 1998	San Andres Unit	Permian Basin	9WC/0.195/5.6	oil wet	0.1	5.6	19.5
Schneider, 1976	San Andres Unit	Permian Basin	-	moderately oil wet	0.16	135	20.3
Alizadet et al, 2007	Asmari	Iran	-	water wet	0.1	0.21	11.5
Alizadet et al, 2007	Asmari	Iran	-	water wet	0.15	0.21	11.5
Masalmeh, S., 2002	Different formations	Middle East	MW	mixed wet	0.1	1-8	
Masalmeh, S., 2002	Different formations	Middle East	WW	water wet	0.1	0.1-3	
Masalmeh, S., 2002	Different formations	Middle East	OW	oil wet	0.1		
Bennion and Bachu, 2010	Wabamun	Canada	1		0.595	0.018	7.9
Bennion and Bachu, 2010	Wabamun	Canada	2		0.569	66.98	14.8
Bennion and Bachu, 2010	Wabamun	Canada	3		0.852	54.3	15.4
Bennion and Bachu, 2010	Nisku	Canada	1		0.33	45.92	9.7
Bennion and Bachu, 2010	Nisku	Canada	2		0.492	21.02	10.4
Bennion and Bachu, 2010	Nisku	Canada	3		0.397	74.4	10.9
Bennion and Bachu, 2010	Grosmont	Canada	-		0.52	153.9	11.8
Bennion and Bachu, 2010	Morinville Leduc	Canada	-		0.53	371.9	11.6
Bennion and Bachu, 2010	Redwater Leduc	Canada	-		0.665	353.6	16.8
Bennion and Bachu, 2010	Cooking Lake	Canada	1		0.476	65.3	9.9
Bennion and Bachu, 2010	Cooking Lake	Canada	2		0.5963	4.87	16.7
Bennion and Bachu, 2010	Slave Point	Canada	-		0.546	0.217	9.9
Bennion and Bachu, 2010	Winnipegosis	Canada	-		0.2108	3.09	14.8
Nishi and Shibasaki, 1996	-	Offshore Abu Dhabi	-	oil wet	0.18	< 3	19.6-33.5

Nishi and Shibasaki, 1996	-	Offshore Abu Dhabi	-	oil wet	0.18	10-30	19.6-33.5
Nishi and Shibasaki, 1996	-	Offshore Abu Dhabi	-	oil wet	0.18	>100	19.6-33.5
Lucia, 2012	Dolo-grainstone	Lawyer Canyon	RP10B	water wet	0.118	631	18
Lucia, 2012	Dolo-grainstone	Lawyer Canyon	RP11	water wet	0.23	210	16
Lucia, 2012	Dolo-grainstone	Lawyer Canyon	RP7	water wet	0.0975	24	12
Lucia, 2012	Dolo-grainstone	Lawyer Canyon	RP8	water wet	0.086	89	16
Lucia, 2012	Dolo-grainstone	Lawyer Canyon	RP9A	water wet	0.068	14	10
Lucia, 2012	Moldic Grainstone	Lawyer Canyon	RP4A	water wet	0.0789	4	20
Lucia, 2012	Moldic Grainstone	Lawyer Canyon	RP4AA	water wet	0.0789	4	19
Lucia, 2012	Moldic Grainstone	Lawyer Canyon	RP6	water wet	0.0807	6	17
Lucia, 2012	Moldic Grainstone	Lawyer Canyon	RP66	water wet	0.11	5	18
Lucia, 2012	Grain-dominated dolopackstone, fine crystalline dolowackestone	Lawyer Canyon	RP12	water wet	0.19	14	14
Lucia, 2012	same	same	RP13	water wet	0.131	7	20
Lucia, 2012	same	same	RP15	water wet	0.131	4	17

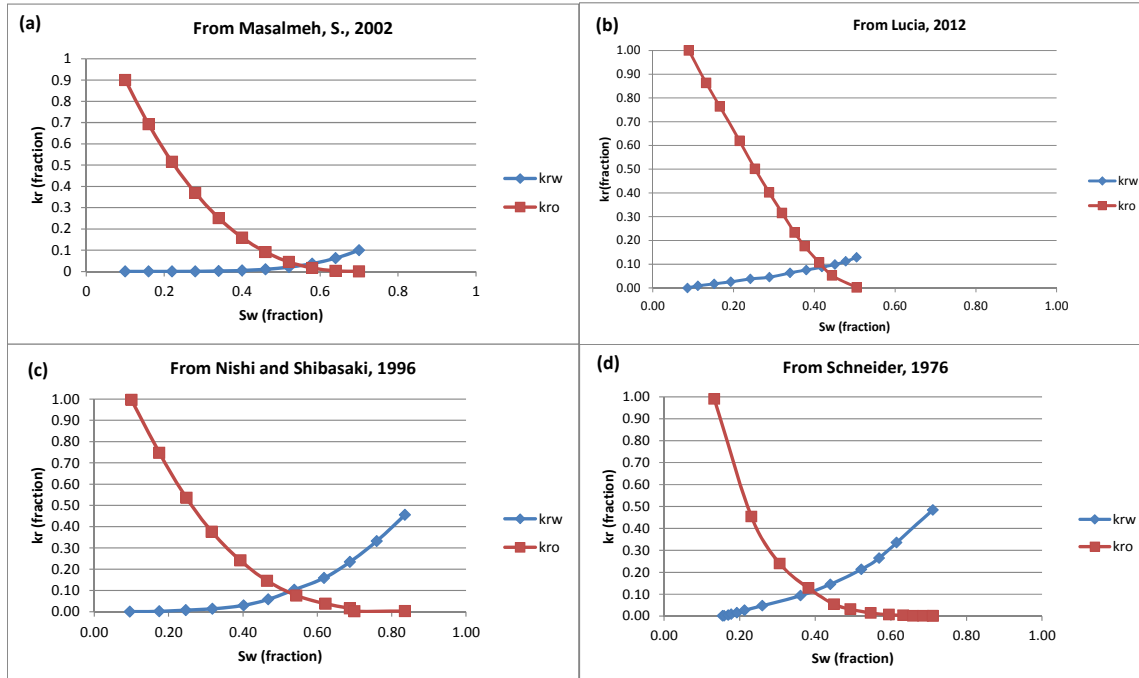


Figure 13. Example of relative permeability curves for different carbonate formations: (a)-(b) water wet rocks and (c)-(d) oil wet rocks

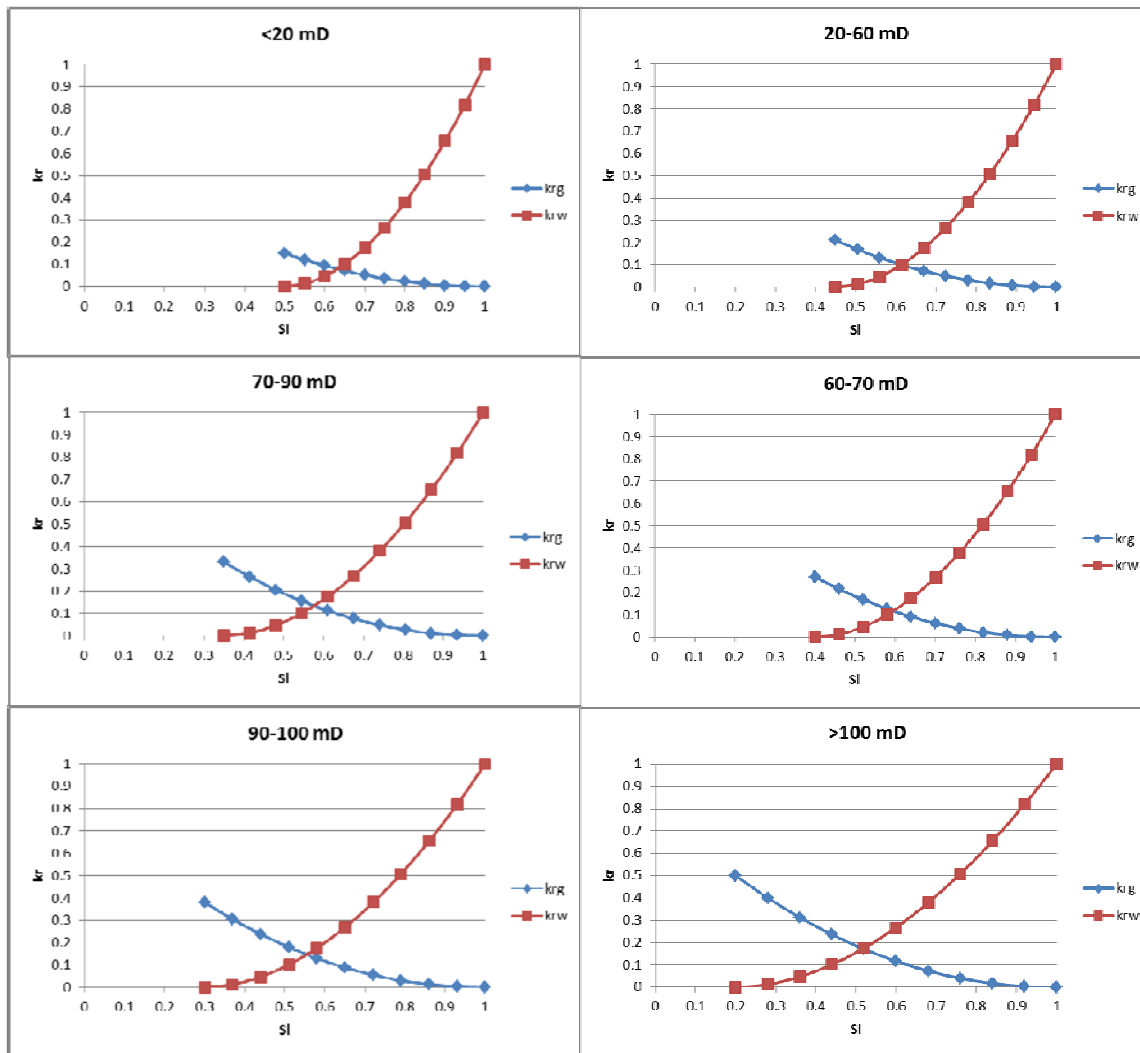


Figure 14. Liquid-gas relative permeability curves for the six rock types used in the carbonate reservoir model

The purpose of the rock-type analysis and relative permeability literature review was to collect enough information to accurately account for reservoir heterogeneity typical of carbonate formations in the simulation model. The final liquid-gas relative permeability curves to be used in the simulation runs for each of the six rock types are shown in Figure 14. The liquid (brine) and gas (CO₂) endpoints as well as the irreducible water saturation were selected for water wet rocks based on the information found in the literature. For each rock type maximum residual gas saturation was defined in the compositional simulator GEM by means of the HYSKRG keyword with values varying between 20% and 35%.

PVT data input for this model was modified from the Frio formation model taking into account Nisku’s salinity of 190,000 mg/L. Binary interaction coefficients were adjusted to this salinity using correlations proposed by Ramachandran and Pope in Appendix A. New BIC’s for simulation runs are shown in Table 3 for 60°C (140°F) and 190,000 mg/L: CO₂ (0.0788), N₂ (-0.1265), O₂ (0.4592), and Ar (0.4165). “Include” files were used in the model to account for the six different rock types and to assign the appropriated rock properties to each of them. These

are: PERMI (permeability array in I-direction), POR (porosity), RTYPE (rock type) and CTYPE (compressibility for each rock type).

II-5. Previous Results

There are many reports and papers dedicated to the geochemical impact of impurities (see specific deliverable by Yang and Nicot) but relatively few investigate flow implications of impurities. Bryant and Lake (2003) examined the impact of SO_x and NO_x on injectivity. A more recent study summarized in Nicot et al. (2008) and focusing on the CO₂-CH₄-N₂ ternary system (with >75% molar CO₂) suggests a tradeoff between plume extent and time during which the plume is mobile. In a gently sloping aquifer, the injected gas mixture will tend to move up vertically until it reaches the ceiling of the formation after which point it moves along the ceiling. As the plume migrates away from the injectors, it leaves behind a trail at residual saturation until it is eventually entirely trapped and no mobile gas remains. Dissolution trapping occurs at the same time but is relatively minor although the Base case was identical to that in the current study with a simple generic reservoir with a uniform permeability of 300 md, a dip of 2°, and porosity of 25%. The gas was injected for 30 years at a depth of about 6,000 ft and at a rate of 26 MMSCFD (equivalent to 0.5 Mt/yr of pure CO₂) in a single well located in the downdip section of the model and perforated in the lower third of the 1,000-ft thickness of the injection formation. Temperature is constant at 135°F.

The study showed that the CH₄- and/or N₂-rich plume (75% CO₂ and 25% N₂ or CH₄) will travel farther and faster than the single-component CO₂ plume. In addition, storage capacity analysis also suggests that CH₄/N₂-containing systems trap CO₂ faster. More CO₂ is trapped in these systems even if less of it is injected. It is only between 100 and 200 yr after start of injection that the pure CO₂ system can secure a larger amount of nonmobile CO₂ within a given distance from the injection well. Considering the whole domain, at 1,000 yr after start of injection, all gas in the CO₂-CH₄ and CO₂-N₂ cases has been immobilized, although only 85% in the neat CO₂ case. Risk-wise, these results imply that N₂ or CH₄ impurities in the injection will help immobilize the plume faster, but the plume will travel farther. Sensitivity analysis on permeability, vertical permeability anisotropy, porosity, dip, and other parameters suggests that injection-stream composition dominates system behavior. The injection-stream base case consisted of a 95% CO₂ stream with 2.5% CH₄ and N₂ and the base case geometry included baffles (Figure 4). Permeability, anisotropy, and porosity changes performed as expected with unsurprising behavior: time to reach the top is larger with lower permeability or with larger porosity and metrics can vary by a factor of 2 or more, as much as with variations in composition. However, because of the geometry of the model, formation dip had a more complex behavior. Time to reach the top increased with increasing dip as distance to the top increased. Presence of baffles accentuated variations from the base case for the 5° case because a substantial amount of gas was directed toward the baffles and could not contribute to feeding that part of the plume moving upward to the formation top. Plume extent seemed to follow the influence of two opposing effects. When the dip was small, little gas was diverted by the baffles, and most of the gas was directed toward the top of the formation, where the main tongue resides. Similarly, when the dip was large, most of the gas flow was immediately captured by the lowermost tongue. With an intermediate dip, as in the base case, gas distribution was more balanced between the different tongues. It follows that when one tongue dominates, maximum extent is larger than when gas was distributed more uniformly between tongues.

A recent report by a Canadian Agency sponsored by the International Energy Agency Greenhouse gas (IEAGHG, 2011; Wang et al., 2011) addressed topics very similar to those discussed in this document. They focused on the capacity issues and reported that non-condensables such as N_2 , O_2 , and Ar impact capacity and that the impact is maximal at a certain pressure under a given temperature. Our own calculations (see Section III-1) confirm, although pressure and temperature are correlated in the subsurface and cannot be let vary freely, the presence of minimum density a relatively shallow depths. They also mentioned that injectivity (defined as a mass permeation flux approximated by the ratio of density over viscosity) could follow a similar model with a minimum but less pronounced than that of capacity.

III. Results

We present results for two sets of analyses: (1) variations from base cases Stream A and Stream C for a four-component system (Table 6), and (2) variations from a neat CO₂ system for binary systems. Simulations for each set are performed for the GC shallow and GC deep reservoir conditions and with and without dissolution. The four-component (CO₂, N₂, Ar, O₂) simulations were performed with enough incremental changes to build ternary diagrams as presented in the Results section. The section also presents histograms comparing the two composition base cases to the limit of the range of one individual component at a time. For example, increasing N₂ to 15% according to specifications while depressing CO₂ mole fraction by an adequate value and keeping the gas gases as in the base case. Table 41 in Appendix D displays parameters of all multi-component and binary simulation runs.

III-1. Impact on Capacity and Injectivity

We addressed capacity of structural traps by comparing density of net CO₂ vs. density of CO₂-rich mixtures as a function of depth. The impact on capacity (with density ratio of mixture to neat CO₂ as a proxy) is a strong function of the geothermal and pressure gradient (Figure 15). For reasonably low and high geothermal gradient, density ratio plots show a large drop in capacity around 3000 ft, which is slightly below the accepted depth to keep CO₂ stream in a supercritical state. In other words, the impact on capacity decreases with increasing depth. The ratio is even smaller for lower geothermal gradient (only 40% of neat CO₂ capacity) because the density contrast between neat CO₂ and mixture is more pronounced in that case. This report does not discuss further impact on capacity. A more systematic way of addressing structural trapping capacity changes would be, for example, to build a numerical model with a structural trap and a spill point and compute the maximum amount of CO₂ stored before it leaks in various combinations of depth, geothermal gradient, and mixture composition.

Injectivity as defined by volume flow rate, is approximated by the ratio of the inverse values of viscosity (Figure 16). Its impact is also strongly dependent on the geothermal gradient but all cases show that it is significantly improved in mixtures because of the general decrease in viscosity of the fluid. As with capacity this beneficial effect decreases with depth. However, the important parameter, rather than volume, is the mass of CO₂/impurities injected. Addition of impurities decreases the density of the mixture beyond a simple linear rule and this may balance the positive effects of the decrease in viscosity. Figure 17, based on the ratio of the density over viscosity ratios, suggests that mass rate injectivity is not much affected by impurities except at relatively shallow depths at which it may show a decrease by a maximum of approximately 20% and <10% in most likely compositions (streams A and C). Impurities may have a small positive effect by increasing mass flow rate at locations with a low geothermal gradient. This result assumes thermal equilibrium between the CO₂ stream and the formation which, depending on the flow rate, is not necessarily the case.

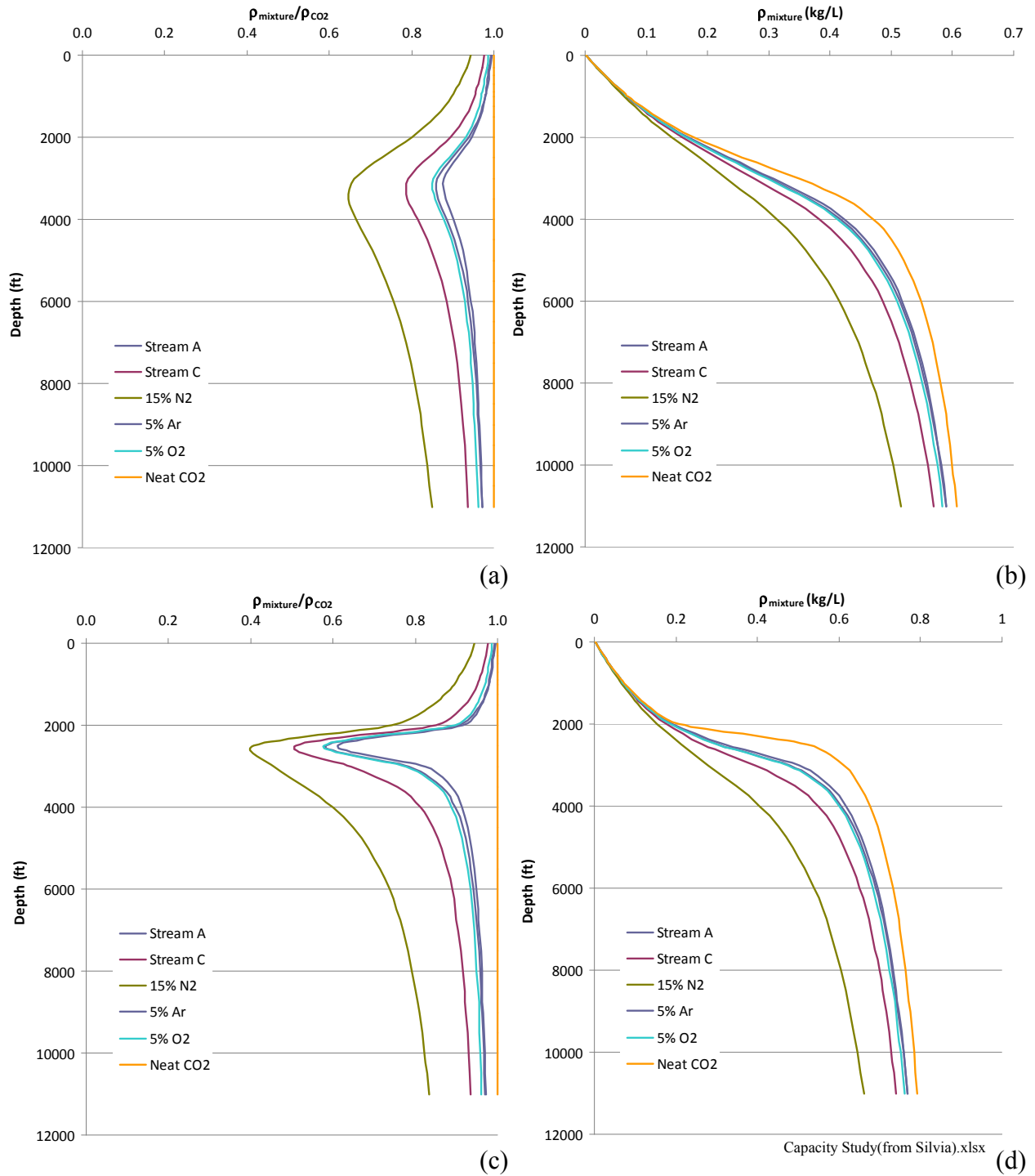


Figure 15. Mixture density relative to neat CO₂ (a and c) and mixture density (b and d) as a function of depth. Pressure gradient is 0.465 psi/ft (all) and geothermal gradient is 18°F/1000ft (a and b) or 10°F/1000ft (c and d).

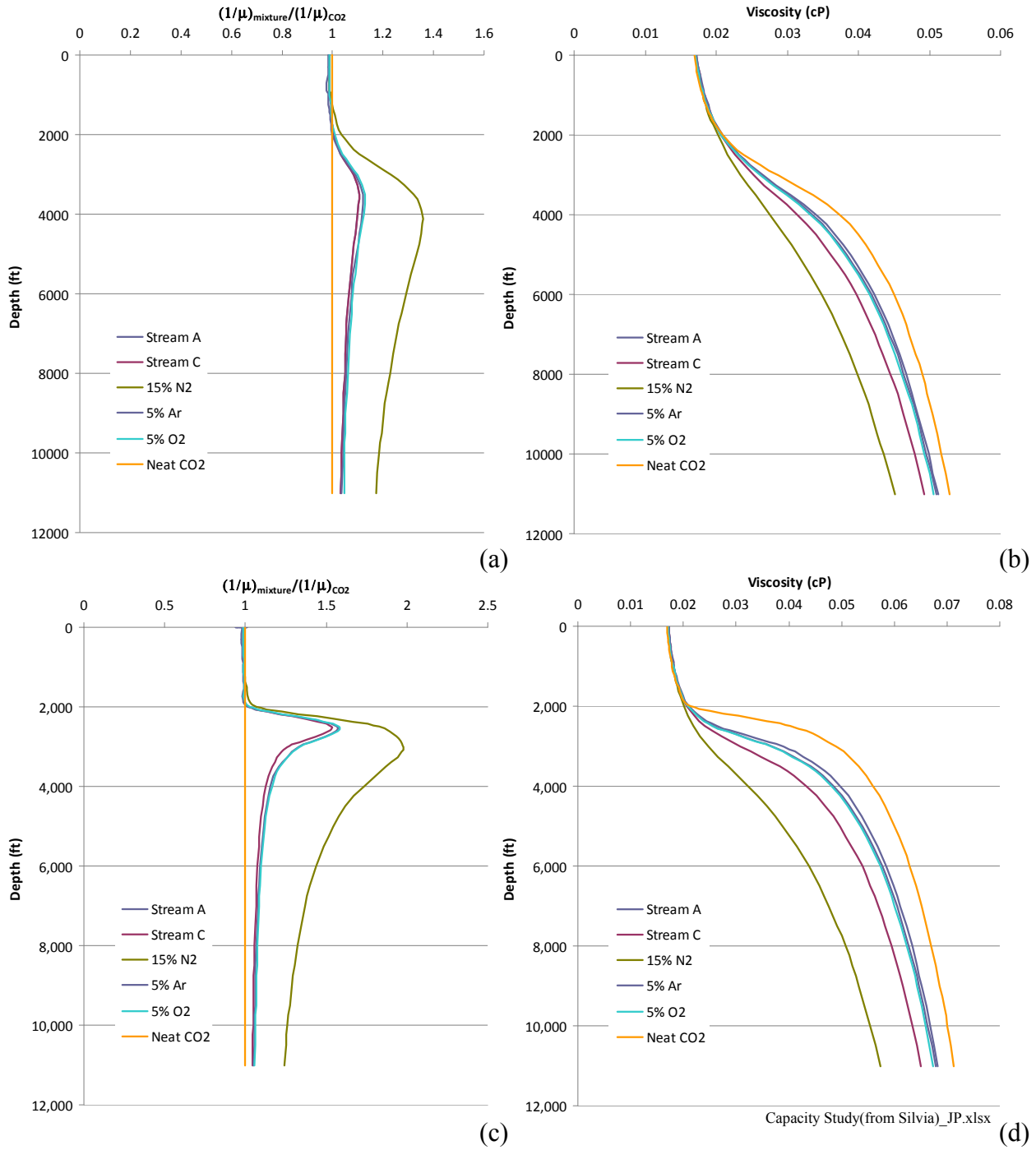


Figure 16. Inverse of mixture viscosity relative to that of neat CO₂ (a and c) and inverse of mixture density (b and d) as a function of depth. Pressure gradient is 0.465 psi/ft (all) and geothermal gradient is 18°F/1000ft (a and b) or 10°F/1000ft (c and d).

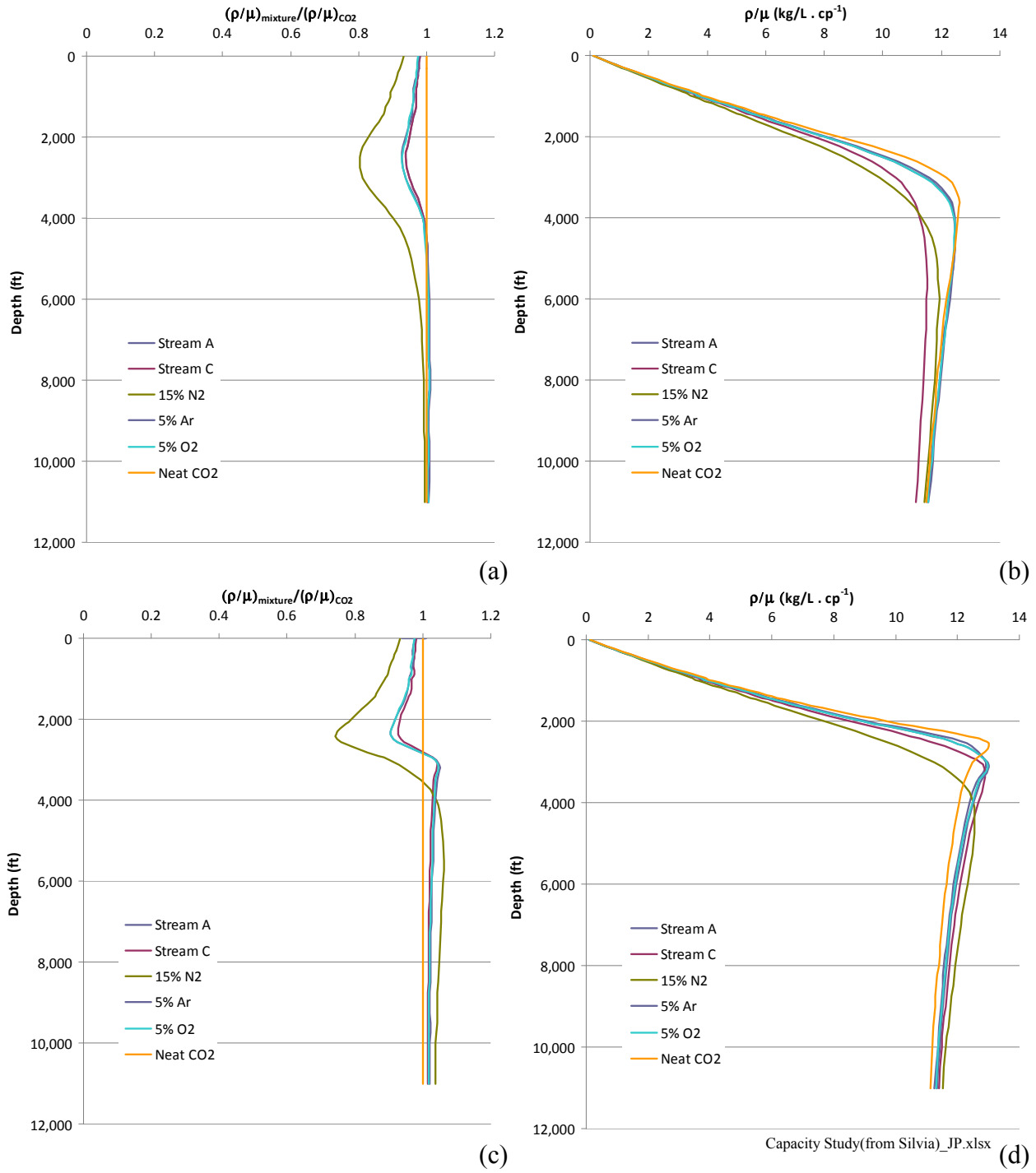


Figure 17. Mixture density-viscosity ratio relative to that of neat CO₂ (a and c) and density-viscosity ratio (b and d) as a function of depth. Pressure gradient is 0.465 psi/ft (all) and geothermal gradient is 18°F/1000ft (a and b) or 10°F/1000ft (c and d).

III-2. Generic Model Results

Results are summarized according to three metrics (e.g., Kumar, 2008; Nicot et al., 2008): time to hit the top, maximum lateral extent updip of the injection well, and fraction of gas still mobile after a given time.

Time to hit the top is visually defined in output cross sections as the time at which the first cell of the top layer has nonzero gas saturation. Figure 2 illustrates the process for the base case (Case #3). Maximum lateral extent is the distance from the injected well beyond which there is no gas saturation at 100 yr (Figure 2b). In many simulations, this state is reached before the end of the runs. *Time to reach the top* is defined as the time it takes for the model to have nonzero gas saturation in a top-layer cell (Figure 2a).

As noticed by Kumar (2008), a coarse grid overestimates residual saturation by the implicit assumption that CO₂ will uniformly invade the whole available space—an assumption harder to meet as grid-block size increases. Similarly, in theory, mobile fraction of gas or of a gas component in a cell should be computed from the total amount of gas/component from which the dissolved amount has been deducted and from which the amount that will stay immobile behind has been subtracted. The Land formula (e.g., Land, 1971), giving residual saturation as a function of maximum saturation, can be used to compute the future immobile amount. Because of the coarseness of the grid and of well-known sweep-efficiency problems, however, we thought that the mobile fraction should be defined as total amount minus dissolved amount in cells where gas is still moving (defined by cells with nonzero relative permeability). Figure 3 illustrates the difference in results between the two definitions of mobile gas. Amount of dissolved gas is identical by construction, but there is a big difference in immobilized gas, especially early on, probably because of the high gas saturation (~100%) reached around the well at early times. At later times, as more and more of the gas is actually trapped, difference between the two approaches decreases. Nicot et al. (2008) presented results for both approaches to compute mobile gas. This study uses the first approach, the most conservative in terms of the amount of mobile gas remaining in the system.

A summary of results in terms of metrics (time to reach the top, maximum extent, and mobile gas as a function of time) is presented below and a more comprehensive list of results is presented in Appendix D.

III-2-1 Parametric Study of Stream Composition

The injection-stream composition fundamentally impacts the three metrics, and plotting results on a mole fraction ternary diagram is a convenient way to visualize them (Figure 18 to Figure 21). The diagrams are based on the 25% of the injection stream that varies between the three poles of 100% (of the 25%) CO₂, N₂, Ar, O₂, or CH₄. The remaining 75% is always CO₂, and there is no need to include them in the ternary diagrams. Because there are four gases of interest, we used several types of ternary diagrams with poles: CO₂, N₂, and either Ar-O₂-CH₄. The top pole represents an injection stream of 75% CO₂ and 25% N₂, the left-hand-side bottom pole represents a 100%-CO₂ stream, whereas the right-hand-side bottom pole represents 75% CO₂ and 25% Ar, O₂, or CH₄. ternary diagrams are completed for both shallow and deep Gulf Coast cases. Only 16 points were used to draw the diagrams and, although the general trends are valid, local deviations in the curves most likely represent a paucity of data points rather than a real

fluctuation of isolines. In any case, as expected, metrics vary smoothly with injection-stream composition but not necessarily linearly.

The time to reach the top (Figure 18 and Figure 19) in the shallow case varies from 13.7 to 30 yr for injection stream compositions of 75% CO₂ and 25% N₂ and 100% CO₂, respectively while in the deep case varies from 16.44 to 25 yr for the same compositions. Cases with stream composition of 75% CO₂ and 25% CH₄, are close to the N₂ and O₂ cases for shallow and deep instances, with times of 13.7 yr and 16.44 yr respectively. Injection ended at the same time as the gas reached the top only in the case of neat CO₂. Such behavior can be explained if the two following mechanisms were acting in the same direction to maximize time to reach the top: (1) higher dissolution of CO₂ into the aqueous phase attenuating its upward migration but (2) stronger buoyancy forces when the injection stream contains a significant amount of CH₄ and N₂. See Kumar (2008) for details. He did a detailed analysis of plume dynamics on a simplified system similar to the one used in this study. He determined that time to hit the top was controlled by a Gravity Number N_{gv} defined as

$$N_{gv} = \frac{k_v \Delta \rho g \cos \alpha}{\mu u}$$

where k_v is vertical permeability, $\Delta \rho$ is density difference between brine and gas phase at aquifer temperature and pressure, α is dip angle, μ is gas viscosity, and u is total velocity. The only terms varying with injection-stream composition are $\Delta \rho / \mu$ and u . The term u can be reasonably assumed constant, and changes to $\Delta \rho / \mu$ dominate the behavior of the system. Buoyancy forces are initially stronger in the CO₂-N₂ mixture than in the CO₂-CH₄ mixture (Figure 92 and Figure 93—Appendix B), explaining the shorter time to reach the top for the former. Overall, all plots show the same pattern, including in the general directions and the magnitude of the isolines, a decrease in time to hit the top

For the remainder of the section, we focus on plume extent (Figure 20 and Figure 21). Maximum plume extent controls on elements such as size of the area-of-review, area in which wells penetrating the seal and injection formation must be examined and possibly fixed if they could allow leakage, and impacts other important costs such as the extent of the monitoring footprint. Examination of Figure 22 suggests that neat CO₂ has always the smallest footprint and that an increase in impurities also increases the plume extent in a relatively linear fashion (if impurity mole fraction is doubled, additional plume extent is also approximately doubled). Another observation, corroborating previous findings, is that the shallow case generates larger extent compared to the same injectate composition in the shallow case. the case without dissolution (Figure 23) displays very similar results but with a slightly higher plume extent. Figure 24 compares with and without dissolution cases side by side. It shows that dissolution has a variable (but small) impact on the extent and that the contrast between the 2 dissolution end-members decreases with increasing depth.

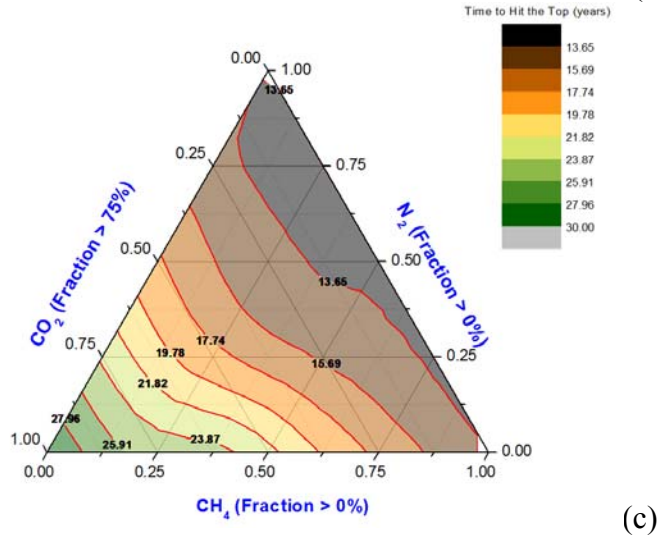
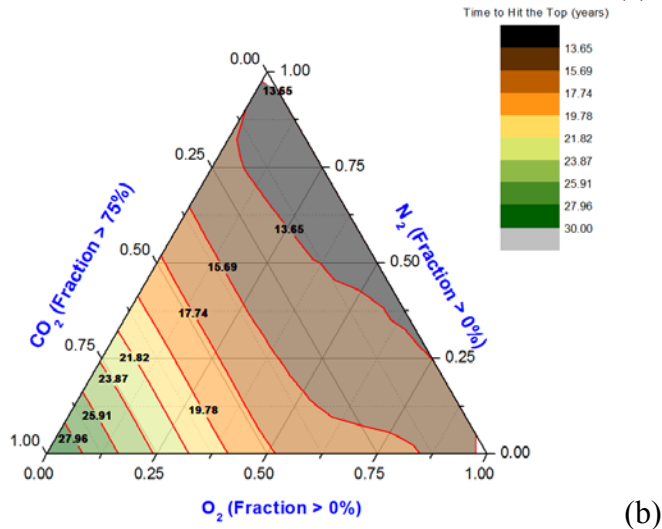
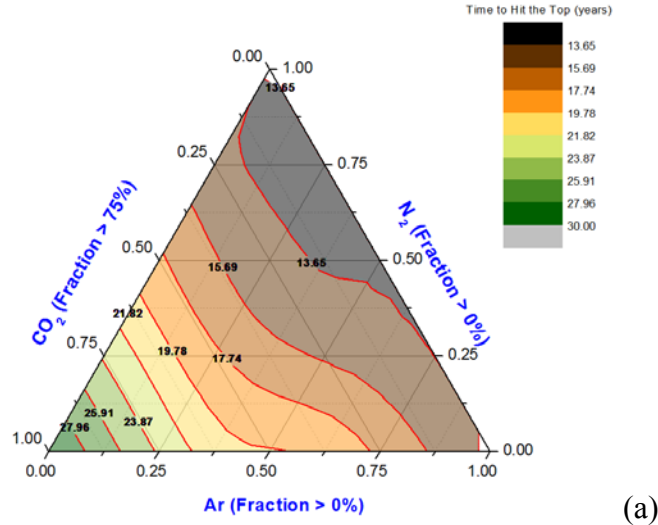
Binary runs with increasing mole fraction of a single impurity (5, 15, and 25%) illustrates that a small concentration, all impurities have a similar impact on flow behavior and that deep systems are much less impacted by impurities in terms of flow.

Comparing results from the shallow and deep cases (Figure 25) show that for small impurity mole fraction (~5%) plume extent is slightly larger for the GC deep case than for the GC shallow case (Figure 25a). The effect is more pronounced for neat CO₂. Higher impurity levels generate a

reversal in lateral plume extent with the shallow GC cases displaying a larger extent than the deep GC case.

Figure 26 to Figure 29 displays the same results in terms of change relative to the neat-CO₂ base case as opposed to the absolute values as above (only cases with dissolution). All plots use the same vertical scale to ease comparisons. Figure 30 along with Appendix B explains why impurities have less and less impact as depth increase: properties such as density, viscosity, and compressibility become more alike for various mixtures. Figure 26 to Figure 29 also show the mobile fraction at a given time (100 years).

The amount of mobile gas decreases through, initially fast for 200 years and then slower (Table 12) as illustrated in Figure 31 to Figure 33. Note that the timing is a function of the permeability of the system, assumed here to be uniform at 300 md. A model with a smaller permeability would show a similar behavior but over a longer time period (not shown). Plotting the same data points on the same graph for several compositions (neat CO₂, stream A, and Stream C) for the shallow and deep GC cases (Figure 34) shows that different mixtures behave similarly but in a more complex way with curves crossing each other at several occasions. Some of the curve irregularities are due to the coarseness of the modeling grid used to determine maximum extent. To clarify their relationship, Figure 35 shows the same results separately for the shallow and deep case and for different time ranges (0-50, 0-100, and 100-1000 years). As observed several times, mixtures behave similarly in the deep case, more so than in the shallow case. At early times, at a given time, neat CO₂ shows more mobile gas than the mixtures (Figure 35b, c), that is, impurities help trap the gas faster even if the plume extent is greater. At later times (after 100-200 years in this case), when more than 70% of the injected stream has been trapped (Figure 35d), results show less obvious trends and are obscured by the lack of sufficient grid resolution of the modeling.



TERNARY DIAGRAMS CCP3 -ALL 06-21-2011.pptx

Figure 18. Time (years) to reach the top of various ternary mixtures at shallow Gulf Coast conditions: CO₂-N₂-Ar (a), CO₂-N₂-O₂ (b), CO₂-N₂-CH₄ (c). (injection period is 30 years)

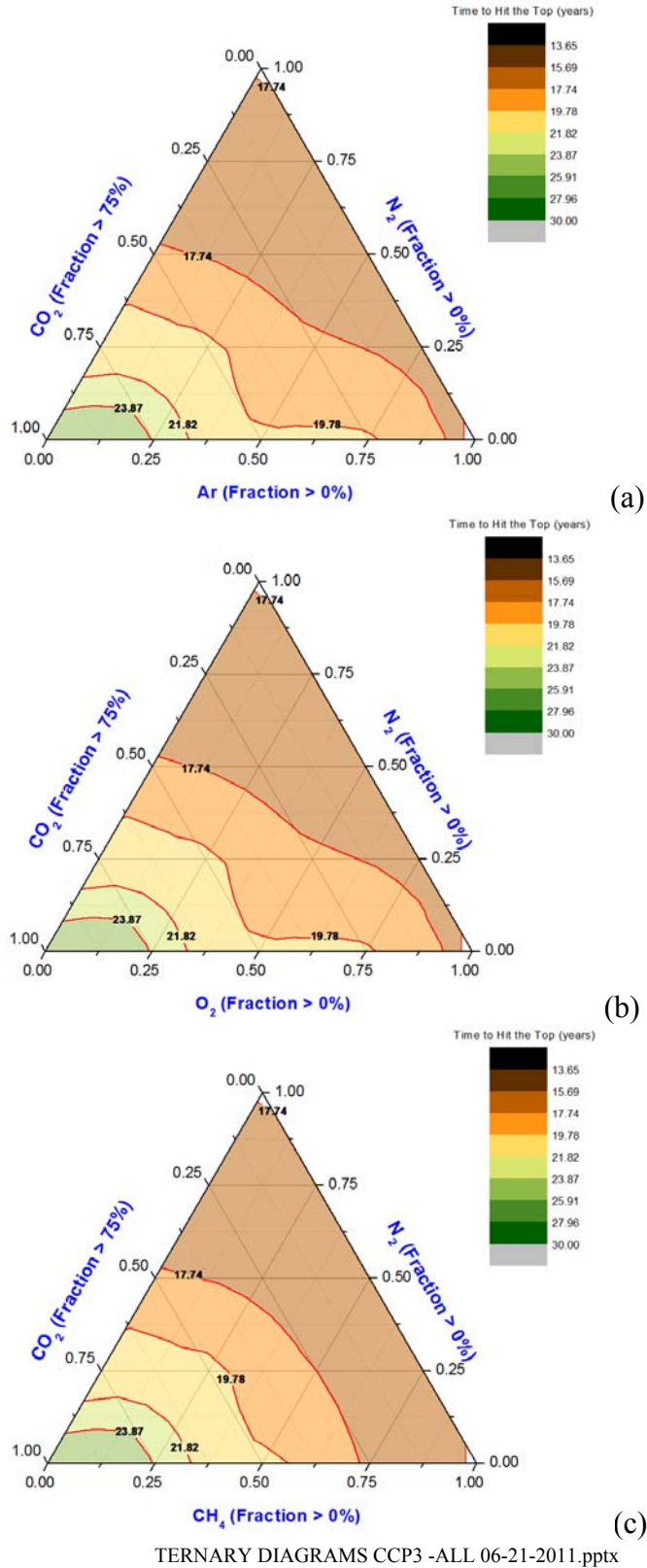
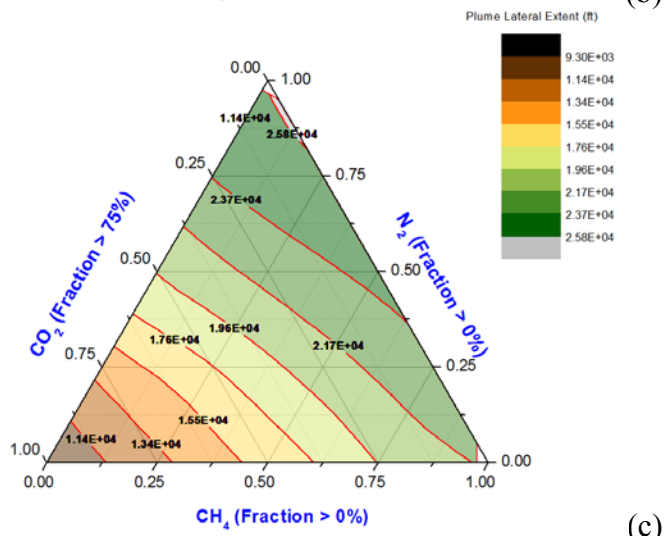
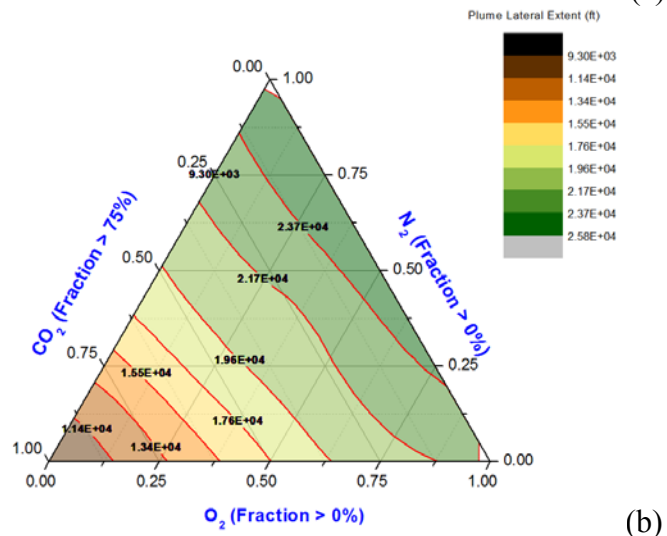
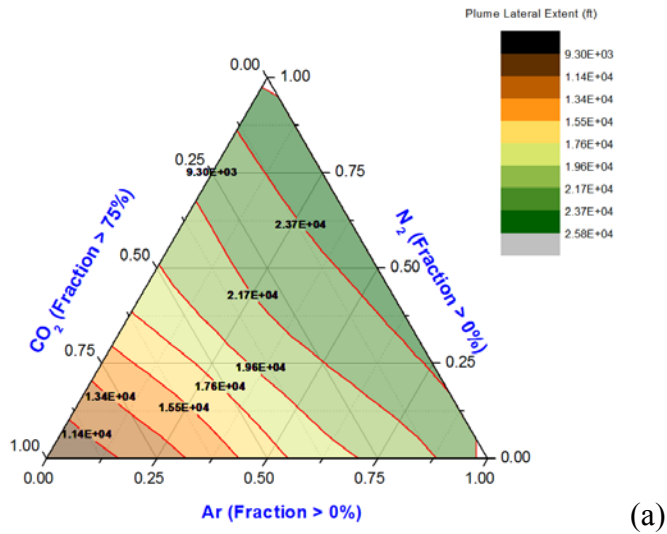
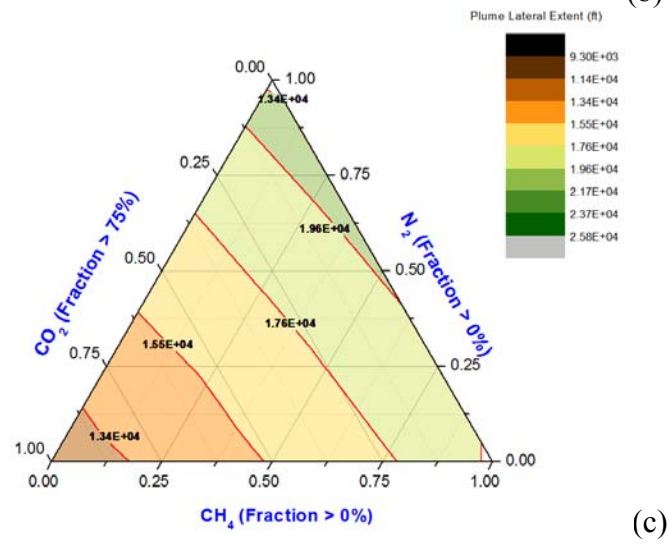
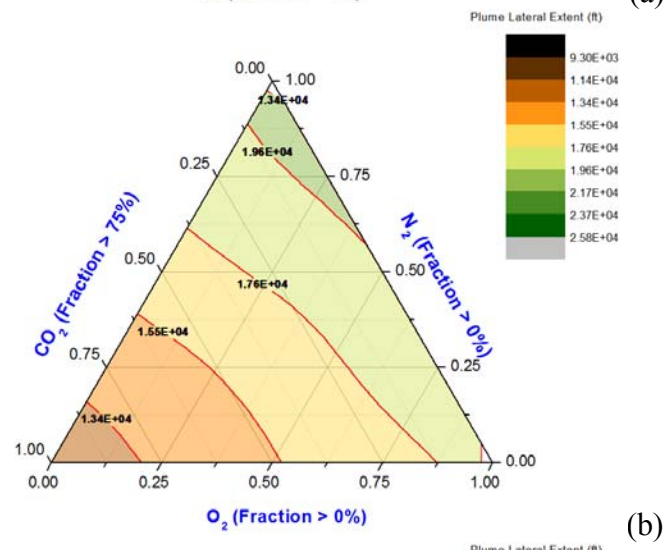
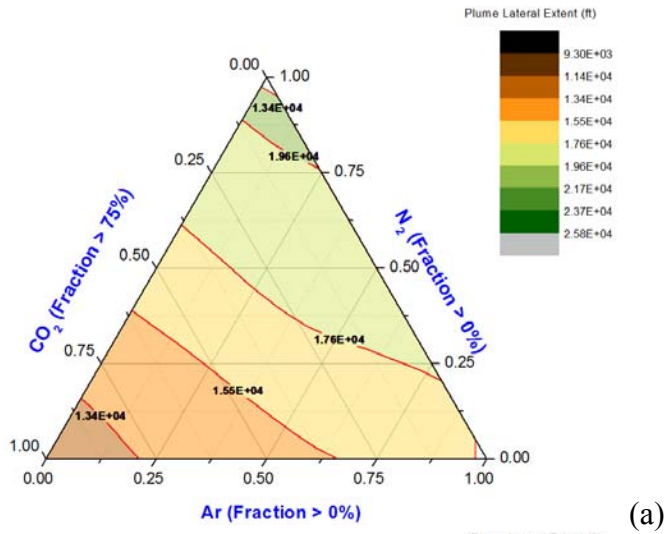


Figure 19. Time (years) to reach the top of various ternary mixtures at deep Gulf Coast conditions: CO₂-N₂-Ar (a), CO₂-N₂-O₂ (b), CO₂-N₂-CH₄ (c). (injection period is 30 years)



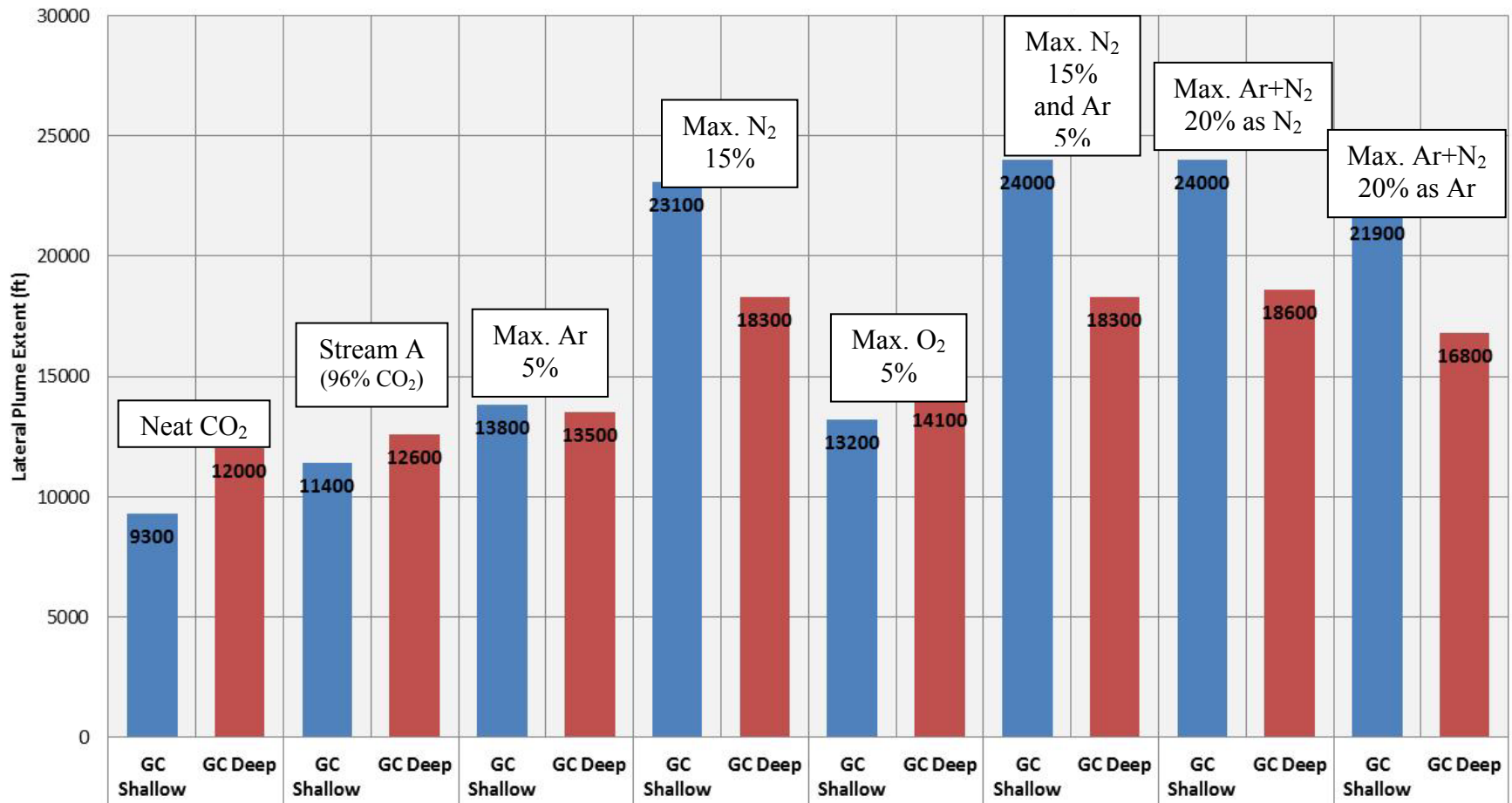
TERNARY DIAGRAMS CCP3 -ALL 06-21-2011.pptx

Figure 20. Plume extent (ft) of various ternary mixtures at shallow Gulf Coast conditions: CO₂-N₂-Ar (a), CO₂-N₂-O₂ (b), CO₂-N₂-CH₄ (c). (injection period is 30 years)



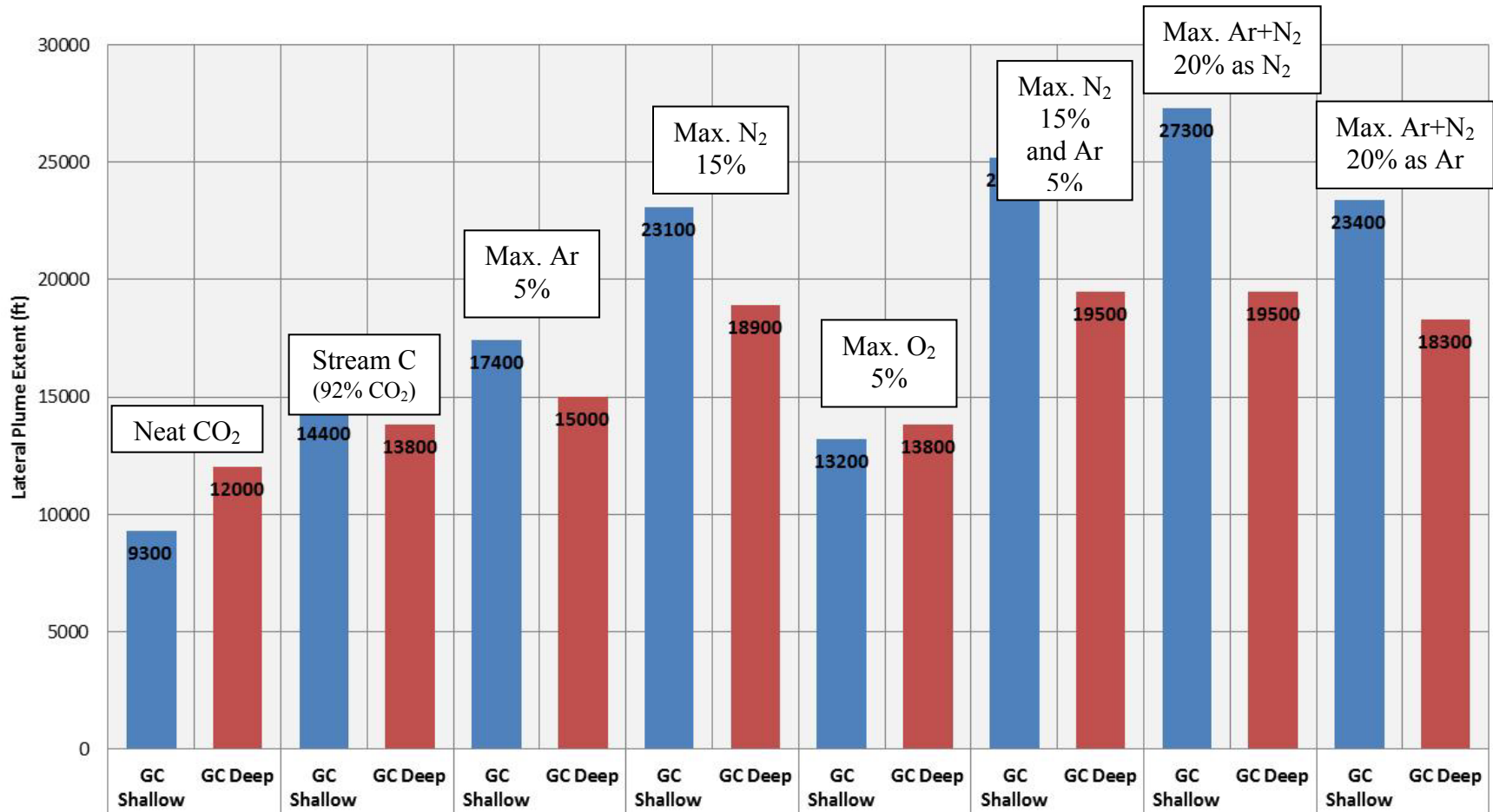
TERNARY DIAGRAMS CCP3 -ALL 06-21-2011.pptx

Figure 21. Plume extent (ft) of various ternary mixtures at deep Gulf Coast conditions: CO₂-N₂-Ar (a), CO₂-N₂-O₂ (b), CO₂-N₂-CH₄ (c). (injection period is 30years)



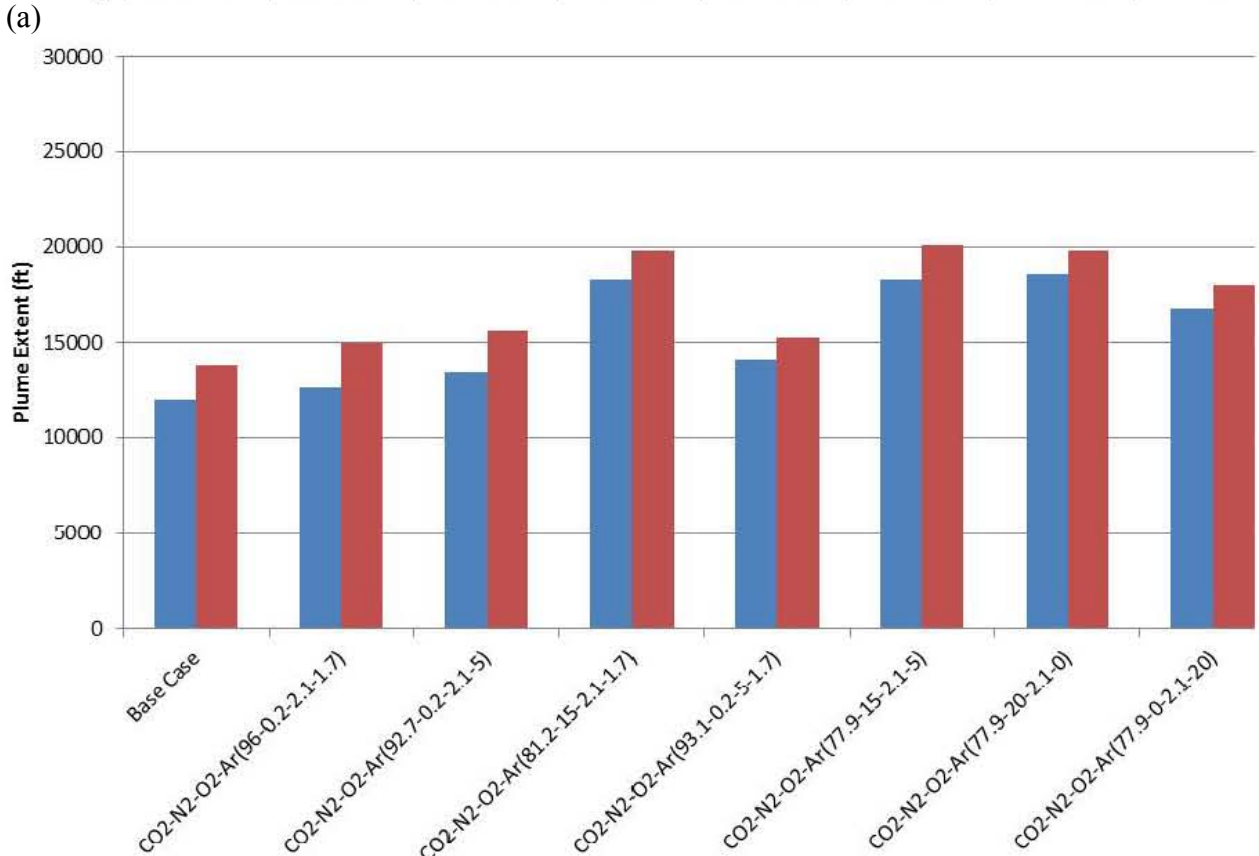
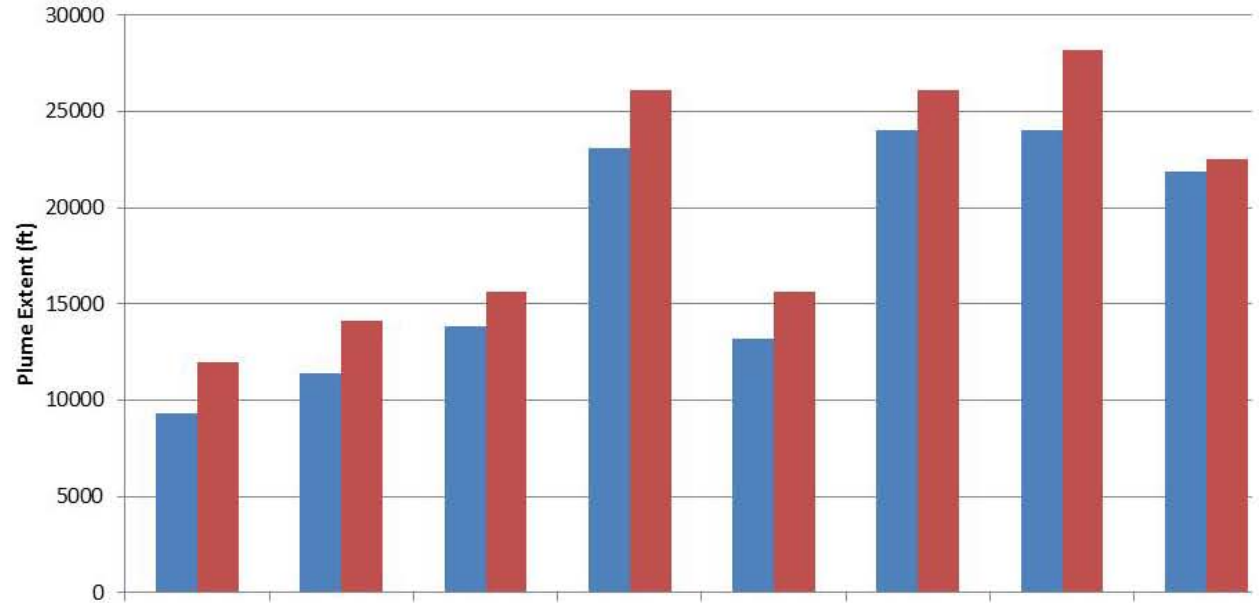
Note: components in mole fraction

Figure 22. Plume extent for the 4-component Composition A system, GC shallow and deep cases (with dissolution, at 100 years)



Note: components in mole fraction

Figure 23. Plume extent for the 4-component Composition C system, GC shallow and deep cases (with dissolution, at 100 years)



(b)
 Note: left column (blue) = dissolution; right column (red) = no dissolution

Figure 24. Impact of dissolution on results for GC shallow (a) and deep (b) cases.

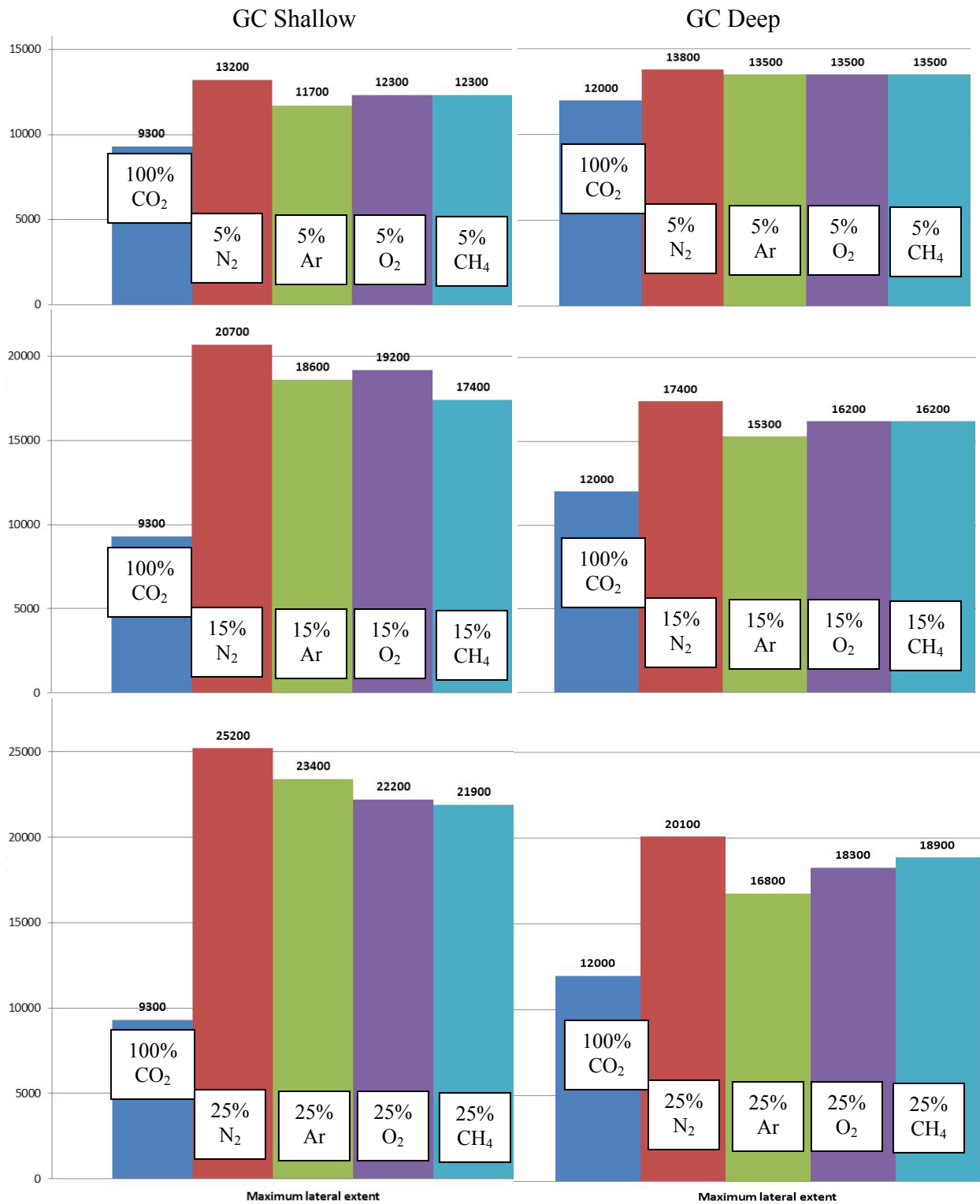
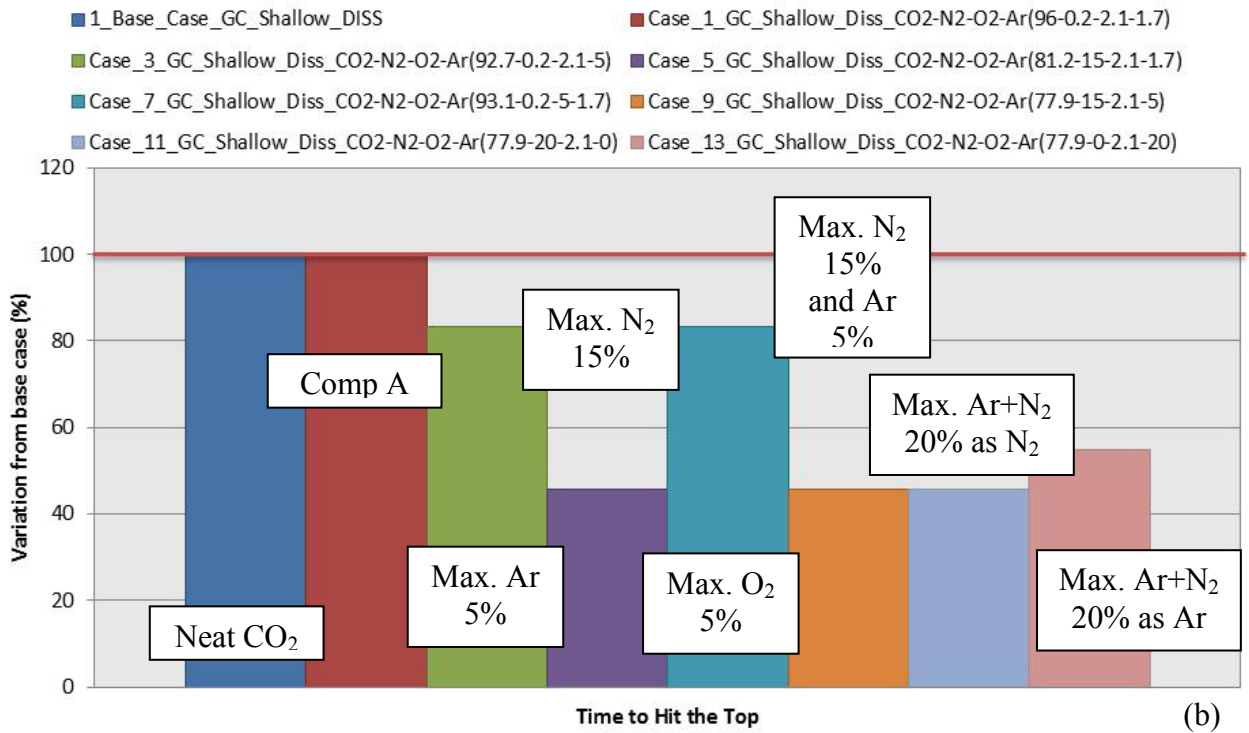
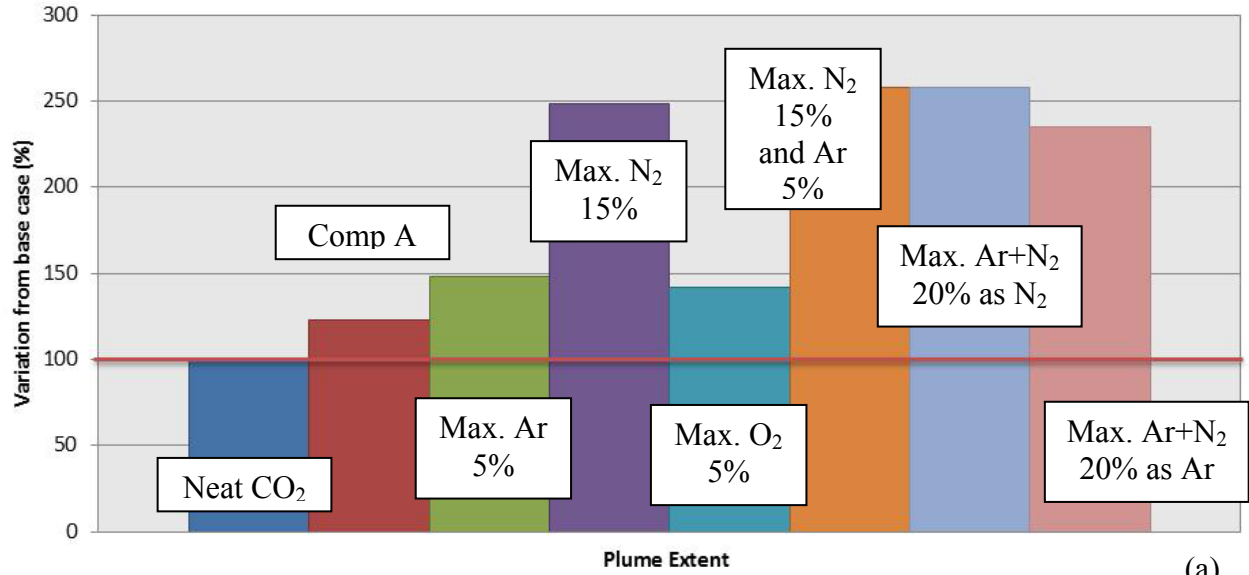
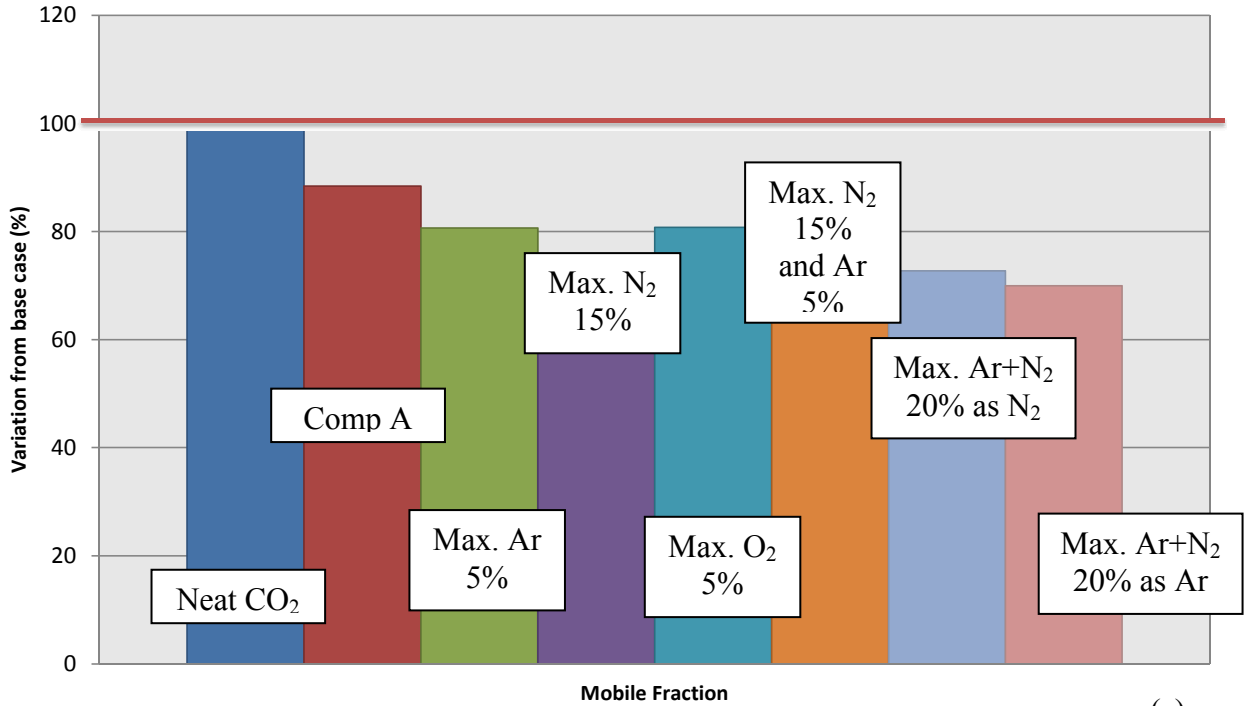


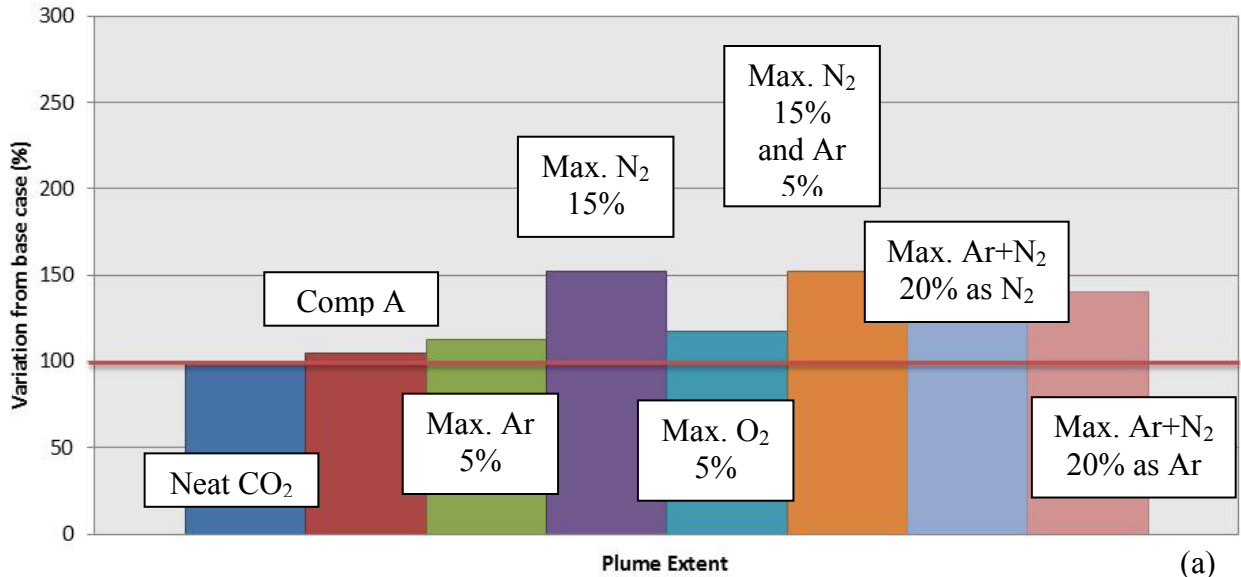
Figure 25. Plume extent in feet at 100 years with dissolution for GC Shallow and GC deep cases





- 1_Base_Case_GC_Shallow_DISS
- Case_1_GC_Shallow_Diss_CO2-N2-O2-Ar(96-0.2-2.1-1.7)
- Case_3_GC_Shallow_Diss_CO2-N2-O2-Ar(92.7-0.2-2.1-5)
- Case_5_GC_Shallow_Diss_CO2-N2-O2-Ar(81.2-15-2.1-1.7)
- Case_7_GC_Shallow_Diss_CO2-N2-O2-Ar(93.1-0.2-5-1.7)
- Case_9_GC_Shallow_Diss_CO2-N2-O2-Ar(77.9-15-2.1-5)
- Case_11_GC_Shallow_Diss_CO2-N2-O2-Ar(77.9-20-2.1-0)
- Case_13_GC_Shallow_Diss_CO2-N2-O2-Ar(77.9-0-2.1-20)

Figure 26. Composition A, dissolution, GC shallow – relative plume extent (a), time to hit the top (b), and mobile fraction at 100 years (c)



- 3_Base_Case_GC_Deep_DISS
- Case_2_GC_Deep_Diss_CO2-N2-O2-Ar(96-0.2-2.1-1.7)
- Case_4_GC_Deep_Diss_CO2-N2-O2-Ar(92.7-0.2-2.1-5)
- Case_6_GC_Deep_Diss_CO2-N2-O2-Ar(81.2-15-2.1-1.7)
- Case_8_GC_Deep_Diss_CO2-N2-O2-Ar(93.1-0.2-5-1.7)
- Case_10_GC_Deep_Diss_CO2-N2-O2-Ar(77.9-15-2.1-5)
- Case_12_GC_Deep_Diss_CO2-N2-O2-Ar(77.9-20-2.1-0)
- Case_14_GC_Deep_Diss_CO2-N2-O2-Ar(77.9-0-2.1-20)

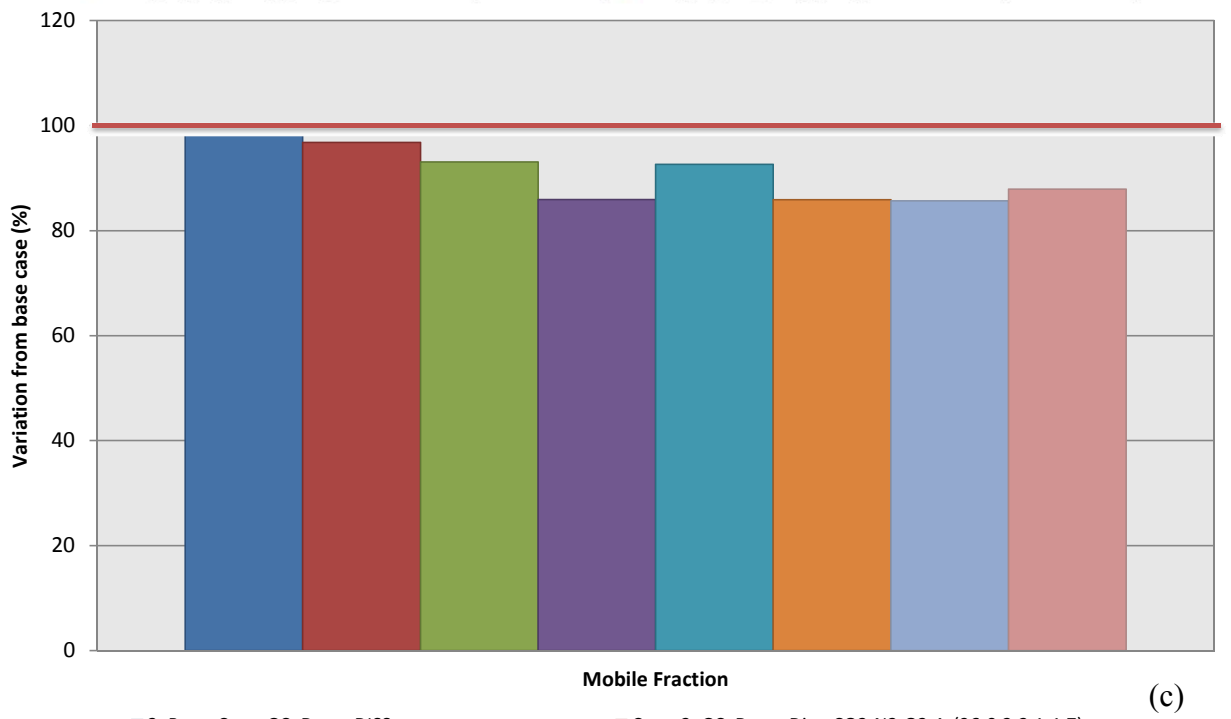
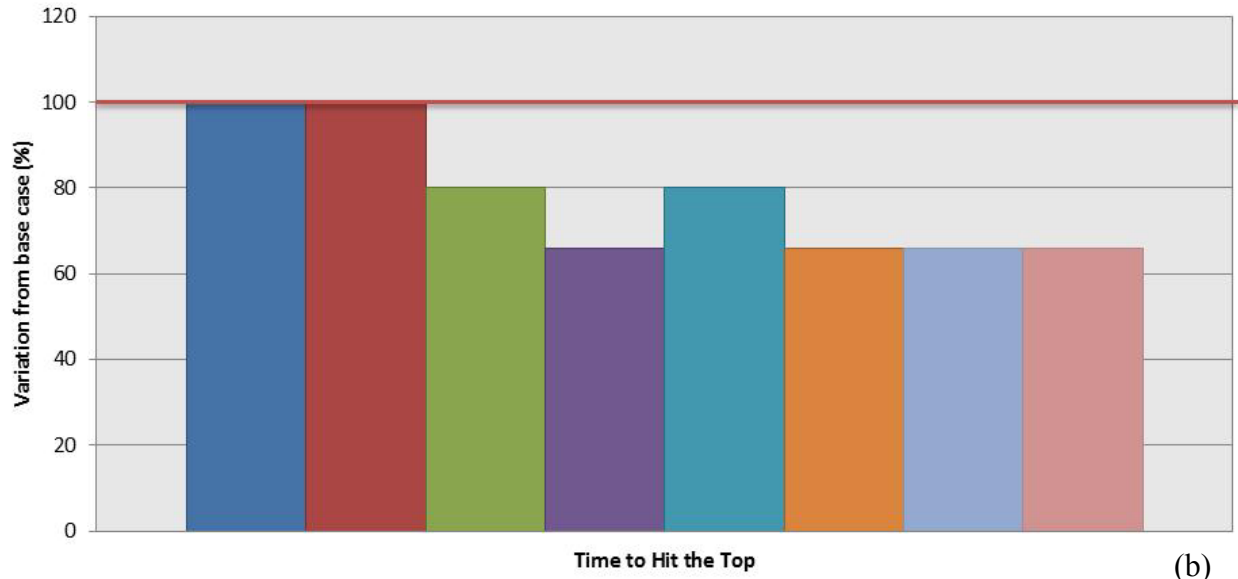
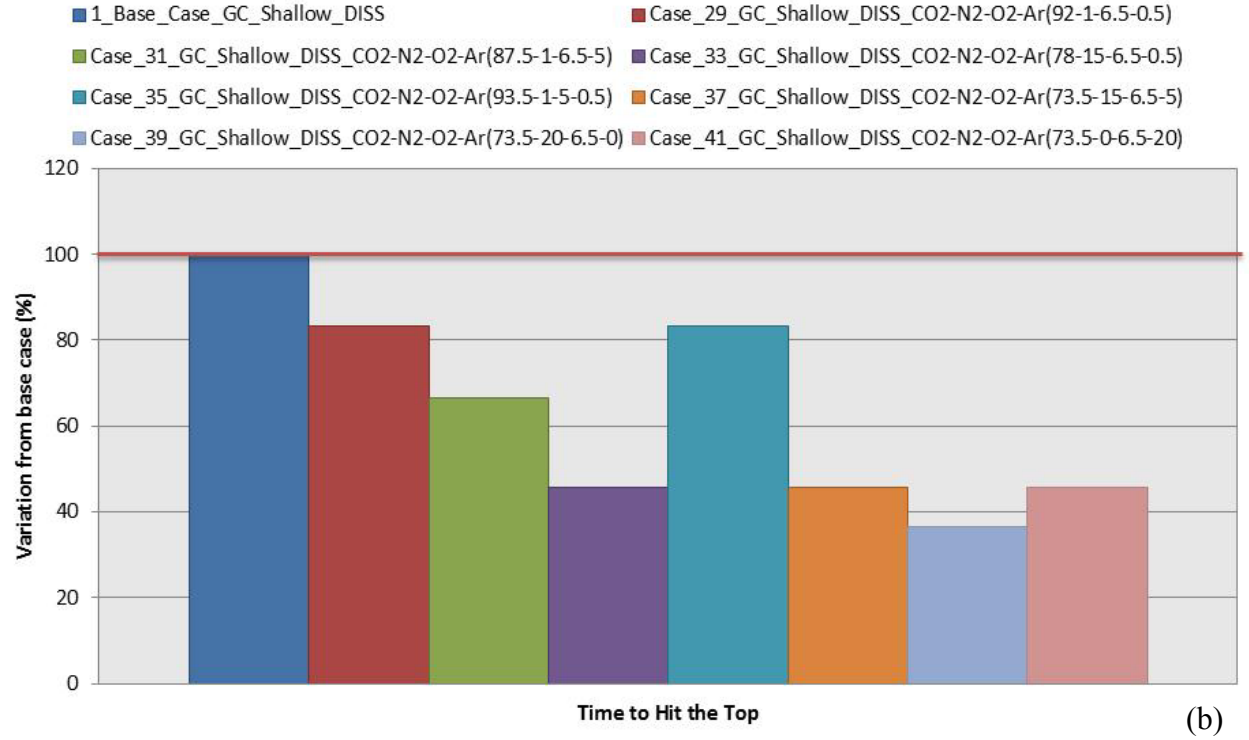
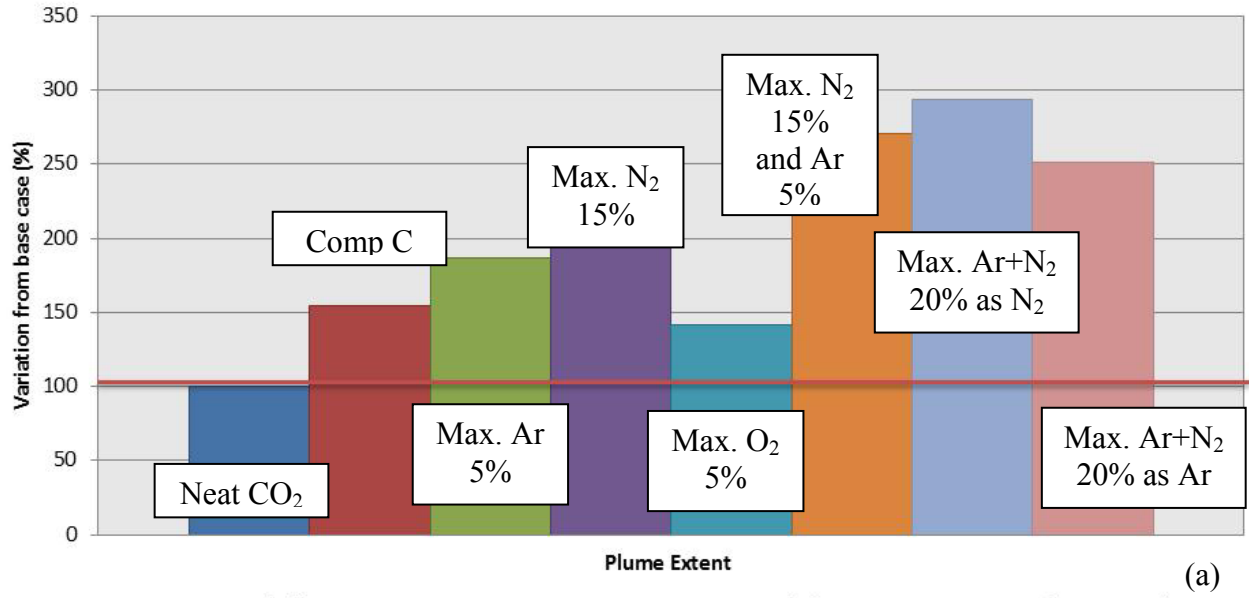


Figure 27. Composition A, dissolution, GC deep – relative plume extent at 100 years (a), time to hit the top (b), and mobile fraction at 100 years (c)



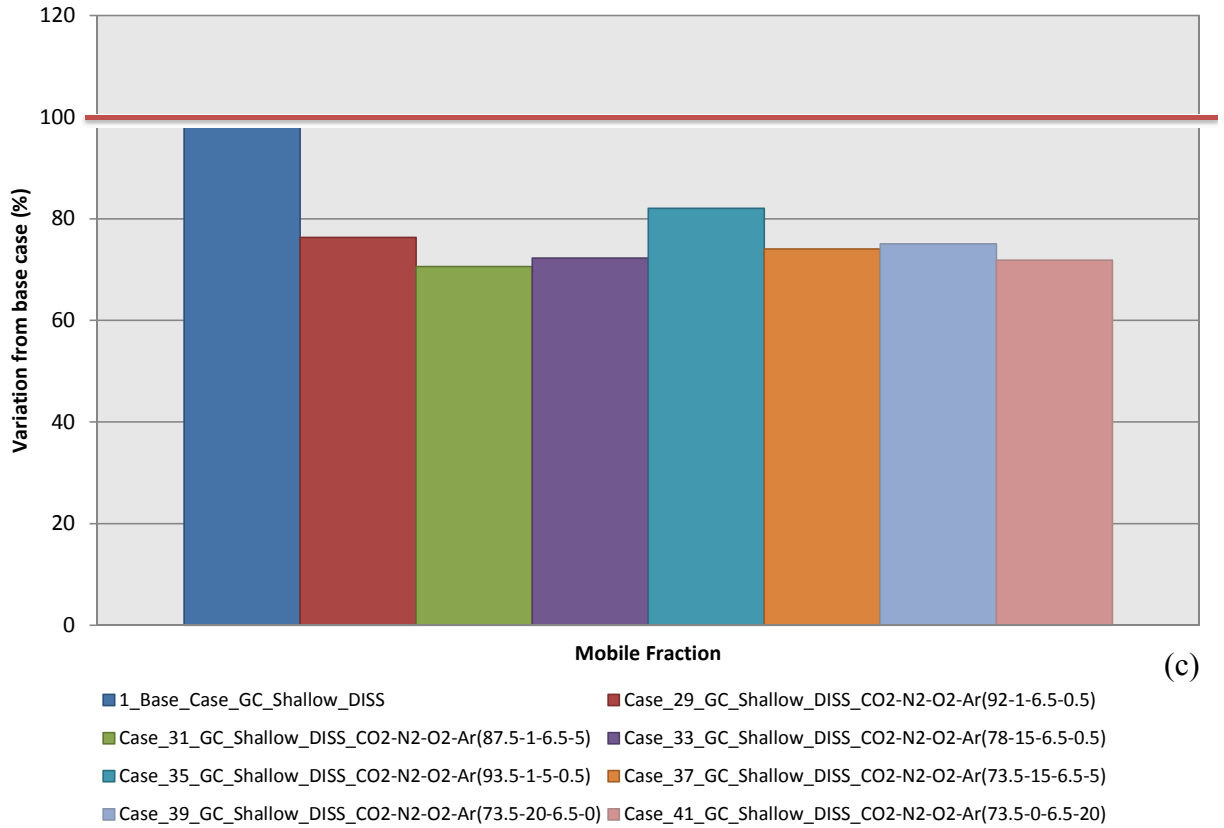
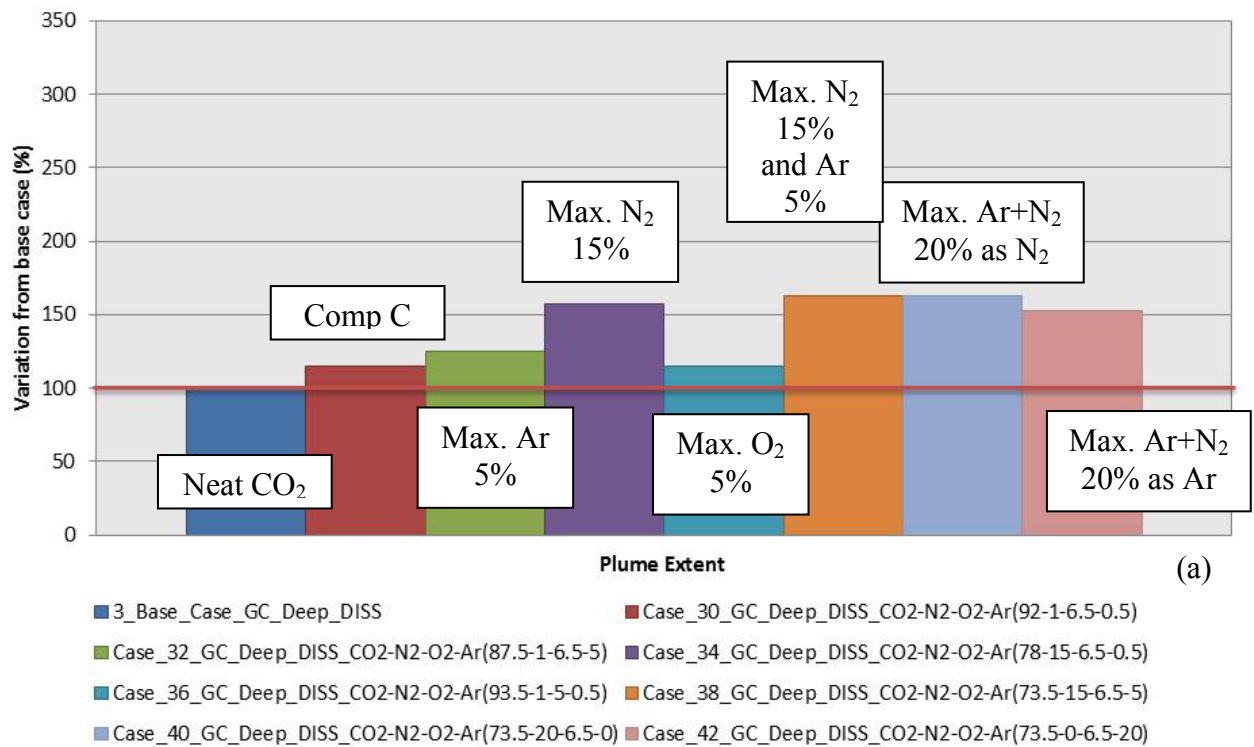


Figure 28. Composition C, dissolution, GC shallow – relative plume extent (a), time to hit the top (b), and mobile fraction at 100 years (c)



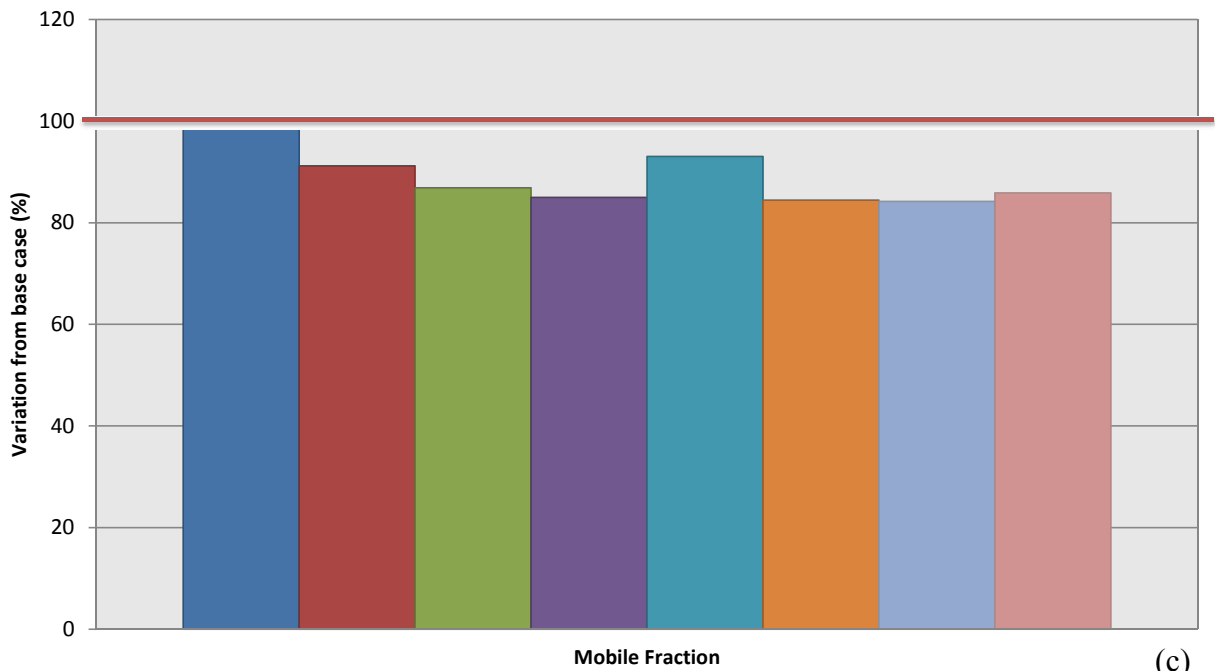
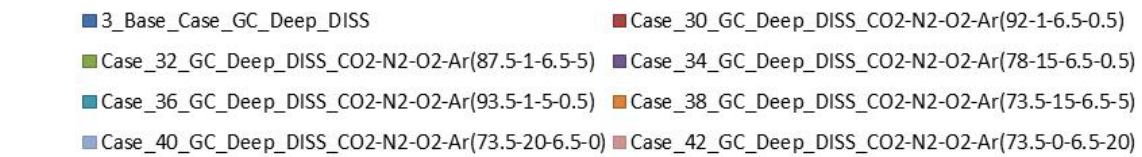
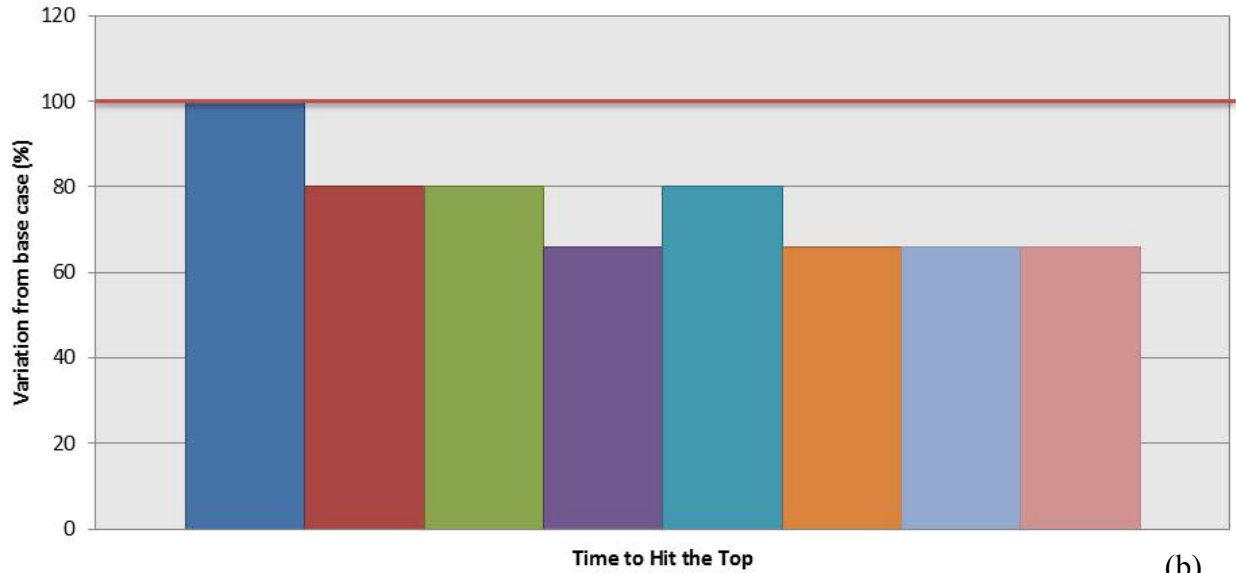
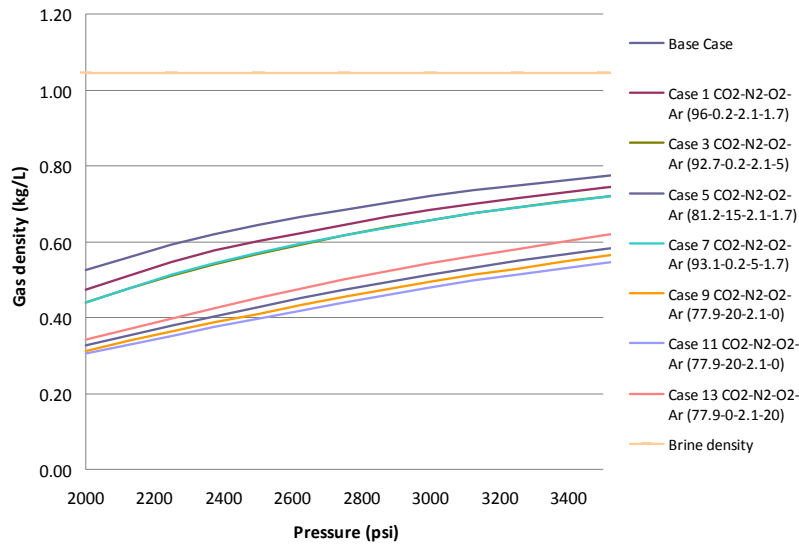
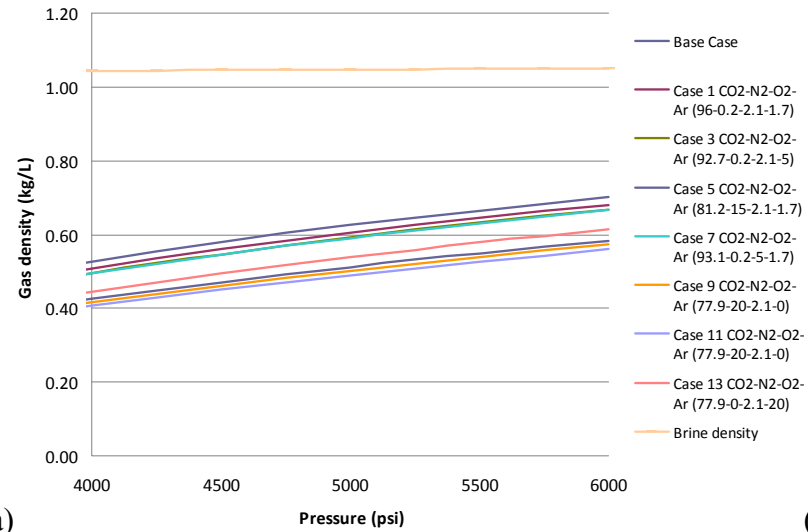


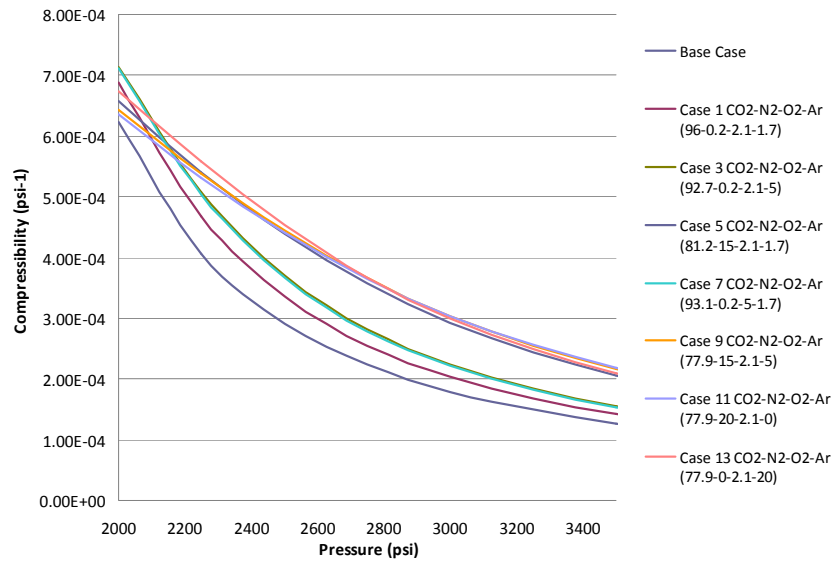
Figure 29. Composition C, dissolution, GC deep – relative plume extent (a), time to hit the top (b), and mobile fraction at 100 years (c)



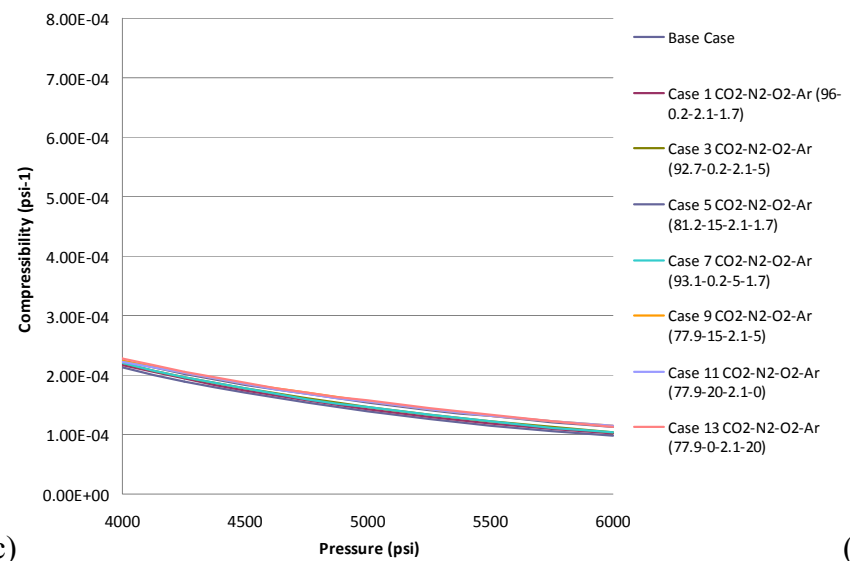
(a)



(b)



(c)



(d)

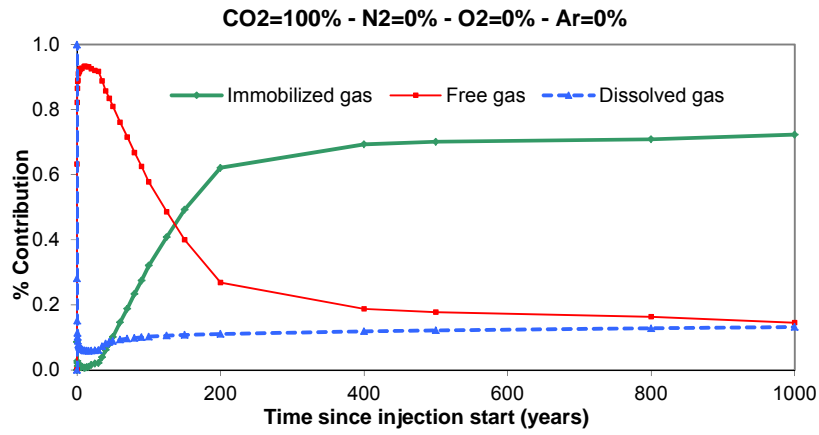
Figure 30. Gas density (a and b) and compressibility (c and d) for variations in injection stream, GC shallow (a and c) and deep (b and d) reservoirs.

Viscosity_Density_Compressibility_Results_Shallow_and_Deep_Stream A(from Silvia).xlsx

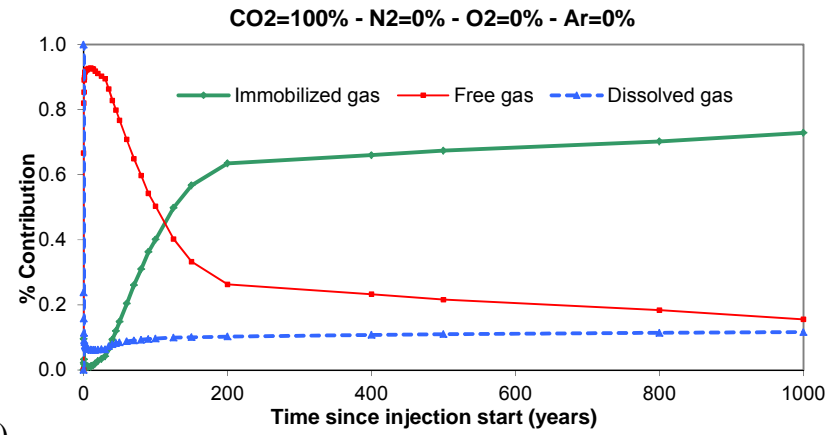
Table 12. Mobile gas fraction (mass fraction) through time for neat CO₂, Stream A, and Stream C injection streams

Time (yr)	Base Case GC Shallow	Base Case GC Deep	Stream A GC Shallow	Stream A GC Deep	Stream C GC Shallow	Stream C GC Deep
0.0	0.0000	0.0000	0.0000	0.0000	0.0000	0.0000
0.0027	0.0000	0.0000	0.0000	0.0000	0.0000	0.0000
0.0274	0.6327	0.6666	0.6397	0.6939	0.6648	0.7593
0.2738	0.8218	0.8201	0.8162	0.8775	0.8561	0.8845
0.5476	0.8653	0.8539	0.8435	0.8769	0.8630	0.8878
1.0	0.8870	0.8911	0.8932	0.8967	0.8886	0.9028
1.37	0.8905	0.8983	0.8901	0.9106	0.8984	0.9131
2.06	0.9098	0.9148	0.9107	0.9238	0.9133	0.9222
2.77	0.9155	0.9176	0.9043	0.9259	0.9146	0.9258
3.42	0.9172	0.9200	0.9159	0.9309	0.9168	0.9310
4.11	0.9227	0.9234	0.9222	0.9266	0.9233	0.9260
4.79	0.9245	0.9229	0.9234	0.9329	0.9243	0.9281
5.48	0.9260	0.9233	0.9253	0.9324	0.9251	0.9308
6.84	0.9268	0.9263	0.9233	0.9333	0.9249	0.9314
10.0	0.9323	0.9275	0.9290	0.9327	0.9242	0.9289
11.0	0.9335	0.9261	0.9248	0.9316	0.9236	0.9274
13.7	0.9320	0.9247	0.9215	0.9271	0.9200	0.9205
16.4	0.9314	0.9185	0.9213	0.9214	0.9124	0.9146
20	0.9256	0.9107	0.9194	0.9163	0.9056	0.9081
25	0.9201	0.9028	0.9061	0.9037	0.8976	0.8960
30	0.9174	0.8950	0.8985	0.8969	0.8891	0.8914
35	0.8882	0.8629	0.8700	0.8653	0.8537	0.8587
40	0.8576	0.8281	0.8364	0.8324	0.8202	0.8169
45	0.8348	0.7987	0.8000	0.7924	0.7791	0.7811
50	0.8097	0.7673	0.7783	0.7605	0.7488	0.7474
60	0.7608	0.7081	0.7166	0.6924	0.6740	0.6776
70	0.7159	0.6486	0.6623	0.6297	0.6093	0.6107
80	0.6682	0.5975	0.6056	0.5803	0.5483	0.5572
90	0.6253	0.5427	0.5561	0.5314	0.4882	0.5034
100	0.5775	0.5028	0.5104	0.4867	0.4407	0.4585
125	0.4862	0.4023	0.4029	0.3934	0.3520	0.3739
150	0.3996	0.3326	0.3269	0.3281	0.2897	0.3235
200	0.2684	0.2630	0.2316	0.2754	0.2554	0.2896
400	0.1877	0.2323	0.2032	0.2415	0.2131	0.2505
500	0.1775	0.2161	0.1884	0.2250	0.1878	0.2277
800	0.1634	0.1838	0.1554	0.1703	0.1529	0.1748
1000	0.1452	0.1554	0.1323	0.1414	0.1151	0.1311

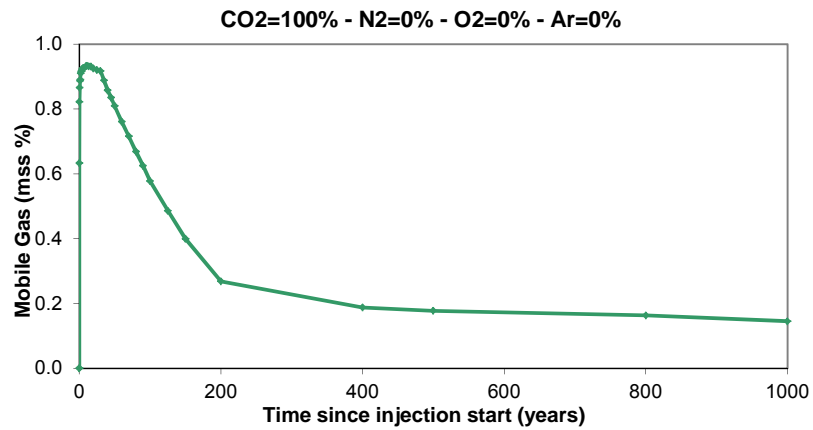
Note: unlike most of other results presented at 100 years after start of injection, this table includes results up to 1,000 years



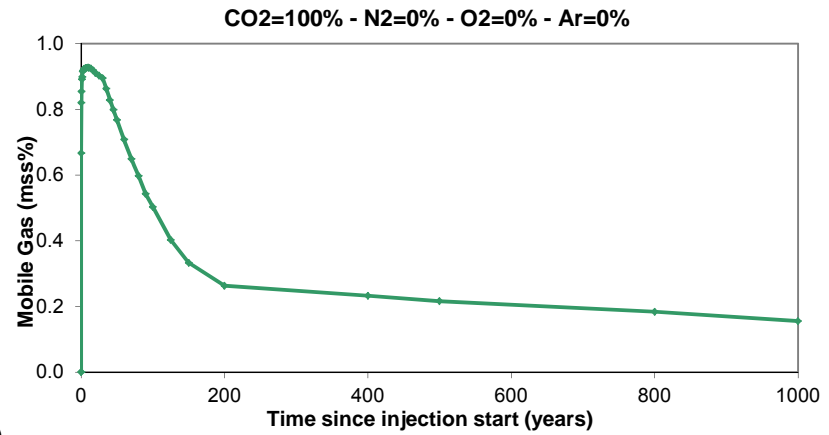
(a)



(b)



(a)



(b)

Figure 31. Neat CO₂ phase distribution through time: shallow Gulf Coast (a) and deep Gulf Coast (b) cases

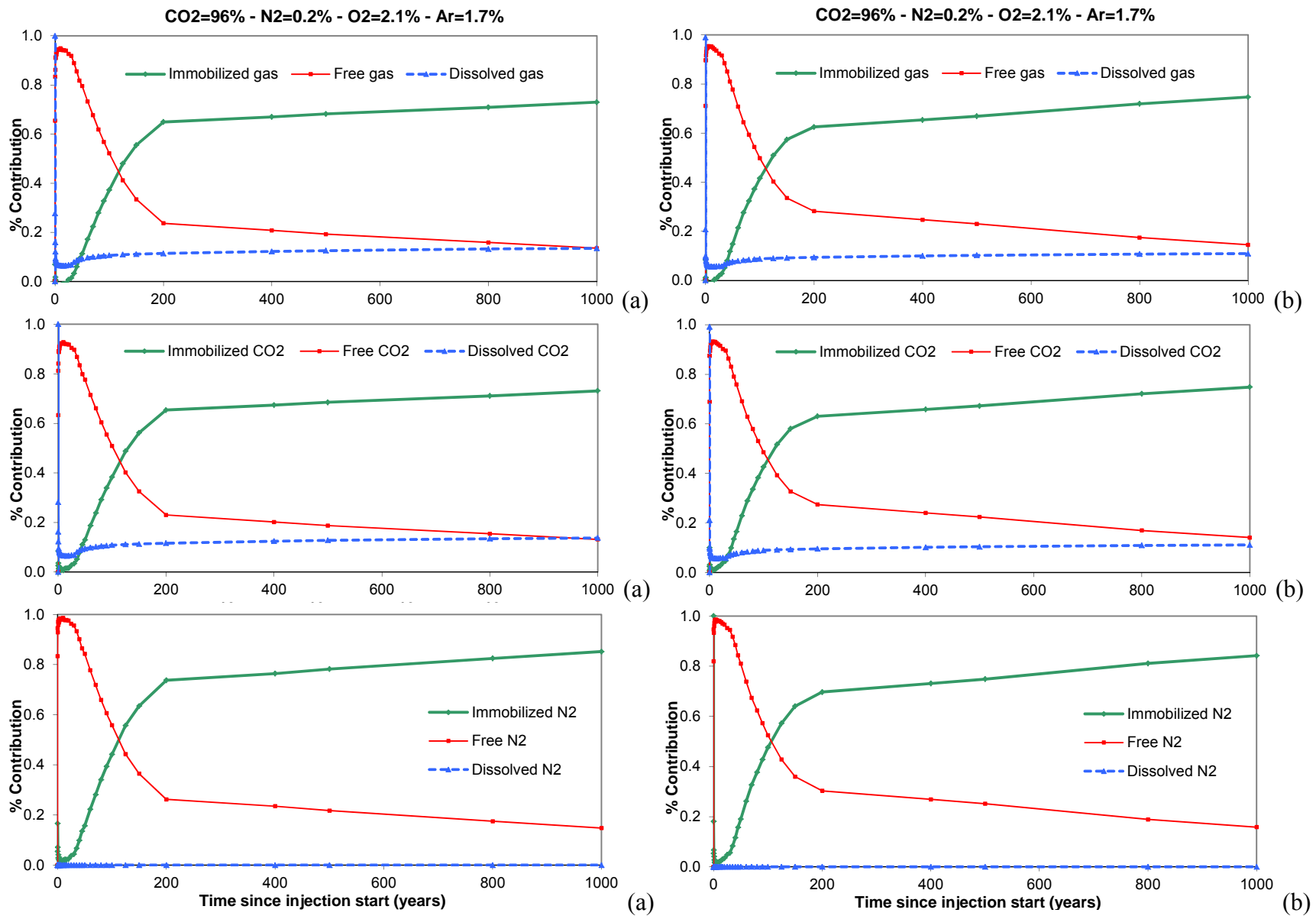


Figure 32. Phase distribution of components of Injection Stream A through time: shallow GC (a) and deep GC (b) cases

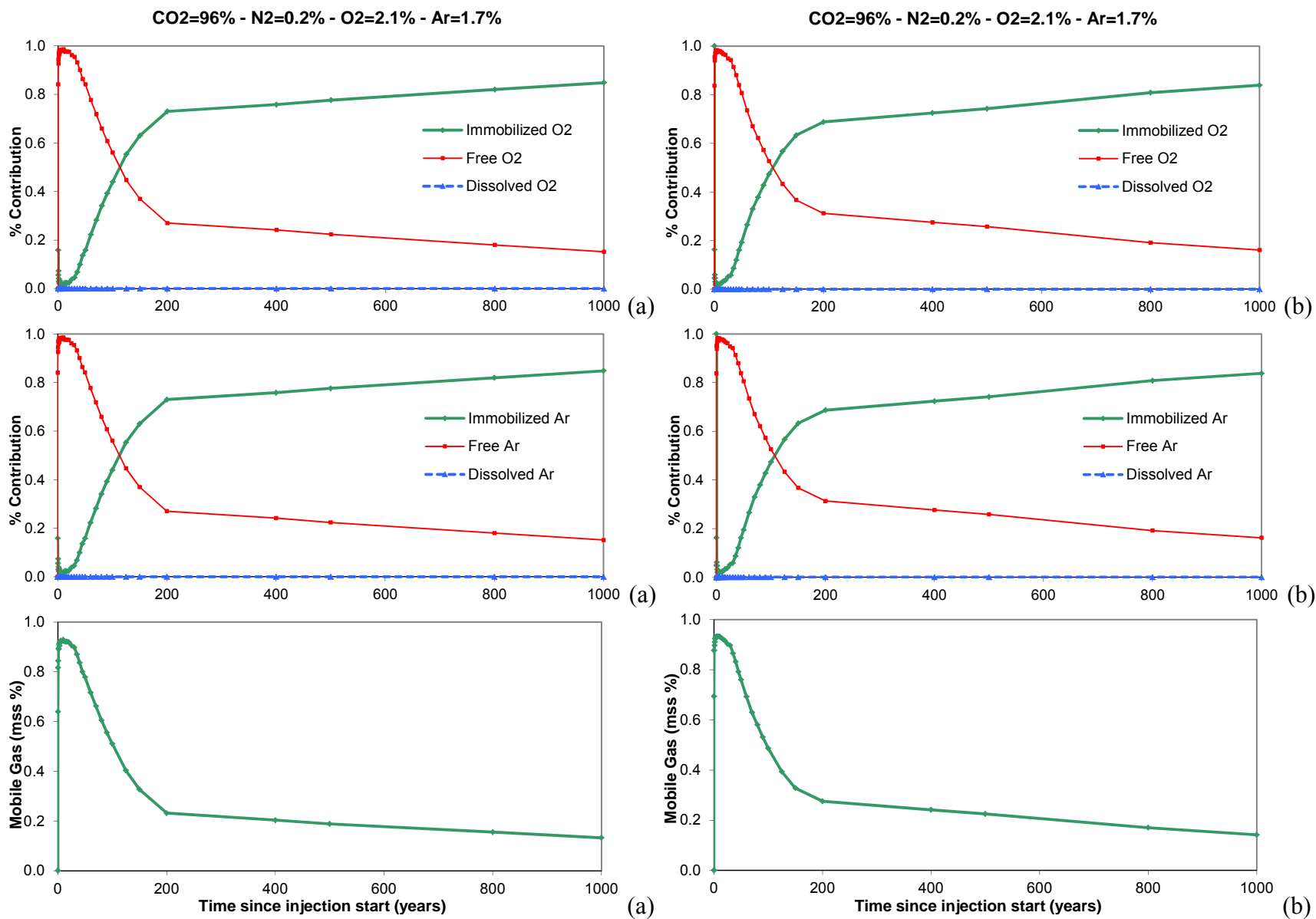


Figure 32. Phase distribution of components of Injection Stream A through time: shallow GC (a) and deep GC (b) cases (continued)

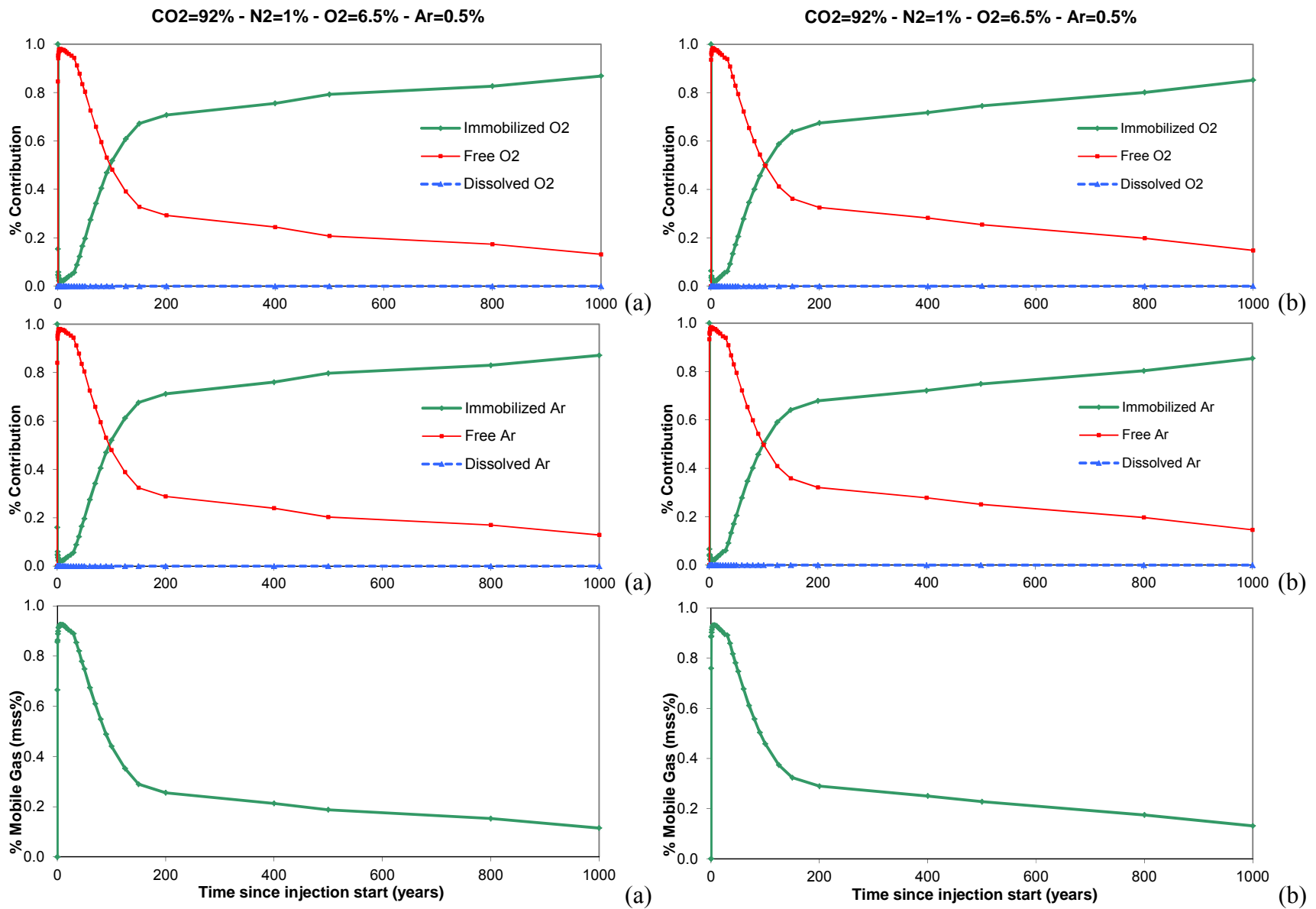
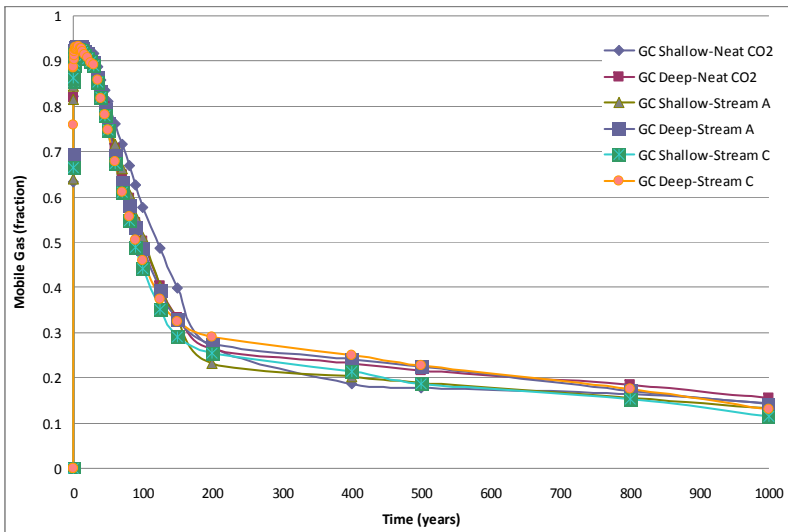
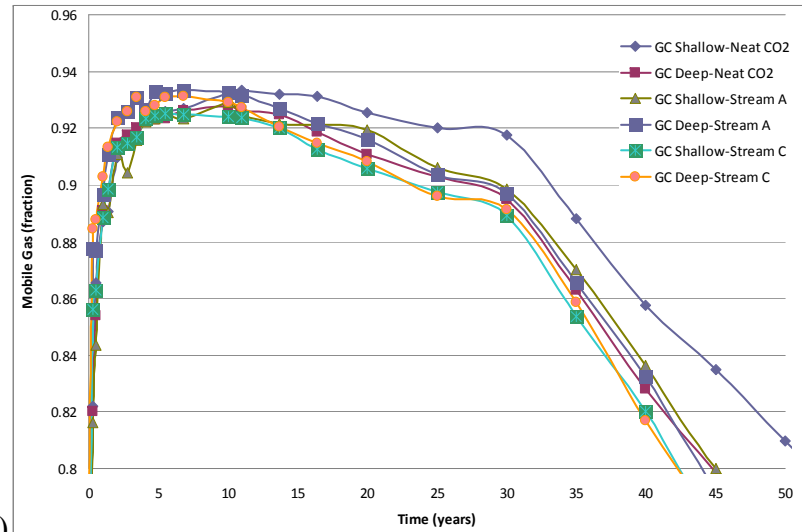


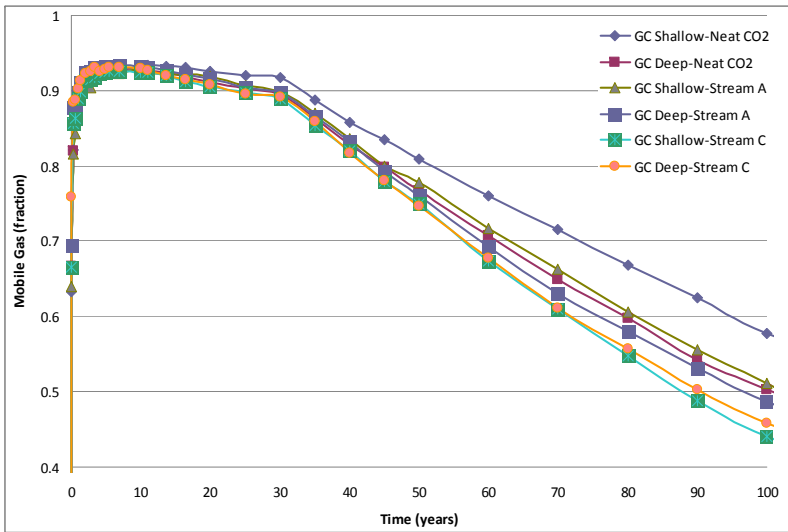
Figure 33. Phase distribution of components of Injection Stream C through time: shallow GC (a) and deep GC (b) cases (continued)



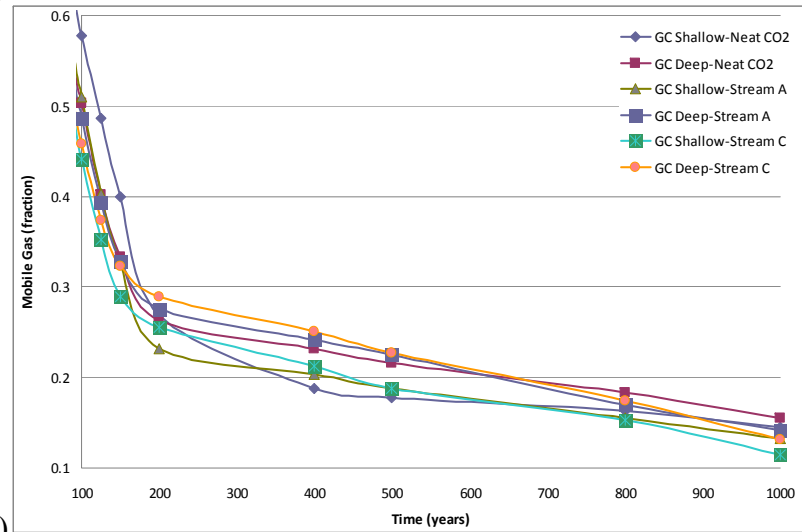
(a)



(b)



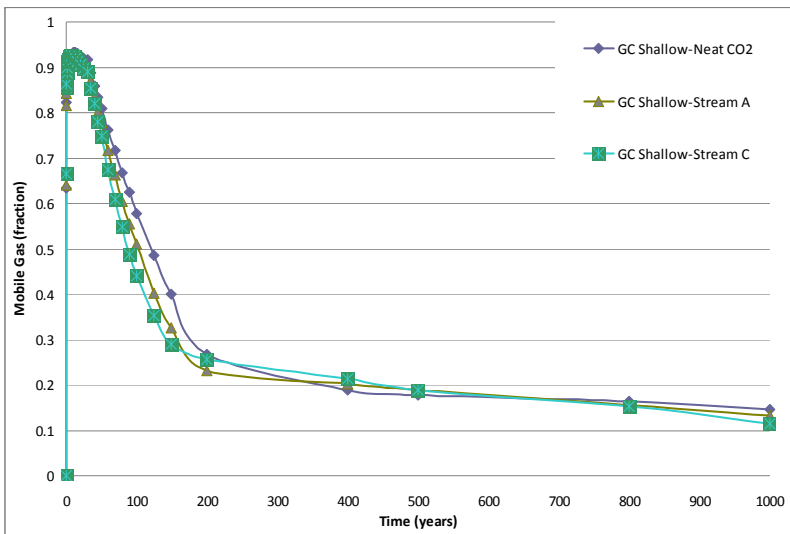
(c)



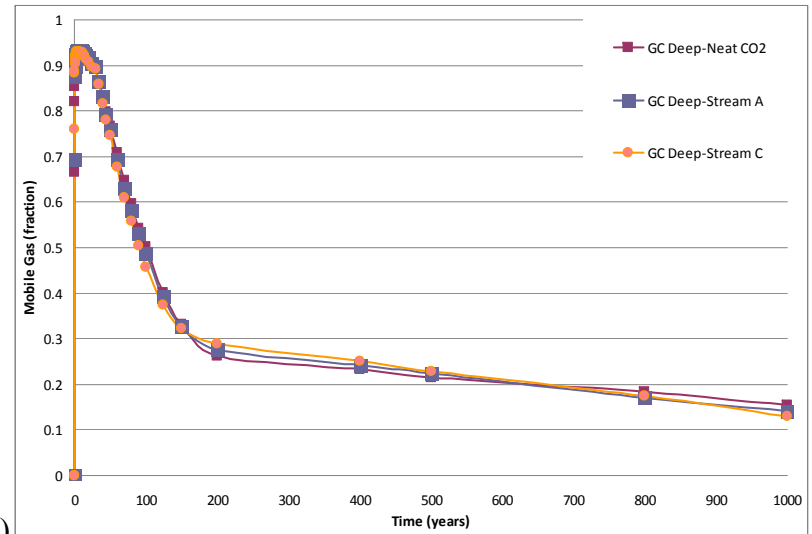
(d)

MobileFraction_(from Silvia)_JP.xls

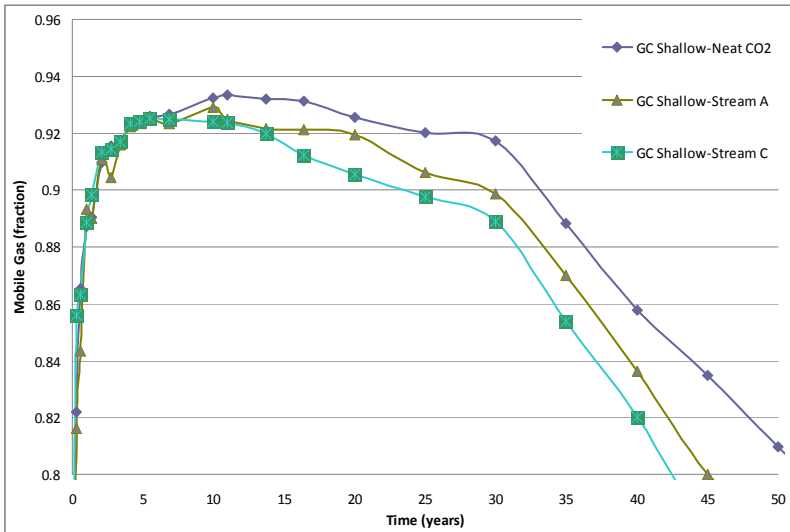
Figure 34. Mobile fraction as a function of time (a) 0-1000 years; (b) 0-50 years; (c) 0-100 years; and (d) 100-1000 years



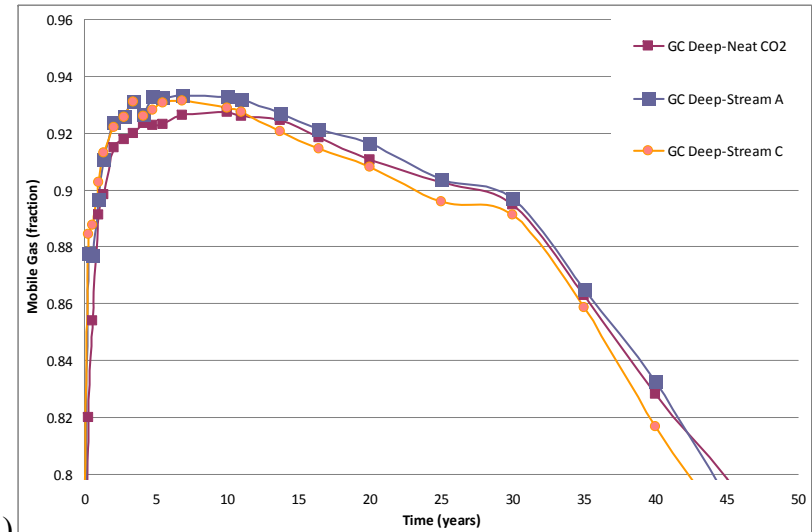
(a1)



(a2)

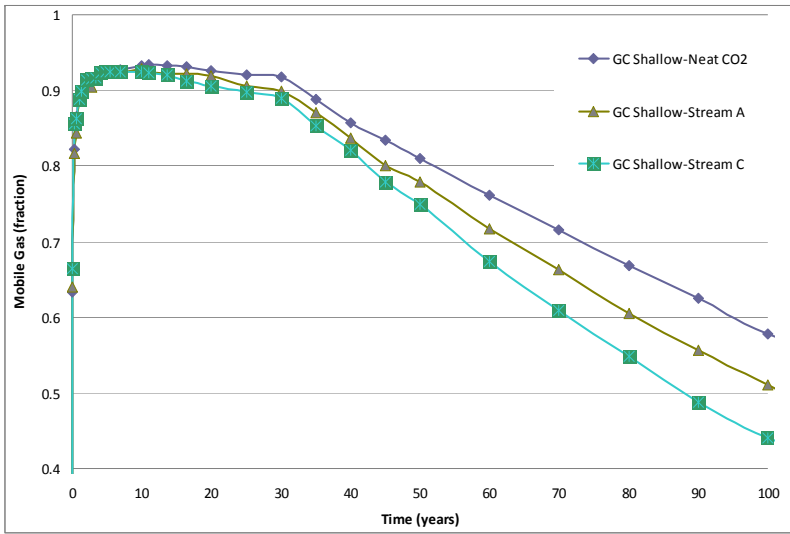


(b1)

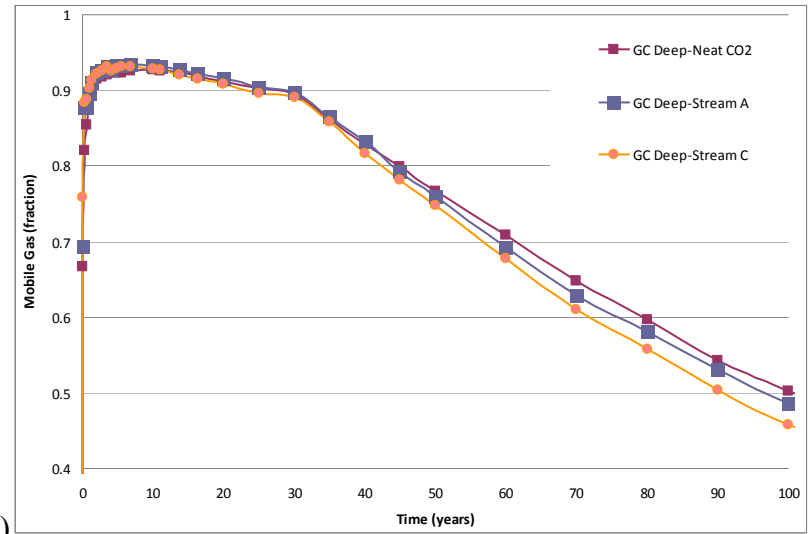


(b2)

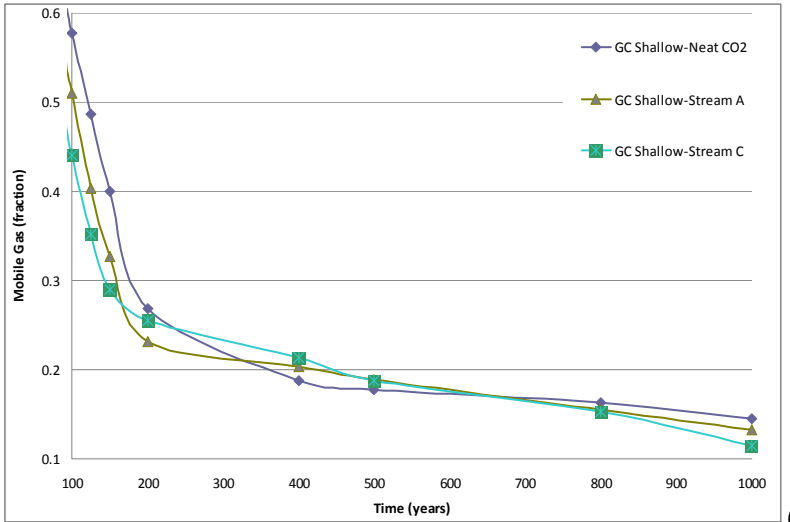
Figure 35. Mobile fraction as a function of time (a) 0-1000 years; (b) 0-50 years; (c) 0-100 years; and (d) 100-1000 years for the shallow (1) and deep (2) Gulf Coast case.



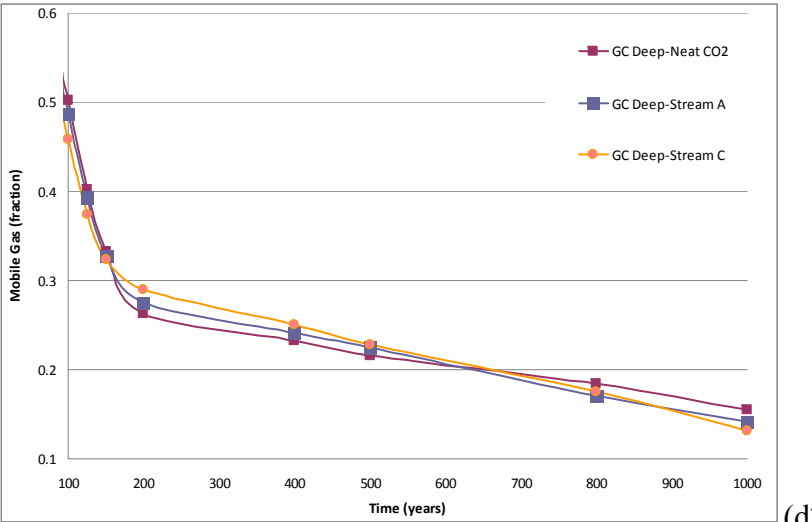
(c1)



(c2)



(d1)



(d2)

Figure 35. Mobile fraction as a function of time (a) 0-1000 years; (b) 0-50 years; (c) 0-100 years; and (d) 100-1000 years for the shallow (1) and deep (2) Gulf Coast case. (continued)

III-3. Tentative Specifications for Mixed CO₂ Stream

In the context of integrating results from this impurities study into the larger economic framework, in particular determining trade-offs between capture costs of increasing the purity of the CO₂ stream and plume size, we determined the impurity level of a given binary system to increase the plume extent by a given amount (15% or 25%) (Table 13). The table was constructed by plotting and interpolating between results presented in the previous sections (Figure 36). The relative coarseness of the curves may be artifacts of the gridding process and the way the plume extend is manually compiled. Results are clearly consistent with previous findings: the deep system is less sensitive to impurities and can afford a mole fraction 2.5 to 3.5 times higher than the shallow system for a similar plume extent. From a practical standpoint, in terms of combining impurities in order to model a simplified a system, using Ar properties seems the most conservative.

Table 13. Binary system impurity level at which the plume extend is increases by some amount.

	Concentration needed for a <u>15%</u> increase in lateral plume extent (mol%)		Concentration needed for a <u>25%</u> increase in lateral plume extent (mol%)	
	GC Shallow	GC Deep	GC Shallow	GC Deep
N ₂	2.02	5.24	3.36	8.73
Ar	2.46	8.97	4.10	14.95
O ₂	2.43	6.99	4.05	11.65
CH ₄	2.63	6.40	4.38	10.66

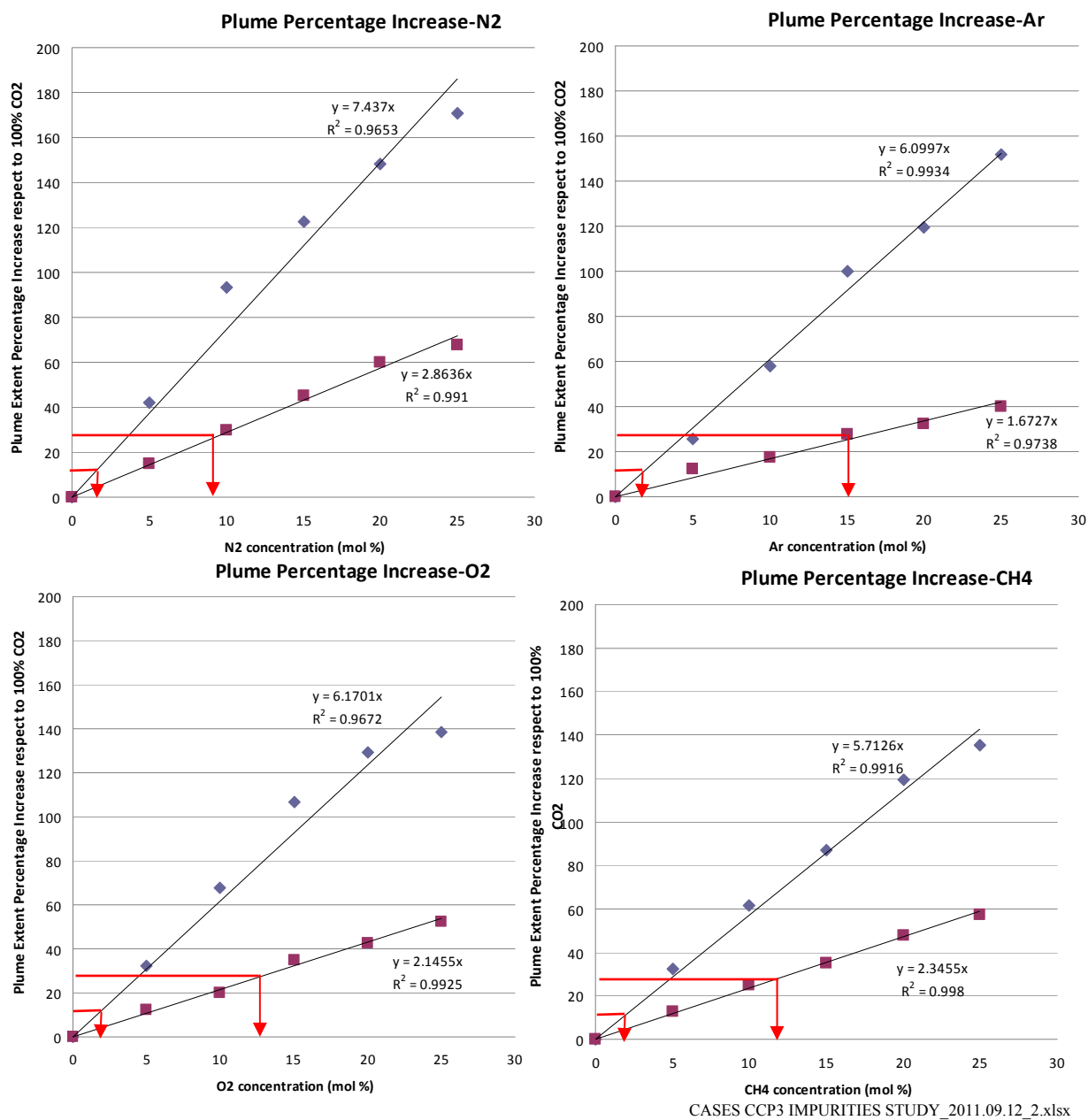


Figure 36. Relative increase in plume extent relative to neat CO₂ for various binary systems for GC shallow (a, squares) and GC deep (b, diamonds) sites

III-4. Impact of Heterogeneity

The previous generic cases use a simple homogeneous permeability field. In this section we test the assumption that lateral extent of multi-component mixtures relative to the neat CO₂ case is not a strong function of the permeability field. We use a system similar to the generic case but with baffles and a fully stochastic field of which we used 3 realizations as displayed in Figure 40 (variogram type: spherical; mean k= 255 mD; standard deviation k=700 mD; vertical correlation length=100 ft; nugget=0).

In the system with baffles (Figure 37), the longest tongue is retained but it is not necessarily the same in all cases. Maximum lateral extent in the case with baffles is always smaller than in the homogeneous case (Figure 38) because the CO₂ mixture is distributed across several stacked layers.

Each plot shows a comparison between homogenous and heterogeneous permeability distribution in shallow and deep reservoirs for three injection stream compositions (neat CO₂, stream A and stream C). Realization numbers corresponding to a companion work done on the deep Gulf Coast site (not discussed in this document). Variation in plume lateral extent after 100 years in heterogeneous cases exhibits the same trend as homogenous cases. Comparing plume extent for a given homogeneous /heterogeneous (stochastic) and shallow/deep combination shows that the previously observed rule that impurities increase plume length at 100 years still applies (Figure 40). However the increase may be relatively small as seen on Figure 40c for the heterogeneous shallow and deep cases. The plots also illustrate the lateral plume extent reversal above 5% impurities. Base case (neat CO₂) and stream A (4% impurities) display a longer plume extent at depth than stream C (8% impurities) that shows the reverse: plume extent smaller at depth if impurities >5%.

Results from realizations #8 and #13 (Figure 40b and c, respectively) show a different trend for the case with 92% CO₂ concentration (Stream C). For realization #8, the plume lateral extent after 100 years for injection stream C in the deep reservoir case is larger than the shallow reservoir case (the opposite was observed in the homogenous cases and realization #7 which happens due to the a larger gas-brine density difference for this stream composition at shallow depths). For realization #13 no variation was observed with changes in stream composition in the deep heterogeneous cases. Due to the different permeability distributions, and especially for those where low permeability areas are around the injector well, we might need longer simulation times to observe the same trend as homogenous cases and realization # 7. Plume in neither realization # 8 nor # 13 reaches the top seal and both exhibit very slow movement in the lateral direction.

Overall, from the relatively small number of simulations undertaken for this study, heterogeneity seems to have a dampening effect on the impact of impurities (Table 14). The most likely explanation resides in the multiple number of tongues that can be created in an heterogeneous systems as clearly seen in the case with only baffles. However, the case in which the plume is channeling through a high-permeability streak and reinforce the impact of heterogeneity is also a possibility (see realization #7 in Table 14). It suggests that elements of operational strategy such as location of the perforated interval(s) and position relative to known heterogeneity can help in negating the impact of impurities on flow dynamics.

Table 14. Comparison of Stream A, stream C, and neat CO₂ (base case) plume extent in various conditions of heterogeneity (GC shallow case)

	Uniform	w/ Baffles	Real#7	Real#8	Real#9	Real#10	Real#13
Neat CO ₂	9,300	8,400	10,500	6,900	5,100	5,100	7,200
Stream A	11,400	9,300	15,300	7,200	5,400	5,100	7,800
Stream C	14,400	10,800	19,800	7,500	5,400	6,900	7,800
A / neat	1.23	1.11	1.46	1.04	1.06	1.00	1.08
C / neat	1.55	1.29	1.89	1.09	1.06	1.35	1.08

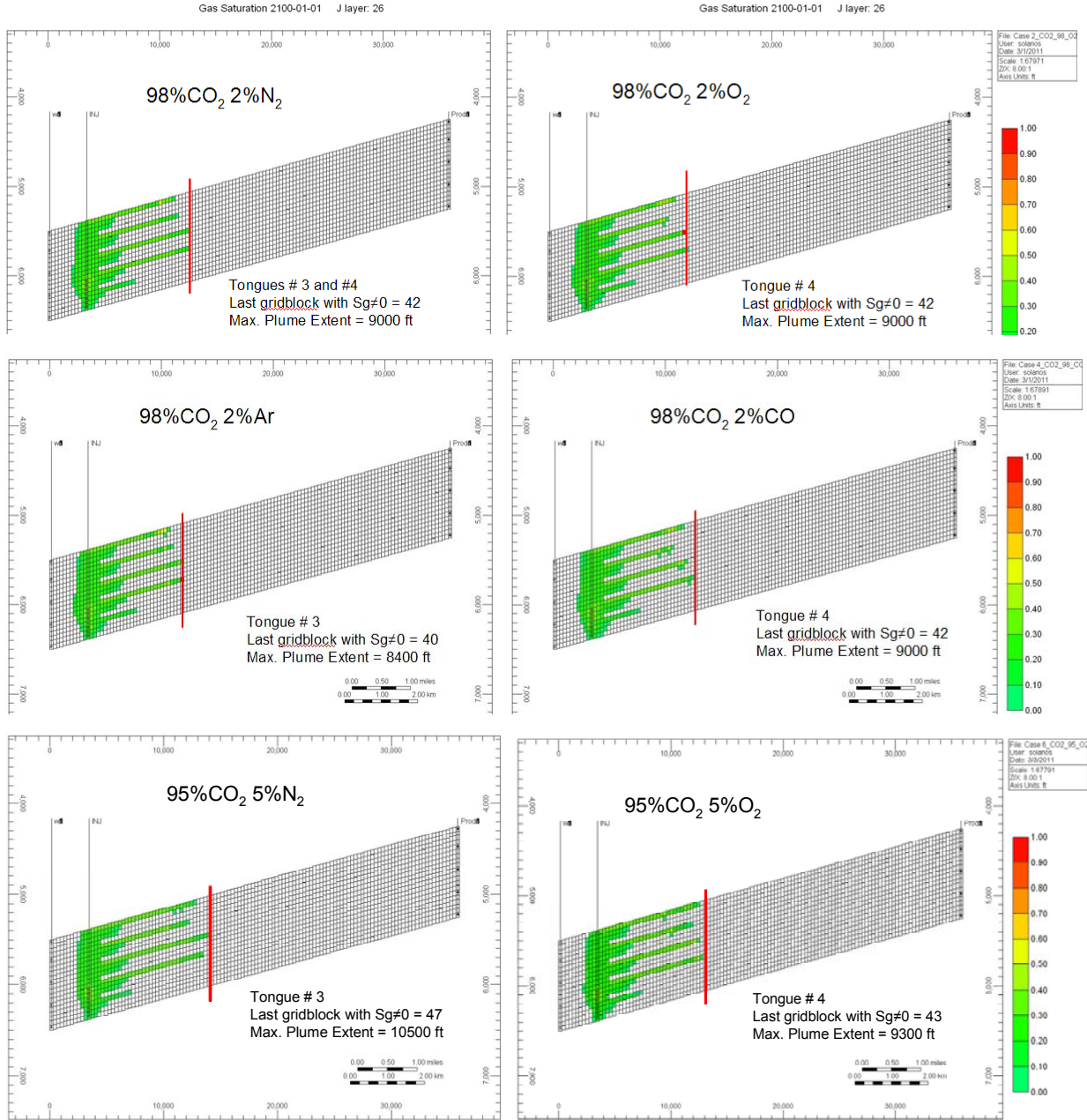


Figure 37. Simple homogeneous case with baffles displaying vertical cross sections along main axis of model for various binary mixtures

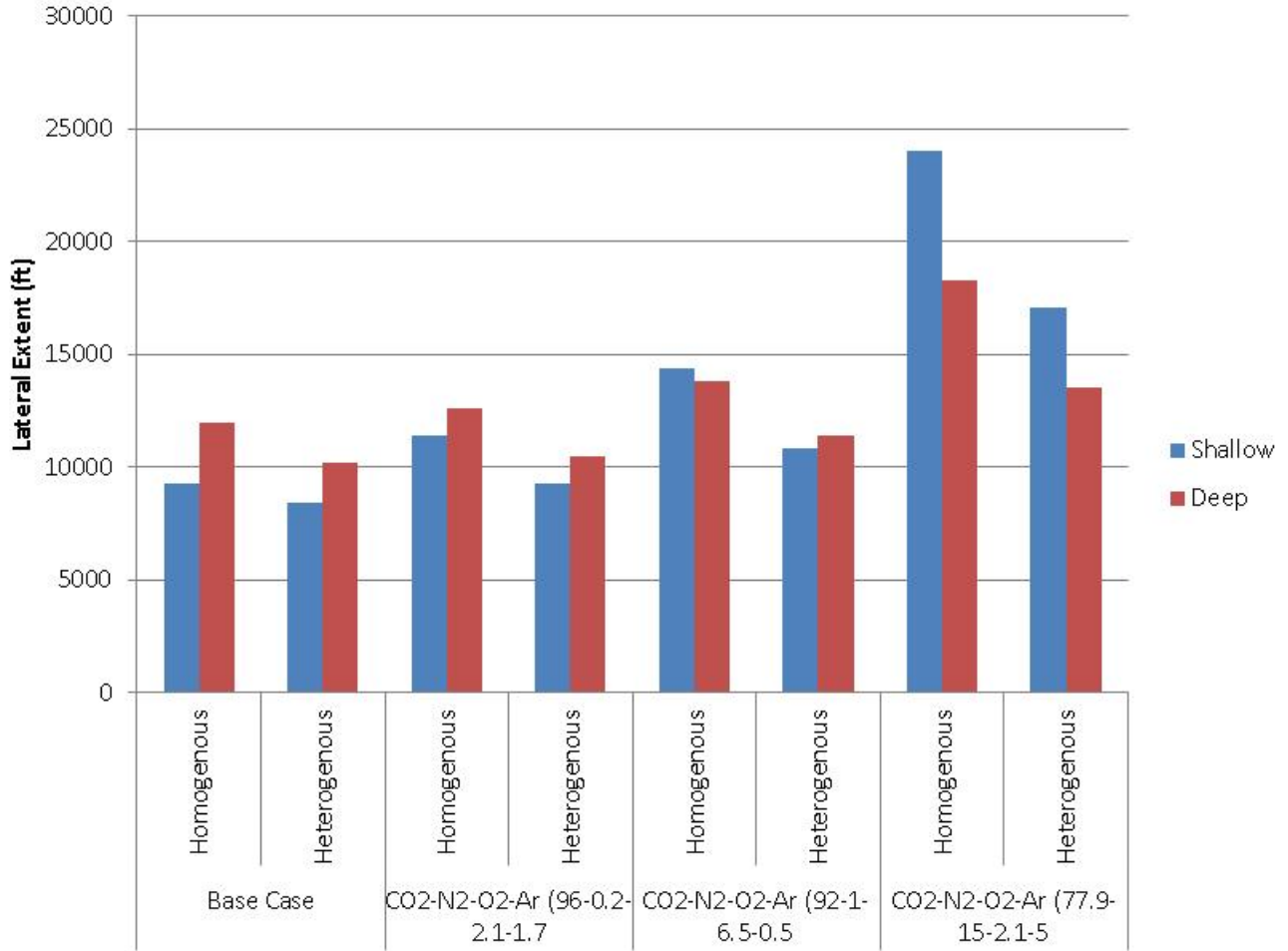


Figure 38. Comparison of plume extent of homogeneous permeability cases with homogeneous with baffles (“heterogeneous”).

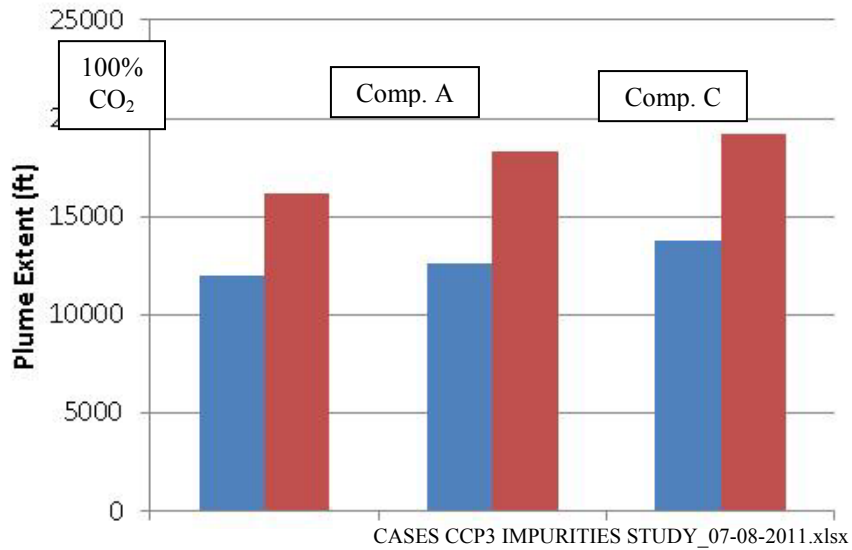
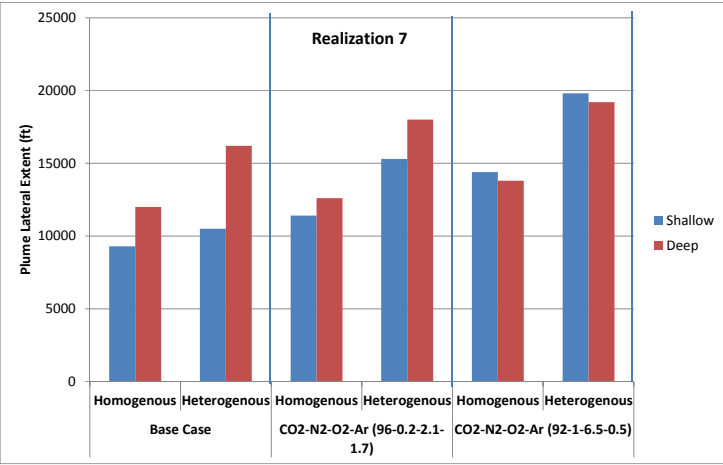
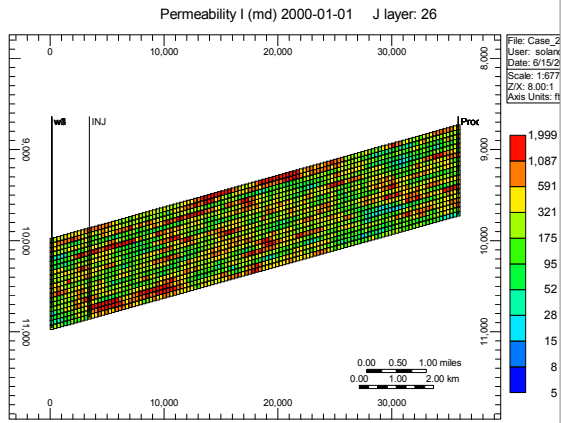
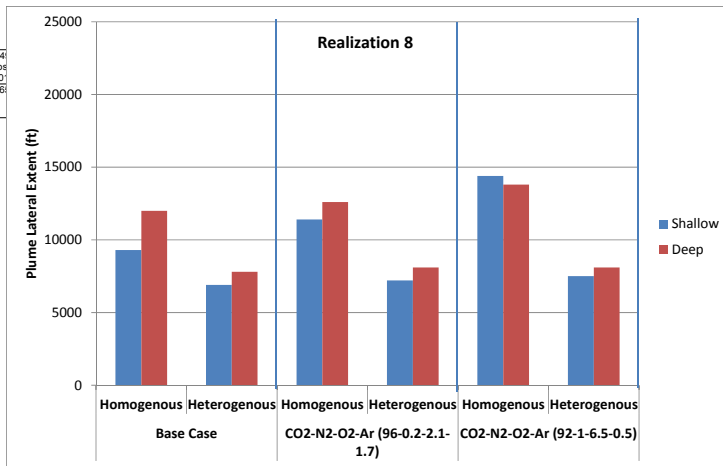
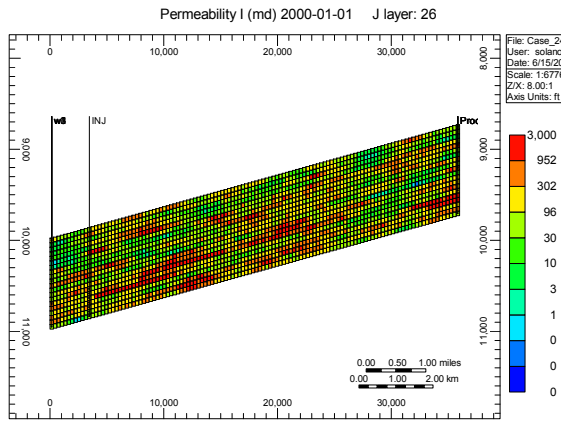


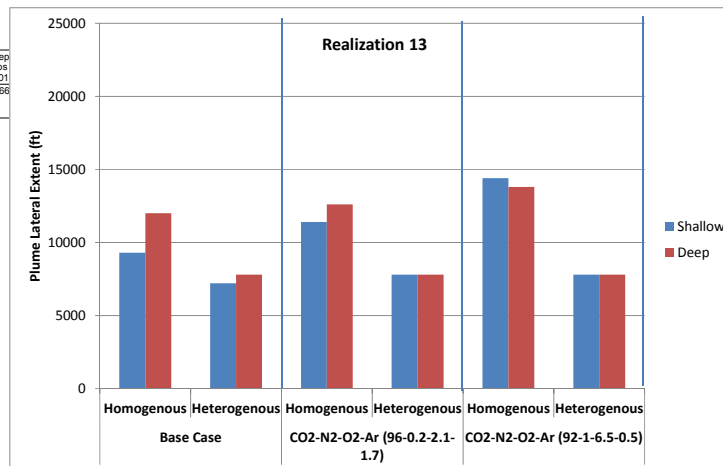
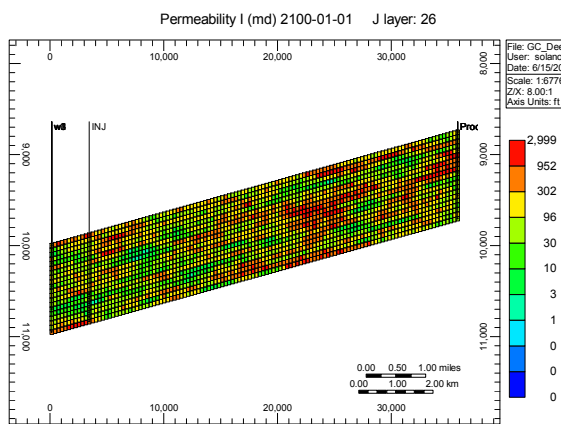
Figure 39. Comparison of plume extent (deep GC case) for 2 realizations



(a)



(b)



(c)

Results_JUNE_CCP3_Heterogeneous+Cranfield.doc

Figure 40. Permeability field (cross-section) and simulation results (plume extent after 100 years) from Realization #7 (a), #8 (b), and #13 (c) assuming injection stream of neat CO₂, Stream A, and Stream C. LHS plots compared plume extent for homogenous and heterogenous fields.

III-5. Results from Actual Field Cases

III-5-1 Gulf Coast Cases

Two well locations have been considered (Figure 41, Figure 42, Figure 43, Figure 44) for the shallow Gulf Coast case. Results consider only time to reach a specific point but before gas accumulation starts in the reservoir to be consistent with the rest of this document. Since the gas tends to accumulate in the upper part of the reservoir after relatively short time, the metric used for comparison was the time for the gas plume to reach a specific cell before accumulation starts.

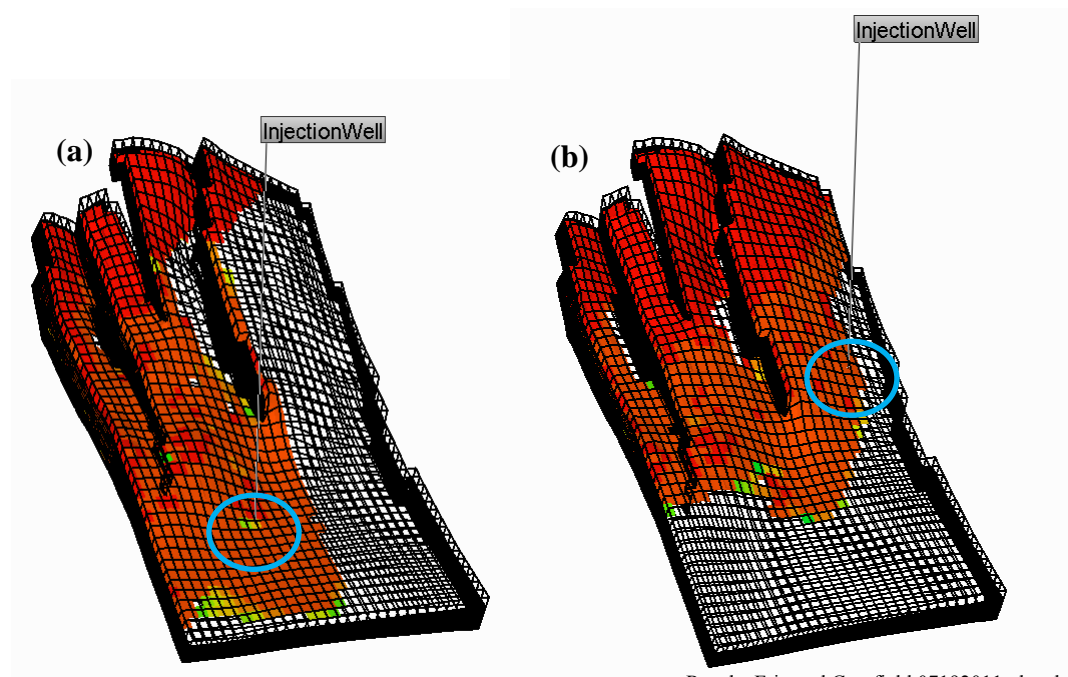
Modeling results from the Gulf Coast deep case are similar to those corresponding to the generic case. The main differences between the two models are variable permeability distribution, variable dip, presence of a fault and a smaller total volume (7×10^9 ft³ instead of 2×10^{11} ft³). Simulation runs were performed for two realizations and three stream compositions (neat CO₂, Stream A and Stream C) with open and closed boundaries. Figure 45 shows plume distribution for the neat CO₂ case with open downdip boundary (30 years of CO₂ injection at a rate of 4.73×10^6 scf/day-Plume extent measured in the updip direction). Figure 46 and Figure 47 present a comparison between realizations at 100 yr and 1000 yr respectively. It can be observed that the plume extent for different stream compositions follows the same trend as in the generic cases, stream composition C has larger extent than stream A and neat CO₂.

Results from an analogous study with a closed-boundary reservoir model are shown in Figure 48, Figure 49, and Figure 50. The difference observed between open and closed boundary cases occurs due to the pressure behavior in the open boundary case where lower pressures are observed downdip for some years until longer simulation time allows equilibration of the system. This in turn causes downdip movement of the injected gas while the opposite is observed in the closed boundary case where movement takes place mostly in the updip direction. Hence for the open boundary case the plume extent is shorter than for the closed boundary case despite having a smaller gas-brine density difference (higher reservoir pressure).

Consistent with previous results (Table 14 and Table 15), the general conclusion is that models with actual field geometry and the heterogeneities they brought imply a limited impact of impurities relative to neat CO₂ behavior. Heterogeneities seem to dampen the differences seen in uniform-permeability models.

Table 15. Comparison of Stream A, stream C, and neat CO₂ (base case) plume extent in various conditions of heterogeneity (GC shallow and deep case)

GC shallow case:									
	Uniform	Baffles	Real#7	Real#8	Real#9	Real#10	Real#13		
Neat CO ₂	9,300	8,400	10,500	6,900	5,100	5,100	7,200		
Stream A	11,400	9,300	15,300	7,200	5,400	5,100	7,800		
Stream C	14,400	10,800	19,800	7,500	5,400	6,900	7,800		
A / neat	1.23	1.11	1.46	1.04	1.06	1.00	1.08		
C / neat	1.55	1.29	1.89	1.09	1.06	1.35	1.08		
GC deep case:									
	Uniform	Baffles	Real#7	Real#8	Real#9	Real#10	Real#13	Cran-R1	Cran-R2
Neat CO ₂	12,000	10,200	16,200	7,800	5,400	6,000	7,800	12,600	15,600
Stream A	12,600	10,500	18,000	8,100	5,400	6,600	7,800	12,600	15,900
Stream C	13,800	11,400	19,200	8,100	5,700	7,200	7,800	12,900	15,900
A / neat	1.05	1.03	1.11	1.04	1.00	1.10	1.00	1.00	1.02
C / neat	1.15	1.12	1.19	1.04	1.06	1.20	1.00	1.02	1.02



Results Frio and Cranfield 07192011.xlsx.docx

Figure 41. Shallow Gulf Coast case, injector well location (a) Case 1: Injector located in lower part of the reservoir (b) Case 2: Injector well located in the upper part of the reservoir (well location of original model)

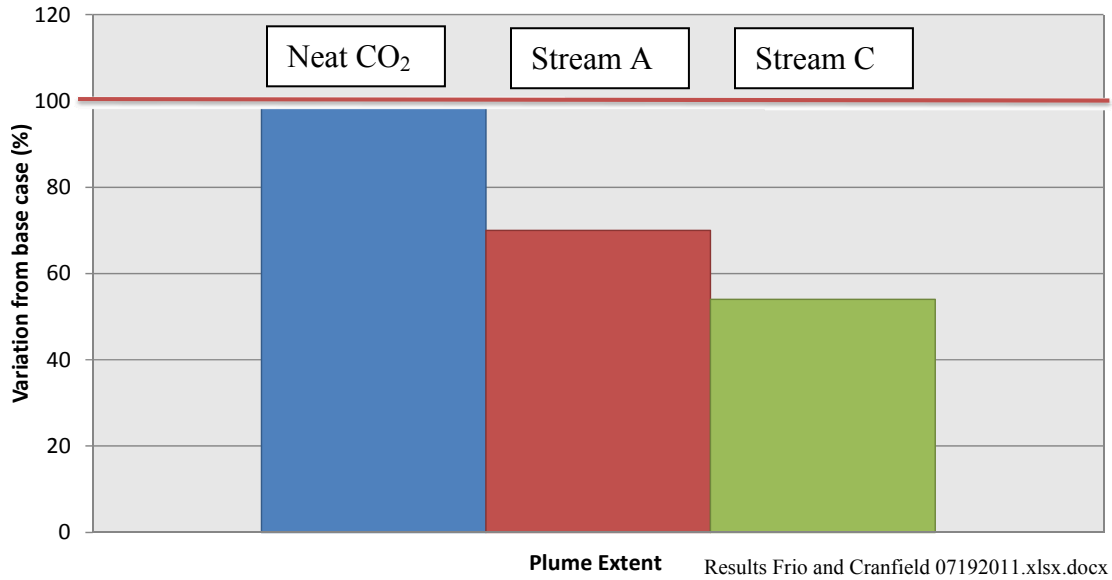


Figure 42. Results (time to reach the top) for injector well located downdip

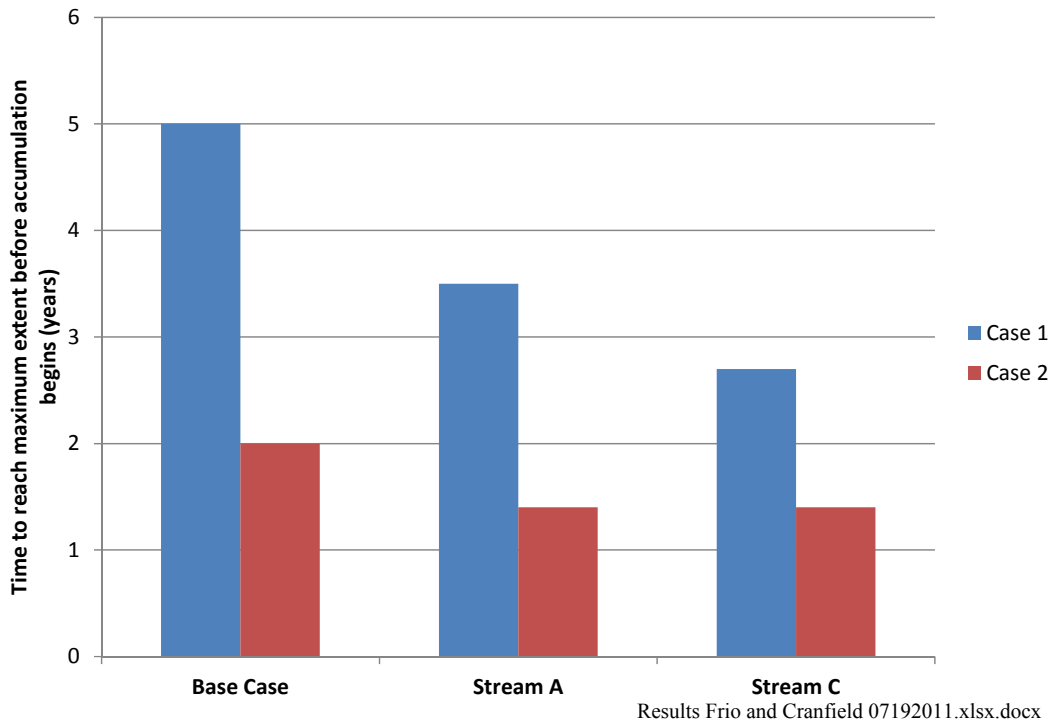


Figure 43. Results comparison for different well locations (Case 1: Injector down dip, Case 2: Injector up dip)

After 5 years (end of injection period)

After 10 years

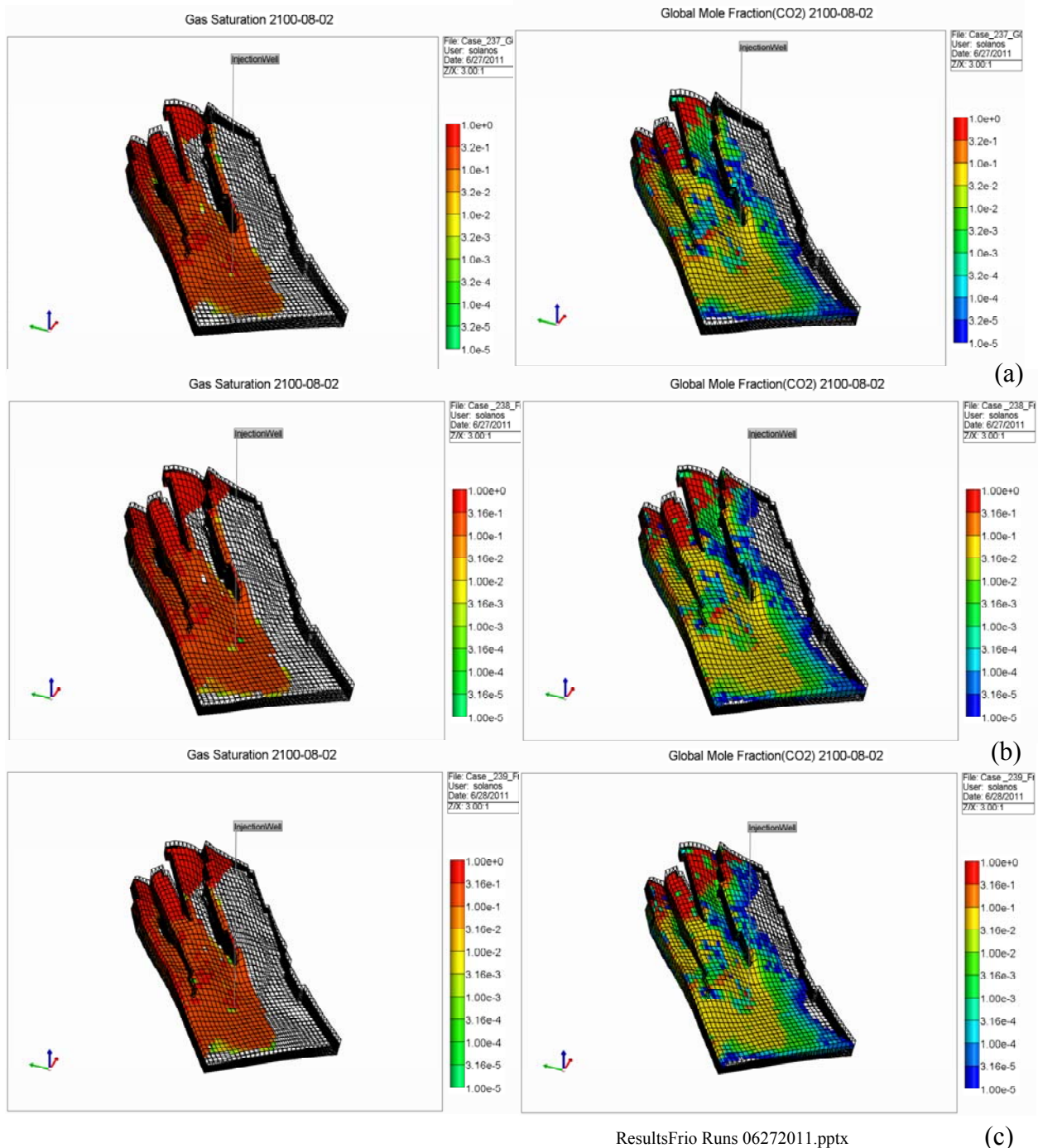


Figure 44. 3D view of shallow Gulf Coast case (injection period 5 years, injection rate 4.73×10^6 scf/day, gas saturation and global mole for: 100% CO₂ (a); Stream A (b); Stream C (c).

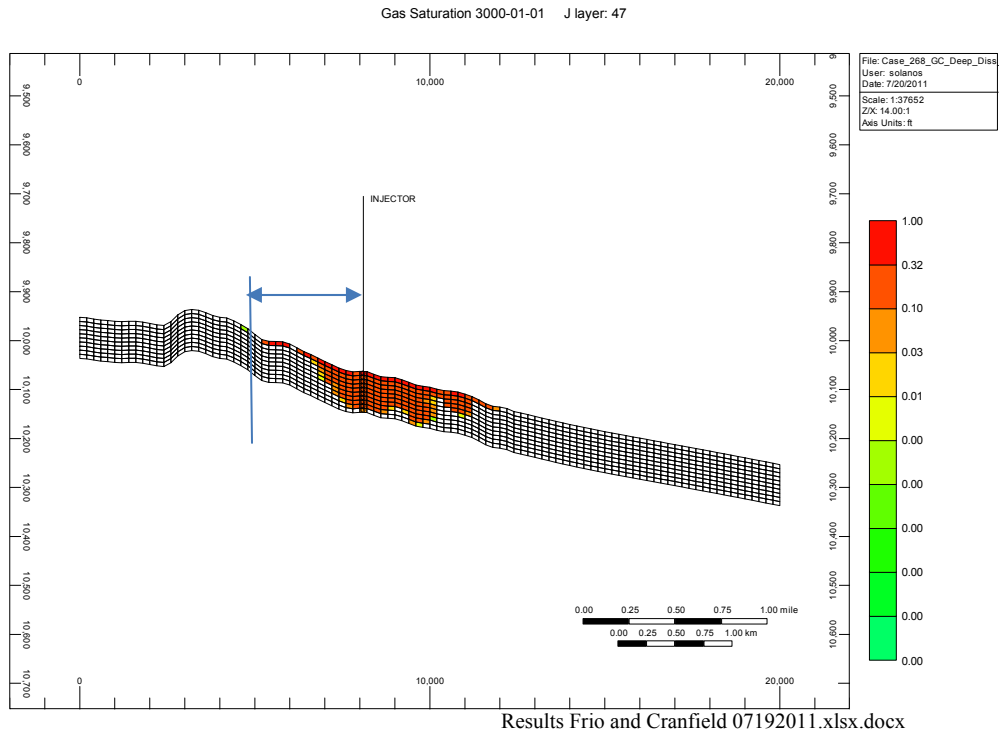


Figure 45. Gas Saturation cross-sectional view GC Deep -Stream composition 100% CO₂ (Realization # 2) after 1000 years

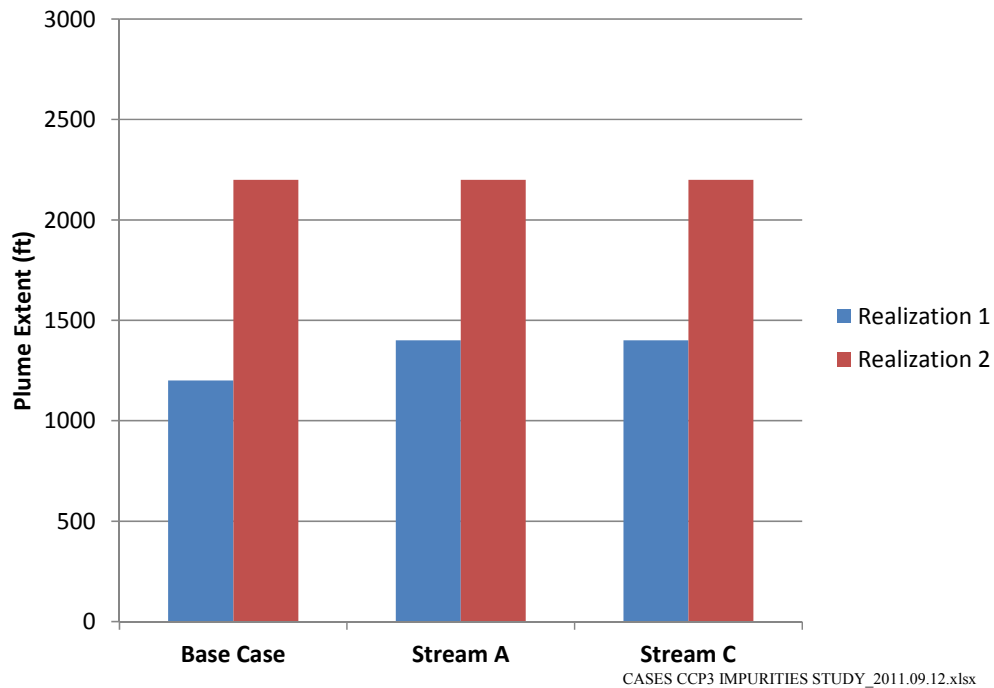


Figure 46. Plume extent for 2 realizations of the deep Gulf Coast case for 3 injection streams: neat CO₂, Stream A, and Stream B after 100 years of injection, open downdip boundary.

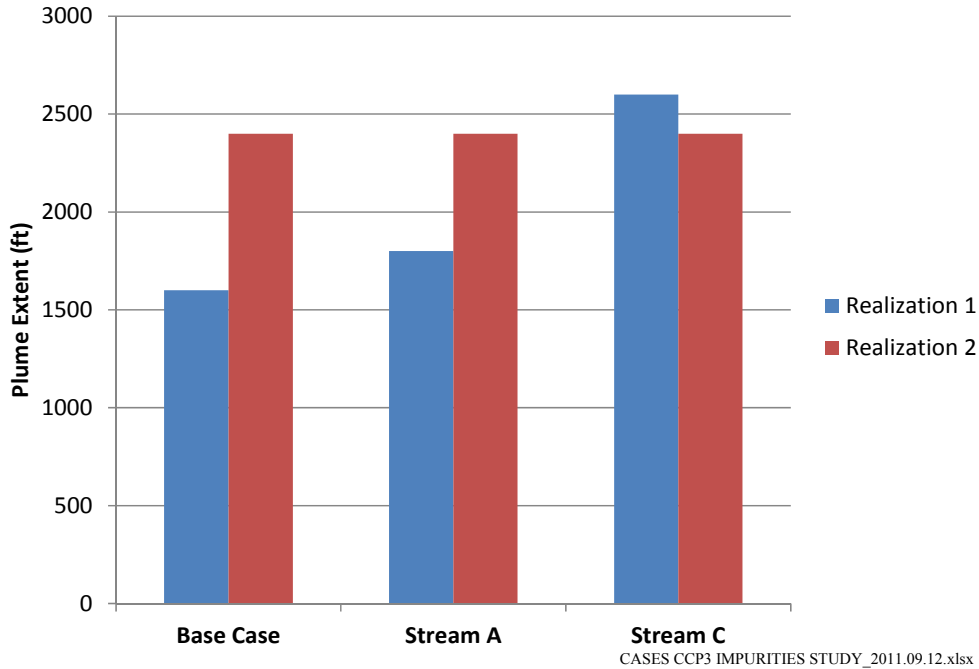


Figure 47. Plume extent for 2 realizations of the deep Gulf Coast case for 3 injection streams: neat CO₂, Stream A, and Stream B after 1000 years of injection, open downdip boundary.

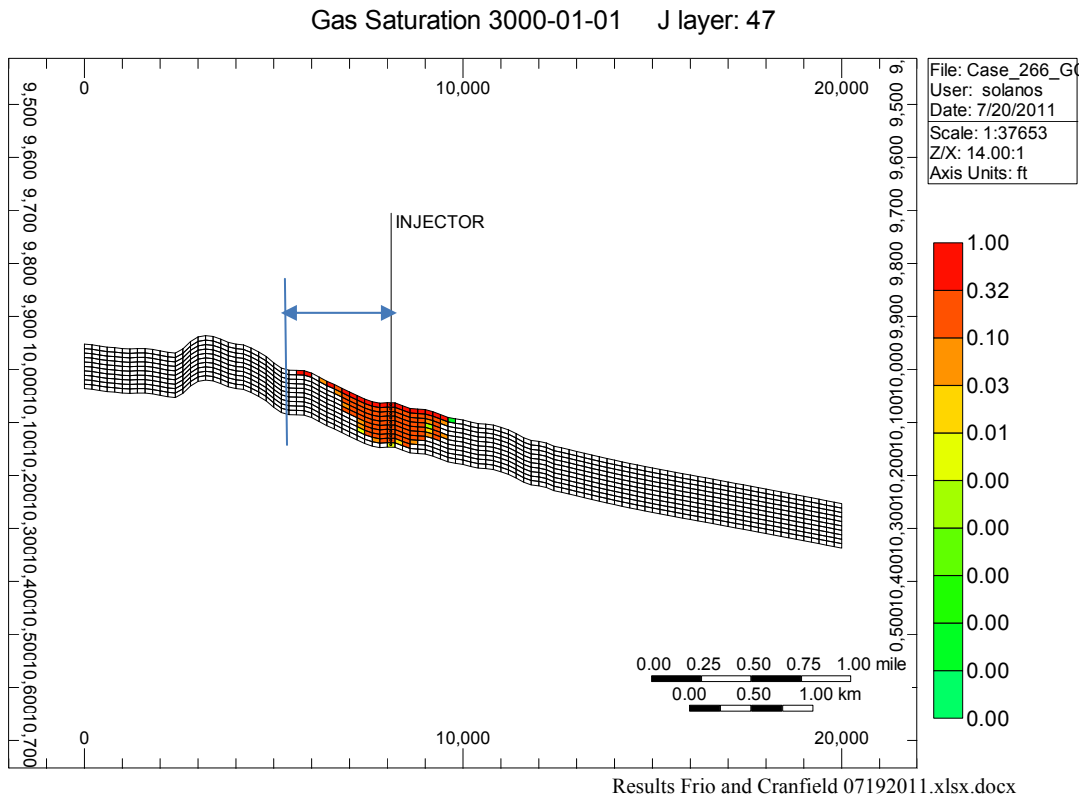


Figure 48. Gas Saturation after 1000 years (closed boundaries – GC deep)

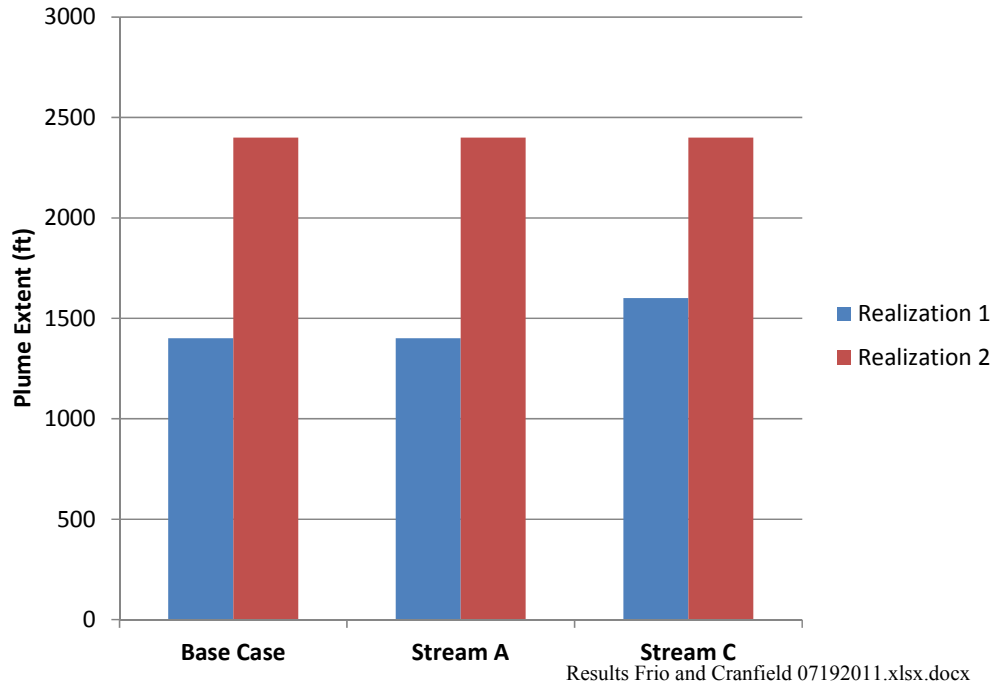


Figure 49. Plume extent for 2 realizations of the deep Gulf Coast case for 3 injection streams: neat CO₂, Stream A, and Stream B after 100 years of injection, closed boundaries

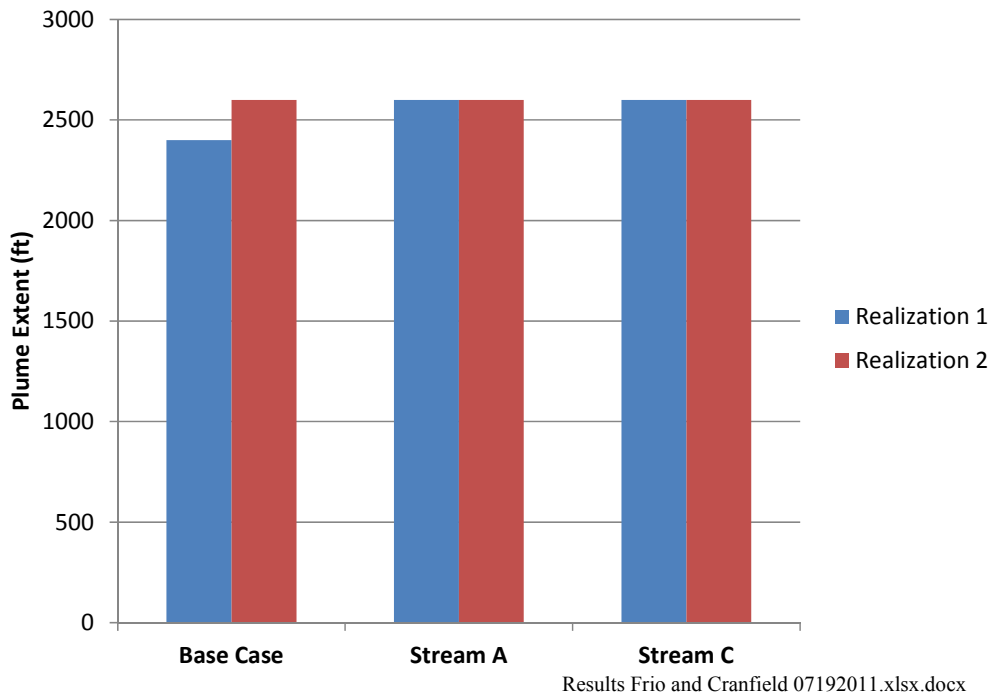


Figure 50. Plume extent for 2 realizations of the deep Gulf Coast case for 3 injection streams: neat CO₂, Stream A, and Stream B after 1000 years of injection, closed boundaries

III-5-2 Carbonate Aquifer Case

The same three different stream compositions are considered in this section: neat CO₂, stream A (CO₂-96%; N₂-0.2%; O₂-2.1%; Ar-1.7%) and stream C (CO₂-92%, N₂-1%, O₂-6.5%, Ar-0.5%). Gas saturation cross-sectional views for these three cases after 1000 yr are shown in Figure 51. As observed in previous results, the plume migrates a larger distance in the case of injection stream C whereas the neat CO₂ and stream A cases show similar results. Plume extent in the stream C case exhibits a 6.25% increase after 1000 yr. respect to the neat CO₂ and stream A cases (Figure 52b). Time to hit the top for the neat CO₂, stream A and stream C cases has the same value of 1.5 yr (Figure 52c).

In addition to the results for stream compositions A and C, Figure 53, Figure 54, and Figure 55 show the effect of increasing mole fraction for a single component on plume extent and time to hit the top. Impurity composition varies from 5% to 25% mole fraction. As observed in previous studies, the smaller impurity concentration (5%) displays a small change in plume extent relative to the neat CO₂ base case. At low impurity concentration, time to hit the top remains the same for all instances. As the impurity concentration increases, the divergence of the neat CO₂ case in both metrics becomes more significant especially for the CO₂-N₂ and CO₂-O₂ cases. This behavior is entirely consistent with the results observed in the generic models and the Frio and Cranfield models.

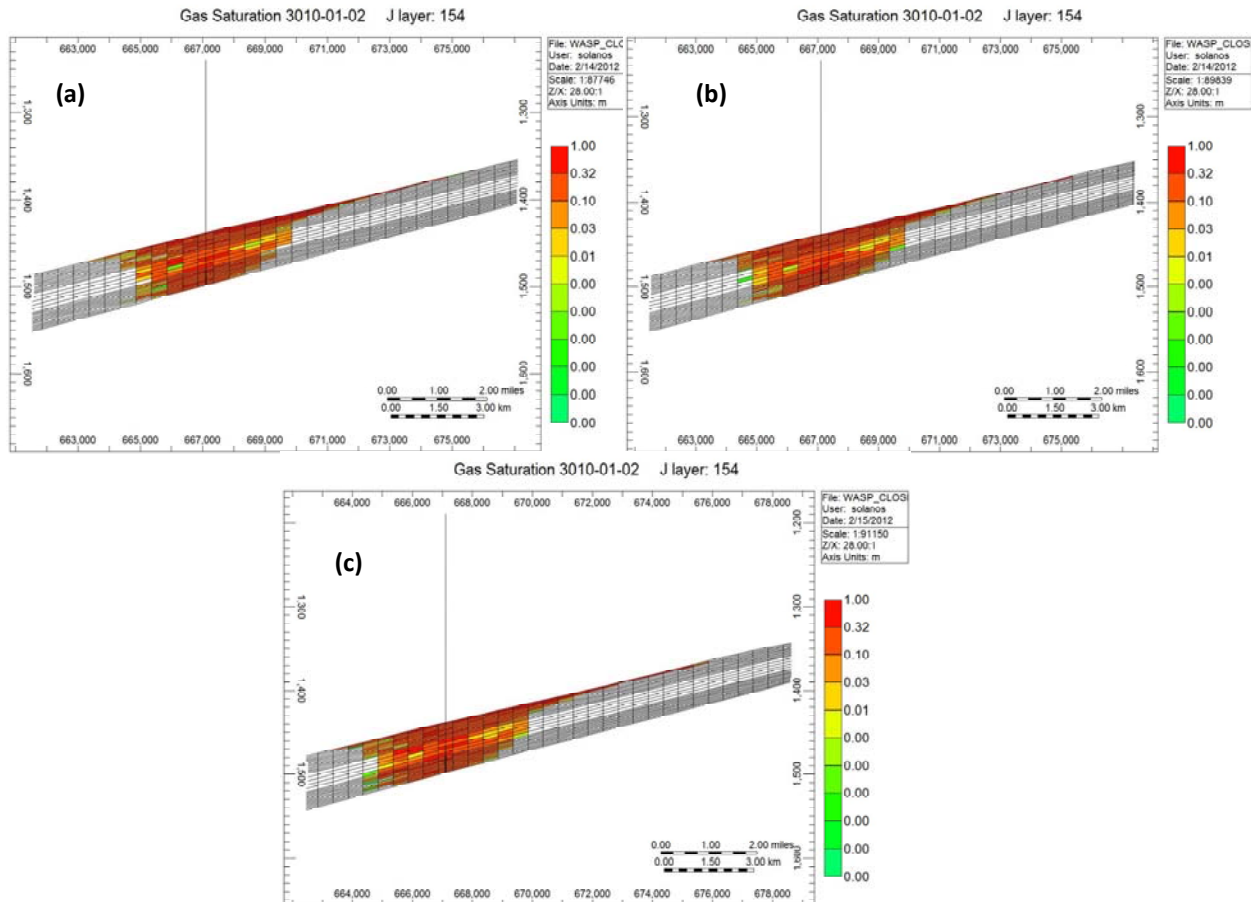


Figure 51. Gas saturation cross-section for: (a) neat CO₂; (b) stream composition A; and (c) stream composition C.

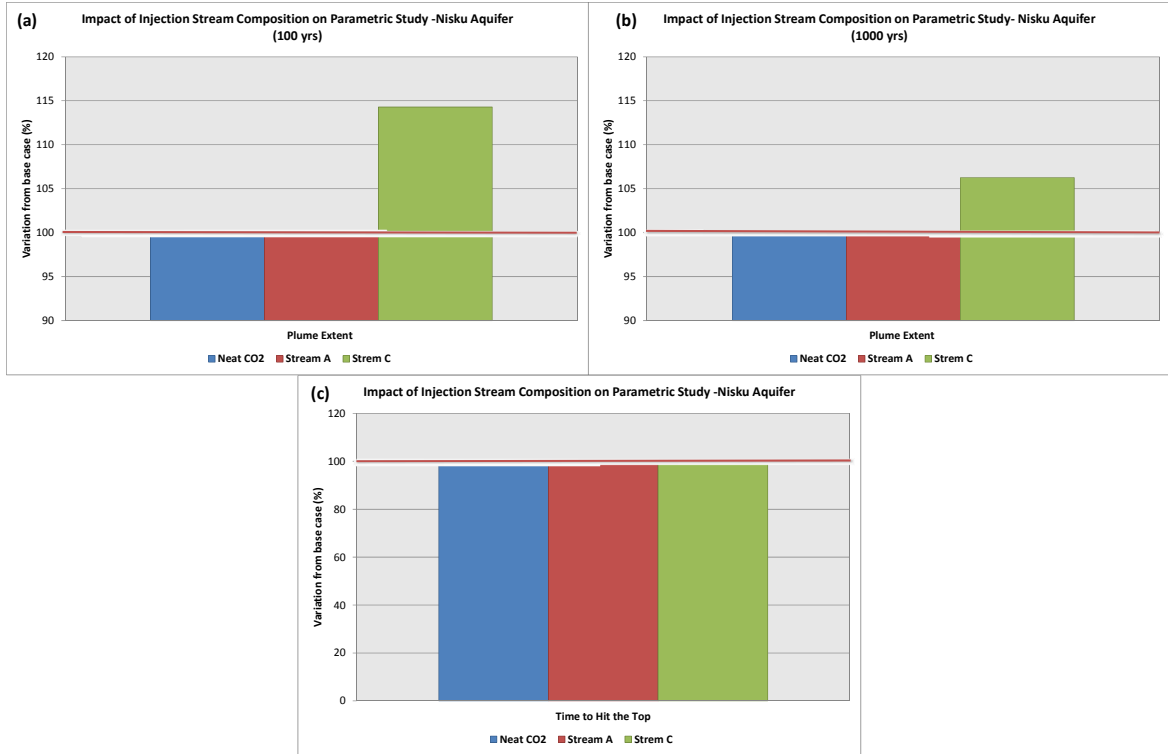


Figure 52. Impact on injection stream composition on parametric study for Nisku aquifer: (a) plume extent at 100 yr; (b) plume extent at 1000 yr; and (c) time to hit the top

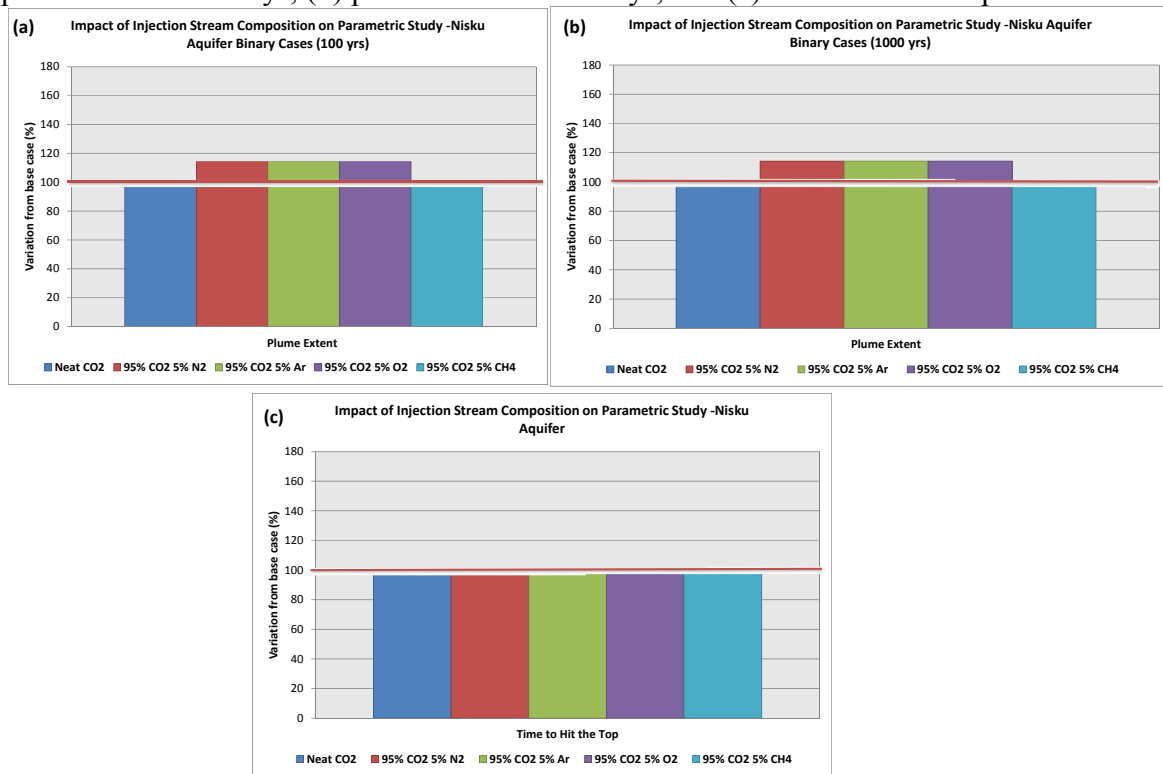


Figure 53. Impact on injection stream composition (95% CO₂) on parametric study for Carbonate Aquifer: (a) plume extent at 100 yr; (b) plume extent at 1000 yr; and (c) time to hit the top

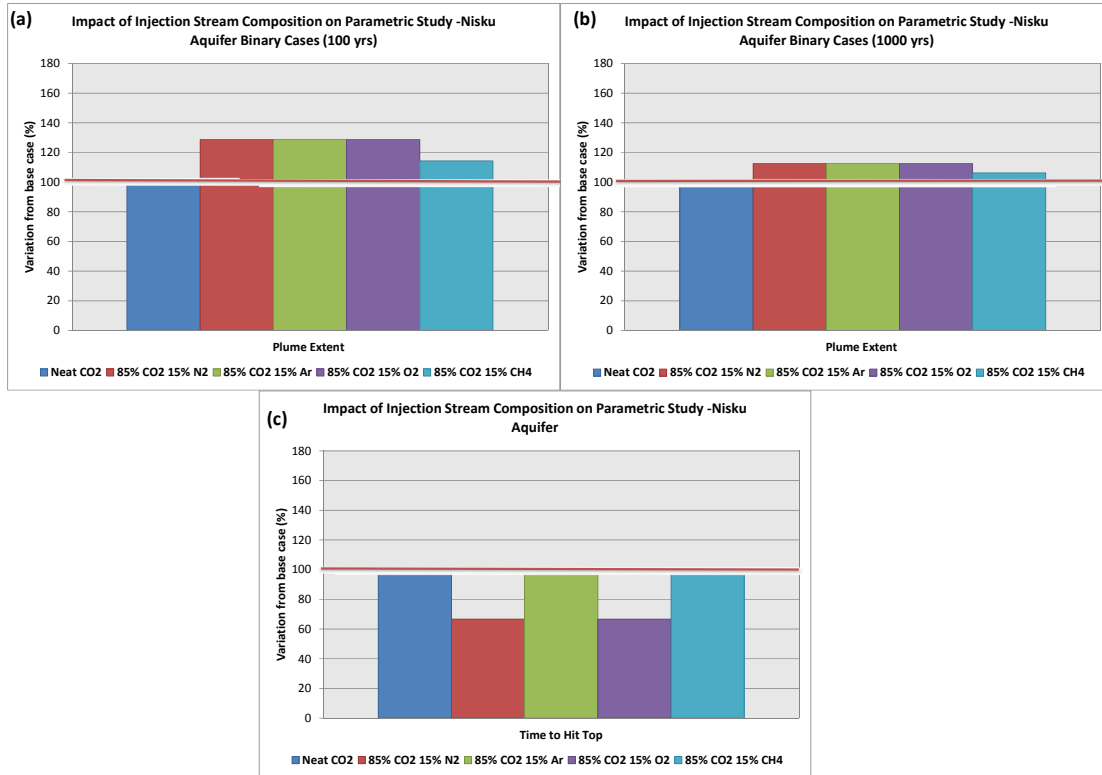


Figure 54. Impact on injection stream composition (85% CO₂) on parametric study for Carbonate Aquifer: (a) plume extent at 100 yr; (b) plume extent at 1000 yr; and (c) time to hit the top

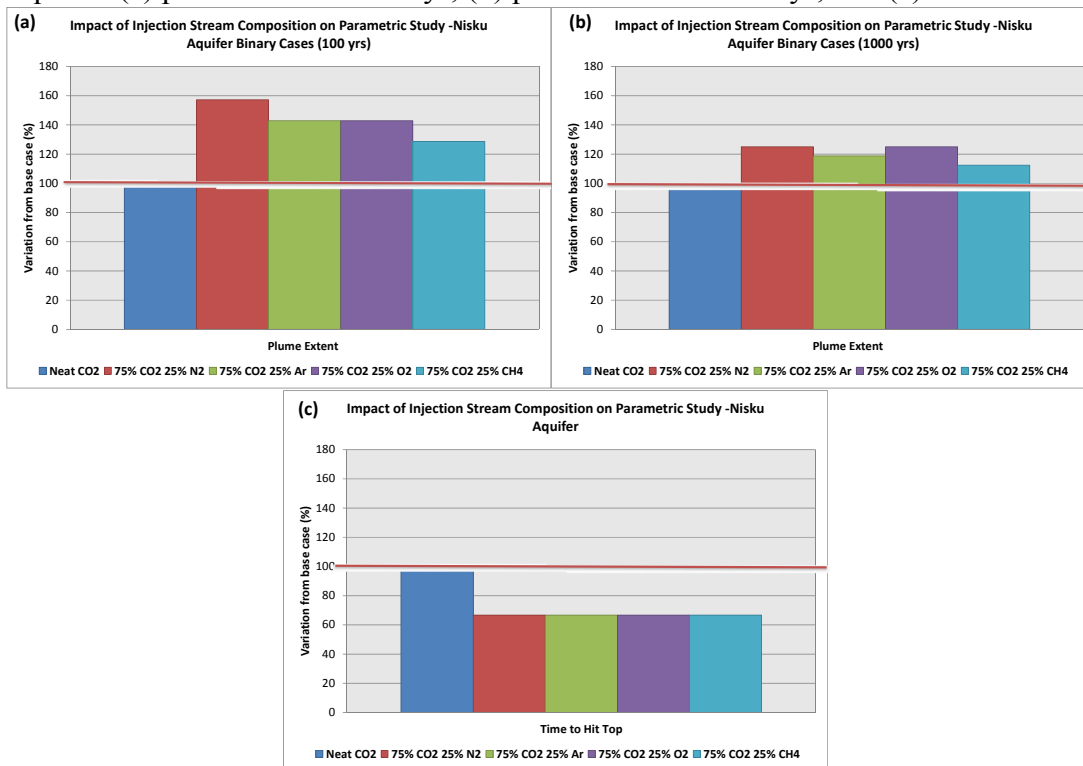


Figure 55. Impact on injection stream composition (75% CO₂) on parametric study for Carbonate Aquifer: (a) plume extent at 100 yr; (b) plume extent at 1000 yr; and (c) time to hit the top

III-6. Associated Issues

Results suggest that, from a flow standpoint, N₂, O₂, and Ar can be combined as N₂ or Ar, at least for small concentrations (5% overall). Figure 26 to Figure 29 illustrates that even with 20% mole fraction impurities, N₂ and Ar provide similar results but Figure 36 suggests Ar is more conservative in terms of plume extent than N₂.

Consistent with Nicot et al. (2008)'s findings, in the homogeneous case, injecting CO₂ in a CH₄-saturated brine reduces time to hit the top and increases plume extent. Time to hit the top went from 30 years in the neat case to 25 years in the CH₄-saturated case. Maximum CH₄ gas mole fraction was at the plume edge, the average CH₄ gas mole fraction in the plume was ~14%. Maximum plume extent was 11,700 ft after 100 years, 26% more than in the neat CO₂ case. The plume was out of the domain in the CH₄-saturated case after 1000 yrs.

Adding impurities (Table 16) decreases the impact of methane outgassing because the impurities themselves have a behavior similar to that of methane. Impurities do not impact the amount of methane outgassing.

Table 16. Impact of methane-saturated brine of plume metrics

Case	Time to hit the top (yr)	Plume Extent (ft) (after 100 yr)	Plume extent increase-compared to non-saturated brine	CH₄ average mole fraction in plume at 100 yr
Neat CO ₂	25	11,700	26%	14.1%
Stream A	25	14,100	24%	14.2%
Stream C	20	16,800	17%	14.4%

IV. Conclusions

This work investigates the impact of impurities on CO₂ plume dynamics. Because of the lack of accurate data on viscosity and density, a series of experiments were performed at selected pressure and temperature and for selected multi-component gas mixtures to accurately determine PVT data. In addition, a comprehensive literature survey helped in estimating aqueous solubility of the mixture components at various pressure, temperature, and salinity conditions. The accurate modeling of simplified systems according to a matrix of reservoir simulations with binary, ternary, and complex mixtures yielded the following results.

In terms of plume shape and extent, the impact of impurities is more marked at shallow depth where the contrast in density and viscosity with neat CO₂ is the largest. The impact of impurities decreases with depth. For example, about 4% mole fraction in a binary system suffices to increase plume length in “shallow” low-dip sloping layers by 25% whereas 9 to 15%, depending on the component, are needed in a “deep” system. In all cases, plume extent is greater with impurities, however, as already noticed in a previous work (Nicot et al., 2008), residual trapping occurs faster. This relationship mostly holds for all systems whatever the level of heterogeneity and complexity. The contrast is most extreme in very simple systems and heterogeneity, assuming adequate operational choices, seems to dampen impacts of impurities, likely because of the multiple tongues developing in heterogeneous systems. The modeling also shows differential dissolution at the front and edges of the plume owing to the highest CO₂ solubility in all subsurface conditions.

As noted in Nicot et al. (2008), it also suggests a trade-off between plume extent (area of review) and decreased risk owing to faster trapping. This study underlines the conflicting effects of having a significant amount of impurities in a CO₂-dominated injection stream: the plume stabilizes faster with them but also flows farther from the injection well. In contrast, a pure CO₂ plume travels less but stays mobile longer. This general conclusion holds under different sets of reservoir parameters. However, increased mobility of the gas mixture can be an issue if leakage occurs.

Many aspects remain to be investigated. Because the results depends on viscosity and density models, their sensitivity must be tested to alternate EOS and formulations of the flow parameters. Impact of IFT changes due to impurities on residual saturation and relative permeability curves also need to be examined. The scope of sensitivity analysis can be further extended to include various formation dip angles, anisotropy ratio, and closed boundary conditions. Other interesting exercises such as monitoring leakage through a (leaking) well located at some distance from the injection well as a function of injection-stream composition could also be performed. Geochemical impacts are still being investigated and will be released in a future document, however its findings are unlikely to challenge the conclusions of the present report. Any detrimental reaction will likely occur close to the wellbore and would be handled by sound operational approaches.

V. References

- Aimard N., Lecanne, , Prevende, C., Cieutat, D., Sanchez-Molinero, I., and Tsiava, R., 2008, The Integrated CO₂ Pilot in the SW of France (Oxycombustion and Geological Storage): A Potential Answer to CO₂ Mitigation in Bitumen Production, SPE 117600
- Alizadeh, A.H., Keshavarz, A.R. and Haghghi, M., 2007, Flow Rate Effect on Two-Phase Relative Permeability in Iranian Carbonate Rocks, SPE 104828.
- Bennion, B. and Bachu, S., 2005, Relative permeability characteristics for supercritical CO₂ displacing water in a variety of potential sequestration zones in the western Canada sedimentary basin, SPE95547.
- Bennion, B. and Bachu, S., 2010, Drainage and Imbibition CO₂/Brine Relative Permeability Curves at Reservoir Conditions for Carbonate Formations, SPE 134028.
- Birkholzer, J., Apps, J. A., Zheng, L. Zhang, Y., Xu, T., Tsang, C-F., 2008, Water quality effects caused by CO₂ intrusion into shallow groundwater, US Environment Protect Agency (EPA), Lawrence Berkeley National Laboratory, LBNL-1251E.
- Bryant, S. L., and L. W. Lake, 2003, CO₂ Impurities Tradeoff: Sub Surface, in CO₂ Capture Project-An Integrated, Collaborative Technology Development Project for Next Generation CO₂ Separation, Capture and Geologic Sequestration, Department of Energy Final Report, Section 2.2.5. prepared by The University of Texas at Austin, Department of c Petroleum and Geosystems Engineering.
- Burton, M., 2008, Surface Dissolution: Addressing Technical Challenges of CO₂ Injection and Storage in Brine Aquifers, MS thesis, The University of Texas at Austin.
- Choi, Jong-Won, Nicot, J. -P., Meckel, Timothy, and Hovorka, S. D., 2011, Numerical modeling of CO₂ injection into a typical U.S. Gulf Coast anticline structure, in Energy Procedia, v. 4, Proceedings of 10th International Conference on Greenhouse Gas Control Technologies GHGT10, September 19-23, Amsterdam, The Netherlands, p. 3486-3493
- Doughty, C., 2007, Modeling geologic storage of carbon dioxide: Comparison of non-hysteretic and hysteretic characteristic curves, Energy Conversion and Management, 48, 1768-1781.
- Ghomian, Y., Pope, G. A., and Sepehrnoori, K., 2008, Reservoir simulation of CO₂ sequestration pilot in Frio brine formation, USA Gulf Coast, Energy, doi:10.1016/j.energy.2008.02.011.
- Holtz, M. H., 2002, Residual gas saturation to aquifer influx: A calculation method for 3-D computer reservoir model construction, SPE75502.
- Hosseini, S., Lashgari, H., Nicot, J.P., and Choi, J.-W., 2011, Model for Deep Subsurface History Match, Report for the Southeast Regional Carbon Sequestration Partnership, Bureau of Economic Geology.
- Hovorka, S. D., Doughty, Christine, Benson, S. M., Freifeld, B. M., Sakurai, Shinichi, Daley, T. M., Kharaka, Y. K., Holtz, M. H., Trautz, R. C., Nance, H. S., Myer, L. R., and Knauss, K. G., 2006, Measuring permanence of CO₂ storage in saline formations: the Frio experiment, Environmental Geosciences, 13, 105-121.

- Hovorka, S. D., Doughty, C. Benson, S. M., Pruess, K., and Knox, P. R., 2004, The impact of geological heterogeneity on CO₂ storage in brine formations: a case study from the Texas Gulf Coast, in Baines, S. J., and Worden, R. H., eds., Geological storage of carbon dioxide: Geological Society, London, Special Publications, 233, p. 147-163.
- IEAGHG, 2011, Effects of Impurities on Geological Storage of CO₂, 2011, report 2011/04 prepared by CanmetENERGY, Natural Resources Canada, June 2011, 63 pages + Appendices.
- Kumar, A., 2004, A Simulation Study of Carbon Sequestration in Deep Saline Aquifers, MS thesis, The University of Texas at Austin.
- Kumar, N., 2008, CO₂ Sequestration: Understanding Plume Dynamics and Estimating Risks, MS thesis, The University of Texas at Austin.
- Land, C.S., 1971, Comparison of calculated with experimental imbibition relative permeability, SPE 3360.
- Lucia, J., 2012, Personal Communication.
- Masalmeh, S., 2002, The Effect of Wettability on Saturation Functions and Impact on Carbonate Reservoirs in the Middle East, SPE 78515.
- Nicot, J. -P., Choi, J.-W., Meckel, T. A., Chang, C. Y., Hovorka, S. D., and Solano, S. V., 2009, Results of numerical investigations at SECARB Cranfield, MS field test site, in Eighth Annual Conference on Carbon Capture and Sequestration: DOE/NETL, May 4–7, Pittsburgh, Pennsylvania, 11 p.
- Nicot, J.-P., Choi, J.-W., Ghomian, Y., and Duncan, I. J., 2008, Impact of mixed gas stream on CO₂ plume characteristics during and after carbon storage operations in saline aquifers: The University of Texas at Austin, Bureau of Economic Geology, final report Chevron Energy Technology Company, Houston, Texas, 137 p. + 2 DVD's.
- Nishi, K. and Shibasaki, T., 1996, Capillary Pressure Effect on Injected Water Movement and Upscaled Relative Permeability in a Heterogeneous Carbonate, SPE 36177.
- Okasha, T.M., Funk, J.J., and Al-Rashidi, H.N., 2007, Fifty Years of Wettability Measurements in the Arab-D Carbonate Reservoir, SPE 105114.
- Ozah, R., 2005, Numerical Simulation of the Storage of CO₂ and CO₂-H₂S Gas Mixture in Deep Saline Aquifers, MS thesis, The University of Texas at Austin.
- Schneider, F.N, 1976, Relative Permeability Studies of Gas-Water Flow Following Solvent Injection in Carbonate Rocks, SPE 5554.
- Tiab, D. and Donaldson, E.C., 2004, Petrophysics Theory and Practice of Measuring Reservoir Rock and Fluid Transport Properties, 2nd edition, p.121-126.
- Wang, F., Lucia, J., and Kerans, C., 1998, Integrated Reservoir Characterization Study of a Carbonate Ramp Reservoir: Seminole San Andres Unit, Gaines County, Texas, SPE Reservoir Evaluation & Engineering, SPE 36515.
- Wang, J., 2011, D. Ryan, E. J. Anthony, N. Wildgust, and T. Aiken, Effects of impurities on CO₂ transport, injection and storage, Energy Procedia, Vol.4, p. 3071-3078.

Wilkinson, M., Simmonds, M., Allam, R. and White, V., 2003, Oxyfuel Conversion of Heaters and Boilers for CO₂ Capture, 2nd National Conference on Carbon Sequestration, May 5-8, Washington, DC.

Wilkinson, M., Boden, J., Panesar, R. and Allam, R., 2001, CO₂ Capture via Oxyfuel Firing: Optimization of a Retrofit Design Concept for a Refinery Power Station Boiler, 1st National Conference on Carbon Sequestration, May 15-17, Washington, DC.

Yamamoto, H., Doughty, C., Investigation of gridding effects for numerical simulations of CO₂ geologic sequestration. *Int. J. Greenhouse Gas Control* (2011),doi:10.1016/j.ijggc.2011.02.007

Zanganeh, K., Shafeen, A. and Thambimuthu, K., 2004, A comparative Study of Refinery Fuel Gas Oxy-Fuel Combustion Options for CO₂ Capture using Simulated Process Data, Proceedings of the 7th International Conference on Greenhouse Gas Control Technologies (GHGT-7), Vancouver, Canada.

VI. Appendix A: Phase Behavior Modeling of Gas Mixtures

VI-1. Flow Properties of the Gas Mixtures

VI-1-1 Summary

We obtained consistent viscosity and density data for pure CO₂ and two CO₂ mixtures diluted with N₂, O₂, and Ar at three elevated pressures and temperatures. We also examined the literature for available experimental data, but no data was found in the temperature and pressure range of interest. We tuned the Peng-Robinson EOS to match the densities and found that zero binary interaction parameters did better than the default values. We then tuned four different viscosity models to the viscosity data using the densities from the PREOS as input. The best viscosity model was found to be the Jossi, Stiel and Thodos correlation (JST).

The material of this section was prepared by Dr. Russel Johns, at the time at the Department of Petroleum and Geosystems Engineering, and one of his graduate students: Ashwin Venktraman. The objective of this task is to quantify and predict the effect of contaminants like N₂, CH₄ and CO on the physical properties of CO₂. A cubic EOS model is then tuned to experimental data for prediction of the plume viscosities and densities. Besides pure CO₂, we found no experimental data in the temperature, pressure, and composition range of interest (between 2000 psia and 6000 psia, and 140°F and 210°F, and CO₂ mole greater than 0.70). As described below, data does exist for several binary mixtures of interest but either at lower pressures or lower temperatures. Most of the data is measured for liquid-vapor equilibrium, e.g. densities and viscosities at vapor pressures.

VI-1-2 Literature review and available experimental data

We performed a literature review of cubic EOS models developed for CO₂ mixtures especially for CO₂ capture applications. We have further compiled a list of experiments done for various temperature pressure ranges involving CO₂ mixtures reported in the literature. The results from this study aided in defining the temperatures, pressures, and compositions required for additional experiments.

EOS model

Li and Yan (2009) evaluated different cubic equations of states (Peng-Robinson (PR), Patel-Teja (PT), Redlich-Kwong (RK), Redlich-Kwong-Soave (SRK) and 3P1T) for predicting vapor-liquid equilibrium (VLE) of binary mixtures with CO₂ and CH₄/H₂S/SO₂/Ar/N₂/O₂. They identified the best EOS to be used for a particular binary mixture based on tuning the binary interaction parameters to the saturation pressures. Generally, the PR, PT and SRK were found to be superior to RK and 3P1T and they recommended PR for density calculations of CO₂/CH₄ and CO₂/H₂S mixtures; PT for CO₂/O₂, CO₂/N₂ and CO₂/Ar; while 3P1T is recommended for calculations of CO₂/SO₂ mixture.

We used the Peng-Robinsons EOS (PR) in this task since this model is used in GEM, and it was satisfactory for all of their measurements. Further, the PR model is widely used in the petroleum industry to model CO₂ floods.

Experimental density measurements for mixtures

Table 17 gives a summary of data that we have found in the literature.

VLE experiments of CO₂-N₂ binary mixture have been widely reported for various pressure temperature ranges (rows 9 to 14 of Table 17). Esper et al (1989) performed volumetric and density measurements for near equimolar mixture of CO₂ and N₂. These measurements were made at constant volume and constant temperatures. Isometric measurements are coupled with measurements at 300 K and densities have been derived from them using a virial equation of state. Arai et al (1971) have also developed PVTX relation for CO₂-N₂ mixtures and have measured molar volume. Al-Sahhaf (1990) has obtained the VLE data for ternary mixture comprising of CO₂, N₂ and CH₄ at 230 K and 250 K at various pressures.

The VLE experiments for the CH₄-CO₂ system reported in the literature are mostly at low temperatures and pressures (rows 1, 3 and 4 of Table 17). Klimech et al (2001) performed high pressure measurements of density but only for pure CH₄ and pure CO₂ rather than for mixtures.

Lasangan and Smith (1993) gave thermophysical properties of binary mixtures of CO₂ with C1/C2/C3/C4 at 1500 psi and 105 K. This forms a good data set that will be used for our EOS model predictions in addition to new experimental measurements we will make.

Table 18, Table 19, and Table 20 give a detailed list of the densities and viscosity data that we found for CO₂ mixtures.

Table 17. Experimental data for various mixtures of CO₂ in the literature

Sr	Type of data	Min press (psi)	Max press (psi)	Min temp (F)	Max temp (F)	Reference
1	VLE of CH ₄ -CO ₂ system	73.5	1000	-184	127.4	Mraw et al (1978)
2	PVTX relation for CO ₂ -Argon system	352.8	2205	59		Sarashina et al (1971)
3	PVTX for CO ₂ -N ₂ and CO ₂ -CH ₄ system	294	2205	-4	59	Arai et al (1971)
4	Phase equilibrium in CO ₂ -CH ₄ system	215	1146	-89	100	Donnelly and Katz (1954)
5	VLE in CO ₂ -SO ₂ system at isothermal conditions	36.75	1323	14	140	Lachet V., et al (2009)
6	Compressibility factor Z measurements done for CO ₂ -dry gas mixture (gas contains 96.5% C1)	50	5000	100	220	Adisoemarta, P.S. Et al., 2004 (SPE 89466)
7	VLE data for N ₂ , CO ₂ and CH ₄ mixture	914	1411	-45.4		Al-Sahhaf, T.A., 1990
8	Volumetric and density measurements for near-equimolar mixture of CO ₂ +N ₂ mixture	14.7	2256	-90.4	116.6	Esper et al (1989)
9	VLE of N ₂ + CO ₂ mixture	41.6	2041.8	-66.73	32.27	Zenner and Dana (1963)
10	VLE of N ₂ + CO ₂ mixture	811	1764	32.27		Muirbrook and Prausnitz (1965)
11	VLE of N ₂ + CO ₂ mixture	745.29	1872.78	-39.7	68.27	Kaminshi and Toriumi (1966)
12	VLE of N ₂ + CO ₂ mixture	513.03	1737.54	32.27		Yorizane et al.(1970)
13	VLE of N ₂ + CO ₂ mixture	470.4	1813.98	26.6		Somait and Kidnay (1978)
14	VLE of N ₂ + CO ₂ mixture	471.87	2459.31	-57.73	32.27	Dorau et al. (1983)
15	VLE of N ₂ + CO ₂ mixture	735	1470	-57.73	32.27	Weber, W., et al (1984)
16	Pure CH ₄ and pure CO ₂ (P,density, T) experimental measurement	29.4	4410	-58	482	Klimeck et al (2001)
		29.4	4410	-27.4	476	
17	VLE data for CH ₄ -CO ₂ and ternary C1-C ₂ -CO ₂	191.1	1176	-45.4	26.6	Davalos et al (1976)
18	VLE of CH ₄ and H ₂ S	294	1176	33.08	212	Bierlein and Kay (1953)
19	Viscosity and density of binary and ternary mixtures of CO ₂ with C1/C ₂ /C3/C ₄	1500		105		Lansangan and Smith (1993)

Sr	Type of data	Min press (psi)	Max press (psi)	Min temp (F)	Max temp (F)	Reference
20	VLE for gas composition of CO ₂ (99.5%) and impurities SO ₂ , N ₂ and CO	1000		-425	100	Nogueira, M.C., and Mamora, D. D., (SPE 94906)
21	Ternary diagram plots available for CO ₂ , N ₂ , C1 mixture	1471	3675			Ulysses de Ribeiro Augusto Lino (SPE 59343)
22	VLE of N ₂ + CO ₂	88.2	2454.9	-63.4	-27.4	Al-Sahhaf et al (1983)
23	VLE of CH ₄ and CO ₂	85.26	1251.117	-64.7	26.6	
24	VLE of ternary N ₂ +CH ₄ +CO ₂	893.76	1787.52	-63.4	-27.4	
25	VLE of CO ₂ -CO, CO ₂ -Ar, CO ₂ -CH ₄ and ternary CO ₂ -H ₂ -CO		2940	-58	68	Kaminishi et al (1968)

Table 18. Available density data for various mixtures of CO₂ in the literature

Kreglewski and Hall (1983)					
CO ₂ (mol frac)	N ₂ (mol frac)	Pc (bar)	Tc (K)	Density (mol/litre)	Reference
1	0	73.825	304.21	10.6	
0.838	0.162	98.1	288.15	12.4	Arai et al (1971)
0.72	0.28	118.8	273.15	13.7	Arai et al (1971)
0.707	0.293	120	273.15	12.9	Muirbrook and Prausnitz (1965)
0.605	0.395	144.4	253.15	15.8	Arai et al (1971)
CO ₂ (mol frac)	C1 (mol frac)	Pc (bar)	Tc (K)		
0.834	0.166	81.6	288.15	11.7	Arai et al (1971)
0.7	0.3	85.5	273.15	12.2	Arai et al (1971)
0.525	0.475	83.5	253.15	12.5	Arai et al (1971)
0	1	46.04	190.58	10.1	
Esper et al (1989)					
CO ₂ (mol frac)	CH ₄ (mol frac)	P (Mpa)	T (K)	Density (mol/m ³)	Comments
0.4761	0.5239	5.8323	219.04	18660	
		8.2926	249.47	11867	
		7.6382	256.16	7551	
		6.1774	255.47	4806	
		4.5179	249.2	3075	
		2.0055	229.1	1245.6	
		0.5199	205.41	321	
		7.1919	233.22	16599	
		8.2922	252.65	10522	
CO ₂ (mol frac)	N ₂ (mol frac)	P (Mpa)	T (K)	Density (mol/m ³)	
0.447	0.553	15.7565	239.82	14389	
		12.3775	254.51	9555	
		9.3638	257.8	6345	
		6.7163	253.89	4214	
		4.6236	245.67	2798	
		3.1253	236.76	1858	
		1.573	221.19	939.4	
		0.6851	208.53	414.1	
		18.1517	224.95	17783	

		14.0798	248.97	11818	
		16.8088	233.19	15998	
Klimech et al (2001)					
		P (MPa)	T K	Density (kg/m3)	Comments
CO ₂	(pure)	13.1391	340	437.466	159 values for pure methane and 118 values for pure CO ₂ have been carried out in temp range 240 K to 520 K and at pressures up to 30 Mpa
		14.0576	340	489.683	
		14.9395	340	532.769	
		14.7057	360	375.618	
		15.0451	390	288.08	
		15.1	430	228.017	
		24.0874	240	1147.882	
		24.0469	260	1081.552	
		24.0253	323.15	825.825	
		30.0981	240	1159.86	
		30.0501	300	959.843	
		30.0864	360	717.383	
		30.0735	470	395.41	
Sarashina et al (1971)					
CO ₂ (mol frac)	Ar (mol frac)	P(atm)	T(Cel)	Density (gmole/cm ³)	
0.81	0.19	128	15	0.01607717	1) Specific volumes have been reported and I have converted these to densities
0.81	0.19	143.4	15	0.017182131	
0.793	0.207	128	15	0.015455951	2) CO ₂ Ar is two phase in these conditions and I have reported only the gas phase properties
0.793	0.207	143.4	15	0.016666667	
0.752	0.248	124.1	15	0.0135318	
0.752	0.248	143.4	15	0.015625	3) selected values for range of interest from given table
0.7	0.3	124.1	15	0.011441648	
0.7	0.3	143.4	15	0.013736264	
Arai et al (1971)					
CO ₂ (mol frac)	N ₂ (mol frac)	P (atm)	T (Cel)	Density (g-mole/cc)	
0.897	0.103	135.6	15	0.016556291	
0.812	0.188	134.6	15	0.015898251	
0.801	0.199	131.8	15	0.015128593	1) Specific volumes have been reported and I have converted these to densities
0.801	0.199	143.3	15	0.016	
0.736	0.264	143.3	15	0.013850416	2) CO ₂ mixtures are two phase in these conditions and I have reported only the gas phase properties
0.702	0.298	143.3	15	0.012738854	
0.694	0.306	135.5	0	0.014367816	3) selected values for range of interest from given tables
0.694	0.306	143.2	0	0.014992504	
0.492	0.508	143.2	0	0.009803922	
CO ₂ (mol frac)	CH ₄ (mol frac)	P (atm)	T (Cel)	Density (g-mole/cc)	
0.833	0.167	124.1	15	0.017605634	
0.833	0.167	143.4	15	0.018315018	
0.753	0.247	124.1	15	0.015625	
0.753	0.247	143.3	15	0.016977929	
0.7	0.3	143.3	15	0.015625	

0.679	0.321	131.7	0	0.016556291	
0.679	0.321	143.2	0	0.017152659	
0.592	0.408	127.8	0	0.014285714	
0.592	0.408	143.2	0	0.015360983	
0.492	0.508	127.8	0	0.011976048	
0.492	0.508	143.2	0	0.013351135	

Table 19. Available viscosity data for various mixtures of CO₂ in the literature

Kestin and Leidenfrost (1959)					
CO ₂ (mol frac)	N ₂ (mol frac)	P (atm)	T (celcius)	Viscosity (cp)	Comments
0.904	0.1	21	20	0.153	1) viscosity measured using oscillating-disk viscometer
0.787	0.21	21	20	0.157	2) Measurement accuracy of 0.05 %
0.657	0.34	21	20	0.161	3) Viscosity experimentally measured but Density calculated using Benedict-Webb-Rubin EOS and hence I have not reported in this table
0.505	0.49	21	20.1	0.166	
0.375	0.62	21	20	0.170	
0.233	0.77	21	20	0.174	
0.106	0.89	21	20	0.177	4) selected values for range of interest from given tables
Kestin et al (1966)					
CO ₂ (mol frac)	N ₂ (mol frac)	P (atm)	T (Celsius)	Viscosity (cp)	Comments
1	0	25	20	0.151	1) viscosity measured using oscillating-disk viscometer
1	0	20	20	0.149	2) Measurement accuracy of 0.0 ₄ %
0.813	0.19	26	20	0.158	3) Selected values for range of interest from given tables
0.688	0.31	23	20	0.161	
0.506	0.49	24	20	0.167	
0.31	0.69	25	20	0.173	
0.074	0.93	25	20	0.178	
1	0	25	31	0.156	
0.813	0.19	25	31	0.163	
0.31	0.69	25	31	0.178	
0.074	0.93	26	31	0.183	
0	1	25	31	0.184	
CO ₂ (mol frac)	Ar (mol frac)	P (atm)	T (Celsius)	Viscosity (cp)	
0.917	0.08	25	20	0.157	
0.843	0.16	25	20	0.163	
0.634	0.37	25	20	0.179	
0.54	0.46	25	20	0.187	
0.332	0.67	24	20	0.203	
0.268	0.73	26	20	0.208	
0	1	25	20	0.229	
1	0	25	30	0.156	
0.917	0.08	24	30	0.162	
0.843	0.16	25	30	0.168	
0.634	0.37	25	30	0.185	
0.54	0.46	25	30	0.193	
0.332	0.67	24	30	0.209	

0.268	0.73	25	30	0.214	
0	1	25	30	0.235	

Table 20. Available viscosity and density data for various mixtures of CO₂ in the literature

Fluid (mol frac)					Pressure	Temperature	Density (g/cm ³)	Viscosity (cp)	Source/Comment
SPE 21017-PA									
CO ₂	C1	C2	C3	C4	1500 psia	105 F			Lansangan and Smith (1993)
1							0.6374	0.503	1) Ely, J.F., and Huber, M.L.: "NIST Thermophysical Properties of Hydrocarbon Mixtures Database, " Version 1.0, Standard Reference Data Program, Natl. Inst. Of Standards & Technology (1990). http://www.nist.gov/srd/nist3.htm
0.9	0.1						0.3315	0.02691	
0.9		0.1					0.5022	0.03888	
0.9			0.1				0.6218	0.05349	
0.9				0.1			0.6929	0.06724	
0.8	0.1	0.1					0.307	0.02588	
0.8	0.1		0.1				0.397	0.03154	
0.8	0.1			0.1			0.5123	0.04298	
0.8		0.1	0.1				0.544	0.04666	
0.8		0.1		0.1			0.6176	0.05926	
0.8			0.1	0.1			0.6617	0.06983	

References for Table 18, Table 19, and Table 20

1. Adisoemarta, P.S., Frailey, S.M., & Lawal, A.S., 2004, Measured Z factor of CO₂-Dry Gas/Wet Gas/Gas Condensates for CO₂ Storage in Depleted Gas Reservoirs, SPE 89466.
2. Al-Shahaf, T.A., Kidnay, A.J., and Sloan, E.D., 1983, Liquid+vapor equilibria in the N₂+ CO₂ + CH₄ system, 1983, 22, 372-380
3. Al-Shahaf, T.A., 1990, Vapor liquid equilibria for the ternary N₂+ CO₂ + CH₄ system at 230 and 250 K, 55: 159-172.
4. Arai, Y., Kaminishi, G., and Saito, S., The Experimental determination of the P-V-T-X Relations for the CO₂-N₂ and CO₂-CH₄ systems, 1971, Journal of Chemical Engineering of Japan, 4, 2, 113-122.
5. Bierlein, J.A., and Kay, W.B., Phase-Equilibrium Properties of System Carbon dioxide-Hydrogen Sulphide, 1953,, 45(3), 618-624.
6. Davalos, J., Anderson, W.R., Phelps, R.E., Kidnay, A.J., Liquid-Vapor Equilibria at 250 K for systems containing Methane, Ethane, and Carbon dioxide, Journal of Chemical and Engineering Data, 1976, 21, 1, 81-84.
7. Donnelly, H.G., and Katz, D.L., Phase equilibria in the carbon dioxide-methane system, Ind. Eng. Chem., 1954, 46(3): 511-517
8. Dorau, W., Al-Wakeel, J.M., and Knapp, H., 1983, VLE data for CO₂-CF₂Cl₂, N₂-CO₂, N₂-CF₂Cl₂ and N₂-CO₂-CF₂Cl₂, Cryogenics: 29-35
9. Esper, J., Bailey, D.M., Holste, J.C., and Hall, K.R., 1989, Volumetric behavior of near-equimolar mixtures for CO₂+ CH₄ and CO₂+N₂
10. Kaminishi, G.J., and Rorumi, T., 1966, Gas-liquid equilibrium in the CO₂-H₂, CO₂-N₂ and CO₂-O₂ systems, J. Chem. Soc. Jpn., Ind. Chem. Sect., 69: 175-178
11. Kaminishi, G., Arai, Y., Saito, S., and Maeda, S., Vapor-Liquid Equilibria for Binary and Ternary Systems Containing Carbon Dioxide, 1968, 1 (2), 109-116
12. Kestin J., Kobayashi Y., and Wood R.T., " The Viscosity of Four Binary, Gaseous Mixtures at 20 C and 30 C, *Physica*, Vol 32, 1966, 1065-1089

13. Kestin J., and Leidenfrost W., " The Effect of Pressure on the Viscosity of N₂-CO₂ mixtures," *Physica*, Vol 25, 1959, 525-536.
14. Klimeck, J., Kleinrahm, R., and Wagner, W., 2001, Measurements of the (p, rho, T) relation of methane and carbon dioxide in the temperature range 240 K to 520 K at pressures up to 30 Mpa using a new accurate single sinker densimeter, *J. Chem. Thermodynamics*, 2001, 33, 251-267
15. Lachet V., Bruin T., Ungerer P., Coquelet C., Valtz, A., Hasanov, V., Lockwood F., & Richon D., Thermodynamic behavior of the CO₂ + SO₂ mixture: experimental and Monte Carlo simulation studies
16. Lasangan, R.M., and Smith, J.L., Viscosity , Density and Composition Measurements of CO₂/West Texas Oil systems, *SPE Reservoir Engineering*, 1993
17. Li, H., and Yan, J., Impacts of equation of state (EOS) and impurities on the volume calculation of CO₂ capture and storage (CCS) processes, *Applied Energy*, 2009, Volume 86, Issue 12, 2760:2770
18. Li, H., and Yan, J., Evaluating cubic equations of state (EOS) for calculation of vapor liquid equilibrium of CO₂ and CO₂ mixtures for CO₂ capture and storage processes, *Applied Energy*, 2009, Volume 86, Issue 6, :826:836
19. Liley, P.E., Thermophysical Properties Research Center Report 15, Purdue University, February 1963.
20. Lohrenz, J., Bray, B.C., and Clark, C.R., 1964, The viscosity of pure substances in dense gaseous and liquid phases, *J. Pet. Tech*, 1171-1176.
21. Mraw, S.C., Shuen-Cheng and Kobayshi, R., 1978, Vapor-Liquid equilibrium of the CH₄-CO₂ system at low temperatures, *Journal of Chemical and Engineering Data*, 23(2): 135-139
22. Muirbrook, N.K., and Prausnitz, J.M., 1965, Multicomponent vapor liquid equilibria at high pressures, *Am. Inst. Chem. Eng. J.*, 13: 1092:1096
23. Nogueira, M.C., and Mamora, D.D., Effect of Flue Gas impurities on the process of injection and storage of CO₂ in depleted Gas Reservoirs, *SPE 94906*
24. Sarashina E., Arai, Y., and Saito S., The PVTX relation for the carbon-dioxide-argon system, *Journal of Chemical Engineering of Japan*, 1971, 4, 4, 379-381.
25. Somait, F.A., and Kidnay, A.J., 1978, Liquid-vapor equilibria at 270 K for systems containing nitrogen. Methane and carbon dioxide, *J. Chem. Eng. Data*, 23: 301-305
26. Ulysses de Ribeiro Augusto Lino (SPE 59343), Compositional and Phase Behavior Experimental and Theoretical work on Hydrocarbon Mixtures and Several Solvents (CO₂, N₂ and Flue Gases)
27. Webber, W., Zeck, S., and Knapp, H., Gas Solubilities in liquid ternary system solvents at high pressure apparatus and results for ternary systems of N₂, CO₂ and CH₃OH, 1984, *Fluid Phase Equilibria*, 18: 253-278.
28. Yorizane, M., Yoshimura, S., Masuoka, H., and Nakamura, M., 1971, *J. Chem. Eng. Jpn.*, 4:10
29. Zenner, G.H., and Dana, L.T., 1963, Liquid-vapor equilibrium compositions of carbon oxygen-nitrogen mixtures, *Chem. Eng. Prog. Symp. Ser.*, 59: 36-41

VI-1-3 New experimental data

We contracted Schlumberger (see Section VI-2) to make density and viscosity measurements for a variety of gas mixtures with CO₂. The gas compositions selected were chosen based on the expected temperature, pressure, and composition range of interest. The expected minimum contaminant composition of the fluid (by volume fraction) is 68.85% CO₂, 15% N₂, 5% O₂, 4%

H₂, 2% CO, 5% Ar, and 0.15% SO₂. By mole fraction these volumes convert (assuming ideality) to about 83.96% CO₂, 7.778% N₂, 3.06% O₂, 0.15% H₂, 1.05% CO, 3.82% Ar, and 0.18% SO₂. The analysis is done based on mole fractions, not volume fractions. We estimated that all gas compositions are within the single-phase region based on PREOS calculations, and some saturation pressure measurements made in the literature. We also estimated viscosities for several gases to ensure that the viscosities were not too low so that the values will be within the range of the equipment accuracy. Table 21 gives the pressures and temperatures of the densities and viscosity measurements as they were planned. Table 22 shows the planned gas compositions. Calibration gases were obtained by Schlumberger and viscometer calibration checked (Table 23). They also completed some gas density measurements for pure nitrogen and checked this against tabulated data in the literature (NIST data base). Figure 56 shows the nitrogen calibration measurements. These calibrations were done for all pure fluids. Table 24 shows the pure CO₂ viscosities measured at the temperatures and pressures shown in Table 21. These data are consistent with data reported in the literature.

We designed the experiments so that nonlinearities in the viscosity with pressure and temperature could be examined with the minimum number of measurements (three composition, temperature, and pressure measurements). We obtained viscosity and density data for pure CO₂ and two CO₂ mixtures diluted with N₂, O₂, and Ar at three elevated pressures and temperatures. The reported error by Schlumberger in the density measurements is +/- 0.0001 g/cc, while the viscosity error is greater at +/- 0.0018 cp. The results for each fluid considered are given in Table 25 to Table 27.

Table 25 gives the densities and viscosities for pure CO₂ measured at the temperatures and pressures of interest. The pressures used for the measured viscosity and density are not exactly the same, but they are close. We report the approximate pressures in the tables below, although we did use the exact pressures in tuning of the density and viscosity models (see Schlumberger report and the Table captions for the exact pressures for the viscosity measurements). Table 26 and Table 27 give the density and viscosity measurements for the two synthetic gases where CO₂ is contaminated by equal mole fractions of N₂, O₂, and Ar. All of these mixtures are supercritical fluids.

We compared the densities for pure CO₂ against available tabular data. The measured data are in good agreement with tabular data from the literature and are close to or within the reported error of the experimental measurements. Figure 57 compares the measured densities and viscosities of pure CO₂ to those of the NIST database (National Institute of Standards and Technology). The difference in densities is slightly greater at lower pressures (about 0.5%). The viscosity differences are greater as is typically the case. The viscosity measurement at 4000 psia and 175°F is the worst case with a difference of about 6% (or about 0.003 cp). This error is somewhat greater than the reported viscosity error by Schlumberger of about 0.0018 cp. Figure 58 shows the change in densities and viscosities for pure CO₂ and the two mixtures. Both the density and viscosity increase as CO₂ mole fraction increases, which is expected. The trends over this composition range are more linear than the trends of density and viscosity with pressure.

Density Modeling

We used the Peng-Robinson equation-of-state (PREOS) to match the density experimental data. The PREOS is used because it has been found to be superior to other EOS in density predictions (see first quarter report). We took the following steps to model the experimental densities:

- 1) Determine the input parameters for the PREOS for all identifiable components. These

data, such as critical temperature and pressure, are fixed and were not adjusted. Table 28 gives these values.

- 2) Calculate the dimensional volume shift parameters from the Rackett equation. These are considered adjustable parameters. Table 28 gives the initial values for the volume shift parameters.
- 3) Determine the binary interaction parameters based on binary phase behavior data and the PREOS. The BIPs from literature were found to be -0.007 for CO₂/N₂, 0.114 for CO₂/O₂, and 0.163 for CO₂/Ar. These are initially used, but are considered adjustable parameters.
- 4) Tune the adjustable parameters within limits to get the best match to the three supercritical fluid compositions. We followed the idea that the best model is the one where the fewest number of parameters are adjusted and they should not be greatly changed. We also followed the notion that if the BIPs could be zero we should take them as zero.

We first used the standard binary interaction parameter values for the binary pairs, but the density predictions for the mixtures were poor. The BIPs in the literature are generally determined by fitting to saturation pressure data (at two-phase boundaries), which is far from the conditions of our fluids. We found that the predictions for the supercritical fluids are better when the binary interaction parameters are set to zero. This also makes for a simpler model that likely can predict densities better for other components as well.

After adjustment we found that the pure CO₂ densities, which are independent of the BIPs, were still in error. Thus, we optimized the volume shift parameter for CO₂ to get improved density values for all of the experimental data including the two synthetic mixtures. The optimization was done by summing the square of the relative errors in the density values. The best fit value of the volume shift parameter changed from -0.0263 to 0.005. We choose to adjust the volume shift only for this component because most of the gas contains CO₂ and the other mixture density values were closer to the predicted values. After adjustment, the maximum error for pure CO₂ was 6.84% at 2000 psia and 140°F, while the other values were less than 3%. The maximum error for synthetic gas 1 was only 1.72% and for synthetic gas 2 1.79%. Except for the one value at 2000 psia for pure CO₂, these fits are excellent (Table 29).

Viscosity Modeling

We also examined multiple viscosity methods to determine the best model. The densities determined from the optimized PREOS inputs in Table 29 were used for all viscosity calculations. We compared four models to estimate viscosity estimates:

- 1) Jossi, Stiel and Thodos correlation (Jossi, et al., 1962) with the mixture low-pressure viscosity determined from the Herning-Zipperer and Yoon-Thodos formulas (*HZYT option in GEM). This approach uses the concept of residual viscosity. The default values of the coefficients were determined to reproduce gas viscosities. These coefficients are considered to be tuning parameters for the measured experimental data. The critical volumes and molecular weights were not used as tuning parameters, but are required for viscosity calculations.
- 2) Lohrenz-Bray-Clark (Lohrenz, et al., 1964). This model is not available in GEM, but is an extended version of the JST method and is used often in the petroleum field. We used it here to see how well it compared to the other models. The default coefficients for this model are identical to those used by JST. These coefficients are tuning parameters when laboratory data are available. The critical volumes and molecular weights were not used

as tuning parameters, but are required for viscosity calculations.

- 3) Modified Pedersen's corresponding-states correlation (*MODPEDERSEN option in GEM, Pedersen and Fredenslund 1987). This correlation is modified from the original Pedersen correlation to account for heavier components. The correlation uses methane as the reference fluid. The Pedersen correlation takes significantly more computational time than the JST and LBC methods. The Pedersen correlations can be tuned by adjusting five coefficients.

We also examined the JST correlation with the Lee-Eakin formula, but quickly found it to be inferior and is not considered further.

Similar to the PREOS tuning, we minimized the number of tuning parameters and the magnitude of their variations so that the model could be more predictive. We also tried to keep correlations linear by not regressing on exponents that were equal to 1.0.

The untuned results (using the default coefficients) showed that the JST with HZYT mixing rules is generally superior to both LBC and the Modified Pedersen method for these three fluids. The modified Pedersen correlation is poor for pure CO₂, but does much better for synthetic gas 1 and 2. The JST method outperforms the LBC method for synthetic gas 1 and 2. The JST also slightly outperforms the LBC method for all three gases, while the Pedersen method is significantly worse primarily because of its poor estimates for CO₂. We discarded the Modified Pederson model for further analysis.

Next, we tuned the LBC and JST models by allowing their coefficients to change by a maximum of 20%. The JST model still outperformed the LBC model by a slight amount. We allowed for greater variations in the coefficients, but the improvements were marginal at the possible expense of the ability of the models to predict viscosities for other components and compositions. The maximum error in the viscosities estimated from the JST method is 11%, which corresponds to the lower pressure of 2000 psia and 140°F. All other relative differences between the experimental and the predicted viscosities were less than 7%. These viscosity estimates are very good especially considering the uncertainty in the viscosity measurements. Table 30 gives the final coefficients to be used for the JST *HZYT option in GEM.

References

- Jossi, J.A., Stiel, L.I. and Thodos, G., 1962. The viscosity of pure substances in the dense gaseous and liquid phases. *AIChE Journal* 8 1, pp. 59–63
- Lohrenz, J., Bray, B.C., and Clark, C.R., 1964. The viscosity of pure substances in dense gaseous and liquid phases, *J. Pet. Tech*, 1171-1176.
- Pedersen, K.S., and Fredenslund, A., 1987. An improved corresponding states model for the prediction of oil and gas viscosities and thermal conductivities. *Chem. Eng. Sci.* 42, pp. 182–186.
- Robinson, D.B., Peng, D.Y., 1978. The characterization of the heptanes and heavier fractions for the GPA Peng–Robinson programs, Gas processors association, Research report RR-28.

Table 21. Pressure and temperatures for new experimental data.

T (°F)/ P (psia)	2000	4000	6000
140	X		
175	X	X	X
210			X

Table 22. Gas compositions for new experimental data

Compositions	CO ₂	H ₂	CO	N ₂	O ₂	Ar	SO ₂
1	85%			5%	5%	5%	
2	70%			10%	10%	10%	

Table 23. CO₂ viscosity measurements (check of viscometer calibration)

Temp. °F	Temp. °C	Pressure (psi)	Measured Viscosity cP	
			Schlumberger	From Jarrell et al.
140	60	2070	0.041 ± 0.002	0.043
175	79.4	2049	0.030 ± 0.002	0.03225
175	79.4	4022	0.057 ± 0.002	
175	79.4	6009	0.077 ± 0.002	
210	98.89	6014	0.070 ± 0.002	

Table 24. CO₂ viscosity measurements at various temperatures and pressures requested

Temp. °F	Temp. °C	Pressure	Measured
			Viscosity cP
140	60	2070	0.041 ± 0.002
175	79.4	2049	0.030 ± 0.002
		4022	0.057 ± 0.002
		6009	0.077 ± 0.002
210	98.89	6014	0.070 ± 0.002

Table 25. Experimental data for pure CO₂

T (°F)/ P (psia)	2000	4000	6000
140	0.5511 (g/cc) 0.0408 (cp)		
175	0.3792 0.0297	0.7234 0.0571	0.8338 0.0766
210			0.7704 0.0703

Note: the upper number in each cell is the density in g/cc and the lower number is viscosity in cp. (From the lowest temperature and pressure value, the viscosity measurements were made at slightly different pressures of 2070, 2049, 4022, 6009 and 6014 psia.)

Table 26. Experimental data for synthetic gas 1 (mole fract.: 85% CO₂, 5% N₂, 5% O₂, 5% Ar).

T (°F)/ P (psia)	2000	4000	6000
140	0.3635 (g/cc) 0.0298 (cp)		
175	0.2921 0.0283	0.6079 0.0493	0.7453 0.0691
210			0.6847 0.0632

Note: The upper number is the density in g/cc and the lower number is viscosity in cp. (From the lowest temperature and pressure value, the viscosity measurements were made at slightly different pressures of 2017, 2025, 4014, 6019 and 6021 psia.)

Table 27. Experimental data for Synthetic Gas 2 (mole fractions: 70% CO₂, 10% N₂, 10% O₂, 10% Ar).

T (°F)/ P (psia)	2000	4000	6000
140	0.2848(g/cc) 0.0309 (cp)		
175	0.2489 0.0262	0.5071 0.0429	0.6591 0.0616
210			0.6075 0.0555

Note: The upper number is the density in g/cc and the lower number is viscosity in cp. (From the lowest temperature and pressure value, the viscosity measurements were made at slightly different pressures of 2036, 2018, 4017, 6024 and 6018 psia.)

Table 28. Initial input parameters for PREOS for all components

Comp.	T _c (°F)	P _c (psia)	ω	Vol. Shift (ft ³ /lb-mol)	Vol. Shift dimensionless	M _w	Ω _a	Ω _b	V _c (ft ³ /lb-mol)
CO ₂	87.8900	1069.8700	0.2250	-0.0263	-0.0615	44.010	0.45724	0.07780	1.51
N ₂	-232.5100	492.3200	0.0400	-0.0678	-0.1760	28.014	0.45724	0.07780	1.44
O ₂	-181.3900	731.8600	0.0210	-0.0593	-0.1868	31.999	0.45724	0.07780	1.18
Ar	-188.2300	706.8800	-0.0040	-0.0644	-0.2009	39.948	0.45724	0.07780	1.20
H ₂	-399.9280	190.4345	-0.2160	-0.0855	-0.3264	2.016	0.45724	0.07780	1.04
CO	-220.4500	507.4870	0.0480	-0.0675	-0.1715	28.010	0.45724	0.07780	1.51
SO ₂	315.7700	1143.4775	0.2450	-0.0341	-0.0602	64.065	0.45724	0.07780	1.95

Note: The volume shift parameters are the only adjustable parameters. All other parameters are fixed since they are identifiable components.

Table 29. Final input parameters for PREOS for all components that are to be used in GEM

Comp.	T _c (°F)	P _c (psia)	ω	Vol. Shift (ft ³ /lb-mol)	Vol. Shift dimensionless	M _w	Ω _a	Ω _b	V _c (ft ³ /lb-mol)
CO ₂	87.8900	1069.8700	0.2250	0.0050	0.0117	44.010	0.45724	0.07780	1.51
N ₂	-232.5100	492.3200	0.0400	-0.0678	-0.1760	28.014	0.45724	0.07780	1.44
O ₂	-181.3900	731.8600	0.0210	-0.0593	-0.1868	31.999	0.45724	0.07780	1.18
Ar	-188.2300	706.8800	-0.0040	-0.0644	-0.2009	39.948	0.45724	0.07780	1.20
H ₂	-399.9280	190.4345	-0.2160	-0.0855	-0.3264	2.016	0.45724	0.07780	1.04
CO	-220.4500	507.4870	0.0480	-0.0675	-0.1715	28.010	0.45724	0.07780	1.51
SO ₂	315.7700	1143.4775	0.2450	-0.0341	-0.0602	64.065	0.45724	0.07780	1.95

Note: We adjusted the volume shift for CO₂ as it gave improved density values for the pure CO₂ supercritical fluid. All binary interaction parameters are taken to be zero.

Table 30. Coefficient values for the JST viscosity model

a1	a2	a3	a4	a5
0.10999	0.01168	0.05573	-0.02847	0.00467

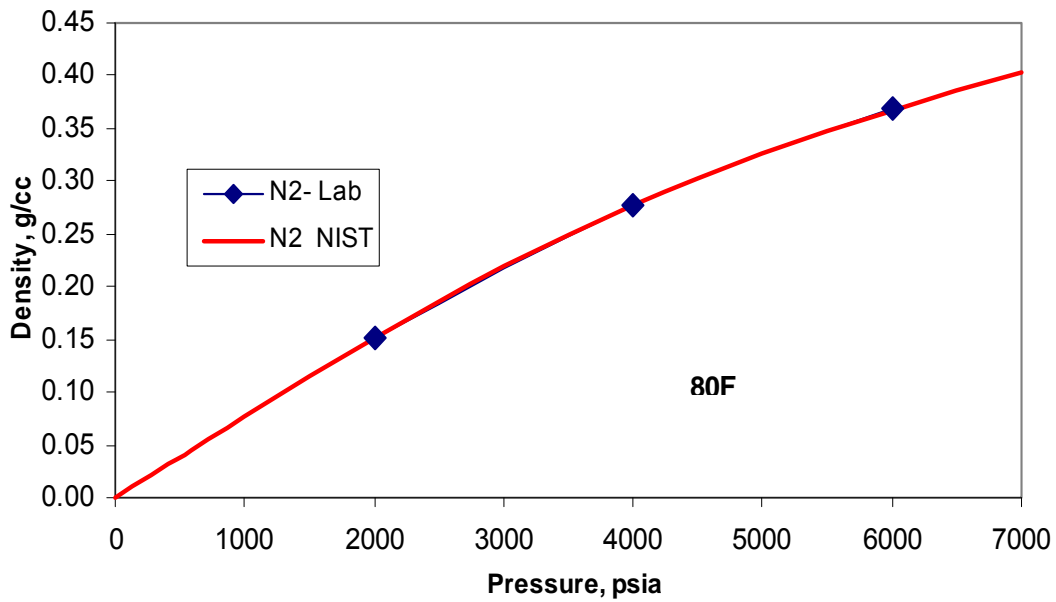
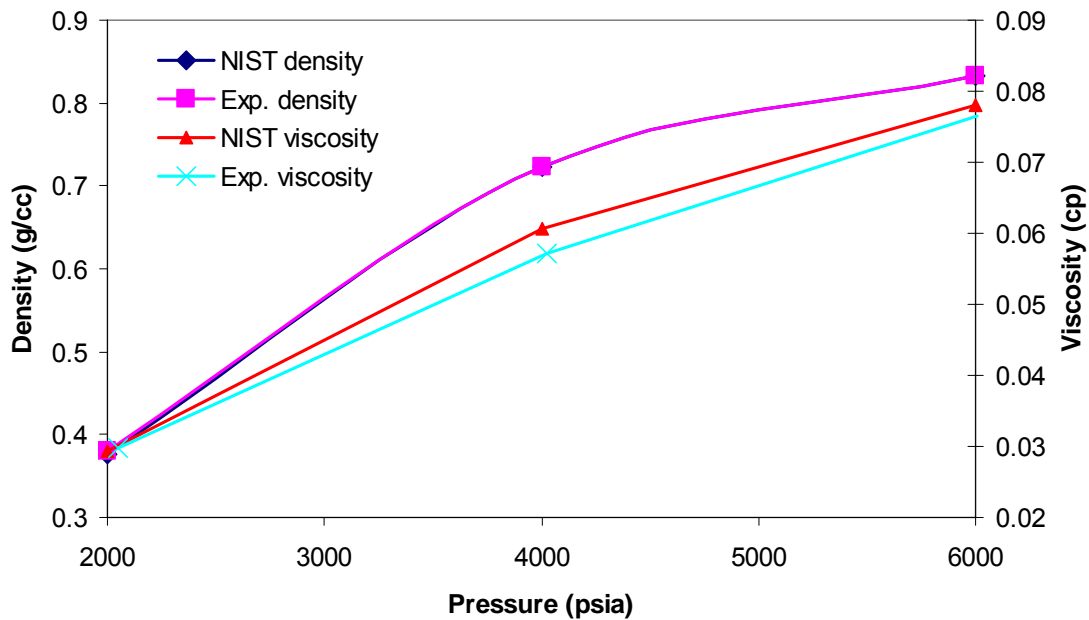
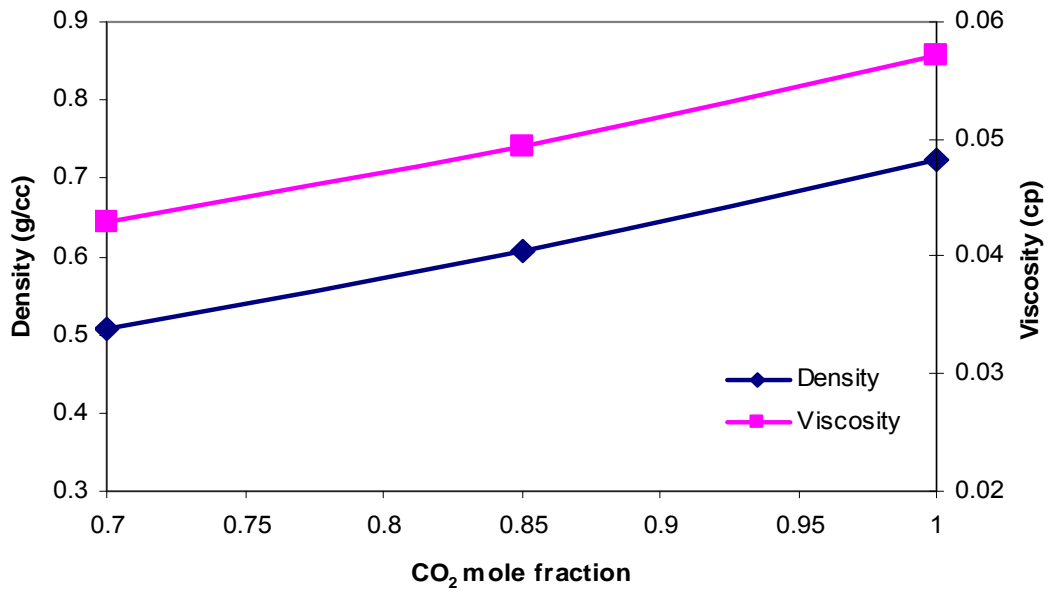


Figure 56. Densities for pure nitrogen at 80°F measured in the lab and from the NIST data base



Note: The agreement is excellent for densities, while the maximum error in viscosities is about 6% at a pressure of 4000 psia.

Figure 57. Comparison of NIST viscosities and densities to measured experimental data for pure CO₂ at 175°F.



Note: The viscosity measurements are made at slightly different pressures than 4000 psia as noted above.
 Figure 58. Change in density and viscosity with composition at 175oF and 4000 psia

VI-2. Synthetic Gas Mix Density and Viscosity Test Report (Schlumberger)

This is a modified version of the final report by Schlumberger untitled “Synthetic Gas Mix Density and Viscosity Test Report” prepared by: S. George Mathews, Schlumberger, Houston, TX, June 7, 2010, Report# 200900184

Standard Conditions Used: Pressure: 14.696 psia; Temperature: 60°F

Objective: The objective of the study was to prepare synthetic gas per compositions supplied and measure density and viscosity at specified conditions.

Introduction: Two gas mixtures containing a majority of Carbon Dioxide (CO₂) with various mixes of Nitrogen (N₂), Oxygen (O₂) and Argon (Ar) making up the remainder components were prepared. Following additional discussions, the procedures were finalized and tests conducted.

Scope of Work: The following steps were taken:

1. The instruments were sent for fresh calibration per client request.
2. The samples were conditioned to collect uniform sub-samples for further testing.
3. The calibrations of the instruments were tested using pure CO₂.
4. The synthetic gas 1 density and viscosity were measured.
5. The synthetic gas 2 density and viscosity were measured.

Results: The results are summarized in the following tables.

Fluids Preparation and Analysis: The samples for testing were synthetically prepared per compositions supplied by client. Ultrahigh Purity Nitrogen and Heptane were used for calibrations of the densitometer. Ultra High Purity CO₂ was used for testing the calibration of the viscometer. Details of the samples are given below. A comparison of the requested and final prepared fluid is also presented below.

Density Measurements: All measurements were performed using an Anton Parr Densitometer Model DMA HPM in conjunction with an MPDS 20000 unit. Calibration runs were performed for each measurement sequence using two fluids which is expected to cover the range in which the estimated fluid densities are expected to lie in. This allows for tight tolerances for error bars. It is not known if the instrument is expected to exhibit memory effects in subsequent measurements. To eliminate memory effects on subsequent measurements, each measurement was conducted independently allowing for instrument stabilization after each measurement point. It should be noted that although the resolution and repeatability of the instrument itself is to 0.00001 g/cc, the accuracy of measurement in this instrument is to 0.0001 g/cc. This report therefore reports density to 4 significant digits.

Viscosity Measurements: All measurements were performed using Cambridge Electromagnetic Viscometer model # SPL 440. The instrument designated for use along with the gas piston was sent back to manufacturer for fresh calibrations. A verification of calibration was performed with pure CO₂ at the pressures and temperatures of the test matrix. Subsequently measurements were performed using the test fluids. Each test measurement point was measured with an independent charge using fresh fluid. Following fluid charge, the pressure was allowed to auto stabilize to prevent any impulse effects of the any pressure adjustment on the fluid phase systems and also on the drag force that is maintained on the gas piston. This allows achievement of excellent instrument accuracy and stability which are required for gas viscosity measurements. It should be noted that the instrument accuracy is $\pm 1\%$ of full scale. The gas viscosity piston full scale is 0.02

– 0.2 cP. Hence the gas viscosity accuracy is expected to be ± 0.0018 . The reported numbers are to maximum resolution possible as previously arranged with client.

Table 1: Samples Planned for Test

Sample ID	CO2	N2	O2	Ar
	Mole%	Mole%	Mole%	Mole%
Synthetic Gas 1	85	5	5	5
Synthetic Gas 2	70	10	10	10

Table 2: Comparison of Fluid Requested – Synthetic gas 1

Component	Requested	Actual
	Mole%	Mole%
CO2	85	85.00
N2	5	4.98
O2	5	5.01
Ar	5	5.01

Table 3: Comparison of Fluid Requested – Synthetic gas 2

Component	Requested	Actual
	Mole%	Mole%
CO2	70	70.00
N2	10	10.01
O2	10	10.00
Ar	10	9.99

Table 4: Density Run with Pure N2 for Calibration at 80°F
(Pure N2)

Pressure (psia)	Density (g/cc)
2000	0.3682
4000	0.2769
6000	0.1522

Table 5: Density Run with Pure Heptane for Calibration at Multiple Temperatures
(Pure Heptane)

Pressure (psia)	Temperature (°F)	Density (g/cc)
2000	80	0.6893
2000	120	0.6735
2000	140	0.6647
4000	80	0.7000
4000	120	0.6856
4000	140	0.6772
6000	80	0.7099
6000	120	0.6965
6000	140	0.6890

Table 6: Viscosity Run with Pure CO2 for Calibration Check
(Pure CO2)

Temperature (°F)	Pressure (psia)	Measured Viscosity (cP)
140	2070	0.0408
175	2049	0.0297
	4022	0.0571
	6009	0.0766
210	6014	0.0703

Table 7: Density Run with Synthetic Gas 1

(Syn Gas 1)

Temperature (°F)	Pressure (psia)	Measured Density (g/cc)
		(g/cc)
140	2000	0.3635
175	2000	0.2921
	4000	0.6079
	6000	0.7453
210	6000	0.6847

Table 8: Viscosity Run with Synthetic Gas 1

(Syn Gas 1)

Temperature (°F)	Pressure (psia)	Measured Viscosity (cP)
		(g/cc)
140	2017	0.0298
175	2025	0.0283
	4014	0.0493
	6019	0.0691
210	6021	0.0632

Table 9: Density Run with Synthetic Gas 2

(Syn Gas 2)

Temperature (°F)	Pressure (psia)	Measured Density (g/cc)
		(g/cc)
140	2000	0.2848
175	2000	0.2489
	4000	0.5071
	6000	0.6591
210	6000	0.6075

Table 10: Viscosity Run with Synthetic Gas 2

(Syn Gas 2)

Temperature (°F)	Pressure (psia)	Measured Viscosity (cP)
		(g/cc)
140	2036	0.0309
175	2018	0.0262
	4017	0.0429
	6024	0.0616
210	6018	0.0555

VI-3. Peng-Robinson EOS model for the estimation of the solubility of flue gas components in brine under a range of P, T, S conditions

This section was initially prepared by Hariharan Ramachandran, graduate student in the Department of Petroleum and Geosystems Engineering, under the direction of Dr. Pope. It was subsequently slightly modified by J.-P. Nicot.

Introduction

In order to understand the storage and trapping mechanism, an appropriately tuned equation of state (EOS) must be used to predict the phase behavior of injected gas-formation water interactions. Li and Yan (2009) evaluated seven different cubic equations of states for predicting vapor-liquid equilibrium (VLE) of binary mixtures with CO₂ and CH₄/H₂S/SO₂/Ar/N₂/O₂. They concluded that for calculations on the volume properties of binary CO₂ mixtures, PR (Peng-Robinson) and PT (Patel-Teja) are superior to others for all of the studied mixtures. They also concluded that the binary interaction parameter has a clear impact on the calculating accuracy of an EOS in the volume calculations of CO₂ mixtures. This study attempts to modify and tune an existing equation of state (Peng-Robinson Equation of State (PREOS)) to predict the phase behavior of flue gas in deep saline aquifers.

A CO₂-dominated flue gas from an oxycombustion process is used as the feed for this study. Its composition is shown in Table 31. This is one of the possible mixture compositions for flue gas. This flue gas composition is going to be set as base case composition for our study.

Table 31. Assumed flue gas composition

Component Name	Vol. percent
N ₂	15
CO ₂	68.85
O ₂	5
CO	2
H ₂	4
SO _x	0.15
Ar	5

The solubility of one substance in another is determined by the balance of the intermolecular forces between them. Binary Interaction Coefficients (BICs) are used to represent these intermolecular forces in cubic equations of state.

There is not enough experimental data on the solubility of flue gas in pure water or brine although there is data available for independent binaries with water or brine from the available literature. Therefore, we have decided to tune the BICs for each component of flue gas as binary mixture with water or brine and combining them in the end. As a first step we have taken CO₂ binary with pure water and brine and tuned the BICs to match the experimental data.

CO₂ Solubility in brine

Duan and Sun (2002) developed a thermodynamic model to predict the solubility of CO₂ in pure water and brine for a wide temperature and pressure range. Their model predictions were very close to experimental data and had a maximum deviation of 7% from experimental data. The

sources for experimental data used in their analysis are reported in their paper. They have built a database of CO₂ solubility for a wide range of salinity, temperature and pressure from their model and published it in their paper. We have used this data to tune the BICs in the Peng-Robinson EOS following the methodology of Kumar (2004). Some of the results are shown in Figure 59 and Figure 60.

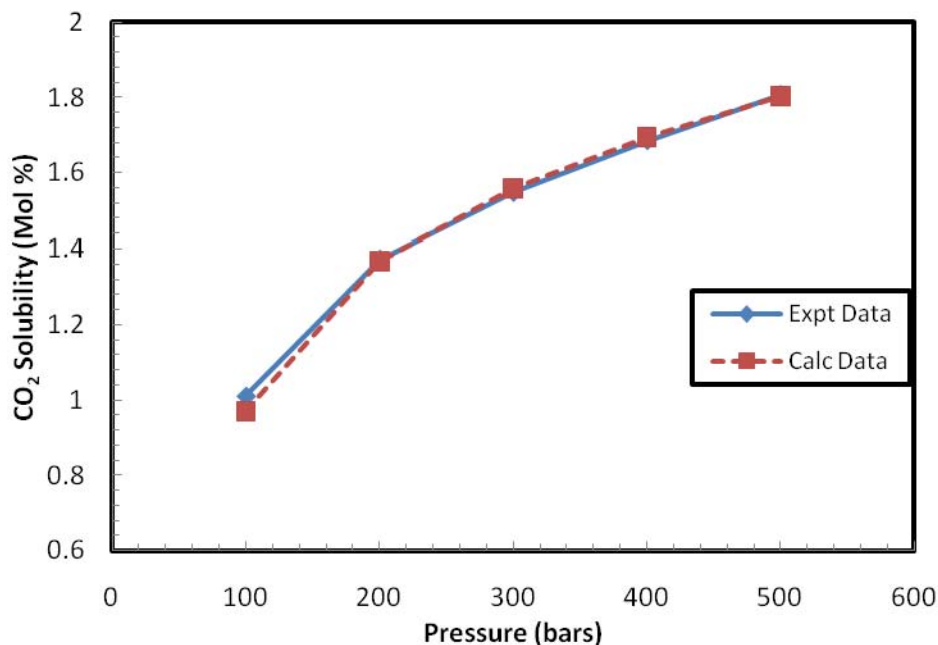


Figure 59. Match between experimental and calculated data a T = 194°F and S = 34750 ppm

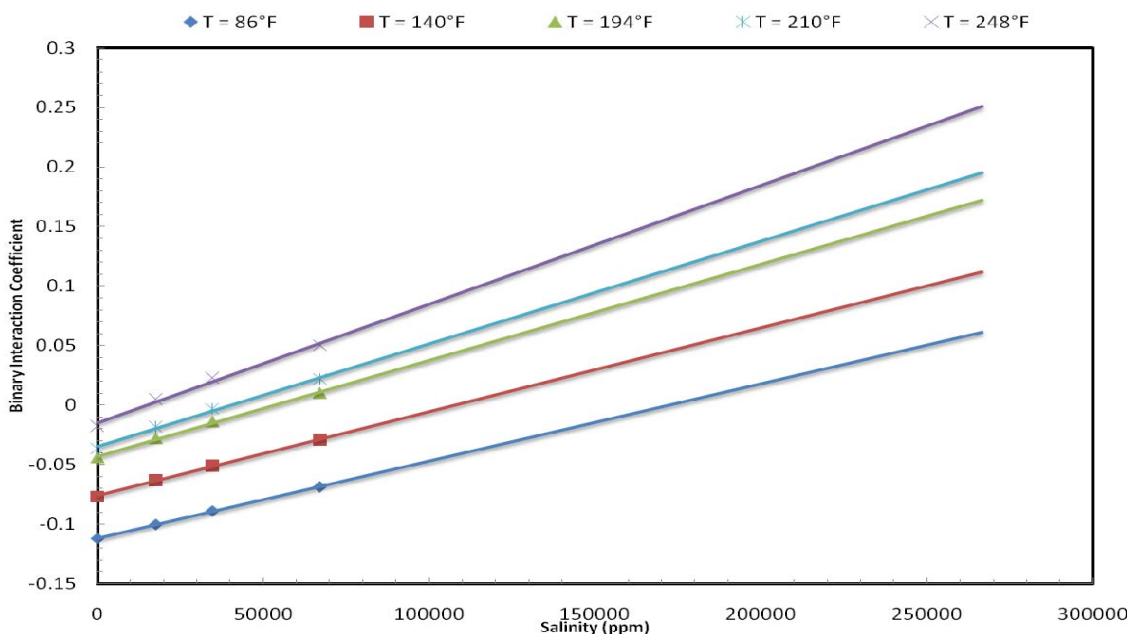


Figure 60. Variation of BICs for H₂O-CO₂ pair with salinity

Figure 60 shows the match between the Duan and Sun (2003) values with the calculated value obtained by tuning the BICs. Figure 61 shows the variation of BICs with salinity.

Gehrig (1980) reported a very interesting observation regarding the variation of CO₂ solubility with respect to temperature. At high pressures, CO₂ solubility decreases with increase in temperature till a point and again starts increasing. In order to investigate this, we tuned the BICs for a system with high temperature (248°F) and observed that the BICs vary differently compared to other lower temperatures. Figure 61 shows the variation of CO₂ solubility with temperature for different pressures for pure water.

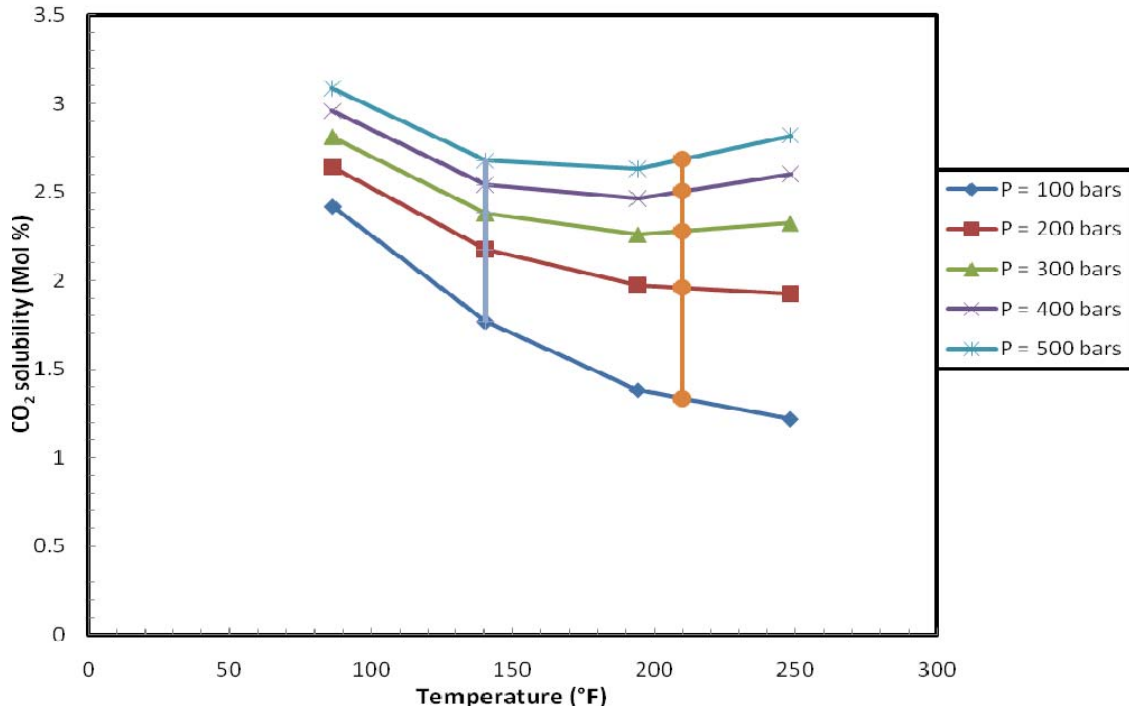


Figure 61. Variation of CO₂ solubility with temperature for different pressures for pure water

The final correlation equation relating the binary interaction parameter to salinity (in ppm) and temperature (in °F) is given as

$$BIC = -0.1720306 + 0.0006667 \times T + 8.287991 \times 10^{-7} \times S$$

N₂ Solubility in brine

Duan and Mao (2006) have developed a thermodynamic model to predict the solubility of N₂ in pure water and brine for a wide temperature and pressure range. Their model predictions were very close to experimental data and had deviations within experimental uncertainty. The sources for experimental data used in their analysis are reported in their paper. They had built a database of N₂ solubility for a wide range of salinity, temperature and pressure from their model and published it in their paper. We have used this data to tune the BICs by following the methodology of Kumar (2004). Figure 62 shows the match between Duan and Mao's (2006) values with our calculated value obtained by tuning the BICs. Figure 63 shows the variation of BICs with salinity.

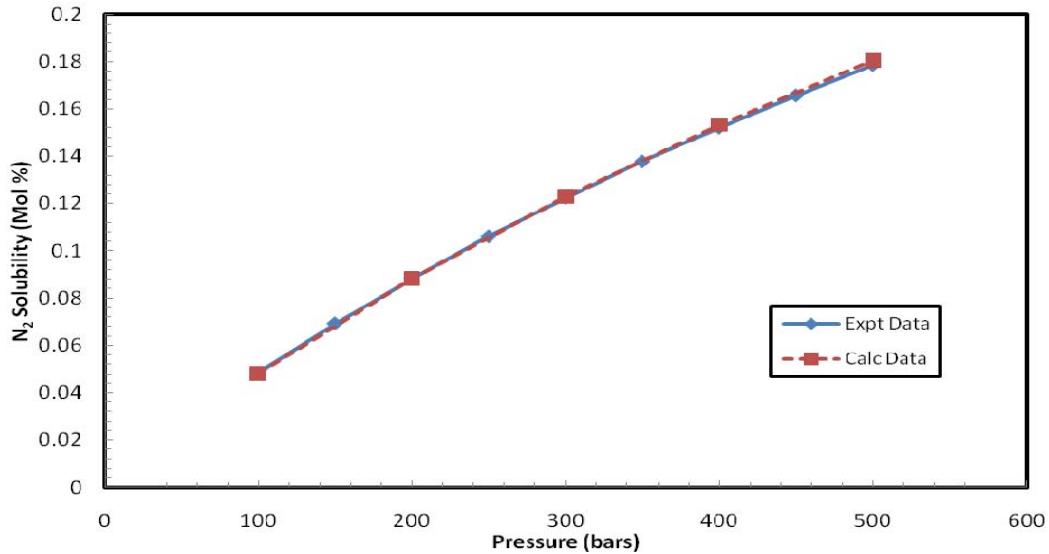


Figure 62. Match between experimental and calculated data at $T = 194^{\circ}\text{F}$ and $S = 34,750$ ppm

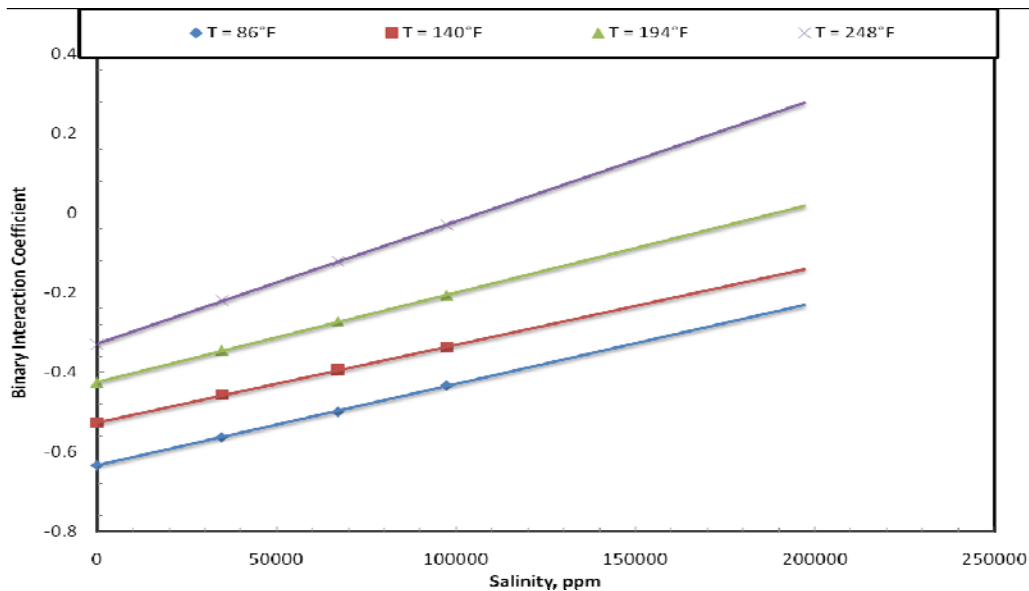


Figure 63. Variation of BICs for H₂O-N₂ pair with salinity

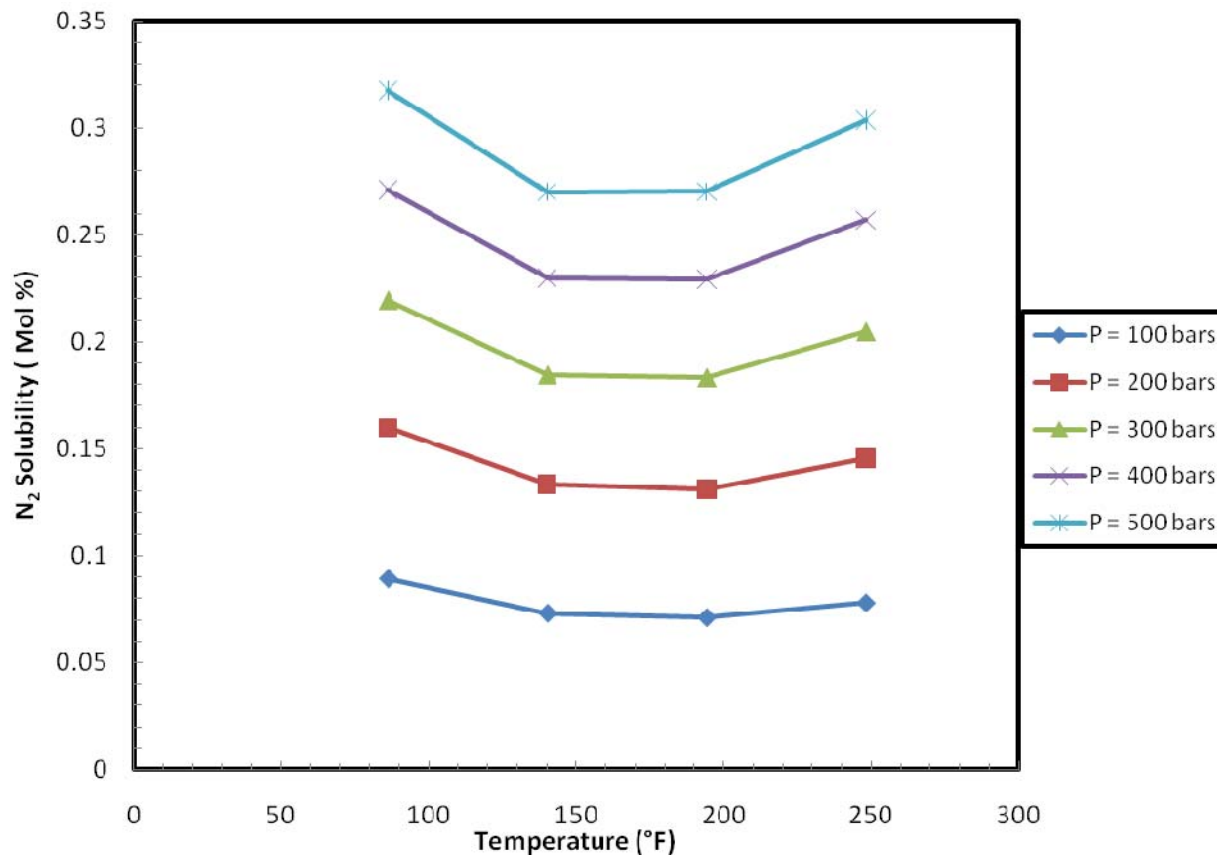


Figure 64. Variation of N₂ solubility with temperature for different pressures for pure water

The final correlation relating the binary interaction parameter to salinity (in ppm) and temperature (in °F) is given as

$$BIC = -0.8143386 + 0.002031 \times T + 2.1235958 \times 10^{-6} \times S$$

O₂ Solubility in brine

Geng and Duan (2010) developed a thermodynamic model to predict the solubility of O₂ in pure water and brine for a wide temperature and pressure range. Their model predictions were very close to experimental data and had deviations within experimental uncertainty. The sources for experimental data used in their analysis are reported in their paper. They had built a database of O₂ solubility for a wide range of salinity, temperature and pressure from their model and published it in their paper. We have used this data to tune the BICs by following the methodology of Kumar (2004). Figure 65 shows the match between Geng and Duan's (2006) values with the calculated values obtained by tuning the BICs. Figure 66 shows the variation of BICs with salinity.

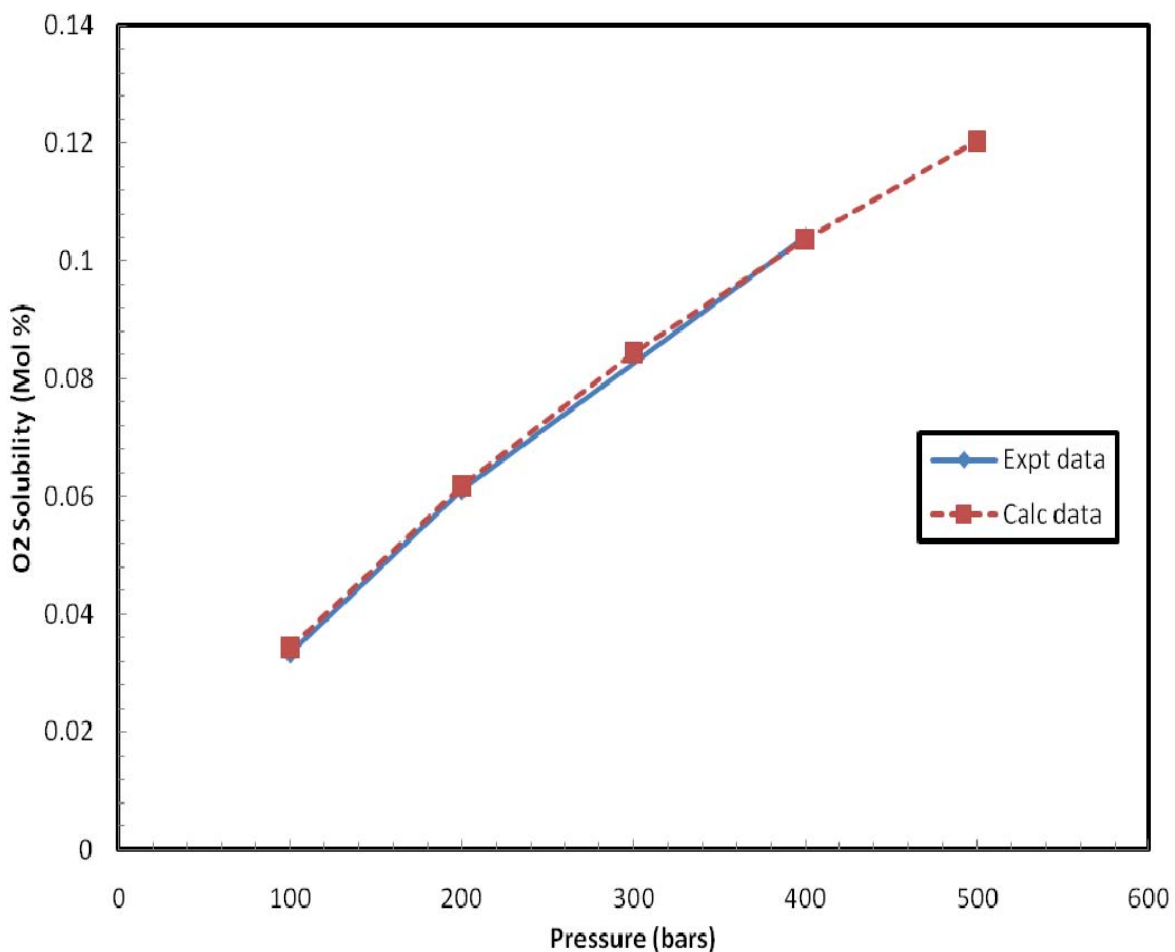


Figure 65. Match between experimental and calculated O₂ solubility data at T = 194°F and S = 67,216 ppm

The final correlation relating the binary interaction parameter to salinity (in ppm) and temperature (in °F) is given as:

$$BIC = -0.4891455 + 0.0021875 \times T + 3.3794839 \times 10^{-6} \times S$$

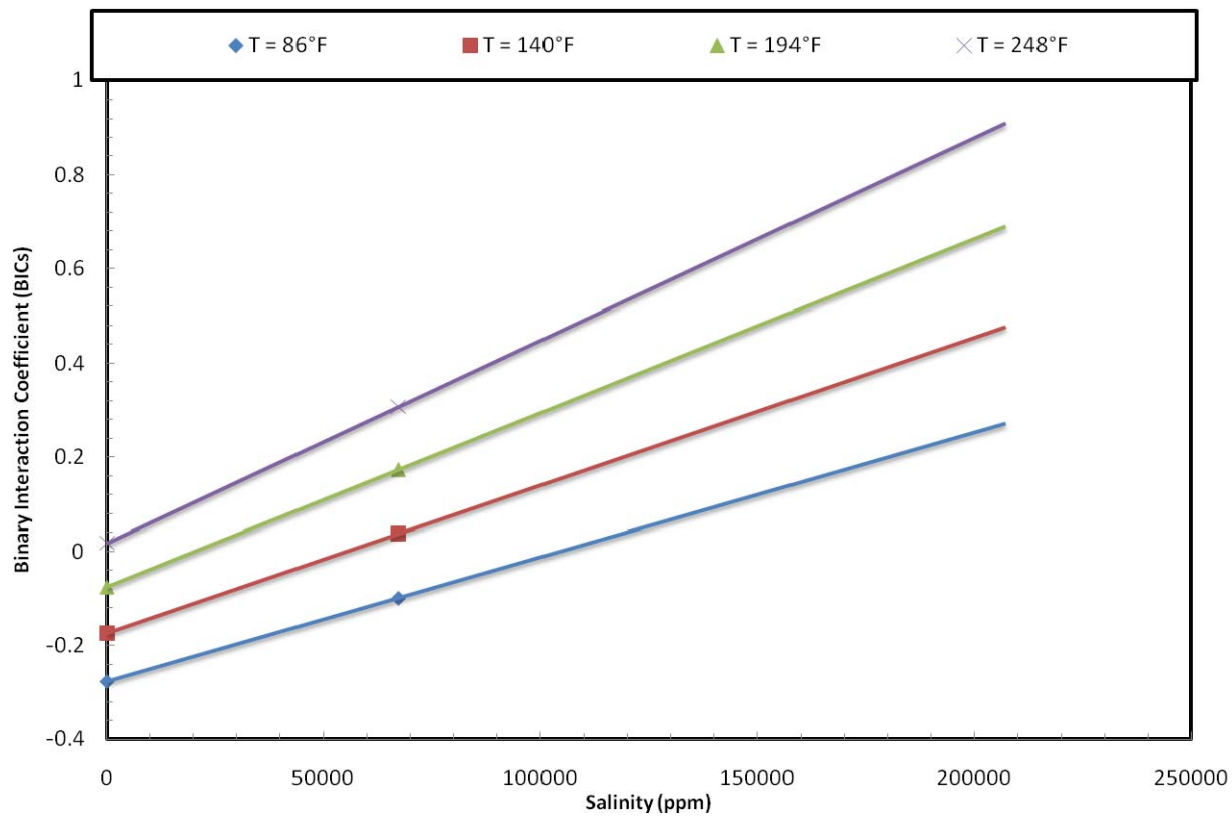


Figure 66. Variation H₂O-O₂ BICs with salinity

Argon Solubility in brine

Sisskind (2010) have done some experiments for very high pressure for Ar solubility in pure water. The plot for the above comparison is shown in Figure 67. Murray and Riley (1970) have done some solubility tests for Ar in distilled water and seawater. We have used this data and built a BIC correlation with salinity as shown in Figure 68. We have used this data to tune the BICs by following the methodology of Kumar (2004). Some of the results are shown in Figure 67 and Figure 68.

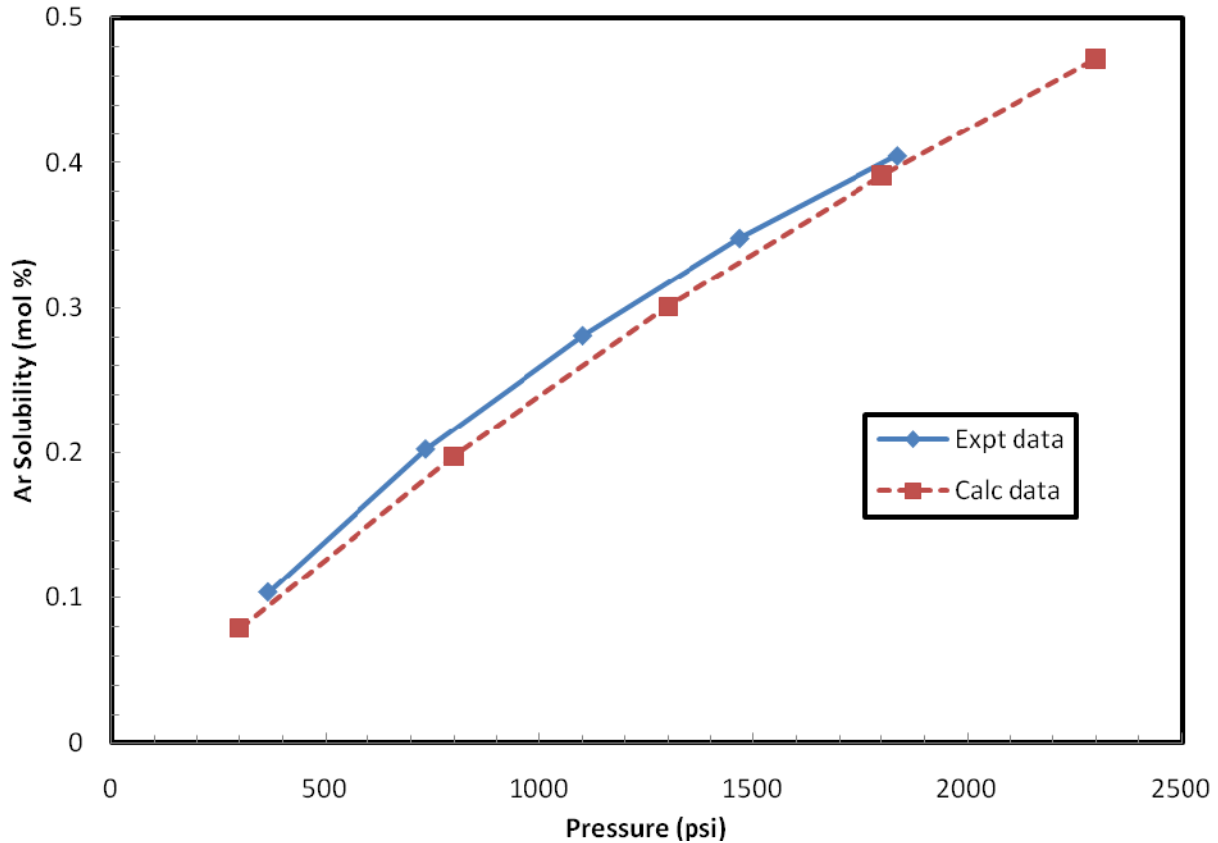


Figure 67. Match between experimental and calculated Ar solubility data a $T = 32.36^{\circ}\text{F}$ and $S = 34,750$ ppm

The final correlation equation relating the binary interaction parameter to salinity (in ppm) and temperature (in $^{\circ}\text{F}$) is given as

$$BIC = -0.5745674 + 0.0029551 \times T + 3.0384615 \times 10^{-6} \times S$$

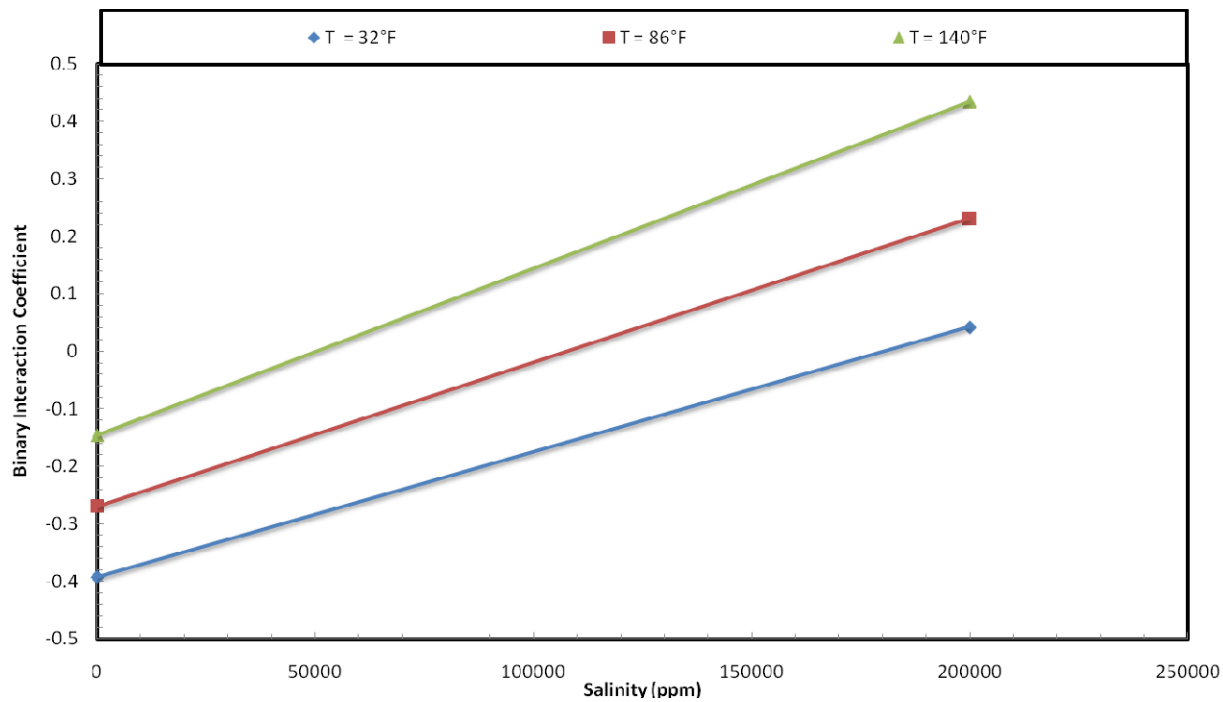


Figure 68. Variation of BICs for H₂O-Ar pair with salinity

Other CO₂ Binary Coefficients

Table 32. BICs for other CO₂ related mixtures from literature

Name	BICs
CO ₂ -Ar	0.163
CO ₂ -O ₂	0.114
CO ₂ -N ₂	-0.007

The binary interaction parameters for other CO₂ related mixtures are shown in Table 32. These values were compiled from Li and Yan (2009). They had built a database for these binaries and published it in their paper.

Flue gas mixture test

A flue gas mixture of composition shown in Table 33 was analyzed for solubility with pure water at 140 F using the BICs established from previous study.

Table 33. Gas mixture used for testing

Name	Mol %
N ₂	15
CO ₂	75
Ar	5
O ₂	5

The binary interaction parameters used are shown in Table 34. BICs for components other than water were taken from Li and Yan (2009).

Table 34. Binary interaction coefficients used for the above mixture at 140°F

BICs	N ₂	CO ₂	H ₂ O	Ar	O ₂
N ₂	0	-0.017	-0.5271	0	0
CO ₂	-0.017	0	-0.0767	0.002	0.002
H ₂ O	-0.5271	-0.0767	0	-0.1456	-0.1741
Ar	0	0.002	-0.1456	0	0
O ₂	0	0.002	-0.1741	0	0

A plot showing the solubility of the above gas mixture in water is shown in Figure 69 and Figure 70.

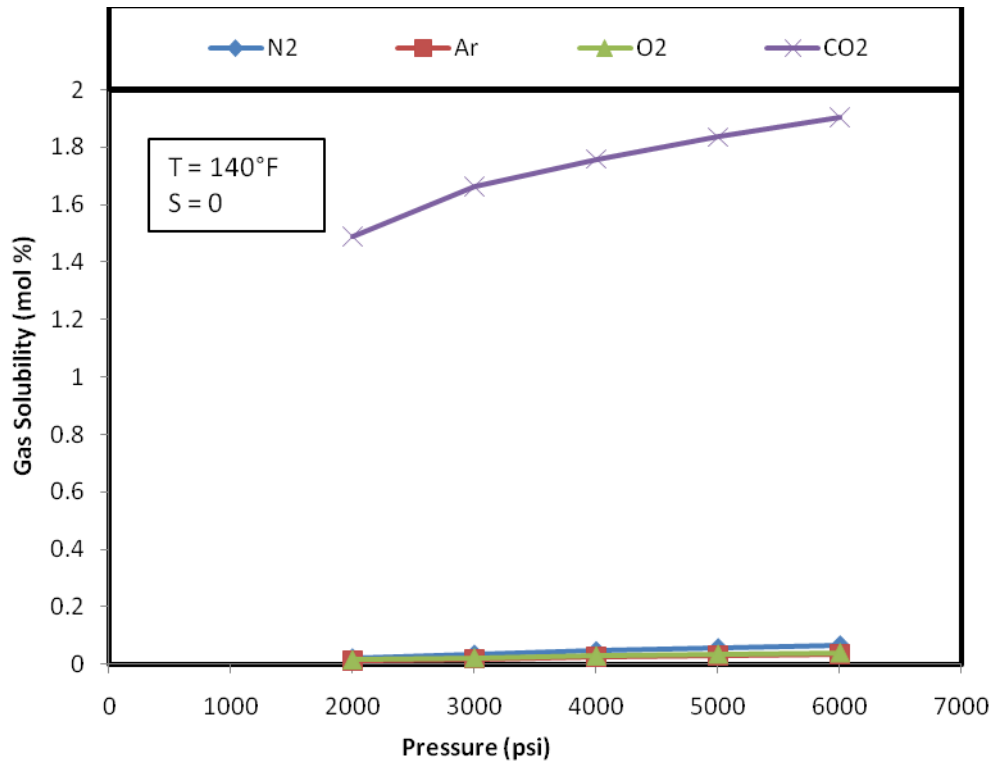


Figure 69. Solubility of gas mixtures in water

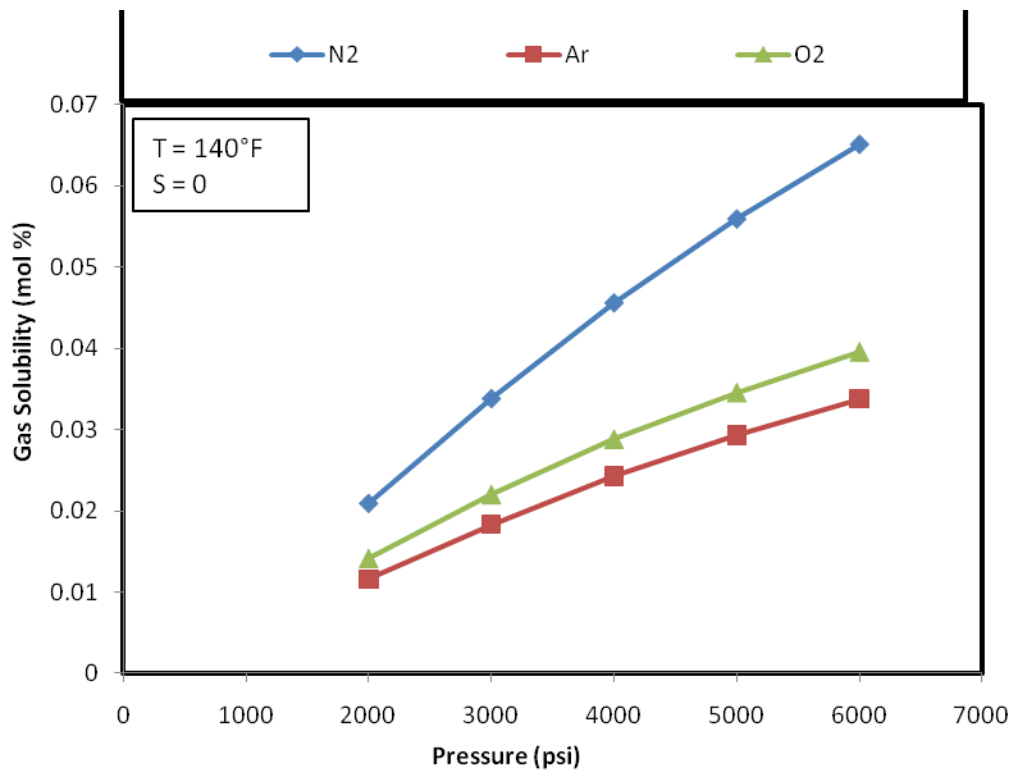


Figure 70. Solubility of gas mixtures in water (blow up of Figure 69)

The binary interaction coefficients used are shown in Table 35 for the gas mixture in brine of salinity of 100,000 ppm and temperature of 140°F.

Table 35. Binary interaction coefficients used for the gas mixture at 140°F

	H ₂ O	N ₂	Ar	O ₂	CO ₂
H ₂ O	0				
N ₂	-0.3176	0			
Ar	0.1429	0	0		
O ₂	0.1550	0	0	0	
CO ₂	0.0042	-0.007	0.163	0.114	0

A plot showing the solubility of the gas mixture is shown in Figure 71 and Figure 72.

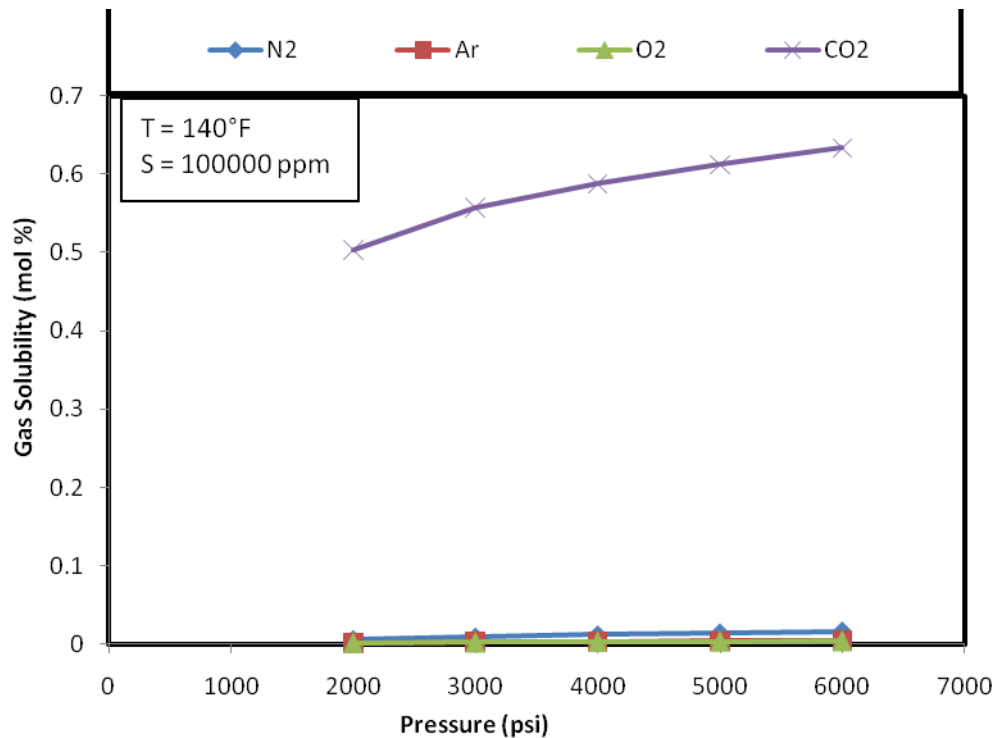


Figure 71. Solubility of gas mixture in 100,000 ppm brine

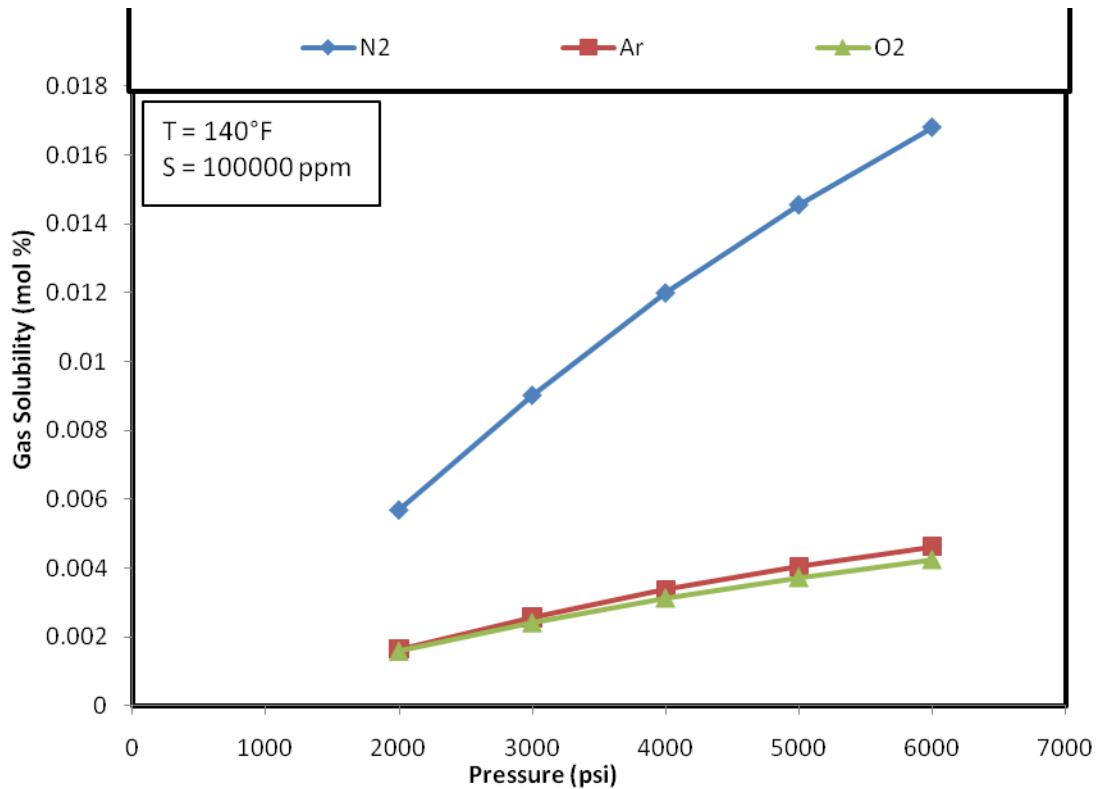


Figure 72. Blow up of Figure 71

The binary interaction coefficients used are shown in Table 36 for the gas mixture in brine of salinity of 200,000 ppm and temperature of 140°F.

Table 36. Binary interaction coefficients used for the gas mixture at 140°F

	H₂O	N₂	Ar	O₂	CO₂
H₂O	0				
N₂	-0.1053	0			
Ar	0.4468	0	0		
O₂	0.493	0	0	0	
CO₂	0.0870	-0.007	0.163	0.114	0

A plot showing the solubility of the gas mixture is shown in Figure 73 and Figure 74.

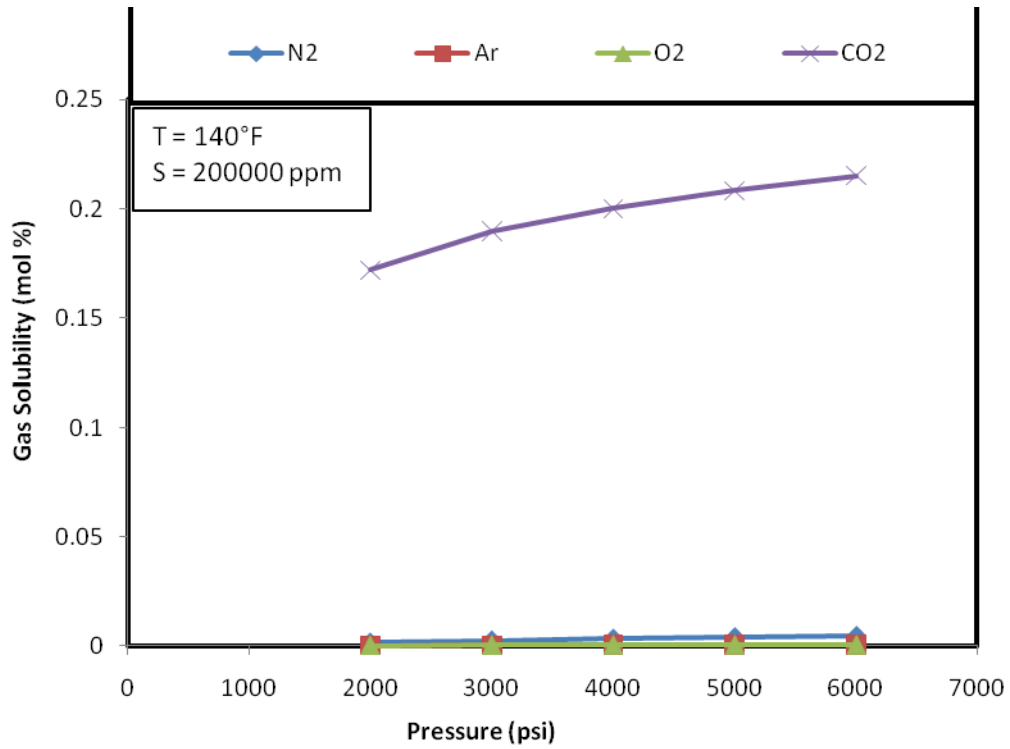


Figure 73. Solubility of gas mixture in 200,000 ppm brine

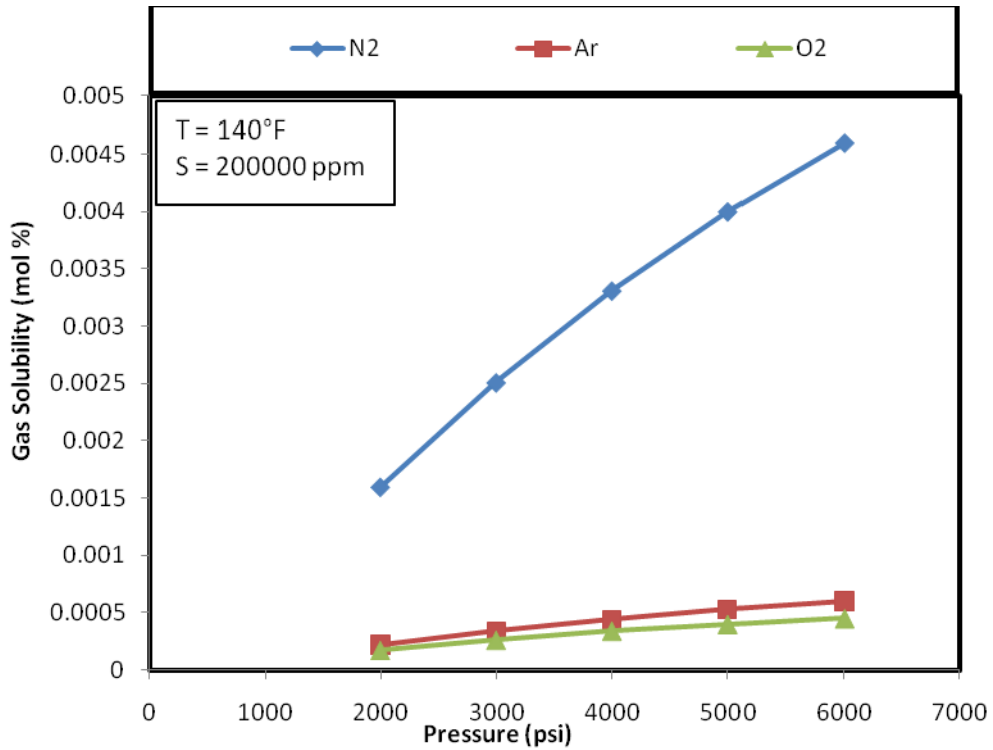


Figure 74. Blowup of Figure 73

The binary interaction coefficients used are shown in Table 37 for the gas mixture in pure water.

Table 37. Binary interaction coefficients used for the gas mixture at 210°F

	H ₂ O	N ₂	Ar	O ₂	CO ₂
H ₂ O	0				
N ₂	-0.3878	0			
Ar	0.046	0	0		
O ₂	-0.0297	0	0	0	
CO ₂	-0.0320	-0.007	0.163	0.114	0

A plot showing the solubility of the gas mixture in pure water is shown in Figure 75 and Figure 76.

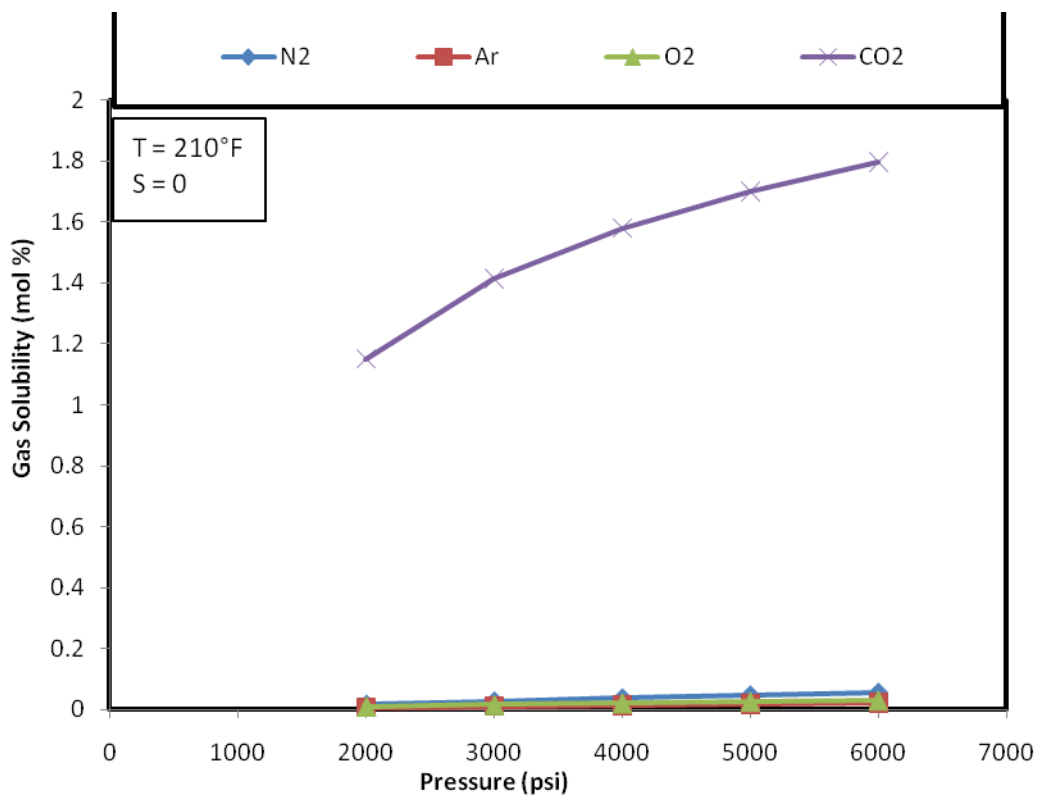


Figure 75. Solubility of gas mixture in pure water

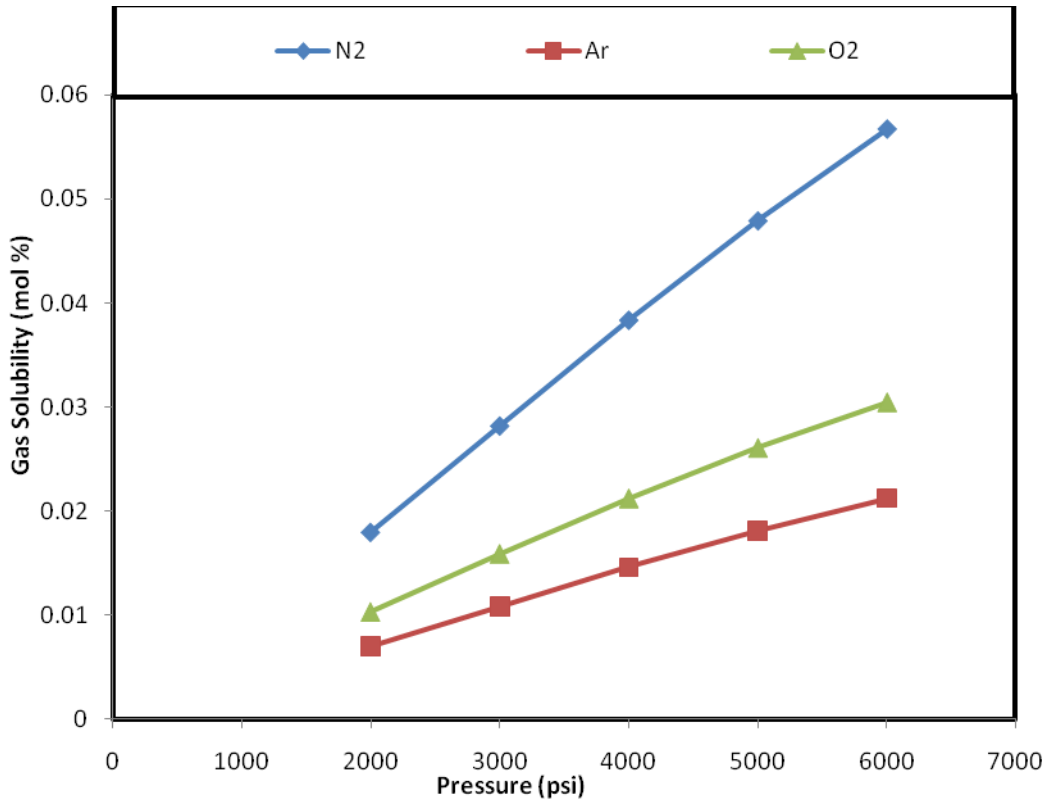


Figure 76. Blowup of Figure 75

The binary interaction coefficients used are shown in Table 38 for the gas mixture in brine of salinity of 100,000 ppm and temperature of 210°F.

Table 38. Binary interaction coefficients used for the gas mixture at 210°F

	H ₂ O	N ₂	Ar	O ₂	CO ₂
H ₂ O	0				
N ₂	-0.1755	0			
Ar	0.3498	0	0		
O ₂	0.3082	0	0	0	
CO ₂	0.0508	-0.007	0.163	0.114	0

A plot showing the solubility of the gas mixture is shown in Figure 77 and Figure 78.

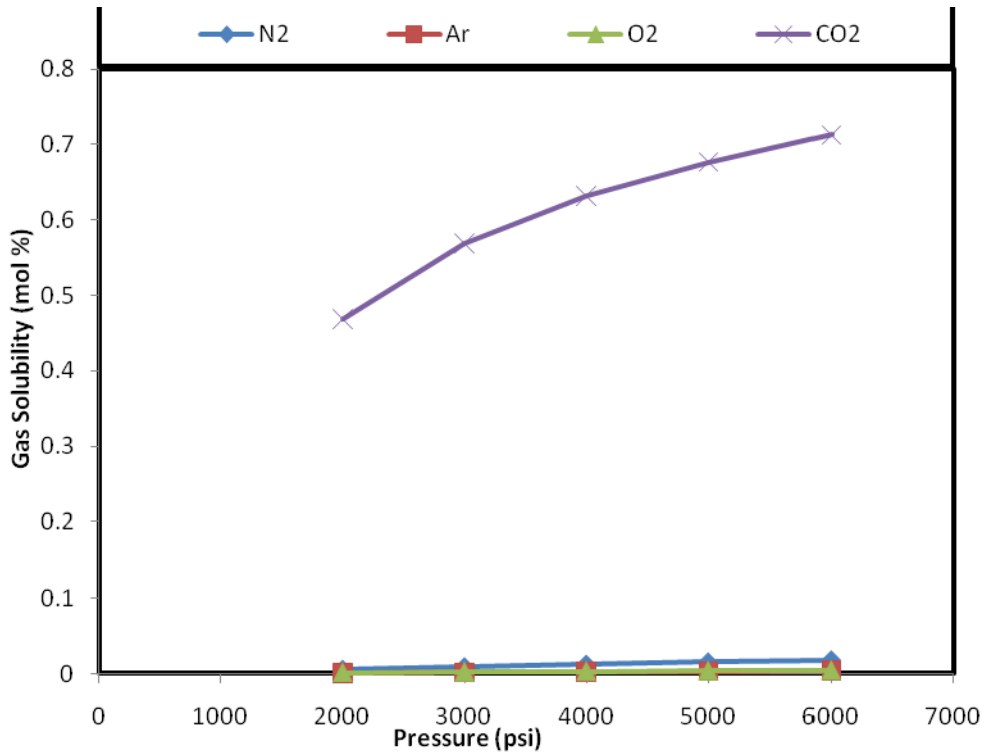


Figure 77. Solubility of gas mixture in 100,000 ppm brine

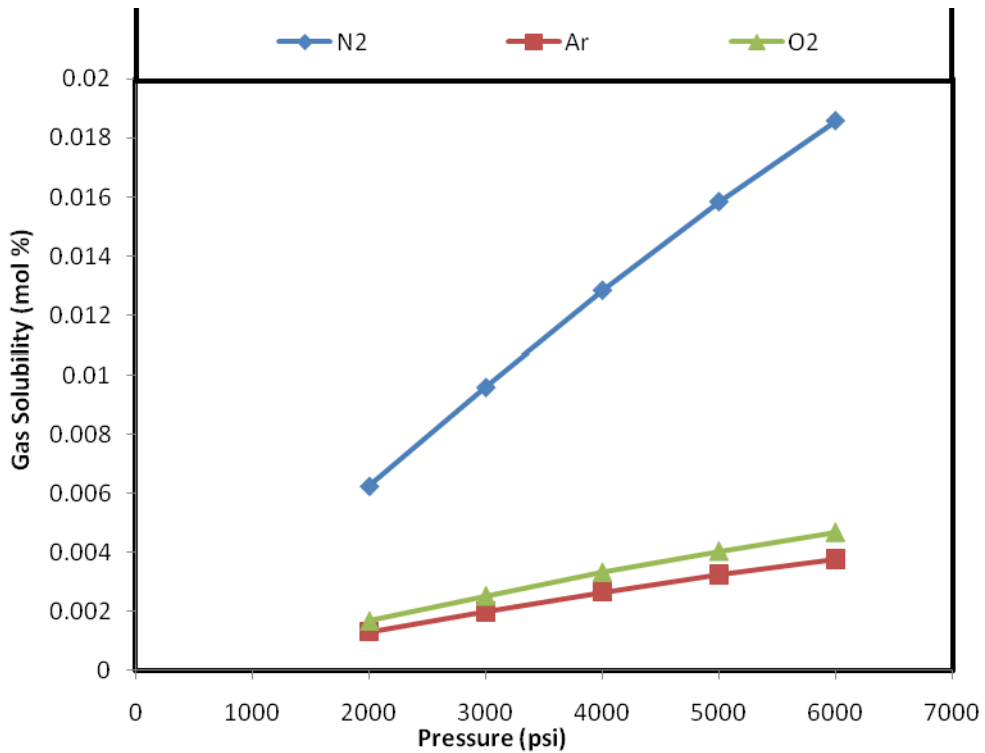


Figure 78. Blowup of Figure 77

The binary interaction coefficients used are shown in Table 39 for the gas mixture in water with salinity of 200,000 ppm and temperature of 210°F.

Table 39. Binary interaction coefficients used for the gas mixture at 210°F

	H ₂ O	N ₂	Ar	O ₂	CO ₂
H ₂ O	0				
N ₂	0.0369	0			
Ar	0.6537	0	0		
O ₂	0.6461	0	0	0	
CO ₂	0.1337	-0.007	0.163	0.114	0

A plot showing the solubility of the gas mixture is shown in Figure 79 and Figure 80.

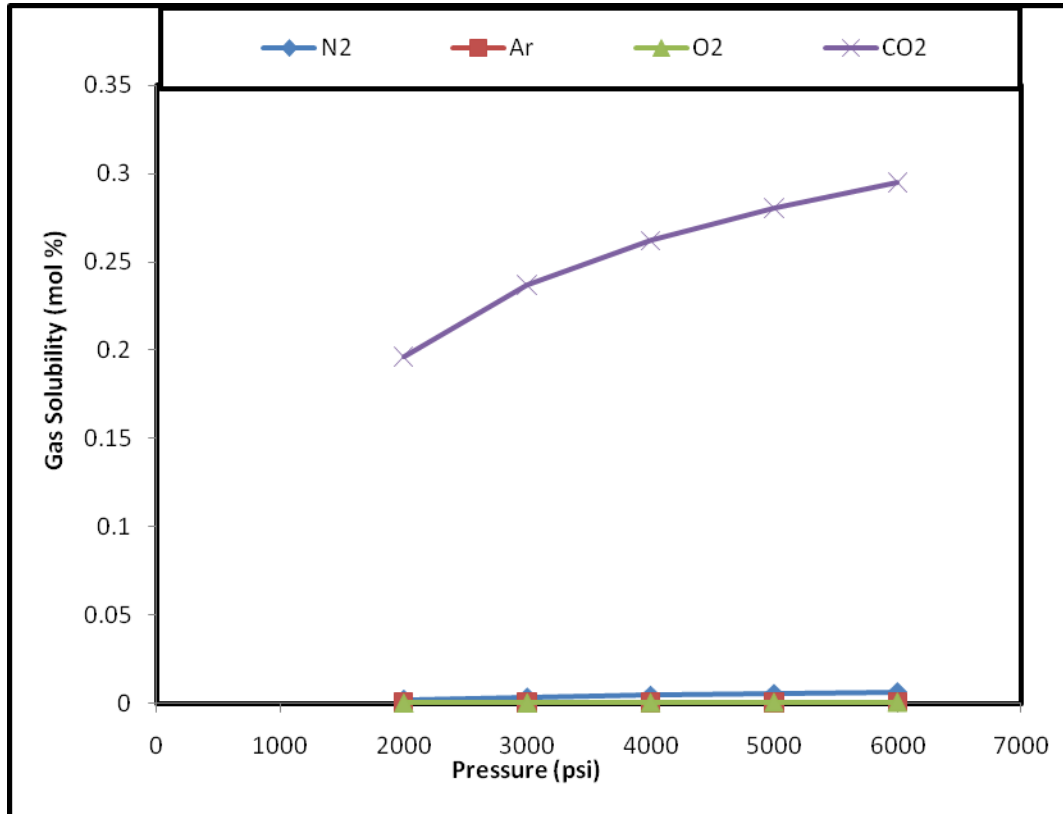


Figure 79. Solubility of gas mixture in 200,000 ppm brine

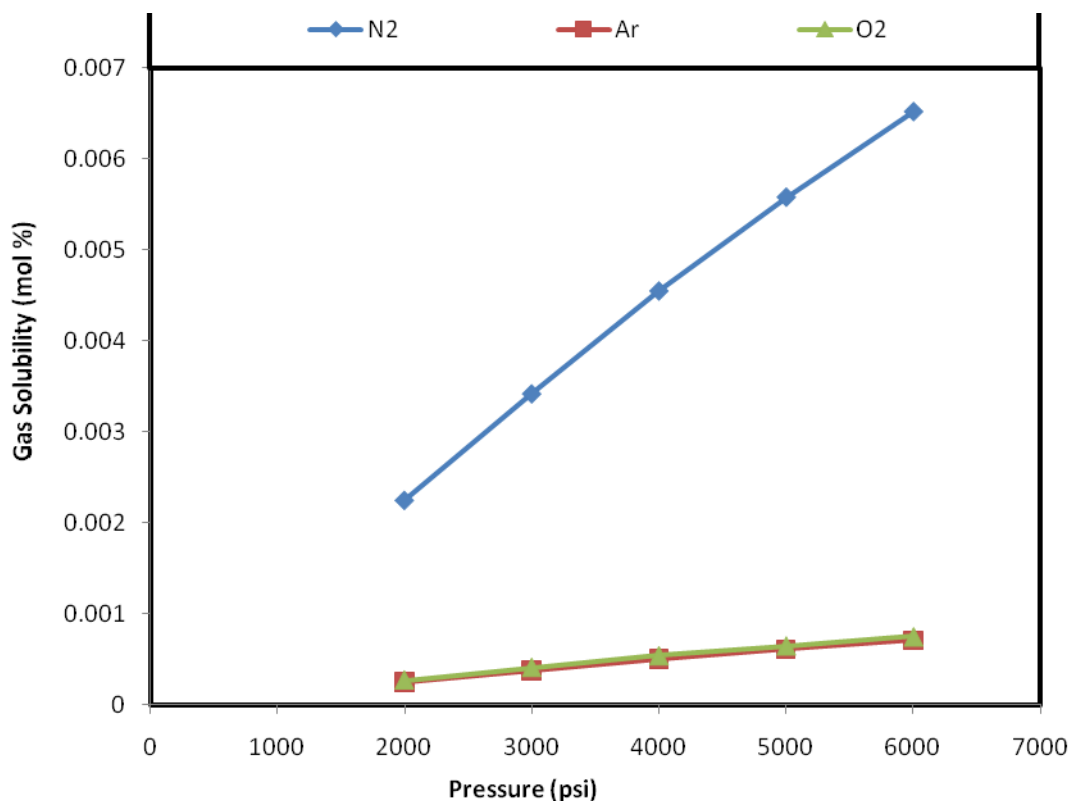


Figure 80. Blowup of Figure 79

References

Duan, Zhenhao, and Sun, Rui., 2003, An improved model calculating CO₂ solubility in pure water and aqueous NaCl solutions from 273 to 533 K and from 0 to 2000 bar, *Chemical Geology*, 193, 257-271

Duan, Zhenhao, and Mao, Shide., 2006, A thermodynamic model for calculating nitrogen solubility, gas phase composition and density of the N₂-H₂O-NaCl system, *Fluid Phase Equilibria*, 248, 103-114

Gehrig, M., 1980, Phasengleichgewichte und pVT-daten ternärer Mischungen aus Wasser, Kohlendioxid und Natriumchlorid bis 3 kbar und 550 C, PhD thesis, Univ. Karlsruhe, Freiburg.

Geng, Ming, and Duan Zhenhao., 2010, Prediction of oxygen solubility in pure water and brines upto high temperatures and pressures, *Geochimica et Cosmochimica Acta* (2010), doi: 10.1016/j.gca.2010.06.034

Kumar, A., 2004, A simulation study of carbon sequestration in deep saline aquifers, MS thesis, The University of Texas at Austin.

Li, H., and Yan, J., 2009, Evaluating cubic equations of state (EOS) for calculation of vapor liquid equilibrium of CO₂ and CO₂ mixtures for CO₂ capture and storage processes, *Applied Energy*, Volume 86, Issue 6, 826:836

Murray, C.N. and Riley, J.P., 1970, The solubility of gases in distilled water and sea water III – Argon, *Deep Sea Research*, Vol. 17, 203-209.

Sisskind, B. Kasamowsky, I., *Z. Anorg. chem*, 1931, 200, 279

EOS Input File

Winprop input file used to generate GEM EOS model

```
**FILE NAME:  SCHLUMB FINAL.DAT
**FILENAMES *OUTPUT *SRFOUT *REGLUMPSPLIT *NONE *GEMOUT *NONE *STARSKV *NONE *GEMZDEPTH *NONE
**IMEXPVT *NONE
**WINPROP  '2008.10'

**=-=-=  TITLES/EOS/UNITS
**REM  Schlumberger Fluid (tuned final)
*TITLE1  "
*TITLE2  "
*TITLE3  'K. Ahmadi'
*UNIT  *FIELD
*INFEED  *MOLE
*MODEL  *PR  *1978

**=-=-=  COMPONENT SELECTION/PROPERTIES
**REM
*NC  7  7

*COMPNAME
'CO2' 'N2' 'O2' 'AR' 'H2'
'CO' 'SO2'
*HCFLAG
3 3 3 3 3
3 3
*PCRIT
72.8 33.5 49.8 48.1 12.958
34.532 77.809
*TCRIT
304.2 126.2 154.6 150.8 33.19
132.9 430.8
*AC
.225 .04 .021 -.004 -.216
.048 .245
*MW
44.01 28.014 31.999 39.948 2.016
28.01 64.065
*VSHIFT
0.0117011 -0.1759955 -0.1867915 -0.2008695 -0.3264287
-0.1715092 -0.0602268
*ZRA
.4664 11.68071 264171.623 102.17864 75140715.1
9.19057 .37512
*VCRIT
.1187 5.4949 1.5849 2.1907 4.9901
5.5762 .1735
*VISVC
.0943 .0899 .0737 .0749 .0649
.0943 .1217
*OMEGA
.45724 .45724 .45724 .45724 .45724
.45724 .45724
*OMEGB
.0778 .0778 .0778 .0778 .0778
.0778 .0778
*SG
.4927 .15852 .21827 .21066 .03013
.16876 .72343
*TB
-152.524 -321.951 -299.75 -303.01 -420.411
-314.939 -20.933
*PCHOR
126.49 77.36 89.7 114.12 1
77.35 186.5
*ENTHALPY
0.00000E+00 4.02638E-02 4.03953E-04 -5.13100E-08 0.00000E+00
0.00000E+00
```

```

0.00000E+00 5.45949E-01 -1.12950E-04 -5.13100E-08 0.00000E+00
0.00000E+00
0.00000E+00 3.39499E-01 2.61877E-04 -5.13100E-08 0.00000E+00
0.00000E+00
0.00000E+00 3.58842E-01 2.36354E-04 -5.13100E-08 0.00000E+00
0.00000E+00
0.00000E+00 2.69420E+00 -1.74254E-02 -5.13100E-08 0.00000E+00
0.00000E+00
0.00000E+00 5.06708E-01 -2.43057E-05 -5.13100E-08 0.00000E+00
0.00000E+00
0.00000E+00 -7.40900E-02 3.94234E-04 -6.14584E-08 0.00000E+00
0.00000E+00
*IDCOMP
-1 -1 -1 -1 -1
-1 -1
*VISCOR *HZYT
*MIXVC 1.0
*VISCOEFF
0.10999 0.01168 0.05573 -0.02847 0.00467

*HREFCOR *HARVEY

*PVC3 1.2
*BIN
0
0 0
0 0 0
0 0 0 0
0 0 0 0 0

0 0 0 0 0
0

**=== COMPOSITION
**REM
**NC 7 7
**COMPONENT ARRAY
*COMPOSITION *PRIMARY
30 20 10 10 10
10 10
**COMPONENT ARRAY
*COMPOSITION *SECOND
0.0000 0.0000 0.0000 0.0000 0.0000
0.0000 0.0000

**=== CMG GEM EOS MODEL_E
****REM To Gem
****NC 7 7

**=== SINGLE-PHASE CALCULATION
*SINGLE
*LABEL "
*FEED *MIXED 1.0
*PRES 2400
*TEMP 170

**=== END

```


VII. Appendix B: Properties of Pure Components and Gas Mixtures

For a better understanding of the behavior of the mixtures, this appendix describes the pure component properties (density, viscosity, and water solubility at different salinity levels) of CO₂, N₂, Ar, O₂, and CH₄ and same properties of two ternary systems: CO₂, N₂, and O₂, and CO₂, Ar, and O₂.

VII-1. Pure Component Properties

Instead of plotting properties independently as a function of temperature and pressure, they are plotted as a function of depth because in the subsurface in natural conditions pressure and temperature are strongly correlated. Average pressure and geothermal gradients of 0.465 psi/ft and 18°F/1000 ft, respectively, were used to perform the property calculations. The values correspond to the GC deep site. The GC shallow site has a slightly lower average geothermal gradient. However, the viscosity and density values obtained at Frio's depth differ from those previously calculated. In Figure 4, gradients were adjusted (0.43 psi/ft and 12°F/1000 ft) to match properties from the GC shallow site.

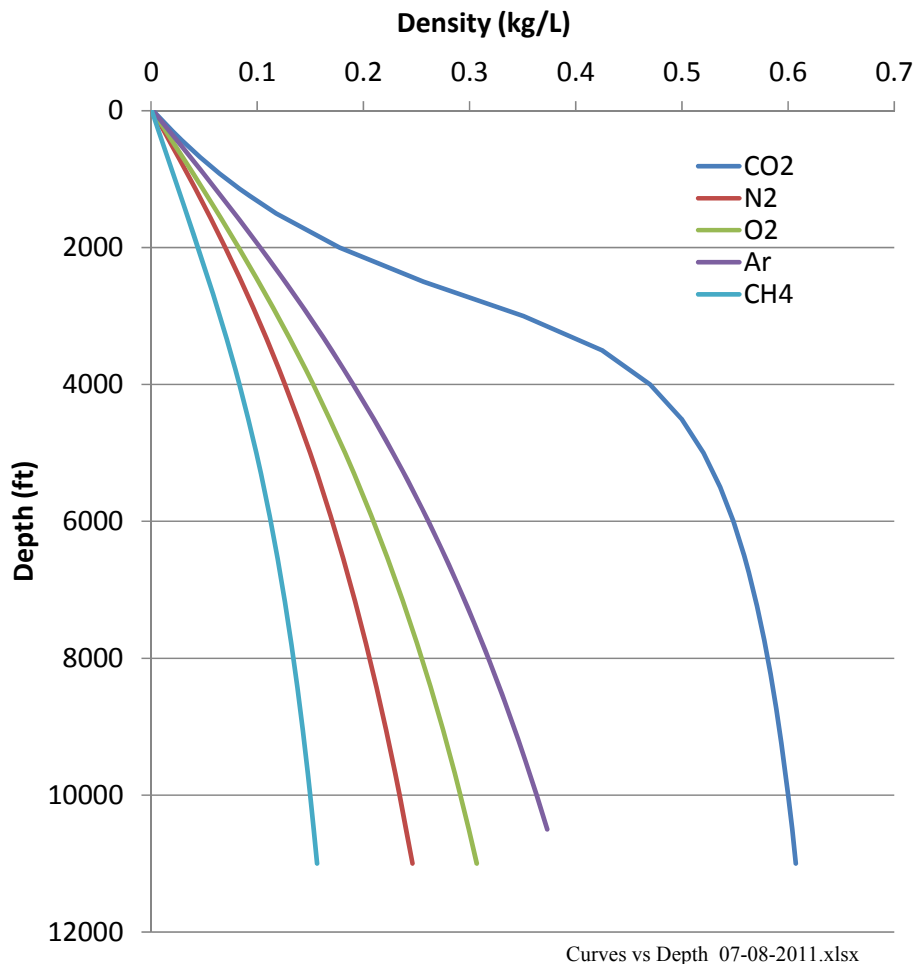


Figure 81. Density vs. depth for pure components (0.43 psi/ft and 12°F/1000 ft). Curves vs Depth_07-08-2011.xlsx

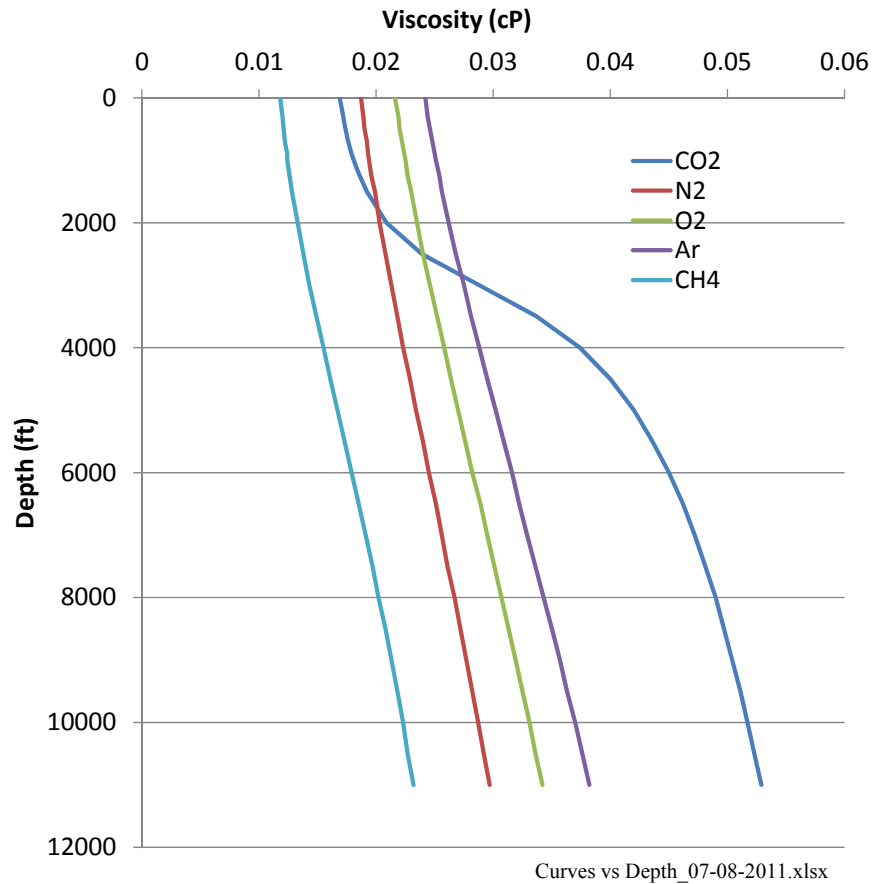


Figure 82. Viscosity vs. depth for pure components (0.43 psi/ft and 12°F/1000 ft)

CO₂ shows the largest density change with depth of all the major components (Figure 81). Although viscosity of all other major components increases slowly and linearly (Figure 82), CO₂ viscosity increases very quickly between 2,000 and 4,000 ft (its density increases quickly in the same depth interval).

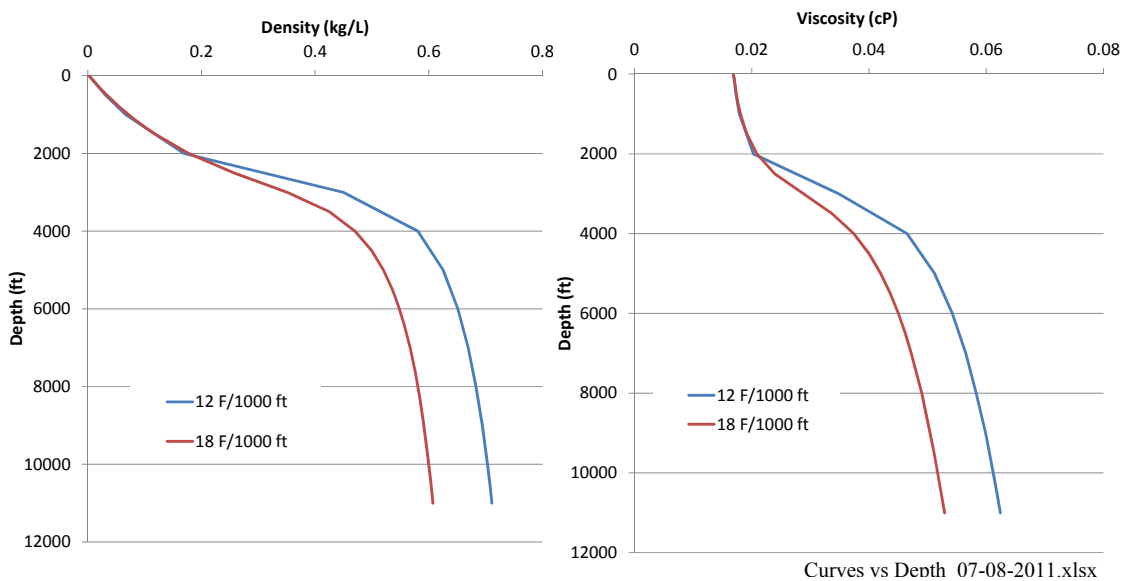


Figure 83. Comparison of CO₂ density with depth for two different temperature gradients

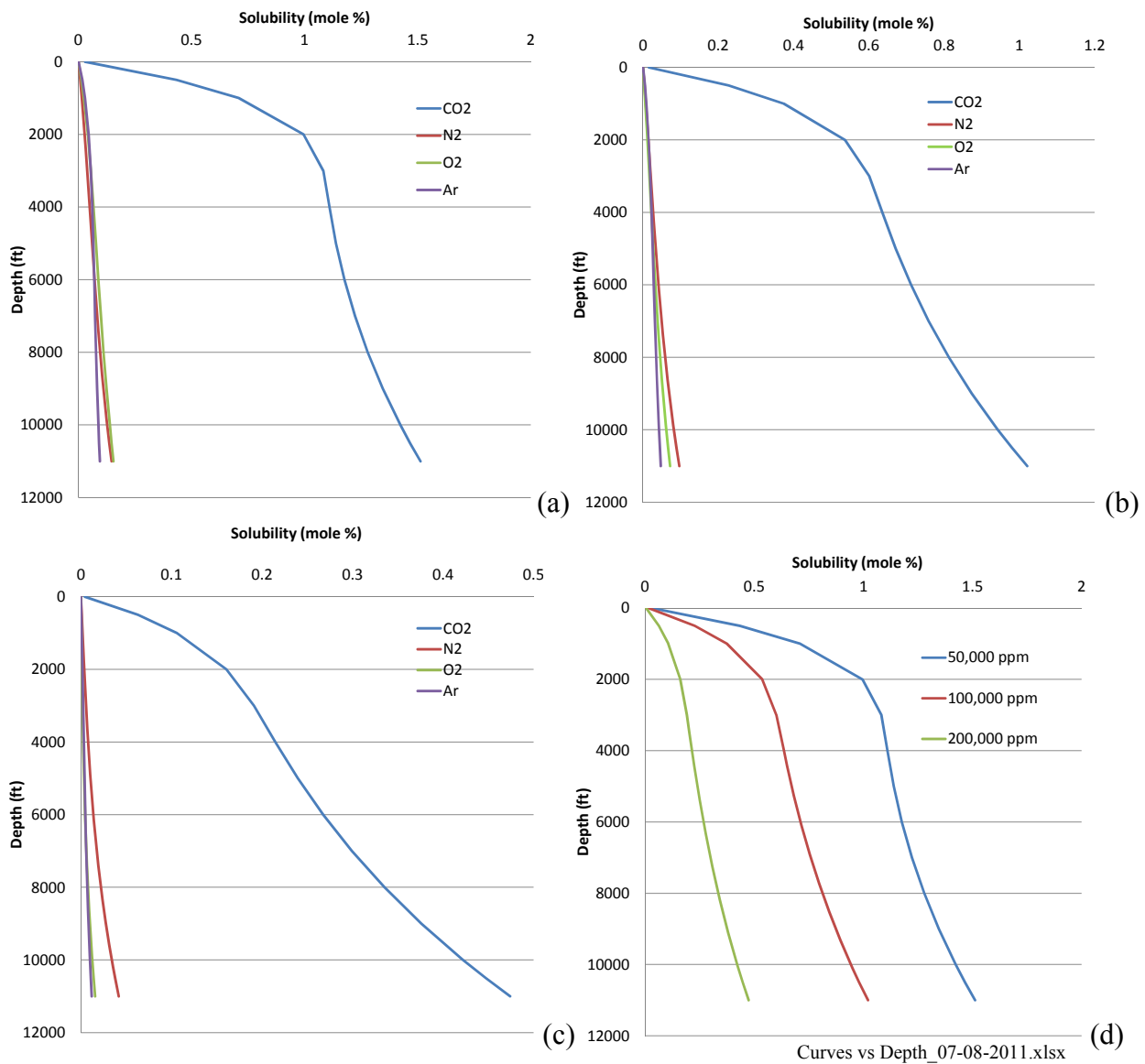
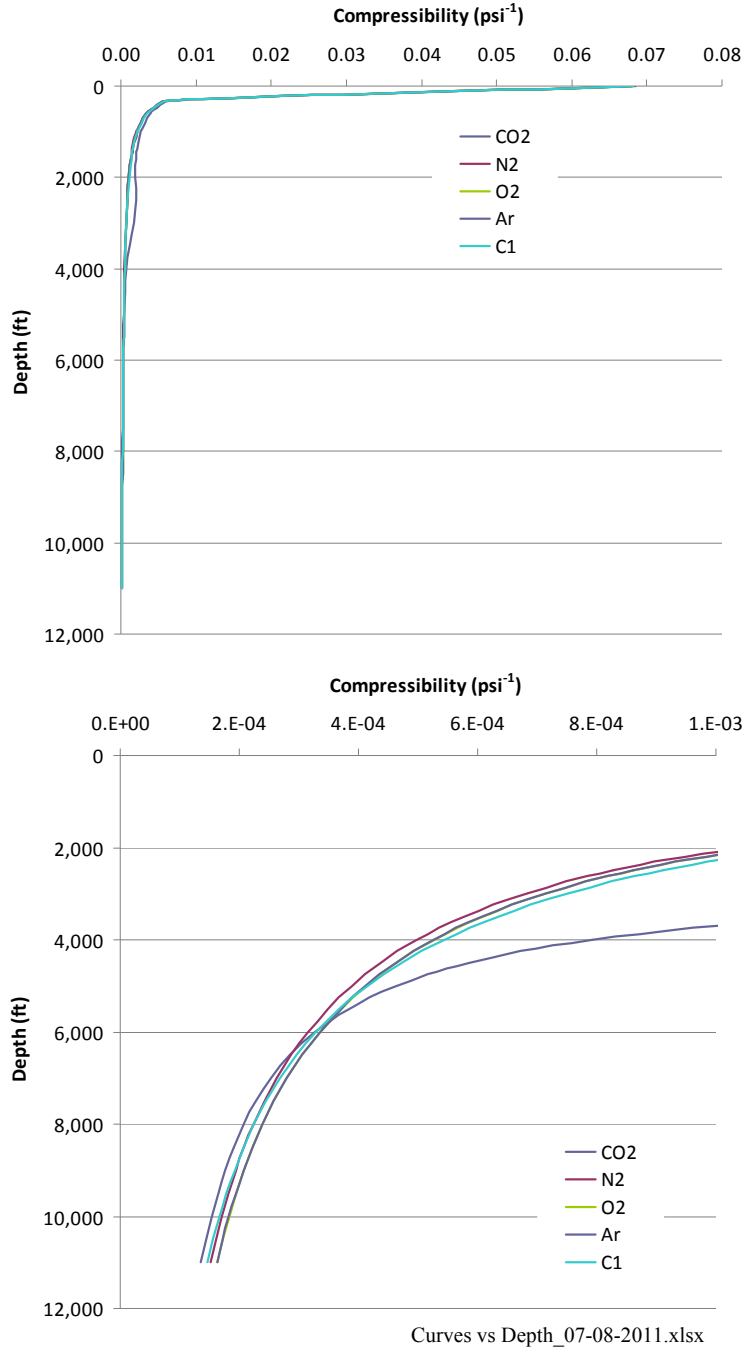


Figure 84. Solubility of CO₂, N₂, O₂, and Ar for a TDS of 50,000 (a), 100,000 (b), and 200,000 ppm (c) as a function of depth; solubility of CO₂ for various TDS as a function of depth(d).

Compressibility shows a large range for all gases from the surface to deep conditions (Figure 85) but decreases by a factor of 2 or 3 when only likely depths are considered (>4,000 ft). For relatively shallow depths (<6,000 ft), CO₂ is more compressible than N₂, O₂, Ar, or CH₄ but it falls within the same range as the so-called non-compressible gases at larger depths.



Curves vs Depth_07-08-2011.xlsx

Figure 85. Compressibility vs. depth of pure components

VII-2. Mixture Properties

Density and viscosity of ternary mixtures are presented in Figure 86 to Figure 89. For both shallow and deep case, those properties follow the pattern established in the previous section density $\text{CO}_2 > \text{N}_2 > \text{O}_2 > \text{Ar} > \text{CH}_4$ and viscosity $\text{CO}_2 > \text{N}_2 > \text{O}_2 > \text{Ar} > \text{CH}_4$. However, it is apparent from the lack of regularity in the spacing of isovalue contour lines that density and viscosity of the mixture do not simply vary linearly with the component mole fractions.

Table 40. Single-component viscosity, density, and compressibility of injection stream components as a function of depth.

Depth (ft)	Viscosity (cp)					Density (kg/L)					Compressibility (1/psi)				
	CO ₂	N ₂	O ₂	Ar	CH ₄	CO ₂	N ₂	O ₂	Ar	CH ₄	CO ₂	N ₂	O ₂	Ar	CH ₄
0	0.017	0.019	0.022	0.024	0.012	0.002	0.001	0.001	0.002	0.001	6.84E-02	6.84E-02	6.80E-02	6.81E-02	6.81E-02
300	0.017	0.019	0.022	0.024	0.012	0.020	0.012	0.014	0.017	0.007	6.92E-03	6.92E-03	6.50E-03	6.54E-03	6.54E-03
500	0.017	0.019	0.022	0.025	0.012	0.034	0.019	0.022	0.028	0.011	4.51E-03	4.51E-03	4.06E-03	4.09E-03	4.09E-03
700	0.018	0.019	0.022	0.025	0.012	0.048	0.026	0.031	0.038	0.016	3.44E-03	3.44E-03	2.95E-03	2.98E-03	2.98E-03
900	0.018	0.019	0.022	0.025	0.012	0.063	0.033	0.039	0.048	0.020	2.85E-03	2.85E-03	2.31E-03	2.35E-03	2.35E-03
1000	0.018	0.019	0.023	0.025	0.012	0.071	0.037	0.043	0.054	0.022	2.64E-03	2.64E-03	2.09E-03	2.12E-03	2.12E-03
1250	0.019	0.020	0.023	0.025	0.013	0.093	0.045	0.053	0.066	0.028	2.30E-03	2.30E-03	1.67E-03	1.71E-03	1.71E-03
1500	0.019	0.020	0.023	0.026	0.013	0.118	0.054	0.063	0.079	0.033	2.10E-03	2.10E-03	1.40E-03	1.43E-03	1.43E-03
2000	0.021	0.020	0.024	0.026	0.013	0.177	0.070	0.082	0.103	0.044	1.96E-03	1.96E-03	1.04E-03	1.08E-03	1.08E-03
2500	0.024	0.021	0.024	0.027	0.014	0.257	0.085	0.101	0.126	0.055	2.02E-03	2.02E-03	8.28E-04	8.62E-04	8.61E-04
3000	0.029	0.021	0.025	0.028	0.014	0.351	0.100	0.119	0.149	0.065	1.80E-03	1.80E-03	6.83E-04	7.15E-04	7.14E-04
3500	0.034	0.022	0.025	0.028	0.015	0.425	0.113	0.136	0.170	0.074	1.18E-03	1.18E-03	5.78E-04	6.08E-04	6.08E-04
4000	0.037	0.022	0.026	0.029	0.016	0.470	0.126	0.153	0.190	0.083	7.93E-04	7.93E-04	4.99E-04	5.27E-04	5.26E-04
4500	0.040	0.023	0.026	0.030	0.016	0.499	0.138	0.168	0.210	0.091	5.85E-04	5.85E-04	4.38E-04	4.64E-04	4.63E-04
5000	0.042	0.023	0.027	0.030	0.017	0.520	0.150	0.183	0.228	0.099	4.62E-04	4.62E-04	3.88E-04	4.13E-04	4.12E-04
5500	0.044	0.024	0.028	0.031	0.017	0.536	0.160	0.196	0.245	0.106	3.82E-04	3.82E-04	3.48E-04	3.70E-04	3.70E-04
6000	0.045	0.025	0.028	0.032	0.018	0.548	0.171	0.210	0.261	0.113	3.27E-04	3.27E-04	3.15E-04	3.35E-04	3.34E-04
6500	0.046	0.025	0.029	0.032	0.019	0.559	0.180	0.222	0.277	0.119	2.85E-04	2.85E-04	2.87E-04	3.06E-04	3.05E-04
7000	0.047	0.026	0.030	0.033	0.019	0.567	0.189	0.233	0.291	0.124	2.54E-04	2.54E-04	2.63E-04	2.80E-04	2.79E-04
7500	0.048	0.026	0.030	0.034	0.020	0.574	0.198	0.244	0.305	0.129	2.28E-04	2.28E-04	2.42E-04	2.58E-04	2.57E-04
8000	0.049	0.027	0.031	0.034	0.020	0.581	0.206	0.255	0.318	0.134	2.08E-04	2.08E-04	2.24E-04	2.39E-04	2.38E-04
8500	0.050	0.027	0.031	0.035	0.021	0.586	0.213	0.265	0.330	0.138	1.91E-04	1.91E-04	2.08E-04	2.22E-04	2.22E-04
9000	0.050	0.028	0.032	0.036	0.021	0.591	0.221	0.274	0.342	0.143	1.77E-04	1.77E-04	1.94E-04	2.08E-04	2.07E-04
9500	0.051	0.028	0.033	0.036	0.022	0.596	0.228	0.283	0.353	0.146	1.64E-04	1.64E-04	1.82E-04	1.95E-04	1.94E-04
10,000	0.052	0.029	0.033	0.037	0.022	0.600	0.234	0.291	0.363	0.150	1.54E-04	1.54E-04	1.71E-04	1.83E-04	1.82E-04
10,500	0.052	0.029	0.034	0.038	0.023	0.604	0.240	0.299	0.373	0.153	0.604	1.44E-04	1.61E-04	1.72E-04	1.72E-04
11,000	0.053	0.030	0.034	0.038	0.023	0.607	0.246	0.307	0.382	0.156	0.607	1.36E-04	1.53E-04	1.63E-04	1.62E-04

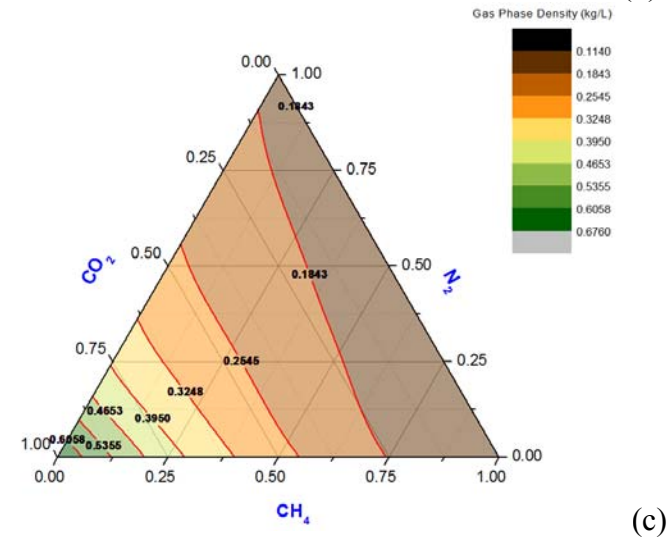
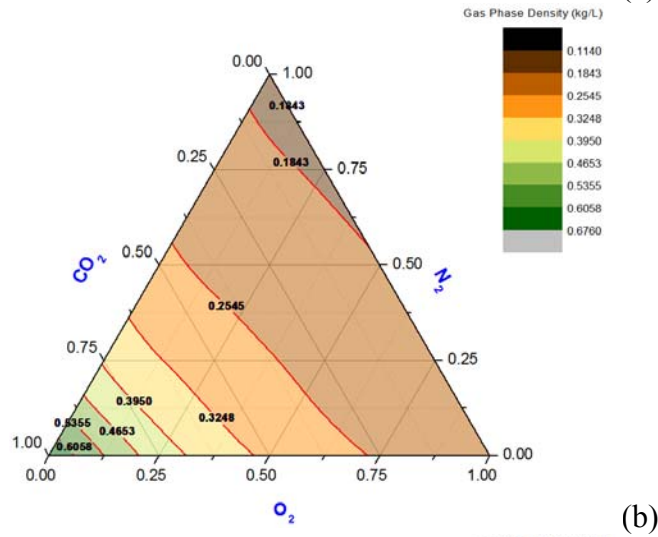
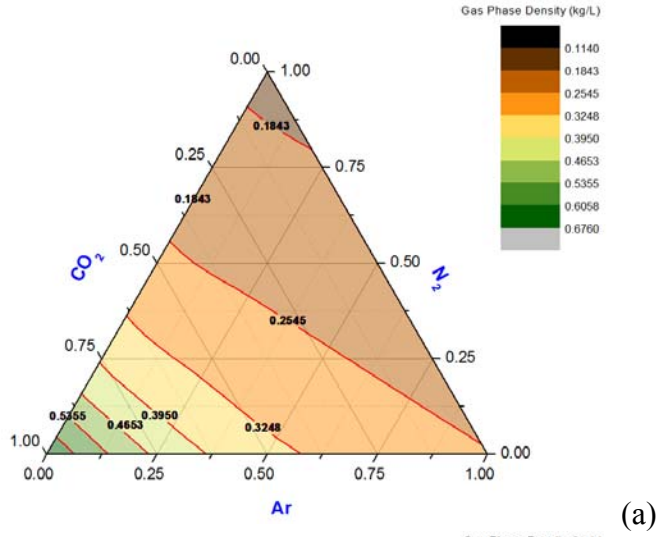
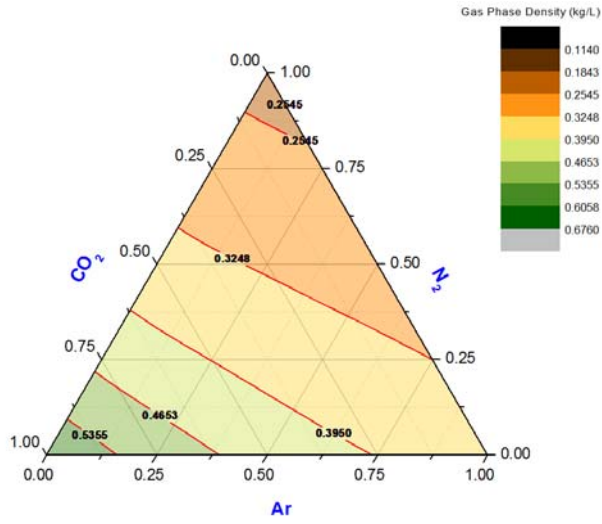
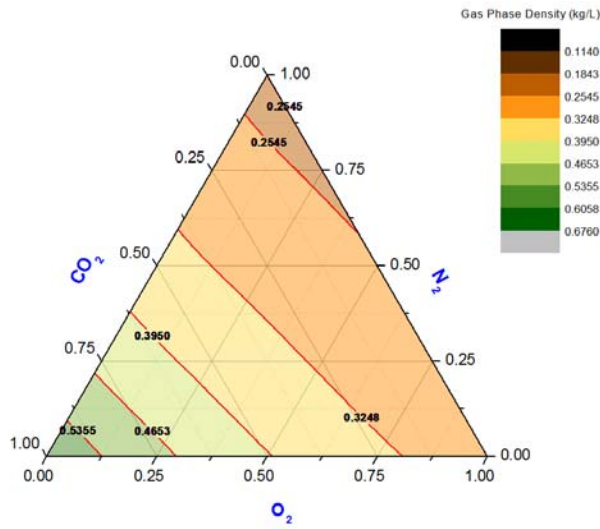


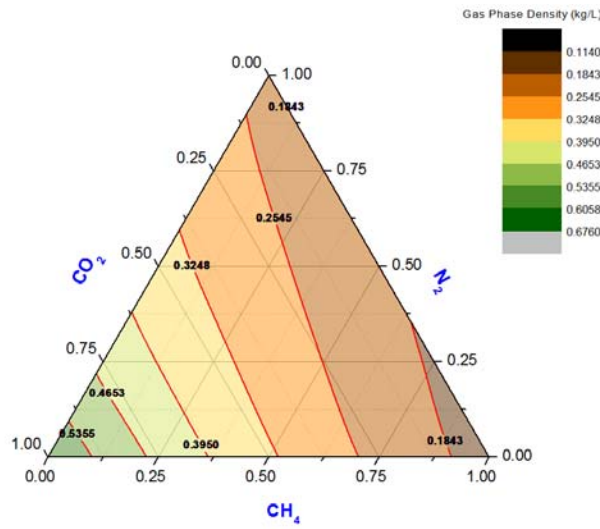
Figure 86. Density (kg/L) of various ternary mixtures at shallow Gulf Coast conditions: CO₂-N₂-Ar (a), CO₂-N₂-O₂ (b), CO₂-N₂-CH₄ (c).



(a)



(b)



(c)

Figure 87. Density (kg/L) of various ternary mixtures at deep Gulf Coast conditions: CO₂-N₂-Ar (a), CO₂-N₂-O₂ (b), CO₂-N₂-CH₄ (c).

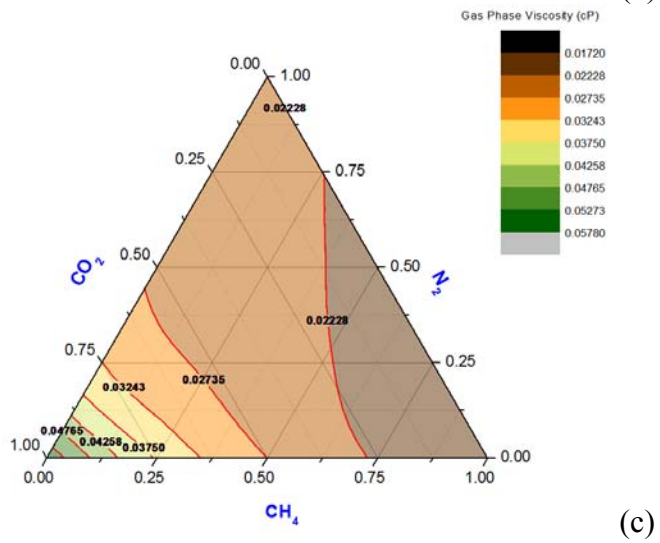
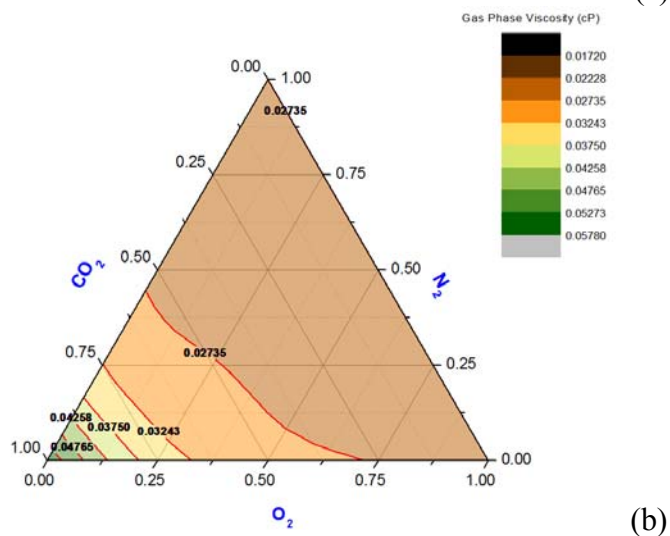
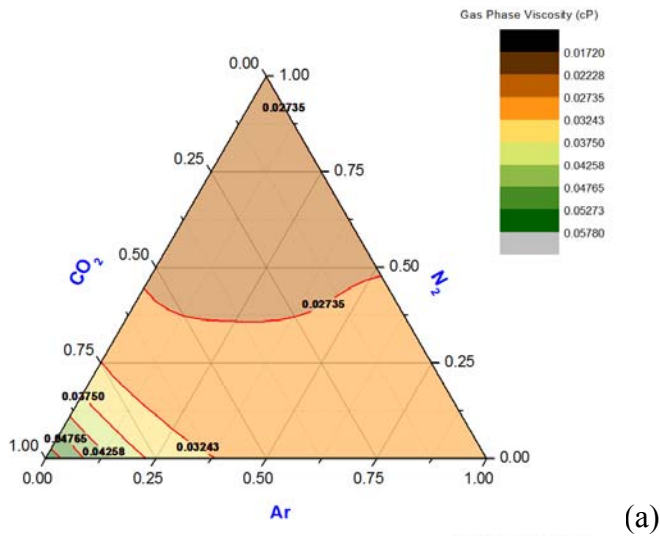


Figure 88. Viscosity (cp) of various ternary mixtures at shallow Gulf Coast conditions: CO₂-N₂-Ar (a), CO₂-N₂-O₂ (b), CO₂-N₂-CH₄ (c).

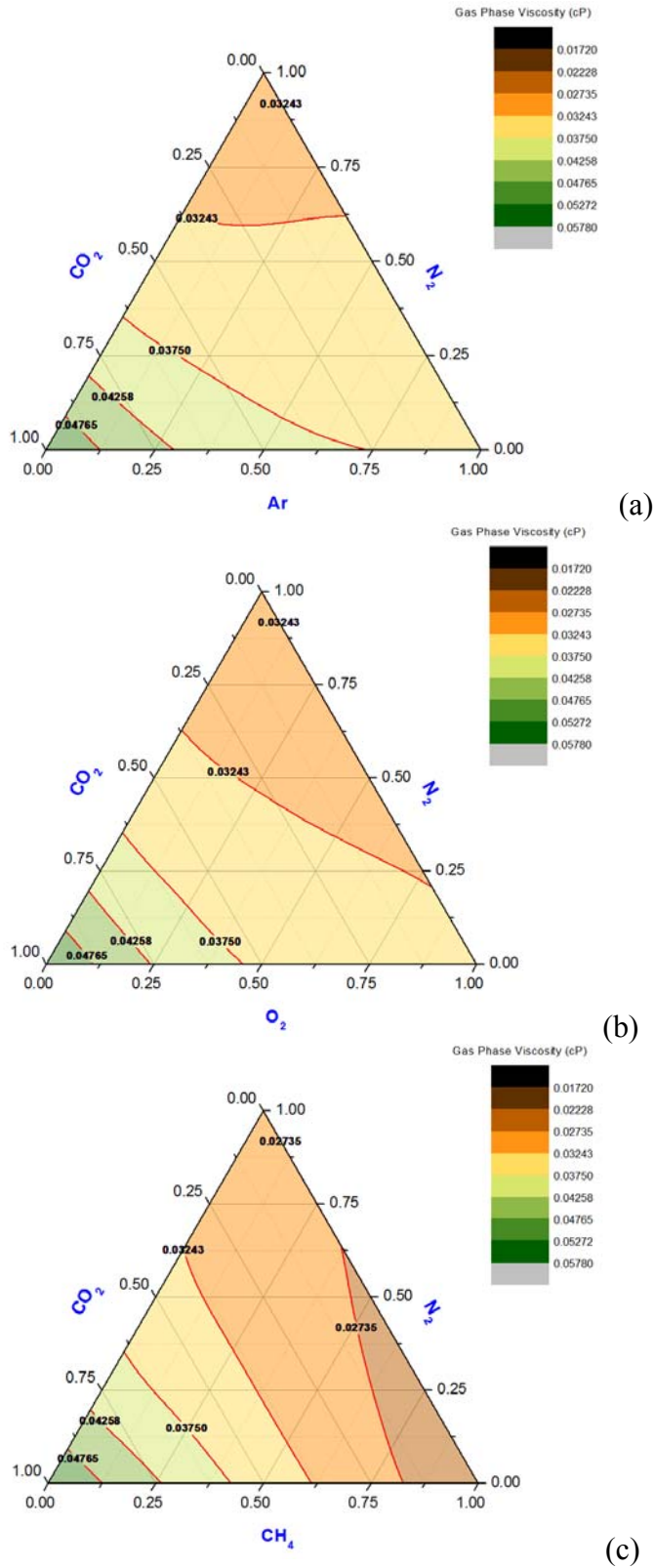


Figure 89. Viscosity (cp) of various ternary mixtures at deep Gulf Coast conditions: CO₂-N₂-Ar (a), CO₂-N₂-O₂ (b), CO₂-N₂-CH₄ (c).

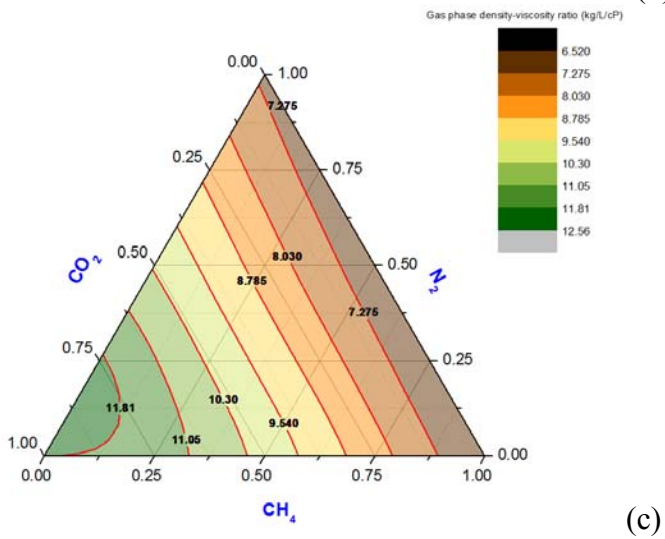
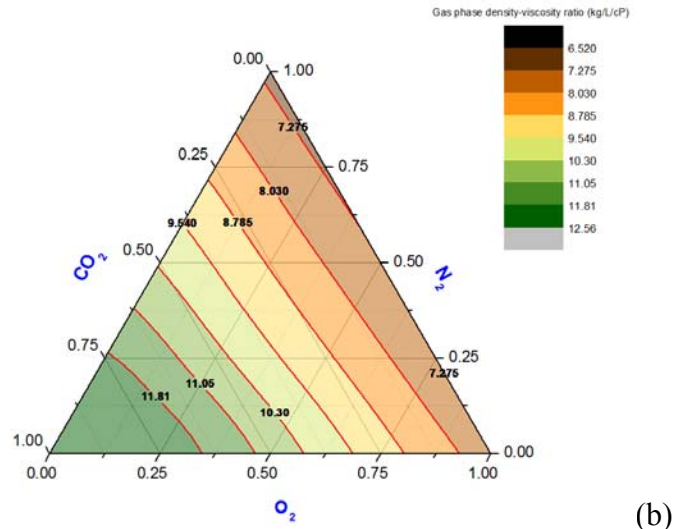
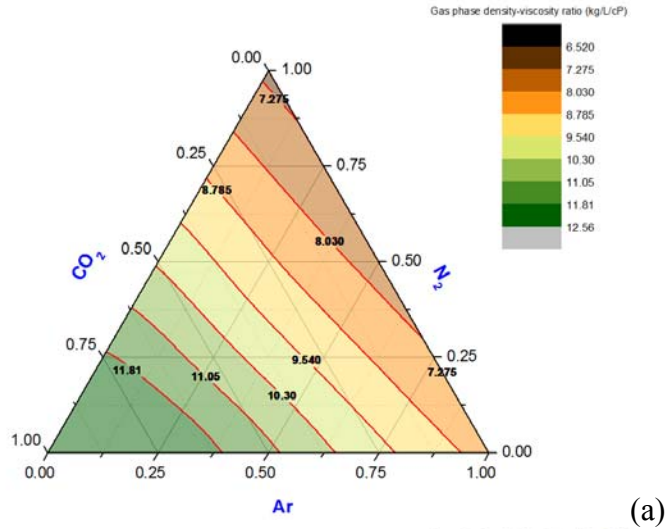


Figure 90. Density/Viscosity ratio of various ternary mixtures at shallow Gulf Coast conditions: CO₂-N₂-Ar (a), CO₂-N₂-O₂ (b), CO₂-N₂-CH₄ (c).

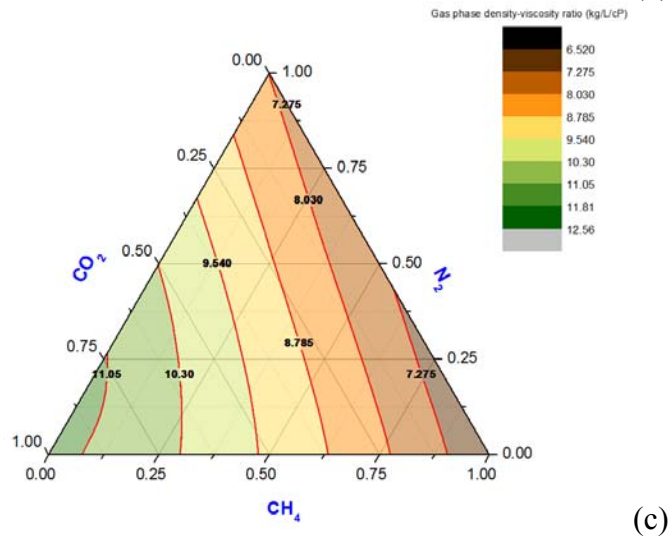
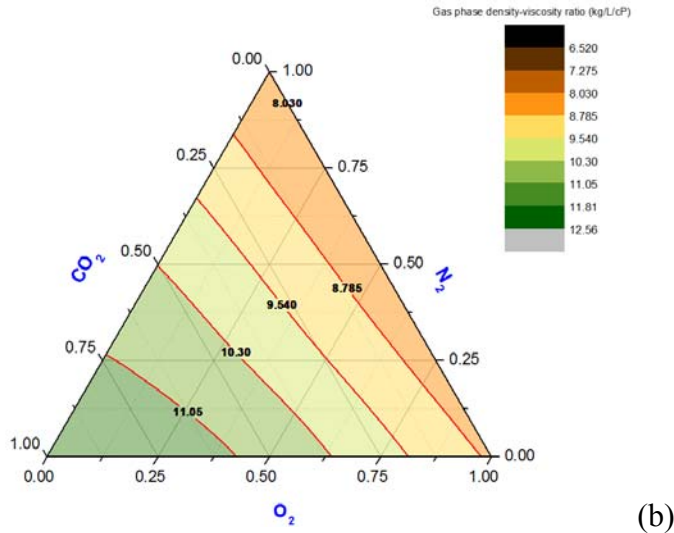
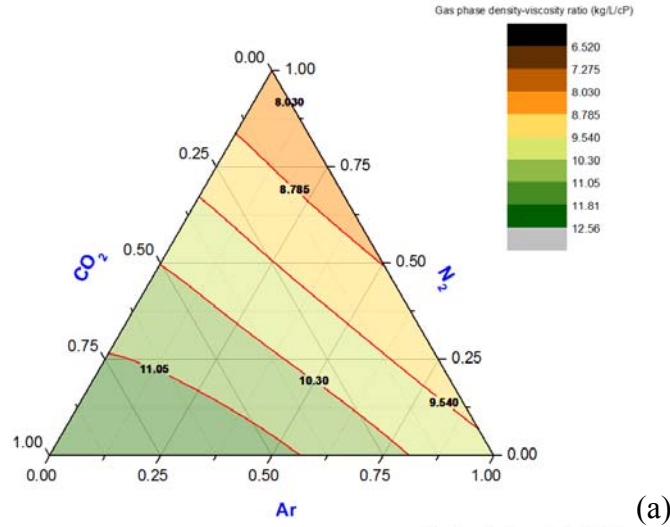
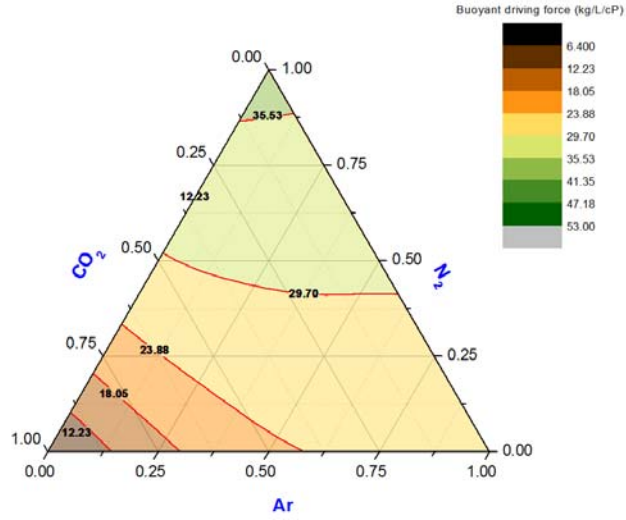
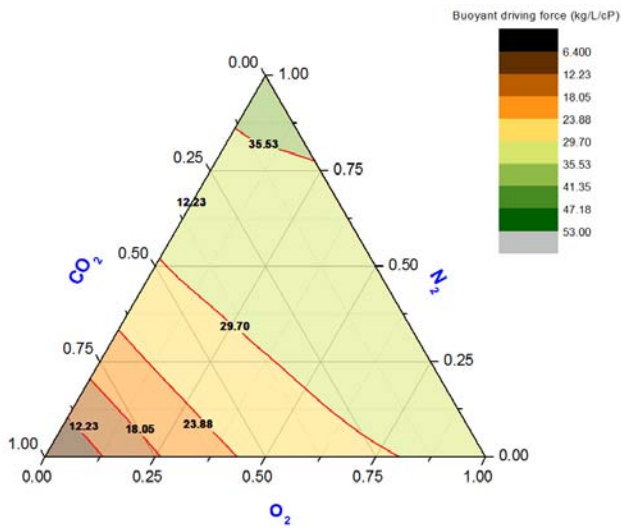


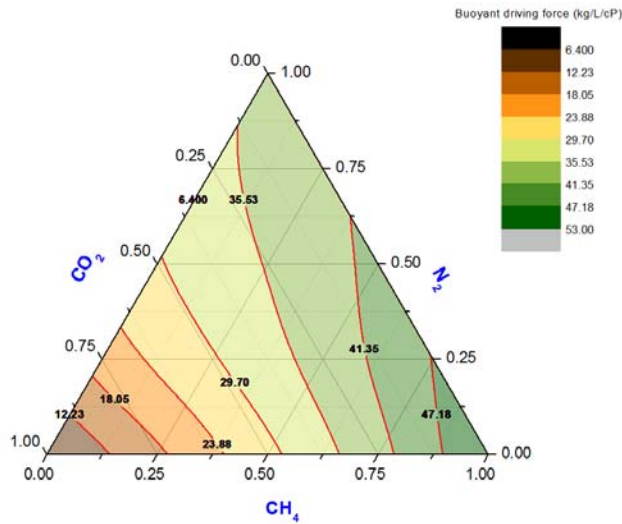
Figure 91. Density/Viscosity ratio of various ternary mixtures at deep Gulf Coast conditions: CO₂-N₂-Ar (a), CO₂-N₂-O₂ (b), CO₂-N₂-CH₄ (c).



(a)

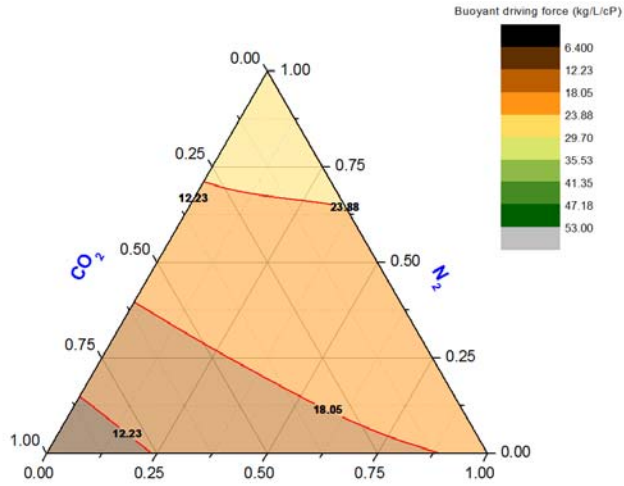


(b)

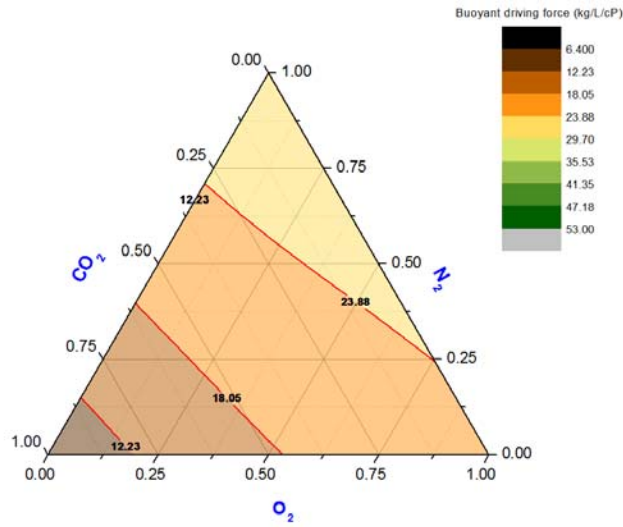


(c)

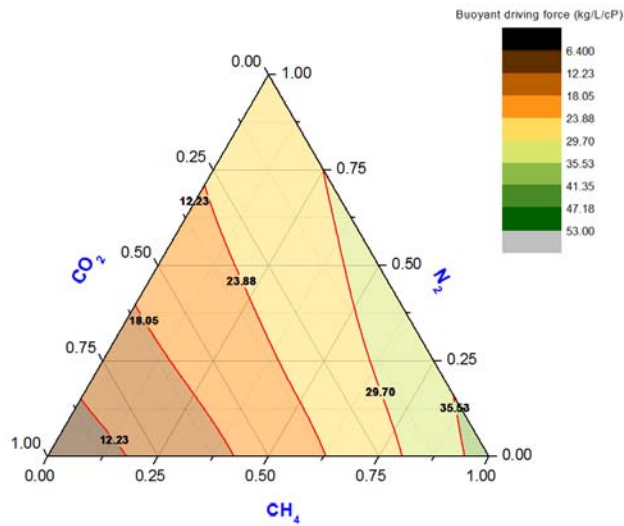
Figure 92. Buoyant driving force of various ternary mixtures at shallow Gulf Coast conditions: CO₂-N₂-Ar (a), CO₂-N₂-O₂ (b), CO₂-N₂-CH₄ (c).



(a)



(b)



(c)

Figure 93. Buoyant driving force of various ternary mixtures at deep Gulf Coast conditions: $\text{CO}_2\text{-N}_2\text{-Ar}$ (a), $\text{CO}_2\text{-N}_2\text{-O}_2$ (b), $\text{CO}_2\text{-N}_2\text{-CH}_4$ (c).

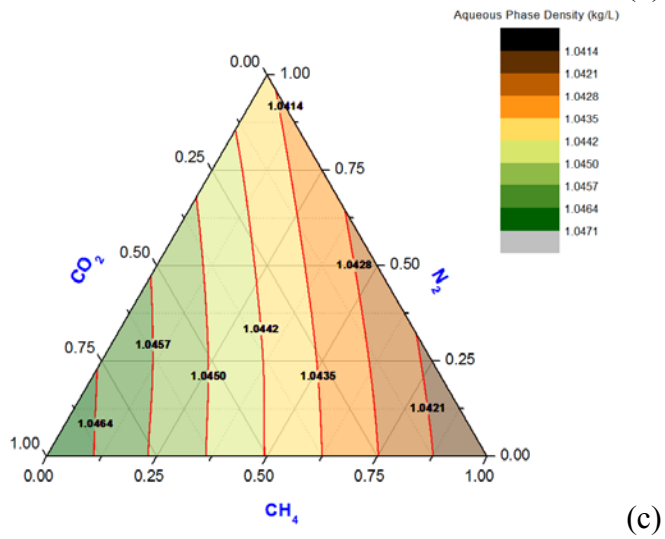
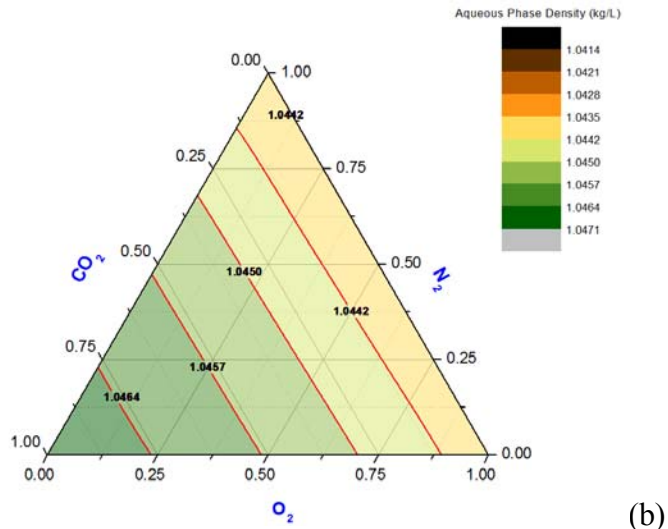
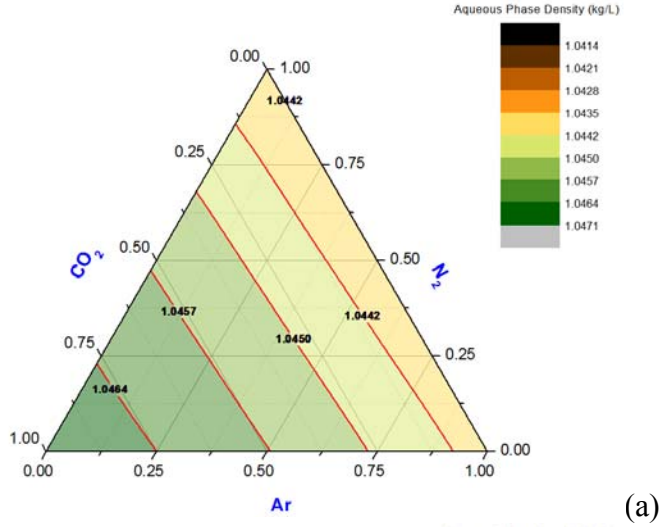


Figure 94. Aqueous phase density (kg/L) of brine at equilibrium with various ternary mixtures at shallow Gulf Coast conditions: CO₂-N₂-Ar (a), CO₂-N₂-O₂ (b), CO₂-N₂-CH₄ (c).

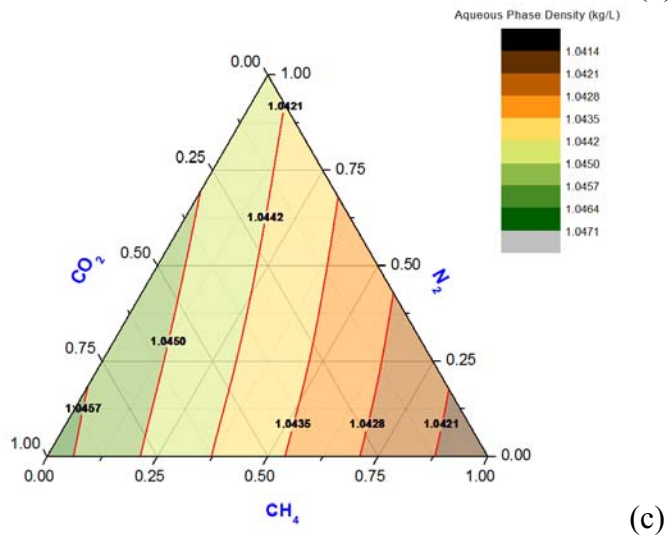
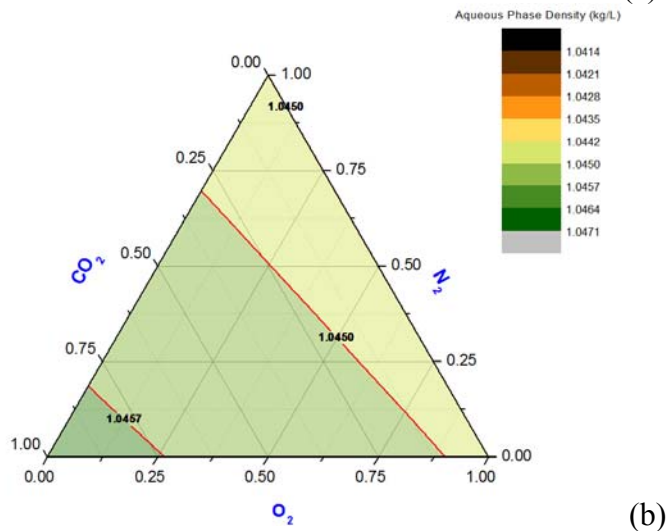
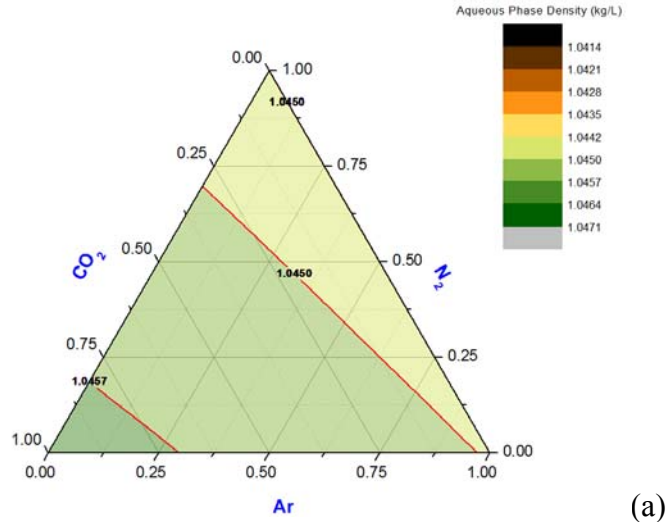


Figure 95. Aqueous phase density (kg/L) of brine at equilibrium with various ternary mixtures at deep Gulf Coast conditions: CO₂-N₂-Ar (a), CO₂-N₂-O₂ (b), CO₂-N₂-CH₄ (c).

VIII. Appendix C: GEM Input Files

Below we present an example of a generic case and of the shallow Gulf Coast model

Generic Case

```
** FILE: Base Case Aquifer Gulf Coast-Deep **
** **
** MODEL: 120-51-20 CARTESIAN GRID CO2 Storage Gas Mixture **
** FIELD UNITS **
** **
**-----**
**-----**
** I/O CONTROL DATA
**-----**
RESULTS SIMULATOR GEM 200710
*INUNIT *FIELD
**DIM MDJCS 200
*DIM MDGRID 800
**DIM MDJCS 2000
*DIM MDICLU 700000 **522387

*DIM DIMSUM
*INTERRUPT *INTERACTIVE
*XDR *ON
*MAXERROR 20
RANGECHECK ON
*WPRN *WELL *TIME
*WPRN *GRID *TIME
*WPRN *ITER *NONE
*WSRF *WELL *TIME
*WSRF *GRID *TIME
*DIARY *CHANGES

*OUTPRN *RES *ALL
*OUTPRN *GRID
*POROS
*KRG
*SG
*RHOG
*Y 'H2O'
*Y 'CO2'
*Y 'N2'
*Y 'O2'
*Y 'AR'
*Y 'H2'
*Y 'CO'
*Y 'SO2'

*SO
*RHO0
*X 'H2O'
*X 'CO2'
*X 'N2'
*X 'O2'
*X 'AR'
*X 'H2'
*X 'CO'
*X 'SO2'

*OUTSRF *WELL *PSPLIT

** Variables for GHG
*OUTSRF *WELL *PAVG *GHGTHY *GHGSCRIT *GHGSOL *GHGLIQ *GHGGAS *GHGMNR *GHGAQU *GHGSOL

*OUTSRF *GRID DENG RHOG MWG FRG SG DENO RHO0 PCG PCW SO DENW SW KRG VISG MWO KRO VISO PRES KRW FRG
K 'H2O' Z 'H2O' Y 'H2O' X 'H2O'
K 'CO2' Z 'CO2' Y 'CO2' X 'CO2'
K 'N2' Z 'N2' Y 'N2' X 'N2'
K 'O2' Z 'O2' Y 'O2' X 'O2'
K 'AR' Z 'AR' Y 'AR' X 'AR'
K 'H2' Z 'H2' Y 'H2' X 'H2'
K 'CO' Z 'CO' Y 'CO' X 'CO'
K 'SO2' Z 'SO2' Y 'SO2' X 'SO2'

*OUTSRF *RES *ALL
```

```

**-----**
** RESERVOIR DATA
**-----**

*GRID *CART 120 51 20
*KDIR *DOWN

*DEPTH *TOP 1 1 1 9976.0
*DIP 2 0

*DI *CON 300.0
*DJ *CON 300.0
*DK *CON 50.0
**$ Property: NULL Blocks Max: 1 Min: 1
**$ 0 = null block, 1 = active block
NULL CON          1

*POR *CON 0.25
*PERMI *CON 300
PERMJ EQUALSI
PERMK EQUALSI * 0.01
PINCHOUTARRAY CON 1

*CPOR 5.0E-06
*PRPOR 14.7

**-----**
** FLUID COMPONENT DATA
**-----**

*MODEL *PR
*NC      8      8
*TRES    257.000
*COMPNAME
      'CO2'      'N2'      'O2'      'AR'
      'H2'      'CO'      'SO2'     'H2O'
*SG      4.9270000E-01  1.5852000E-01  2.1827000E-01  2.1066000E-01
      3.0130000E-02  1.6876000E-01  7.2343000E-01  1.0000000E+00
*TB      -1.5252400E+02 -3.2195100E+02 -2.9975000E+02 -3.0301000E+02
      -4.2041100E+02 -3.1493900E+02 -2.0933000E+01  2.1200000E+02
*PCRIT   7.2800000E+01  3.3500000E+01  4.9800000E+01  4.8100000E+01
      1.2958000E+01  3.4532000E+01  7.7809000E+01  2.1760000E+02
*VCRIT   1.1870000E-01  5.4949000E+00  1.5849000E+00  2.1907000E+00
      4.9901000E+00  5.5762000E+00  1.7350000E-01  5.6000000E-02
*TCRIT   3.0420000E+02  1.2620000E+02  1.5460000E+02  1.5080000E+02
      3.3190000E+01  1.3290000E+02  4.3080000E+02  6.4730000E+02
*AC      2.2500000E-01  4.0000000E-02  2.1000000E-02 -4.0000000E-03
      -2.1600000E-01  4.8000000E-02  2.4500000E-01  3.4400000E-01
*MW      4.4010000E+01  2.8014000E+01  3.1999000E+01  3.9948000E+01
      2.0160000E+00  2.8010000E+01  6.4065000E+01  1.8015000E+01
*HCFLAG  0          0          0          0
      0          0          0          0
**BIN from Dr. Pope's Report-BIN for 'H2' 'CO' 'SO2' are set equal to zero
*BIN
  0
  0          0
  0          0          0
  0          0          0          0
  0          0          0          0          0
  0          0          0          0          0
  0.1402  0.0686  0.6476  0.7014  0  0  0

*VSHIFT   1.1701100E-02 -1.7599550E-01 -1.8679150E-01 -2.0086950E-01
      -3.2642870E-01 -1.7150920E-01 -6.0226800E-02  0.295774

**VSHIFT FOR WATER SET EQUAL TO 0.295774 (Calculated from Kumar's Vshift correlation for water at 257F and
170000 ppm)

*VISCOR *HZYT
*MIXVC    1.0000000E+00
*VISVC    9.4300000E-02  8.9900000E-02  7.3700000E-02  7.4900000E-02
      6.4900000E-02  9.4300000E-02  1.2170000E-01  5.6000000E-02
*VISCOEFF 1.0999000E-01  1.1680000E-02  5.5730000E-02 -2.8470000E-02
      4.6700000E-03
*OMEGA    4.5724000E-01  4.5724000E-01  4.5724000E-01  4.5724000E-01
      4.5724000E-01  4.5724000E-01  4.5724000E-01  4.572353E-01
*OMEGB    7.7800000E-02  7.7800000E-02  7.7800000E-02  7.7800000E-02
      7.7800000E-02  7.7800000E-02  7.7800000E-02  7.7796074E-02
*PCHOR    1.2649000E+02  7.7360000E+01  8.9700000E+01  1.1412000E+02
      1.0000000E+00  7.7350000E+01  1.8650000E+02  5.2000000E+01

```

*PHASEID *DEN

** ROCK FLUID

*ROCKFLUID

RPT 1 DRAINAGE SCALING-OLD

*SWT

** Not used

0	0	1	**290
0.05	1E-10	0.95	**105.044278
0.1	0.00000001	0.86	**50.89774296
0.15	0.000001 0.76		**32.84889794
0.2	0.0001	0.65	**23.82447543
0.25	0.002923977	0.5265	**18.40982192
0.3	0.016391711	0.416	**14.80005292
0.35	0.044319935	0.3185	**12.22164649
0.4	0.088235294	0.234	**10.28784166
0.45	0.147653281	0.1625	**8.783771243
0.5	0.220387362	0.104	**7.580514909
0.55	0.303070525	0.0585	**6.596032453
0.6	0.391805812	0.026	**5.775630407
0.65	0.482781457	0.0065	**5.08144406
0.7	0.572718844	0.001	**4.486427191
0.75	0.659104078	0.0001	**3.970745905
0.8	0.740228803	0.00001	**3.519524779
0.85	0.815104022	0.000001	**3.121388492
0.9	0.88331325	0.0000001	**2.76748957
0.95	0.94485456	0.00000001	**2.450843166
1	1	0	**2.165861402

*SLT

** water/gas

**Sw	krw	Pc	
0	1	0	**221.2336384
0.05	0.894160584	0.0000002	**107.9838121
0.1	0.788321168	0.000005	**52.70673921
0.137	0.71	0.00005	**31
0.190938	0.604208	0.000561	**14.3
0.244875	0.508485	0.003645	**7.76
0.298813	0.42249	0.010892	**5.02
0.35275	0.345869	0.023683	**3.8
0.406688	0.278253	0.043261	**3
0.460625	0.21926	0.070776	**2.8
0.514563	0.168486	0.10731	**2.35
0.5685	0.125512	0.153893	**2.28
0.622438	0.089888	0.21151	**2.16
0.676375	0.061142	0.28111	**2.01
0.730313	0.03876	0.36361	**1.91
0.78425	0.022188	0.459902	**1.86
0.838188	0.010808	0.570851	**1.75
0.892125	0.003922	0.697303	**1.69
0.946063	0.000693	0.840084	**1.54
1	0	1	**1.4

*HYSKRG 0.300

** INITIAL CONDITIONS

INITIAL

** Set up brine aquifer

**Under *VERTICAL *DEPTH_AVE *WATER_OIL, the water-oil contact depth (*DWOC), together with a reference pressure (*REFPRES) at a reference depth (*REFDEPTH) must be specified. One composition vector (entered under *ZOIL), representing the averaged reservoir fluid composition, is required. This composition is assigned to all grid blocks. This option is used for undersaturated oil reservoirs in which the added accuracy in initial amounts in place made possible by the depth averaging is wanted.]

*VERTICAL *DEPTH_AVE *WATER_OIL

*ZOIL 0. 0. 0. 0. 0. 0. 1.

**PSI

REFPRES

4701.5

**FT

REFDEPTH

9976.0

**FT

DWOC
8100.0

** NUMERICAL METHODS CONTROL

*NUMERICAL
*DTMAX 1
*DTMIN 1.E-06
*NORM *PRESS 2000
*MAXCHANGE *GMOLAR 0.2
*MAXCHANGE *SATUR 0.2
*AIM *STAB 1
*CONVERGE *PRESS 0.15
*MAXSTEPS 1000000

** WELL DATA

*RUN
*DATE 2000 1 1
*DTWELL 1.0
** **'CO2''N2''O2''AR''H2''CO''SO2''H2O'
** WELL 1 'INJ'
**\$
WELL 'INJ'
INJECTOR 'INJ'
INCOMP SOLVENT 1.0 0. 0. 0. 0. 0. 0. 0.
OPERATE MAX STG 2.603e+007 CONT
**\$ rad geofac wfrac skin
GEOMETRY K 0.5 0.37 1. 0.
PERF GEO 'INJ'
**\$ UBA ff Status Connection
12 26 14:20 1. OPEN FLOW-FROM 'SURFACE' REFLAYER

OPEN 'INJ'
**
** *WELL 2 'w1'
**\$
WELL 'w1'
INJECTOR 'w1'
INCOMP SOLVENT 1. 0. 0. 0. 0. 0. 0. 0.
OPERATE MAX STG 0. CONT
**1 1:25 1 1 OPEN
**\$ rad geofac wfrac skin
GEOMETRY K 40. 0.35 1. 0.
PERF GEO 'w1'
**\$ UBA ff Status Connection
1 1:51 1 1. OPEN FLOW-FROM 'SURFACE' REFLAYER
OPEN 'w1'

** *WELL 3 'w2'
**\$
WELL 'w2'
INJECTOR 'w2'
INCOMP SOLVENT 1. 0. 0. 0. 0. 0. 0. 0.
OPERATE MAX STG 0. CONT
**1 1:25 5 1 OPEN
**\$ rad geofac wfrac skin
GEOMETRY K 40. 0.35 1. 0.
PERF GEO 'w2'
**\$ UBA ff Status Connection
1 1:51 5 1. OPEN FLOW-FROM 'SURFACE' REFLAYER
OPEN 'w2'

** *WELL 4 'w3'
**\$
WELL 'w3'
INJECTOR 'w3'
INCOMP SOLVENT 1. 0. 0. 0. 0. 0. 0. 0.
OPERATE MAX STG 0. CONT
**1 1:25 10 1 OPEN
**\$ rad geofac wfrac skin
GEOMETRY K 40. 0.35 1. 0.
PERF GEO 'w3'
**\$ UBA ff Status Connection
1 1:51 10 1. OPEN FLOW-FROM 'SURFACE' REFLAYER
OPEN 'w3'

```

** *WELL      5      'w4'
**$
WELL 'w4'
INJECTOR 'w4'
INCOMP SOLVENT 1. 0. 0. 0. 0. 0. 0. 0.
OPERATE MAX STG 0. CONT
**1      1:25      15      1      OPEN
**$      rad geofac wfrac skin
GEOMETRY K 40. 0.35 1. 0.
PERF GEO 'w4'
**$ UBA      ff Status Connection
      1 1:51 15 1. OPEN      FLOW-FROM 'SURFACE' REFLAYER
OPEN 'w4'

** *WELL      6      'w5'
**$
WELL 'w5'
INJECTOR 'w5'
INCOMP SOLVENT 1. 0. 0. 0. 0. 0. 0. 0.
OPERATE MAX STG 0. CONT
**1      1:25      20      1      OPEN
**$      rad geofac wfrac skin
GEOMETRY K 40. 0.35 1. 0.
PERF GEO 'w5'
**$ UBA      ff Status Connection
      1 1:51 20 1. OPEN      FLOW-FROM 'SURFACE' REFLAYER
OPEN 'w5'

** *WELL      7      'Prod1'
**$
WELL 'Prod1'
*PRODUCER      'Prod1'
OPERATE MIN      BHP      4184.2 CONT
**60      1:25      1      1      OPEN
**$      rad geofac wfrac skin
GEOMETRY K 40. 0.35 1. 0.
PERF GEO 'Prod1'
**$ UBA      ff Status Connection
      120 1:51 1 1. OPEN      FLOW-TO 'SURFACE' REFLAYER
OPEN 'Prod1'

** *WELL      8      'Prod2'
**$
WELL 'Prod2'
*PRODUCER      'Prod2'
OPERATE MIN      BHP      4268.9 CONT
**60      1:25      5      1      OPEN
**$      rad geofac wfrac skin
GEOMETRY K 40. 0.35 1. 0.
PERF GEO 'Prod2'
**$ UBA      ff Status Connection
      120 1:51 5 1. OPEN      FLOW-TO 'SURFACE' REFLAYER
OPEN 'Prod2'

** *WELL      9      'Prod3'
**$
WELL 'Prod3'
*PRODUCER      'Prod3'
OPERATE MIN      BHP      4374.8 CONT
**60      1:25      10      1      OPEN
**$      rad geofac wfrac skin
GEOMETRY K 40. 0.35 1. 0.
PERF GEO 'Prod3'
**$ UBA      ff Status Connection
      120 1:51 10 1. OPEN      FLOW-TO 'SURFACE' REFLAYER

OPEN 'Prod3'

** *WELL      10      'Prod4'
**$
WELL 'Prod4'
*PRODUCER      'Prod4'
OPERATE MIN      BHP      4480.8 CONT
**60      1:25      15      1      OPEN
**$      rad geofac wfrac skin
GEOMETRY K 40. 0.35 1. 0.
PERF GEO 'Prod4'
**$ UBA      ff Status Connection
      120 1:51 15 1. OPEN      FLOW-TO 'SURFACE' REFLAYER
OPEN 'Prod4'

```

```

** *WELL      11      'Prod5'
**$
WELL 'Prod5'
  *PRODUCER      'Prod5'
  OPERATE MIN    BHP      4586.7  CONT
  **60      1:25      20      1      OPEN
**$
      rad geofac wfrac skin
GEOMETRY K 40. 0.35 1. 0.
PERF GEO 'Prod5'
**$ UBA      ff Status Connection
      120 1:51 20 1. OPEN FLOW-TO 'SURFACE' REFLAYER

```

```
OPEN 'Prod5'
```

```

TIME      1
TIME      10
*DTMAX 100
TIME      100
TIME      200
TIME      365
TIME      500
TIME      750
TIME      1000
TIME      1250
TIME      1500
TIME      1750
TIME      2000
TIME      2500
TIME      3653
TIME      4000
TIME      5000
TIME      6000
TIME      7305
TIME      9131
TIME      10958
SHUTIN 'INJ'
*DTMAX 200
TIME      12784
TIME      14610
TIME      16436
TIME      18263
TIME      21915
*DTMAX 1000
TIME      25568
TIME      29220
TIME      32873
TIME      36525
TIME      45656
TIME      54788
TIME      73050
*DTMAX 3000
TIME      146100
TIME      182625
TIME      292200
TIME      365243
*STOP

```

Gulf Coast Shallow Model

```

*INUNIT *FIELD
**DIM MDJCS 200
DIM DIMSUM
*DIM MDGRID 800
*DIM MDJCS 2000
*DIM MDICLU 700000 **522387
**OUTPRN *GRID *ALL
**OUTPRN *RES *ALL
**OUTSRF *GRID *ALL
*INTERRUPT *INTERACTIVE
*XDR *ON
*MAXERROR 20
RANGECHECK ON
*WPRN *WELL *TIME
*WPRN *GRID *TIME
*WPRN *ITER *NONE
*WSRF *WELL *TIME
*WSRF *GRID *TIME
*DIARY *CHANGES

*OUTPRN *RES *ALL
*OUTPRN *GRID

```

```

*POROS
*KRG
*SG
*RHOG
*Y 'H2O'
*Y 'CO2'
*Y 'N2'
*Y 'O2'
*Y 'AR'
*Y 'H2'
*Y 'CO'
*Y 'SO2'

*SO
*RHOO
*X 'H2O'
*X 'CO2'
*X 'N2'
*X 'O2'
*X 'AR'
*X 'H2'
*X 'CO'
*X 'SO2'

*OUTSRF *WELL *PSPLIT
*OUTSRF *WELL *PAVG *GHGTHY *GHGSCRIT *GHGSOL *GHGLIQ *GHGGAS
*OUTSRF *GRID DENG RHOG MWG FRG SG
      DENO RHOO PCG PCW SO DENW SW KRG VISG
MWO KRO VISO PRES KRW
      K 'H2O' Z 'H2O' Y 'H2O' X 'H2O'
K 'CO2' Z 'CO2' Y 'CO2' X 'CO2'
K 'N2' Z 'N2' Y 'N2' X 'N2'
K 'O2' Z 'O2' Y 'O2' X 'O2'
K 'AR' Z 'AR' Y 'AR' X 'AR'
K 'H2' Z 'H2' Y 'H2' X 'H2'
K 'CO' Z 'CO' Y 'CO' X 'CO'
K 'SO2' Z 'SO2' Y 'SO2' X 'SO2'

*OUTSRF *RES *ALL
*INCLUDE 'Frio-basecase_grid00.inc'
*INCLUDE 'Frio-basecase_por00.inc'
*INCLUDE 'Frio-basecase_perms00.inc'
CPOR MATRIX 10e-6
PRPOR MATRIX 14.7

*MODEL *PR
*NC 8 8
*TRES 140.000
*COMPNAME
      'CO2'          'N2'          'O2'          'AR'
      'H2'          'CO'          'SO2'        'H2O'
*SG      4.9270000E-01  1.5852000E-01  2.1827000E-01  2.1066000E-01
      3.0130000E-02  1.6876000E-01  7.2343000E-01  1.0000000E+00
*TB      -1.5252400E+02 -3.2195100E+02 -2.9975000E+02 -3.0301000E+02
      -4.2041100E+02 -3.1493900E+02 -2.0933000E+01  2.1200000E+02
*PCRIT   7.2800000E+01  3.3500000E+01  4.9800000E+01  4.8100000E+01
      1.2958000E+01  3.4532000E+01  7.7809000E+01  2.1760000E+02
*VCRIT   1.1870000E-01  5.4949000E+00  1.5849000E+00  2.1907000E+00
      4.9901000E+00  5.5762000E+00  1.7350000E-01  5.6000000E-02
*TCRIT   3.0420000E+02  1.2620000E+02  1.5460000E+02  1.5080000E+02
      3.3190000E+01  1.3290000E+02  4.3080000E+02  6.4730000E+02
*AC      2.2500000E-01  4.0000000E-02  2.1000000E-02 -4.0000000E-03
      -2.1600000E-01  4.8000000E-02  2.4500000E-01  3.4400000E-01
*MW      4.4010000E+01  2.8014000E+01  3.1999000E+01  3.9948000E+01
      2.0160000E+00  2.8010000E+01  6.4065000E+01  1.8015000E+01
*HCFLAG  0 0 0 0
      0 0 0 0
**BIN from Dr. Pope's Report-BIN for 'H2' 'CO' 'SO2' are set equal to zero
*BIN
0
0 0
0 0 0
0 0 0 0
0 0 0 0 0
0 0 0 0 0 0
0.0042 -0.3176 0.1550 0.1429 0 0 0

*VSHIFT  1.1701100E-02 -1.7599550E-01 -1.8679150E-01 -2.0086950E-01
      -3.2642870E-01 -1.7150920E-01 -6.0226800E-02  0.234867

```

**VSHIFT FOR WATER SET EQUAL TO 0.234867 (Calculated from Kumar's Vshift correlation for water at 140F and 100000 ppm)

*VISCOR *HZYT

*MIXVC	1.0000000E+00			
*VISVC	9.4300000E-02	8.9900000E-02	7.3700000E-02	7.4900000E-02
	6.4900000E-02	9.4300000E-02	1.2170000E-01	5.6000000E-02
*VISCoeff	1.0999000E-01	1.1680000E-02	5.5730000E-02	-2.8470000E-02
	4.6700000E-03			
*OMEGA	4.5724000E-01	4.5724000E-01	4.5724000E-01	4.5724000E-01
	4.5724000E-01	4.5724000E-01	4.5724000E-01	4.5723553E-01
*OMEGE	7.7800000E-02	7.7800000E-02	7.7800000E-02	7.7800000E-02
	7.7800000E-02	7.7800000E-02	7.7800000E-02	7.7796074E-02
*PCHOR	1.2649000E+02	7.7360000E+01	8.9700000E+01	1.1412000E+02
	1.0000000E+00	7.7350000E+01	1.8650000E+02	5.2000000E+01

*PHASEID *DEN

*ROCKFLUID

RPT 1 DRAINAGE SCALING-OLD

*SWT

0	0	1	790
0.05	1E-11	0.99	671.0894325
0.1	1E-10	0.98	325.1670446
0.15	0.000000001	0.965	209.859582
0.2	0.00000001	0.955	152.2058507
0.25	0.0000001	0.93	117.6136119
0.3	0.000001 0.9		94.55211935
0.35	0.00001	0.75	78.07962469
0.4	0.0001	0.55	65.7252537
0.45	0.001	0.4	56.11629848
0.5	0.007438417	0.2048	48.4291343
0.55	0.041128264	0.0864	42.13963634
0.6	0.108130899	0.0256	36.89838804
0.65	0.206313361	0.0032	32.46348563
0.7	0.326837256	0.0001	28.66214071
0.75	0.457947732	0.000001 25.36764178	
0.8	0.588750003	0.00000001	22.48495521
0.85	0.711413919	1E-10	19.94140824
0.9	0.821582858	1E-12	17.6804776
0.95	0.917695358	1E-14	15.65753966
1	1	0	13.83689552

*SLT

0.91	0.01 0	1190	
0.915625	0.00851	0.0005609	1060
0.92125	0.0071618	0.0036447	900
0.926875	0.0059506	0.0108919	751
0.9325	0.0048714	0.0236831	610
0.938125	0.0039191	0.0432609	490
0.94375	0.0030882	0.0707757	430
0.949375	0.002373	0.1073101	360
0.955	0.0017678	0.1538931	290
0.960625	0.001266	0.21151	250
0.96625	0.0008611	0.2811098	180
0.971875	0.0005459	0.3636104	145
0.9775	0.0003125	0.4599021	120
0.983125	0.0001522	0.5708514	98
0.98875	0.0000552	0.6973033	89
0.994375	0.0000098	0.8400835	83
1	0	1	80

*HYSKRG 0.04503

RPT 2 SCALING-OLD

*SWT

0	0	1	290
0.05	1E-10	0.95	105.044278
0.1	0.00000001	0.86	50.89774296
0.15	0.000001 0.76		32.84889794
0.2	0.0001	0.65	23.82447543
0.25	0.002923977	0.5265	18.40982192
0.3	0.016391711	0.416	14.80005292
0.35	0.044319935	0.3185	12.22164649
0.4	0.088235294	0.234	10.28784166
0.45	0.147653281	0.1625	8.783771243
0.5	0.220387362	0.104	7.580514909
0.55	0.303070525	0.0585	6.596032453
0.6	0.391805812	0.026	5.775630407
0.65	0.482781457	0.0065	5.08144406
0.7	0.572718844	0.001	4.486427191
0.75	0.659104078	0.0001	3.970745905

0.8	0.740228803	0.00001	3.519524779
0.85	0.815104022	0.000001	3.121388492
0.9	0.88331325	0.0000001	2.76748957
0.95	0.94485456	0.00000001	2.450843166
1	1	0	2.165861402

```

*SLT
0.137000 0.710000 0.000000 31.0
0.190938 0.604208 0.000561 14.3
0.244875 0.508485 0.003645 7.76
0.298813 0.422490 0.010892 5.02
0.352750 0.345869 0.023683 3.8
0.406688 0.278253 0.043261 3.0
0.460625 0.219260 0.070776 2.8
0.514563 0.168486 0.107310 2.35
0.568500 0.125512 0.153893 2.28
0.622438 0.089888 0.211510 2.16
0.676375 0.061142 0.281110 2.01
0.730313 0.038760 0.363610 1.91
0.784250 0.022188 0.459902 1.86
0.838188 0.010808 0.570851 1.75
0.892125 0.003922 0.697303 1.69
0.946063 0.000693 0.840084 1.54
1.000000 0.000000 1.000000 1.4

```

```
*HYSKRG 0.276
```

```
*KROIL *STONE2 *SWSG
*INCLUDE 'Frio-basecase_rockarrays00.inc'
```

```

*INITIAL
*USER_INPUT
*INCLUDE 'Frio-basecase_initarrays00.inc'
*NUMERICAL
*DTMAX 365
*DTMIN 1.E-06
*NORM *PRESS 2000
**MAXCHANGE *GMOLAR 0.5
**MAXCHANGE *SATUR 0.5
*AIM *STAB 1
**CONVERGE *PRESS 0.15
*INCLUDE 'Frio-basecase_well00.inc'

```

IX. Appendix D: Generic and Other Cases

Table 41. List of generic cases

Case #	Field	Dissol?	Mole Fraction								Max. Plume Extension (ft) @ 50 yrs	Max. Plume Extension (ft) @ 100 yrs	Time to reach the top (years)
			CO ₂	N ₂	O ₂	Ar	CH ₄	H ₂	CO	SO ₂			
B.C.	GC Sh.	yes	100	0	0	0	0	0	0	0	4,800	9,300	30
B.C.	GC Sh.	no	100	0	0	0	0	0	0	0	6,300	12,000	25
B.C.	GC Dp.	yes	100	0	0	0	0	0	0	0	6,900	12,000	25
B.C.	GC Dp.	no	100	0	0	0	0	0	0	0	7,800	13,800	20
1	GC Sh.	yes	96	0.2	2.1	1.7	0	0	0	0	6,300	11,400	30
2	GC Dp.	yes	96	0.2	2.1	1.7	0	0	0	0	7,500	12,600	25
3	GC Sh.	yes	92.7	0.2	2.1	5	0	0	0	0	7,500	13,800	25
4	GC Dp.	yes	92.7	0.2	2.1	5	0	0	0	0	7,800	13,500	20
5	GC Sh.	yes	81.2	15	2.1	1.7	0	0	0	0	13,500	23,100	137
6	GC Dp.	yes	81.2	15	2.1	1.7	0	0	0	0	10,500	18,300	16.44
7	GC Sh.	yes	93.1	0.2	5	1.7	0	0	0	0	7,200	13,200	25
8	GC Dp.	yes	93.1	0.2	5	1.7	0	0	0	0	7,800	14,100	20
9	GC Sh.	yes	77.9	15	2.1	5	0	0	0	0	14,400	24,000	13.7
10	GC Dp.	yes	77.9	15	2.1	5	0	0	0	0	10,800	18,300	16.44
11	GC Sh.	yes	77.9	20	2.1	0	0	0	0	0	15,000	24,000	13.7
12	GC Dp.	yes	77.9	20	2.1	0	0	0	0	0	11,400	18,600	16.44
13	GC Sh.	yes	77.9	0	2.1	20	0	0	0	0	12,600	21,900	16.44
14	GC Dp.	yes	77.9	0	2.1	20	0	0	0	0	9,900	16,800	16.44
15	GC Sh.	no	96	0.2	2.1	1.7	0	0	0	0	7,500	14,100	25
16	GC Dp.	no	96	0.2	2.1	1.7	0	0	0	0	8,400	15,000	20
17	GC Sh.	no	92.7	0.2	2.1	5	0	0	0	0	8,400	15,600	20
18	GC Dp.	no	92.7	0.2	2.1	5	0	0	0	0	9,000	15,600	20

Case #	Field	Dissol?	Mole Fraction								Max. Plume Extension (ft) @ 50 yrs	Max. Plume Extension (ft) @ 100 yrs	Time to reach the top (years)
			CO ₂	N ₂	O ₂	Ar	CH ₄	H ₂	CO	SO ₂			
19	GC Sh.	no	81.2	15	2.1	1.7	0	0	0	0	14,100	26,100	13.7
20	GC Dp.	no	81.2	15	2.1	1.7	0	0	0	0	11,100	19,800	16.44
21	GC Sh.	no	93.1	0.2	5	1.7	0	0	0	0	8,700	15,600	20
22	GC Dp.	no	93.1	0.2	5	1.7	0	0	0	0	8,700	15,300	20
23	GC Sh.	no	77.9	15	2.1	5	0	0	0	0	15,600	26,100	13.7
24	GC Dp.	no	77.9	15	2.1	5	0	0	0	0	11,700	20,100	13.7
25	GC Sh.	no	77.9	20	2.1	0	0	0	0	0	15,900	28,200	11
26	GC Dp.	no	77.9	20	2.1	0	0	0	0	0	11,100	19,800	13.7
27	GC Sh.	no	77.9	0	2.1	20	0	0	0	0	12,900	22,500	13.7
28	GC Dp.	no	77.9	0	2.1	20	0	0	0	0	10,500	18,000	16.44
29	GC Sh.	yes	92	1	6.5	0.5	0	0	0	0	7,800	14,400	25
30	GC Dp.	yes	92	1	6.5	0.5	0	0	0	0	8,100	13,800	20
31	GC Sh.	yes	87.5	1	6.5	5	0	0	0	0	9,600	17,400	20
32	GC Dp.	yes	87.5	1	6.5	5	0	0	0	0	9,000	15,000	20
33	GC Sh.	yes	78	15	6.5	0.5	0	0	0	0	14,700	23,100	13.7
34	GC Dp.	yes	78	15	6.5	0.5	0	0	0	0	11,100	18,900	16.44
35	GC Sh.	yes	93.5	1	5	0.5	0	0	0	0	7,200	13,200	25
36	GC Dp.	yes	93.5	1	5	0.5	0	0	0	0	7,800	13,800	20
37	GC Sh.	yes	73.5	15	6.5	5	0	0	0	0	15,900	25,200	13.7
38	GC Dp.	yes	73.5	15	6.5	5	0	0	0	0	11,400	19,500	16.44
39	GC Sh.	yes	73.5	20	6.5	0	0	0	0	0	16,200	27,300	11
40	GC Dp.	yes	73.5	20	6.5	0	0	0	0	0	12,000	19,500	16.44
41	GC Sh.	yes	73.5	0	6.5	20	0	0	0	0	14,100	23,400	13.7
42	GC Dp.	yes	73.5	0	6.5	20	0	0	0	0	10,500	18,300	16.44
43	GC Sh.	no	92	1	6.5	0.5	0	0	0	0	9,000	16,500	20
44	GC Dp.	no	92	1	6.5	0.5	0	0	0	0	9,300	15,900	20
45	GC Sh.	no	87.5	1	6.5	5	0	0	0	0	10,800	19,200	16.44

Case #	Field	Dissol?	Mole Fraction								Max. Plume Extension (ft) @ 50 yrs	Max. Plume Extension (ft) @ 100 yrs	Time to reach the top (years)
			CO ₂	N ₂	O ₂	Ar	CH ₄	H ₂	CO	SO ₂			
46	GC Dp.	no	87.5	1	6.5	5	0	0	0	0	9,900	16,800	16.44
47	GC Sh.	no	78	15	6.5	0.5	0	0	0	0	15,300	27,300	13.7
48	GC Dp.	no	78	15	6.5	0.5	0	0	0	0	11,700	20,400	16.44
49	GC Sh.	no	93.5	1	5	0.5	0	0	0	0	8,400	15,900	20
50	GC Dp.	no	93.5	1	5	0.5	0	0	0	0	8,700	15,300	20
51	GC Sh.	no	73.5	15	6.5	5	0	0	0	0	16,500	29,100	11
52	GC Dp.	no	73.5	15	6.5	5	0	0	0	0	12,000	21,000	13.7
53	GC Sh.	no	73.5	20	6.5	0	0	0	0	0	17,100	30,300	11
54	GC Dp.	no	73.5	20	6.5	0	0	0	0	0	12,300	20,700	13.7
55	GC Sh.	no	73.5	0	6.5	20	0	0	0	0	14,700	25,800	13.7
56	GC Dp.	no	73.5	0	6.5	20	0	0	0	0	10,800	18,900	16.44
57	GC Sh.	yes	95	5	0	0	0	0	0	0	7,200	13,200	25
58	GC Dp.	yes	95	5	0	0	0	0	0	0	7,800	13,800	20
59	GC Sh.	yes	95	2.5	0	2.5	0	0	0	0	6,900	12,900	25
60	GC Dp.	yes	95	2.5	0	2.5	0	0	0	0	7,800	13,500	25
61	GC Sh.	yes	95	0	0	5	0	0	0	0	6,600	11,700	25
62	GC Dp.	yes	95	0	0	5	0	0	0	0	7,500	13,500	25
63	GC Sh.	yes	90	10	0	0	0	0	0	0	9,600	18,000	20
64	GC Dp.	yes	90	10	0	0	0	0	0	0	9,000	15,600	20
65	GC Sh.	yes	90	5	0	5	0	0	0	0	9,000	15,900	20
66	GC Dp.	yes	90	5	0	5	0	0	0	0	8,700	14,700	20
67	GC Sh.	yes	90	0	0	10	0	0	0	0	8,400	14,700	20
68	GC Dp.	yes	90	0	0	10	0	0	0	0	8,100	14,100	20
69	GC Sh.	yes	85	15	0	0	0	0	0	0	12,000	20,700	16.44
70	GC Dp.	yes	85	15	0	0	0	0	0	0	9,900	17,400	16.44
71	GC Sh.	yes	85	7.5	0	7.5	0	0	0	0	11,100	20,400	16.44
72	GC Dp.	yes	85	7.5	0	7.5	0	0	0	0	9,300	16,500	20

Case #	Field	Dissol?	Mole Fraction								Max. Plume Extension (ft) @ 50 yrs	Max. Plume Extension (ft) @ 100 yrs	Time to reach the top (years)
			CO ₂	N ₂	O ₂	Ar	CH ₄	H ₂	CO	SO ₂			
73	GC Sh.	yes	85	0	0	15	0	0	0	0	10,200	18,600	20
74	GC Dp.	yes	85	0	0	15	0	0	0	0	9,000	15,300	20
75	GC Sh.	yes	80	20	0	0	0	0	0	0	14,100	23,100	13.7
76	GC Dp.	yes	80	20	0	0	0	0	0	0	10,800	19,200	16.44
77	GC Sh.	yes	80	10	0	10	0	0	0	0	13,200	22,800	13.7
78	GC Dp.	yes	80	10	0	10	0	0	0	0	10,200	18,000	16.44
79	GC Sh.	yes	80	0	0	20	0	0	0	0	12,000	20,400	16.44
80	GC Dp.	yes	80	0	0	20	0	0	0	0	9,600	15,900	20
81	GC Sh.	yes	75	25	0	0	0	0	0	0	16,200	25,200	13.7
82	GC Dp.	yes	75	25	0	0	0	0	0	0	11,700	20,100	16.44
83	GC Sh.	yes	75	12.5	0	12.5	0	0	0	0	15,000	24,300	13.7
84	GC Dp.	yes	75	12.5	0	12.5	0	0	0	0	11,100	18,600	16.44
85	GC Sh.	yes	75	0	0	25	0	0	0	0	13,500	23,400	13.7
86	GC Dp.	yes	75	0	0	25	0	0	0	0	10,200	16,800	16.44
117	GC Sh.	yes	95	5	0	0	0	0	0	0	7,200	13,200	25
118	GC Dp.	yes	95	5	0	0	0	0	0	0	7,800	13,800	20
119	GC Sh.	yes	95	2.5	2.5	0	0	0	0	0	6,900	12,300	25
120	GC Dp.	yes	95	2.5	2.5	0	0	0	0	0	7,800	13,500	25
121	GC Sh.	yes	95	0	5	0	0	0	0	0	6,600	12,300	25
122	GC Dp.	yes	95	0	5	0	0	0	0	0	7,800	13,500	25
123	GC Sh.	yes	90	10	0	0	0	0	0	0	9,600	18,000	20
124	GC Dp.	yes	90	10	0	0	0	0	0	0	9,000	15,600	20
125	GC Sh.	yes	90	5	5	0	0	0	0	0	9,300	16,800	20
126	GC Dp.	yes	90	5	5	0	0	0	0	0	8,700	14,700	20
127	GC Sh.	yes	90	0	10	0	0	0	0	0	8,700	15,600	20
128	GC Dp.	yes	90	0	10	0	0	0	0	0	8,400	14,400	20
129	GC Sh.	yes	85	15	0	0	0	0	0	0	12,000	20,700	16.44

Case #	Field	Dissol?	Mole Fraction								Max. Plume Extension (ft) @ 50 yrs	Max. Plume Extension (ft) @ 100 yrs	Time to reach the top (years)
			CO ₂	N ₂	O ₂	Ar	CH ₄	H ₂	CO	SO ₂			
130	GC Dp.	yes	85	15	0	0	0	0	0	0	9,900	17,400	16.44
131	GC Sh.	yes	85	7.5	7.5	0	0	0	0	0	11,400	20,400	16.44
132	GC Dp.	yes	85	7.5	7.5	0	0	0	0	0	9,600	16,500	20
133	GC Sh.	yes	85	0	15	0	0	0	0	0	10,500	19,200	16.44
134	GC Dp.	yes	85	0	15	0	0	0	0	0	9,300	16,200	20
135	GC Sh.	yes	80	20	0	0	0	0	0	0	14,100	23,100	13.7
136	GC Dp.	yes	80	20	0	0	0	0	0	0	10,800	19,200	16.44
137	GC Sh.	yes	80	10	10	0	0	0	0	0	13,500	21,600	13.7
138	GC Dp.	yes	80	10	10	0	0	0	0	0	10,500	17,700	16.44
139	GC Sh.	yes	80	0	20	0	0	0	0	0	12,300	21,300	16.44
140	GC Dp.	yes	80	0	20	0	0	0	0	0	9,900	17,100	20
141	GC Sh.	yes	75	25	0	0	0	0	0	0	16,200	25,200	13.7
142	GC Dp.	yes	75	25	0	0	0	0	0	0	11,700	20,100	16.44
143	GC Sh.	yes	75	12.5	12.5	0	0	0	0	0	15,300	25,200	13.7
144	GC Dp.	yes	75	12.5	12.5	0	0	0	0	0	11,400	19,500	16.44
145	GC Sh.	yes	75	0	25	0	0	0	0	0	14,100	22,200	13.7
146	GC Dp.	yes	75	0	25	0	0	0	0	0	10,800	18,300	16.44
177	GC Sh.	yes	95	5	0	0	0	0	0	0	7,200	12,900	25
178	GC Dp.	yes	95	5	0	0	0	0	0	0	7,800	13,800	20
179	GC Sh.	yes	95	2.5	0	0	2.5	0	0	0	6,900	12,900	25
180	GC Dp.	yes	95	2.5	0	0	2.5	0	0	0	7,800	14,100	25
181	GC Sh.	yes	95	0	0	0	5	0	0	0	6,600	12,300	25
182	GC Dp.	yes	95	0	0	0	5	0	0	0	7,800	13,500	25
183	GC Sh.	yes	90	10	0	0	0	0	0	0	9,600	18,000	20
184	GC Dp.	yes	90	10	0	0	0	0	0	0	9,000	15,600	20
185	GC Sh.	yes	90	5	0	0	5	0	0	0	9,000	15,600	20
186	GC Dp.	yes	90	5	0	0	5	0	0	0	8,700	15,000	20

Case #	Field	Dissol?	Mole Fraction								Max. Plume Extension (ft) @ 50 yrs	Max. Plume Extension (ft) @ 100 yrs	Time to reach the top (years)
			CO ₂	N ₂	O ₂	Ar	CH ₄	H ₂	CO	SO ₂			
187	GC Sh.	yes	90	0	0	0	10	0	0	0	8,100	15,000	25
188	GC Dp.	yes	90	0	0	0	10	0	0	0	8,400	15,000	20
189	GC Sh.	yes	85	15	0	0	0	0	0	0	12,000	21,300	16.44
190	GC Dp.	yes	85	15	0	0	0	0	0	0	9,900	17,100	16.44
191	GC Sh.	yes	85	7.5	0	0	7.5	0	0	0	11,100	19,200	16.44
192	GC Dp.	yes	85	7.5	0	0	7.5	0	0	0	9,600	16,800	20
193	GC Sh.	yes	85	0	0	0	15	0	0	0	9,900	17,400	20
194	GC Dp.	yes	85	0	0	0	15	0	0	0	9,300	16,200	20
195	GC Sh.	yes	80	20	0	0	0	0	0	0	14,400	24,600	13.7
196	GC Dp.	yes	80	20	0	0	0	0	0	0	10,800	18,900	16.44
197	GC Sh.	yes	80	10	0	0	10	0	0	0	13,200	22,200	13.7
198	GC Dp.	yes	80	10	0	0	10	0	0	0	10,500	18,000	16.44
199	GC Sh.	yes	80	0	0	0	20	0	0	0	11,700	20,400	16.44
200	GC Dp.	yes	80	0	0	0	20	0	0	0	10,200	17,700	16.44
201	GC Sh.	yes	75	25	0	0	0	0	0	0	16,200	25,800	13.7
202	GC Dp.	yes	75	25	0	0	0	0	0	0	12,000	20,700	16.44
203	GC Sh.	yes	75	12.5	0	0	12.5	0	0	0	15,000	24,300	13.7
204	GC Dp.	yes	75	12.5	0	0	12.5	0	0	0	11,700	19,800	16.44
205	GC Sh.	yes	75	0	0	0	25	0	0	0	13,500	21,900	13.7
206	GC Dp.	yes	75	0	0	0	25	0	0	0	11,100	18,900	16.44
237	GC Sh.Res	yes	100	0	0	0	0	0	0	0	-	-	5
238	GC Sh.Res	yes	96	0.2	2.1	1.7	0	0	0	0	-	-	3.5
239	GC Sh.Res	yes	92	1	6.5	0.5	0	0	0	0	-	-	2.7
240	GC Sh.	yes	100	0	0	0	0	0	0	0	6,000	8,400	30
241	GC Dp.	yes	100	0	0	0	0	0	0	0	7,200	10,200	25
242	GC Sh.	yes	96	0.2	2.1	1.7	0	0	0	0	6,600	9,300	25

Case #	Field	Dissol?	Mole Fraction								Max. Plume Extension (ft) @ 50 yrs	Max. Plume Extension (ft) @ 100 yrs	Time to reach the top (years)
			CO ₂	N ₂	O ₂	Ar	CH ₄	H ₂	CO	SO ₂			
243	GC Dp.	yes	96	0.2	2.1	1.7	0	0	0	0	7,500	10,500	20
244	GC Sh.	yes	92	1	6.5	0.5	0	0	0	0	7,500	10,800	20
245	GC Dp.	yes	92	1	6.5	0.5	0	0	0	0	8,100	13,500	20
246	GC Dp.	yes	100	0	0	0	0	0	0	0	6,900	16,200	20
247	GC Dp.	yes	96	0.2	2.1	1.7	0	0	0	0	7,800	18,000	20
248	GC Dp.	yes	92	1	6.5	0.5	0	0	0	0	8,700	19,200	20
249	GC Dp.	yes	100	0	0	0	0	0	0	0	7,200	7,800	-
250	GC Dp.	yes	96	0.2	2.1	1.7	0	0	0	0	7,500	8,100	-
251	GC Dp.	yes	92	1	6.5	0.5	0	0	0	0	7,500	8,100	-
252	GC Dp.	yes	100	0	0	0	0	0	0	0	5,400	5,400	90
253	GC Dp.	yes	96	0.2	2.1	1.7	0	0	0	0	5,400	5,400	80
254	GC Dp.	yes	92	1	6.5	0.5	0	0	0	0	5,400	5,700	80
255	GC Sh.	yes	100	0	0	0	0	0	0	0	4,800	10,500	30
256	GC Sh.	yes	96	0.2	2.1	1.7	0	0	0	0	5,700	15,300	25
257	GC Sh.	yes	92	1	6.5	0.5	0	0	0	0	8,400	19,800	20
258	GC Sh.	yes	100	0	0	0	0	0	0	0	6,600	6,900	-
259	GC Sh.	yes	96	0.2	2.1	1.7	0	0	0	0	6,600	7,200	-
260	GC Sh.	yes	92	1	6.5	0.5	0	0	0	0	7,200	7,500	-
261	GC Sh.	yes	100	0	0	0	0	0	0	0	4,800	5,100	-
262	GC Sh.	yes	96	0.2	2.1	1.7	0	0	0	0	5,100	5,400	90
263	GC Sh.	yes	92	1	6.5	0.5	0	0	0	0	5,400	5,400	80
266	GC Dp. Res	yes	100	0	0	0	0	0	0	0	10,200	12,600	-
267	GC Dp. Res	yes	96	0.2	2.1	1.7	0	0	0	0	10,500	12,600	-
268	GC Dp. Res	yes	92	1	6.5	0.5	0	0	0	0	10,500	12,900	-
269	GC Dp. Res	yes	100	0	0	0	0	0	0	0	12,900	15,600	-
270	GC	yes	96	0.2	2.1	1.7	0	0	0	0	13,200	15,900	-

Case #	Field	Dissol?	Mole Fraction								Max. Plume Extension (ft) @ 50 yrs	Max. Plume Extension (ft) @ 100 yrs	Time to reach the top (years)
			CO ₂	N ₂	O ₂	Ar	CH ₄	H ₂	CO	SO ₂			
	Dp.Res												
271	GC Dp.Res	yes	92	1	6.5	0.5	0	0	0	0	13,500	15,900	-

Note: B.C. = base case; GC Sh. = Gulf Coast Shallow; GC Dp. = Gulf Coast Deep

